

Modeling and Simulation of an Alkaline Fuel Cell

Von der Fakultät für Ingenieurwissenschaften, Abteilung Maschinenbau und Verfahrenstechnik
der

Universität Duisburg-Essen
zur Erlangung des akademischen Grades

eines
Doktors der Ingenieurwissenschaften

Dr.-Ing.
genehmigte Dissertation

von

Felix Andreas Emanuel Kunz
aus
Düsseldorf

Gutachter: Prof. Dr. rer. nat. Angelika Heinzel
Prof. Dr. rer. nat. Werner Lehnert
Tag der mündlichen Prüfung: 16.07.2019

To my wife.

Acknowledgements

This dissertation has been developed in the course of my activities at the Chair of Energy Technology at the University of Duisburg-Essen, Germany, and the project cooperation between the Chair of Energy Technology and the British company AFC Energy PLC.

First of all, I would like to thank Prof. Dr. rer. nat. Angelika Heinzl for giving me the possibility of developing both personally and scientifically over the last five years. Being also the CEO of the hydrogen and fuel cell center (Zentrum für BrennstoffzellenTechnik (ZBT)) in Duisburg, Germany, her interesting activities in the field of fuel cells and her faith in the promising future of fuel cells motivated and inspired me. I would also like to thank Dr.-Ing. Jürgen Roes for his support and his helpful suggestions. In the last years, he has been a valuable advisor to me.

I would like to thank my colleagues at the Chair of Energy Technology for the great team spirit, the constructive discussions, and their collegial support. I am particularly grateful to Florian Nigbur, Christoph Hütten, Dr. rer. nat. Christoph Müller, Dr.-Ing. Sascha Dobrowolny, Dr.-Ing. Kari Holve, Nicolas Witte, and Othmar Verheyen.

Furthermore, I would like to thank AFC Energy for the good project cooperation and the Fuel Cells and Hydrogen Joint Undertaking (FCH-JU) for the financial support, which made the projects happen; special thanks are directed to Dr. Naveed Akhtar for the data exchange and the interesting conversations.

I would like to thank Prof. Dr. Ryan O'Hayre of the Department of Metallurgical and Materials Engineering at the Colorado School of Mines and Prof. Dr. John Newman of the Department of Chemical Engineering at the University of California for being interested in my work and for being outstanding mentors to me. The enlightening conversations have influenced my understanding of electrochemistry significantly.

Finally, I would like to thank my loved family and friends for the understanding and the support. In particular, I would like to thank my brother Robert and my sister Victoria for their encouragement. Also, special thanks are directed to my wife Melanie for her love, her faith and her trust in my work. Her support has made this dissertation possible.

Zusammenfassung

Die alkalische Brennstoffzelle (AFC) stellt ein vielversprechendes Energiesystem im Sinne der Energiewende dar, da sie lediglich Wasser emittiert und über das Potential verfügt, sehr effizient und kostengünstig zu sein. Ihr wohl bekanntester Anwendungsfall ist der Einsatz einer AFC zur Stromversorgung des Raumschiffs in der Apollo Mission der NASA. Für konventionellere Anwendungsbereiche jedoch, muss die AFC insbesondere in Bezug auf ihre Leistungsdichte, Lebensdauer und Herstellungskosten verbessert werden.

In dieser Dissertation wurde ein zweidimensionales (2-D), mathematisches Modell einer AFC mit der Software COMSOL Multiphysics[®] für den stationären Betrieb entwickelt. Das Modell berücksichtigt den Transport von Spezies, Masse, Impuls, Ladung und Energie. Die Kinetik der Elektrodenreaktionen ist auf Grundlage der Butler-Volmer Gleichung und unter Berücksichtigung der Temperaturabhängigkeiten der Austauschstromdichten und der Übertragungskoeffizienten modelliert. Der Ionentransport im Elektrolyten ist basierend auf der Theorie des konzentrierten Elektrolyten beschrieben, wobei die Transporteigenschaften für die Verwendung in der Nernst-Planck Gleichung angepasst wurden.

Das Modell wird durch den Vergleich der prognostizierten Polarisationskurve mit Messungen validiert und durch die Begutachtung der Gradienten und die Diskussion der physikalischen Prozesse in der Zelle verifiziert. Dabei wird die Bedeutung der Kathodenperformance für das Verhalten der Gesamtzelle herausgearbeitet. Um Optimierungspotentiale zu erschließen und die Empfindlichkeit des Modells zu untersuchen, werden gezielt Parameterstudien durchgeführt. Dabei stellt sich heraus, dass für die betrachtete Zelle unter den gewählten Referenzbetriebsbedingungen (60 °C, 1 atm, H₂ auf der Anodenseite, und Luft auf der Kathodenseite) die optimale Elektrolytkonzentration bezüglich der Zellperformance im Bereich von 3 M KOH liegt. Darüber hinaus werden die Erhöhung des Drucks und die Steigerung der Temperatur als effektive Strategien zur Verbesserung der Zellperformance verifiziert. Der Einfluss der Temperaturabhängigkeiten der kinetischen Parameter wird individuell untersucht. Dabei stellt sich heraus, dass insbesondere die Temperaturabhängigkeit der Kathodenaustauschstromdichte in mathematischen Modellen nicht vernachlässigt werden sollte. Die Untersuchung der Sensitivität des Modells in Bezug auf katalysatorspezifische Parameter zeigt, dass die Forschung auf dem Gebiet der Katalysatoren für die Sauerstoffreduktionsreaktion (ORR) in alkalischen Medien sehr vielversprechend ist und die Zelleistung stark verbessern könnte.

Folglich ermöglicht das in dieser Dissertation entwickelte AFC-Modell die Untersuchung der physikalischen Prozesse in der Zelle und das Identifizieren von Optimierungspotenzialen. Dies ermöglicht AFCs für verschiedene Anwendungsbereiche zu entwickeln, womit der wirtschaftliche Erfolg der AFC sichergestellt und ein Beitrag zum Erfolg der Energiewende geleistet wird.

Abstract

The alkaline fuel cell (AFC) is a promising energy system in the sense of the energy transition, as it only emits water and has the potential to be very efficient and cost-effective. Its best-known application is probably the use of an AFC to power the spacecraft in NASA's Apollo mission. However, for more conventional applications the AFC needs to be improved in terms of power density, lifetime and manufacturing costs.

In this dissertation a two-dimensional (2-D) mathematical model of an AFC has been developed with the software COMSOL Multiphysics® for stationary operation. The model considers the transport of species, mass, momentum, charge and energy. The kinetics of the electrode reactions is modelled on the basis of the Butler-Volmer expression and taking into account the temperature dependences of the exchange current densities and of the transfer coefficients. The transport of ions in the electrolyte is described based on the concentrated electrolyte theory, by adapting the transport properties for use in the Nernst-Planck equation.

The model is validated by comparing the predicted polarization curve with measurements and verified by examining the gradients and discussing the physical processes in the cell. The significance of the cathode performance for the behavior of the entire cell is worked out. In order to find optimization potentials and to investigate the sensitivity of the model, specific parameter studies are carried out. It turns out that, under the selected base case conditions (60 °C, 1 atm, H₂ on the anode side, and air on the cathode side), the optimal electrolyte concentration with respect to cell performance is in the range of 3 M KOH. In addition, the increases in pressure and temperature are verified as effective strategies to improve the cell performance. The influence of the temperature dependences of the kinetic parameters are investigated individually. It turns out that particularly the temperature dependence of the cathode exchange current density should not be neglected in mathematical models. The investigation of the sensitivity of the model with respect to parameters specific to the catalysts shows that research in the field of catalysts for the oxygen reduction reaction (ORR) in alkaline media is very promising and could strongly improve cell performance.

Consequently, the AFC model developed in this dissertation allows the investigation of the physical processes in the cell and the identification of optimization potentials. This enables the development of AFCs for different applications, thus ensuring the economic success of the AFC and contributing to the success of the energy transition.

Table of Contents

1. INTRODUCTION.....	1
2. FUNDAMENTALS	3
2.1 THE PRINCIPLE OF A FUEL CELL	3
2.2 THE HISTORY OF THE FUEL CELL	5
2.3 FUEL CELL TYPES	8
2.4 THE DESIGN OF AN AFC.....	10
2.5 AFCs TODAY	12
2.6 CELL VOLTAGE AND POLARIZATION CURVE	13
2.7 THERMODYNAMICS.....	15
2.7.1 Thermodynamic quantities	15
2.7.2 Ideal cell voltage	17
2.7.3 Nernst equation	19
2.8 KINETICS.....	21
2.8.1 Surface overpotential	23
2.8.2 Concentration dependent kinetics	28
2.8.3 Concentration and temperature dependent kinetics	29
2.8.4 Simplified kinetics	33
2.8.5 Determination of the kinetic parameters.....	36
2.9 TRANSPORT PHENOMENA IN ELECTROLYTES	38
2.9.1 Diluted theory	40
2.9.2 Concentrated theory	43
3. FORMER AFC MODELS WITH IMPACT ON THIS WORK.....	49
4. MATHEMATICAL MODELING.....	57
4.1 CELL VOLTAGE AND ELECTRICAL POTENTIALS.....	63
4.2 KINETICS.....	66
4.3 MOMENTUM EQUATION.....	69
4.4 SPECIES TRANSPORT IN THE GAS PHASE	70
4.5 GAS/LIQUID INTERFACE	72
4.6 TRANSPORT OF HYDROGEN AND OXYGEN TO THE CATALYSTS	75
4.7 SPECIES TRANSPORT IN THE ELECTROLYTE SOLUTION.....	78
4.8 MASS SOURCES AND SINKS.....	81
4.9 CHARGE TRANSPORT	84
4.10 HEAT TRANSPORT	86
4.11 PROPERTIES	89

4.11.1 Gas phase.....	89
4.11.2 Gas transport into and through the electrolyte.....	92
4.11.3 KOH electrolyte.....	94
4.11.4 Electrodes	104
4.12 BOUNDARY CONDITIONS.....	106
4.12.1 Momentum transport	106
4.12.2 Species transport in the gas phase	107
4.12.3 Species transport in the liquid phase	107
4.12.4 Charge transport	107
4.12.5 Heat transport	108
4.12.6 Designed gas velocity.....	108
4.12.7 Reference concentrations.....	109
5. SIMULATION AND DISCUSSION	111
5.1 COMPARISON WITH MEASUREMENTS	114
5.2 ANALYSIS OF THE CELL PERFORMANCE	116
5.2.1 Electrolyte concentration.....	116
5.2.2 Temperature distribution	118
5.2.3 Anodic and cathodic gas compositions	120
5.2.4 Analysis of the potential losses	122
5.3 INTERIM CONCLUSION.....	127
5.4 PARAMETER STUDY	129
5.4.1 Electrolyte concentration.....	129
5.4.2 Operating pressure	135
5.4.3 Operating temperature	136
5.4.4 Temperature dependence of kinetic parameters	140
5.4.5 Kinetic parameter	143
5.4.6 Electrolyte film.....	148
6. CONCLUSION	151
7. RECOMMENDATIONS AND OUTLOOK.....	154
REFERENCES	155
LIST OF FIGURES.....	165
LIST OF TABLES	166
LIST OF ABBREVIATIONS	167
LIST OF SYMBOLS	168
SCIENTIFIC CONTRIBUTIONS	176

1. Introduction

Increasing sense of responsibility towards the environment and the future generations motivate the energy transition from fossil and nuclear fuels to renewable energies. Especially the global warming effect due to greenhouse gas emissions, the limitations of fossil and nuclear fuels, the unsolved problem of final disposal of radioactive waste, and the potential danger of nuclear power plants give cause for concerns. Therefore, only clean and secure energy sources can be the future.

In 2000, the German Renewable Energy Sources Act (EEG) entered into effect for the first time and an amended version is valid until today. It pursues rising the power generation from renewable energies and reducing greenhouse gas emissions, for example by assuring renewable energy systems of a financial support. While it was only ca. 6.60 % by 2000, the share of renewables in the gross electricity production has increased up to the year 2018 to ca. 35.20 % [1]. This is particularly due to the replacement of hard-coal and nuclear power by wind energy and photovoltaic. The latest amendment (EEG 2017) aims “to increase the proportion of electricity generated from renewable energy sources as a percentage of gross electricity consumption to 40 to 45 percent by 2025, 55 to 60 percent by 2035, and at least 80 percent by 2050” [2]. As a consequence, in order to achieve these goals in the future, the generation capacity of renewable energy systems must be further expanded.

One highly promising energy system is the fuel cell, being reliable and sustainable. The power generation from a fossil fuel requires typically three energy transformations: First the energy stored in the fossil fuel must be converted into heat (in a combustion chamber), which can then be converted into mechanical energy (in a turbine), and can finally be converted into electrical energy (via an electric generator). In contrast, the fuel cell converts the energy stored in the fuel directly into electrical energy and is therefore much more effective than a conventional energy system such as a combustion engine. Besides electrical power, heat is produced by a fuel cell, so that it can be used as combined heat and power system (CHP), for example for domestic energy supply. In contrast to batteries, where the active components are integrated in the system, a fuel cell can operate as long as fuel and oxidant are fed to the cell. Consequentially, the characteristics of a fuel cell make it particularly attractive for decentralized and mobile applications.

The alkaline fuel cell (AFC) is a hydrogen-oxygen fuel cell with an alkaline electrolyte sandwiched in between the two electrodes of the cell. Besides pure hydrogen cracked ammonia can be fed to the anode, because the AFC would tolerate rest ammonia in the gas. As the potassium hydroxide (KOH) electrolyte of the AFC is poisoned by carbon dioxide, it is generally recommended to feed pure oxygen to the cathode. Compared with other types of fuel cells, the AFC is characterized by an “improved cathode performance, nonprecious metal catalyst potential”, and “inexpensive [...] materials” [3]. The electrolyte can be immobilized (stagnant), for example by being fixed in a matrix, but also circulating (flowing), adding the advantage of a targeted heat management. Additionally, “the exchangeability of the KOH makes it possible to operate on air with less complete removal of CO₂” [4]. Due to its relatively high power density with respect to volume and weight, the AFC has become attractive for space applications and was used for primary electric power supply by the U.S. National Aeronautics and Space Administration (NASA) in the Apollo program and in the Space Shuttle Orbiter. However, for more conventional applications, AFC must be enhanced especially with respect to power density, lifetime, and manufacturing costs.

Experimental studies can become laborious and expensive which may decelerate the progress of research and development. At this point mathematical models can help by replacing experiments and giving deeper insights into the physical processes. Aiming at investigating the processes in an AFC and finding improvement potentials, a two-dimensional (2-D) model of an AFC has been developed in this dissertation, whereas the software COMSOL Multiphysics[®] has been used. The model takes into consideration the transport of species, mass, momentum, charge, and energy and predicts the cell performance under steady state conditions. Kinetics is described temperature dependently by considering the temperature dependences of the exchange current densities and of the transfer coefficients. The transport of ions in the electrolyte is described based on the concentrated electrolyte theory by adapting the transport properties for the use in the Nernst-Planck equation. The model enables investigating the physical processes in the cell and finding improvement potentials. Therefore, it can help improving the economic success of AFCs and can contribute to the success of the energy transition from fossil and nuclear fuels to renewable energies.

2. Fundamentals

This chapter aims at introducing into fuel cell technology and providing a basic understanding of the AFC. For this purpose, it starts with the functional principle of a fuel cell in chapter 2.1 for creating a basic understanding of the processes taking place in a fuel cell and continues with the history of the fuel cell in chapter 2.2. After the presentation of the most common fuel cell types in chapter 2.3, typical designs of AFCs and companies currently working on the commercialization of the AFC are presented in chapter 2.4 and chapter 2.5, respectively. After that, in chapter 2.6 the relationship between the cell voltage and the electrical current density is explained, whereby the meaning of the overpotentials is focused. In order to understand the electrochemistry of a fuel cell, thermodynamics and kinetics are required, which are considered in chapter 2.7 and chapter 2.8, respectively. The electrolyte is an essential component of a fuel cell, thus the transport of ions in diluted and concentrated solutions is discussed in chapter 2.9.

2.1 The principle of a fuel cell

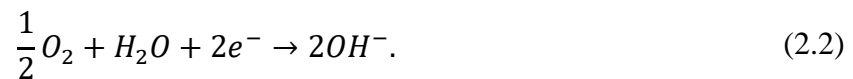
A fuel cell is an electrochemical device consisting of two electrodes and an electrolyte in between. It belongs to the category of the galvanic cells which convert chemical energy directly into electrical energy, whereas a system that works in the opposite direction is called electrolytic cell. When the electrodes of an electrochemical device are externally connected by an electrical conductive material, electrical current is produced at the one electrode, the anode, and consumed at the other electrode, the cathode¹. In case of a fuel cell, the transport of charge in the external circuit occurs spontaneously so that a load can be applied to the cell. The opposite is the case for an electrolytic cell where energy must be supplied to the system, for example via a voltage source. Typically, fuel cells operate due to heterogeneous reactions. In contrast to batteries, where the active components are integrated in the system, in case of a fuel cell the reactants must be fed to the cell for operating [5]. This is an advantage because fuel cells are not limited by an internal reservoir and can operate as long as reactants are fed to the cell. Therefore, fuel cells can neither be charged nor discharged.

¹ The anode is the electrode where the oxidation reaction occurs in which negative charge is transferred from the electrolyte to the electrode. The cathode is the electrode where the reduction reaction arises in which negative charge is transferred from the electrode to the electrolyte. Focusing a fuel cell the names anode and cathode can be used for addressing an electrode even if the cell is not under load, e.g. under equilibrium conditions. Then the name anode means the electrode which is supposed to behave as an anode under load and the name cathode means the electrode which is supposed to behave as a cathode under load. However, if a cell is considered which can be operated in both directions, as a galvanic cell as well as an electrolytic cell, it is suggested to address the electrodes by other names, for example by the names left electrode and right electrode.

The principle of a fuel cell is pictured in Figure 2.1 at the example of an AFC. The fuel which is fed to the anode and the oxidant which is fed to the cathode diffuse through the gas pores of the porous anode and the porous cathode, respectively, in the direction to the electrolyte. At the triple phase boundary (TPB), created between the gaseous reactants, the solid electrode, and the liquid electrolyte, the reactants are consumed in the electrochemical reactions. In case of the AFC, the hydrogen oxidation reaction (HOR) at the anode can be written as



and the oxygen reduction reaction (ORR) at the cathode can be given as



According to the overall reaction of the hydrogen-oxygen fuel cell, given by equation (2.3), water is the only emission, thus it operates absolutely environmentally friendly:



While the electrons are the charge carriers in the external circuit, bringing the negative charge from the anode to the cathode, ions are the charge carriers in the cell. Even if the actual reaction mechanism might be much more complicated, the processes at the anode and the cathode can generally be described by one oxidation reaction (anode half-cell reaction or anode reaction) and one reduction reaction (cathode half-cell reaction or cathode reaction), respectively.

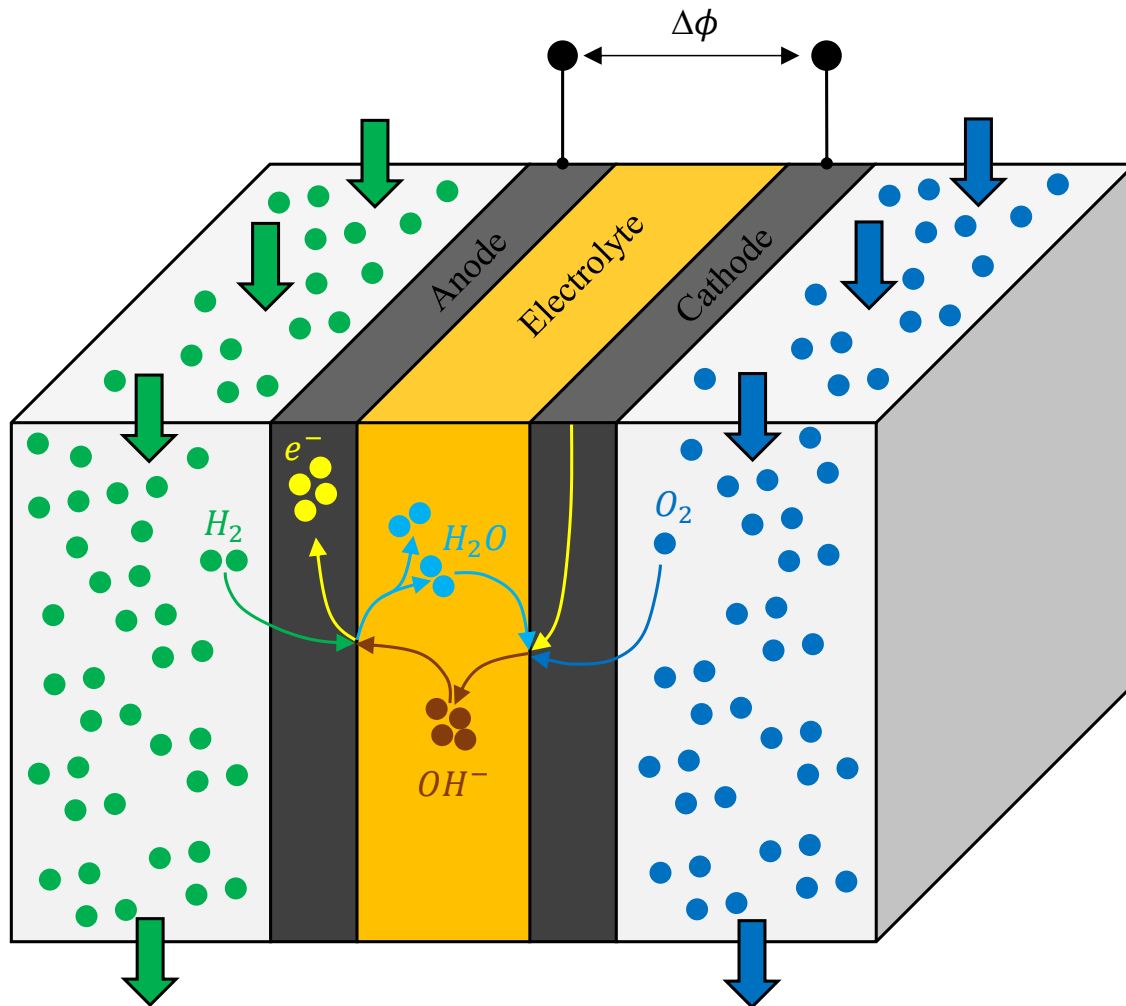


Figure 2.1: Fuel cell operating principle at the example of an AFC.

2.2 The history of the fuel cell

After Christian Friedrich Schönbein discovered the principle of a fuel cell in 1838, Sir William Robert Grove invented the first fuel cell in 1839. When he presented his invention in 1842, he called the device consisting of fifty cells “gaseous voltaic battery” [6]. As illustrated in Figure 2.2, each cell consisted of two glass tubes with platinum electrodes inside immersed in sulfuric acid, whereas one glass tube contained hydrogen and the other oxygen. As the contact area between gas, electrolyte, and electrode was too low to generate enough power to compete with other galvanic cells, Grove decided not to continue his research on the gas voltaic battery [6].

When Ludwig Mond and Carl Langer continued Grove’s work in 1889, they used the name “fuel cell” for the first time [6]. The scientists tried to make Grove’s invention more practical by replacing oxygen with air, hydrogen with Mond gas, and the electrolyte solution by a matrix electrolyte [6]. The result was a fuel cell that provided up to 1.82 W power at ca.

50 % efficiency [7]. However, due to the high costs of the platinum catalyst, which became rapidly poisoned because of the carbon monoxide in the Mond gas, and high polarization losses, they decided that their cell was also not practical and abandoned further research on their cell [6].

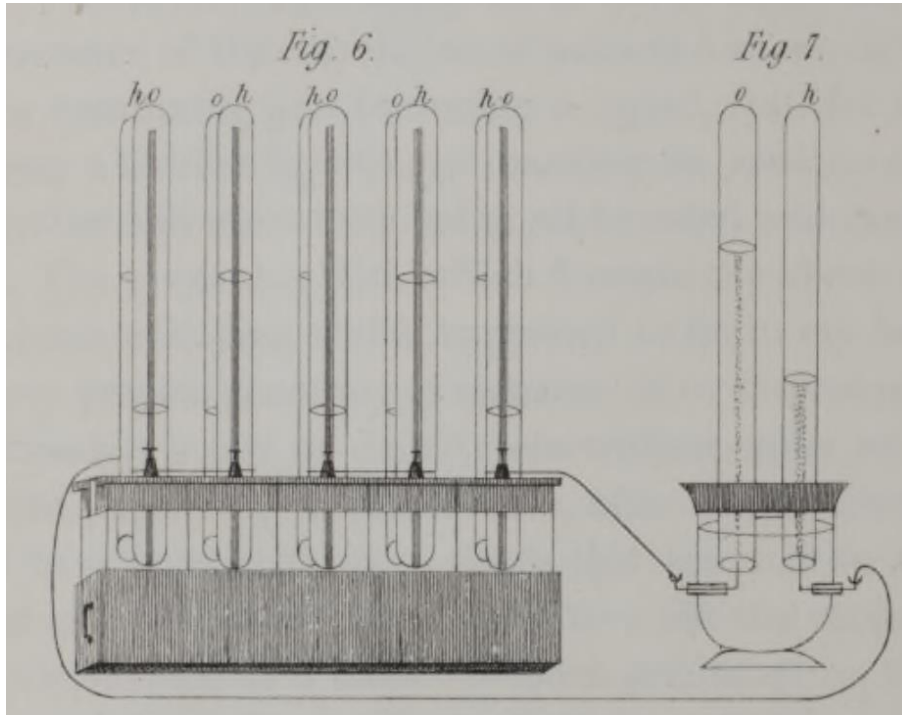


Figure 2.2: Gas voltaic battery by Sir William Robert Grove (taken from [8]; © The Royal Society).

In the following years several attempts to develop a practical fuel cell were unsuccessful until 1932, when Francis Thomas Bacon started his work in this field based on Langer's and Mond's studies. After more than twenty years, Bacon demonstrated a 5 kW fuel cell system in 1959. Identifying the expensive platinum catalyst to be the reason for the unsuccessfulness of fuel cells in the past, Bacon chose nickel electrodes and used a less corrosive alkaline electrolyte instead of an acidic; this was the birth of the AFC. At the high operating temperature of ca. 205 °C, the catalytic behavior of nickel was sufficient enough so that no additional catalysts were needed. In order to prevent electrolyte boiling on the one hand and improving the cell performance on the other, Bacon raised the pressure to ca. 40 MPa. Porous electrodes were used for obtaining large contact surface areas for the electrochemical reactions, whereas they consisted of two layers for managing the gas-liquid interface and preventing electrolyte flooding into the gas compartment (coarse pore side on the gas side, fine-pore side on the electrolyte side). [6]

From then on, the interest in fuel cell technology increased and considerable progress was made. AFC systems were presented in 1959 by Harry Karl Ihring of the Allis-Chalmers Manufacturing Company in the form of a tractor with a 15 kW fuel cell stack, in 1967 by Union Carbide Corp. (UCC) in the form of the 125 kW system that powered the 'Electrovan' of the General Motors Corp, in 1970 by Kordesch in the form of the Austin A-40 powered by a 6 kW H₂ / Air-fuel cell / lead acid battery hybrid system, and also in 1970 by Siemens in the form of a 7 kW system for submarine applications [9].

Due to the relative high power density, fuel cells also have become attractive as primary electrical power source in space applications so that the NASA started a huge research and development program on fuel cells involving industry and universities [6]. As a result, a proton exchange membrane fuel cell (PEMFC), developed by General Electric, was used in the Gemini Program (1960s) and an AFC, developed by Pratt & Whitney Aircraft Division of United Aircraft Corporation on the basis on Bacon's cell, was used in the well-known Apollo program (1960s and 1970s) [6]. These applications were probably the most historic ones in the fuel cell history.

Despite successful applications of fuel cells, the commercialization slowed down. This was especially attributable to the short lifetime, high costs, and the complexity of the fuel cell systems compared to conventional energy converter such as the combustion engine. When the interest in alternative energy systems raised all over the world during the oil crises in 1973 and 1979, not only the USA but also European and Asian countries invested their finances in the research and development of fuel cells [6]. Since then, different fuel cell types have been successfully developed and introduced to the market. Fuel cells which operate at low temperatures are particularly interesting for mobile applications. However, due to the low temperature level most of them require noble metal catalysts which makes them too expensive to compete with conventional energy systems. Fuel cells which operate at higher temperatures are very attractive for combined heat and power generation and therefore for decentralized applications. However, the required temperature resistant materials cause them also to be too expensive. Consequentially, research in the field of fuel cells goes on, whereby the research focus varies dependently on the fuel cell type.

2.3 Fuel cell types

Fuel cells are typically named after their electrolyte. The most common fuel cells are the Polymer Electrolyte Membrane Fuel Cell (PEMFC), also called Proton Exchange Membrane Fuel Cell, the Direct Methanol Fuel Cell (DMFC), the Phosphoric Acid Fuel Cell (PAFC), the Alkaline Fuel Cell (AFC), the Molten Carbonate Fuel Cell (MCFC), and the Solid Oxide Fuel Cell (SOFC). Their characteristics are given in Table 2.1 and described in the following based on [6], [3], [10], [11] and [12].

The PEMFC performs at relatively low temperatures between 60 and 200 °C. It consumes hydrogen on the anode side and oxygen on the cathode side. The charge carriers in the polymer membrane electrolyte are H^+ ions. Reaching the highest power density of all fuel cells, it is particularly interesting for mobile applications. However, the water management is very complicated, and the manufacturing costs of the cell are relatively high, not least because of the required platinum catalysts.

The DMFC operates between only 30 and 80 °C. It consumes methanol and water on the anode side and oxygen on the cathode side. Similar to the PEMFC, the DMFC uses a membrane electrolyte in which H^+ ions bring the positive charge from the anode to the cathode. Also similar to the PEMFC, platinum is used as catalyst, whereas the kinetics of the methanol oxidation reaction is worse than the kinetics of the HOR. The advantage of the DMFC is the direct conversion of methanol with no previous reforming. However, carbon monoxide can occur as product of a side reaction poisoning the catalyst.

The PAFC works between 180 and 200 °C and uses the same electrochemical reactions as the PEMFC when hydrogen is consumed in the anode reaction, oxygen is consumed in the cathode reaction, and H^+ ions are the charge carriers. However, the electrolyte of the PAFC is a phosphoric acid which is relatively inexpensive. Besides expensive platinum catalysts, the corrosive nature of the electrolyte is the biggest disadvantage of the PAFC, so that the electrolyte must permanently be replenished.

The AFC operates between 20 and 220 °C. It consumes hydrogen on the anode side and oxygen and water on the cathode side. The charge carriers in the potassium hydroxide (KOH) electrolyte are OH^- ions. The AFC has the potential to be very inexpensive, as no precious catalysts are required, and the electrolyte is very cheap. As the AFC is intolerant with respect

to carbon dioxide, degrading the electrolyte, it is generally recommended to feed pure reactants to the cell. Another disadvantage is the necessary replenishment of the electrolyte.

The MCFC works at ca. 650 °C. Either hydrogen or carbon monoxide can be converted to carbon dioxide on the anode side, while oxygen and carbon dioxide are consumed on the cathode side. The charge is carried from the cathode to the anode by CO_3^{2-} ions. As electrolyte a porous ceramic matrix is used in which a molten carbonate is immobilized. The biggest advantage of the MCFC is the high temperature level which makes it attractive for combined heat and power applications. Additionally, no precious catalysts are needed. The disadvantages of the MCFC are basically the corrosive nature of the electrolyte and the need for recycle the carbon dioxide.

The SOFC performs in the highest temperature range, which is between 600 and 1000 °C. While it consumes oxygen on the cathode side, it can be operated with hydrogen, carbon monoxide, or methane on the anode side. The electrolyte is typically yttria-stabilized zirconia in which O^{2-} ions are the charge carriers. Just like the MCFC, one of the biggest advantage of the SOFC is the very high temperature level, thus it can perfectly be used for combined heat and power generation and can operate without precious catalysts. The electrolyte is easy to handle, and the fuel can be chosen flexibly. Nevertheless, due to the high temperatures in the cell, expensive temperature resistant materials are required.

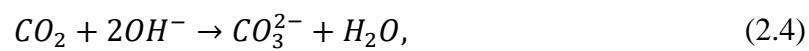
Table 2.1: Common fuel cells and their characteristics

Fuel Cell	T / °C	Electrolyte	Anode Reaction	Cathode Reaction
PEMFC	60-200	Polymer Membrane	$\text{H}_2 \rightarrow 2\text{H}^+ + 2\text{e}^-$	$\frac{1}{2}\text{O}_2 + 2\text{H}^+ + 2\text{e}^- \rightarrow \text{H}_2\text{O}$
DMFC	30-80	Polymer Membrane	$\frac{1}{3}\text{CH}_3\text{OH} + \frac{1}{3}\text{H}_2\text{O} \rightarrow \frac{1}{3}\text{CO}_2 + 2\text{H}^+ + 2\text{e}^-$	$\frac{1}{2}\text{O}_2 + 2\text{H}^+ + 2\text{e}^- \rightarrow \text{H}_2\text{O}$
PAFC	180-200	Phosphoric Acid	$\text{H}_2 \rightarrow 2\text{H}^+ + 2\text{e}^-$	$\frac{1}{2}\text{O}_2 + 2\text{H}^+ + 2\text{e}^- \rightarrow \text{H}_2\text{O}$
AFC	20-220	Potassium Hydroxide	$\text{H}_2 + 2\text{OH}^- \rightarrow 2\text{H}_2\text{O} + 2\text{e}^-$	$\frac{1}{2}\text{O}_2 + \text{H}_2\text{O} + 2\text{e}^- \rightarrow 2\text{OH}^-$
MCFC	650	Lithium / Potassium Carbonate	$\text{H}_2 + \text{CO}_3^{2-} \rightarrow \text{H}_2\text{O} + \text{CO}_2 + 2\text{e}^-$ $\text{CO} + \text{CO}_3^{2-} \rightarrow 2\text{CO}_2 + 2\text{e}^-$	$\frac{1}{2}\text{O}_2 + \text{CO}_2 + 2\text{e}^- \rightarrow \text{CO}_3^{2-}$
SOFC	600 – 1,000	Yttria stabilized Zirconia	$\text{H}_2 + \text{O}^{2-} \rightarrow \text{H}_2\text{O} + 2\text{e}^-$ $\text{CO} + \text{O}^{2-} \rightarrow \text{CO}_2 + 2\text{e}^-$ $\frac{1}{4}\text{CH}_4 + \text{O}^{2-} \rightarrow \frac{1}{2}\text{H}_2\text{O} + \frac{1}{4}\text{CO}_2 + 2\text{e}^-$	$\frac{1}{2}\text{O}_2 + 2\text{e}^- \rightarrow \text{O}^{2-}$

2.4 The design of an AFC

In order to combine the power of a plurality of single fuel cells, they are stacked. In general, two stack designs can be distinguished, the monopolar and the bipolar design. In monopolar stacks, the cells are electrically connected externally, whereas in bipolar stacks, the anode and the cathode of two adjacent cells are electrically connected by the bipolar plate. Consequentially, in case of the monopolar design the electrical current enters and exits the cells in parallel direction with the electrodes (in-plane), whereas in case of the bipolar design it enters and exits the cells in perpendicular direction with the electrodes (through-plane). In the past, monopolar as well as bipolar AFCs have been reported, for example in [13] and [14], respectively. The advantage of the monopolar design is that the “cells can be connected individually in the stack, depending on the voltage-current demand”, and that “[a] single cell can also be disconnected in the case of a failure without major interruptions” [15]. In contrast, the advantage of the bipolar concept is that “the current density over the electrode is uniform and far higher terminal voltages are achieved” [4]. Concerning the distribution of reactants to the cell, the monopolar and the bipolar designs also differ. In case of the monopolar design, two adjacent cells can be arranged that the anodes or the cathodes face each other. Then, a common gas channel can be used for the distribution of the gaseous reactants to two adjacent cells. In contrast, in case of the bipolar design, the gaseous reactants are usually distributed via flow fields in the bipolar plates.

Typically, pure hydrogen is fed to the anode, whereas also “[a]mmonia is an interesting option” as fuel for the AFC, because of the high energy density, the simple availability, the AFC’s tolerance with respect to ammonia, and the simple system design, consisting of an ammonia dissociator and an AFC as described in [4]. The most well-known disadvantage of the AFC is the electrolyte degradation when carbon dioxide enters the cell according to [16]



Therefore, it is usually recommended, feeding pure oxygen to the cathode. However, the impact of carbon dioxide on the AFC can be reduced by the circulation of the electrolyte as described below.

With respect to the electrolyte, basically two types of AFCs can be distinguished, namely the AFC with immobile (stagnant) electrolyte and the AFC with flowing (circulating) electrolyte. In case of an immobile electrolyte, it is generally fixed in a matrix. In contrast, in case of a flowing electrolyte, it typically flows in parallel direction with the electrodes, whereas it can also flow in perpendicular direction with the electrodes, as it is the case in the Eloflux cell (see below). Due to the circulation of the electrolyte, the acceptance of carbonates can be raised as they can easily be removed which increases the life expectancy of the cell [4], [17], [18]. Additionally, it enables a targeted heat management. In contrast, the advantage of the fixed electrolyte is that it does not leak.

The electrodes of a fuel cell must meet a variety of demands. In AFCs multilayer electrodes are typically used where the advantages of different materials are combined. The double layer structure is formed by “an active electrocatalyst layer and a hydrophobic layer” [17]. The hydrophobic gas diffusion layer (GDL), usually made of polytetrafluorethylene (PTFE), “prevents the electrolyte from leaking into the reactant gas flow channels and ensures diffusion of the gases to the reaction side” [17]. The electrical conductivity of the GDL is ensured by adding carbon black. In order to enable the half-cell reactions and enhance the kinetics, catalytic material specific to the desired electrochemical reaction is added to the electrode, forming the catalyst layer (CL), also called reaction layer (RL) or active layer. The most common catalyst is platinum. However, the greatest advantage of the AFC is the possibility to operate without noble catalysts such as Raney nickel on the anode side and silver on the cathode side, as shown in [19] and [20], respectively. As the electrochemical reactions arise in the interface between the gas phase and the liquid phase, the CL is placed on the electrolyte side of the electrode.

In order to provide stability to the electrode, the double layer structure is typically pressed on a third layer called backing material, support layer (SL), or electrode substrate; the latter two names are particularly used in case of a single cell or a monopolar design. In case of the monopolar concept, the SL is connected to the external current collector for bringing the charge in and out the cell. It is typically a nickel mesh or a nickel sheet and placed on the gas side of the electrode. Consequentially, the electrode layers are arranged from the gas side to the electrolyte side in the following order: SL, GDL, CL. An AFC with such electrodes is considered in [21]. In case of a bipolar design, the backing layer “is in direct contact with the bipolar plate”, thus “it can be made of carbon cloth or porous carbon paper” [16]. Also

nickel foam electrodes can be used, like those presented in [22] and [23] for the use in bipolar concepts. Alternatively, both the hydrophobic and the catalytic material can be combined to one layer, completed by a conductive mesh as described below for the Eloflux cell.

In an Eloflux cell the electrodes are separated by a thin, porous separator and the electrolyte moves perpendicular to the active cell surface area. The design of a standard Eloflux cell is described by the company Gaskatel in [24]: The anode consists of PTFE and Raney-Nickel, whereas a nickel-plated copper mesh serves as current collector; in contrast to the anode, the cathode is a mixture of PTFE and silver, attached to a silver-plated copper mesh. Epoxy resin is used for bringing all components together [24]. The Eloflux cell can be operated as alkaline fuel cell as well as alkaline electrolyzer [25]. While the compact design, the removal of produced heat and water, and the reduction of the concentration polarization are advantages of the Eloflux system [24], “the diaphragm perfection is critical as any gas cross leakage would cause a malfunction of the cell” [26].

2.5 AFCs today

A detailed historical overview of the progress on AFCs and the applications of AFCs is provided by Kordesch et al. in [9]. Nowadays there are basically three companies to name, doing research and development on AFCs, namely Independent Power Technologies, GenCell, and AFC Energy.

Independent Power Technologies is a Russian company that developed a 6.25 kW system called “CASCADE-6”. It operates “slightly above atmospheric pressure”, at an operating temperature between “60-80 °C”, and with an overall efficiency [...] in the range between 45-50 %”, which “can be increased up to 80 % in case of additional utilization of the heat produced by the generator” [27]. “It can be used in stationary applications for residential and commercial distributed power generation[,] in mobile applications, such as light trucks and similar type of ground fleet vehicles[,] and in marine applications, such as small commercial vessels, fishing boats and pleasure crafts” [27]. In order to reduce carbon dioxide from air, a “patented zero-waste regenerative scrubber [is] used” [27].

GenCell’s headquarter is located in Israel. The company develops AFC systems for off-grid, backup, and stationary applications. It developed a 5 kW system called “GenCell G5” which operates at temperatures between -40 and 45 °C, pressures between 300 and 500 kPa, and

with electrolyte concentrations in the range between 28 and 30 % KOH. Being also interested in using ammonia as fuel, GenCell developed a “patented ammonia cracking device” called “GenCell A5” that “generates hydrogen-on-demand”. [28]

AFC Energy is located in Great Britain. The company “is edging increasingly closer to delivery of a commercial-scale fuel cell system capable of deployment across a range of markets”. In 2015, a 240 kW “KORE” system was installed in Stade, Germany. Additionally, in 2016, “AFC Energy completed the design and basic engineering on a single cartridge 10 kW system”, for which “[d]etailed engineering & procurement will now commence, to enable commerciali[z]ation to begin”. [29]

2.6 Cell voltage and polarization curve

The cell voltage is the electrical potential difference between the cathode and the anode. This potential difference is piecemeal created in the interfaces between the electrodes and the electrolyte. The reversible cell voltage, also called equilibrium potential or ideal cell voltage, is the cell voltage under equilibrium conditions where the oxidation and the reduction reactions at the electrodes balance² and is the highest theoretical cell voltage the fuel cell can provide; in case of an electrolytic cell, it is the lowest required cell voltage. Under standard conditions, the reversible cell voltage of the hydrogen-oxygen fuel cell is the well-known 1.23 V. However, the open cell voltage (OCV), which is the cell voltage under open circuit conditions, can be smaller than the reversible cell voltage although the electrical current in the external circuit equals zero by definition. Internal currents, which cause potential losses even if no electrical current can be observed in the external circuit, or even undesired side reactions might be the reason.

Under load, additional losses occur which rise with electrical current density and cause the cell voltage therefore to decrease. Hence, the performance of a fuel cell is typically illustrated in the form of the polarization curve, also called IV-curve, obtained by plotting the cell voltage (U) against the current density with respect to the active cell surface area (i). A typical polarization curve is shown in Figure 2.3 following [3]. With rising current density, the cell voltage decreases logarithmically in the region of low current densities,

² At the interface between an electrode and the electrolyte of a cell, oxidation as well as reduction reactions take place. When equilibrium conditions are present at an electrode, the reduction and the oxidation reactions at that electrode balance and no electrical current can be observed. When the cell is under load, the oxidation reaction will dominate at the anode and the reduction reaction will dominate at the cathode.

exponentially in the region of high current densities, and linearly in between both regions. The departure of the cell voltage under load from the equilibrium potential (E_0) is called overpotential (η). In general, three types of losses can be distinguished: the activation losses (η_{Act}), the ohmic losses (η_{Ohm}), and the concentration losses (η_{Conc}). Near the equilibrium, in the region of low current densities, the sluggish kinetics (generally of the ORR) causes the cell voltage to decrease logarithmically with rising electric current, this region is the activation region. As the Ohm's law describes a linear relationship between voltage and electrical current, the following linear decrease of the cell voltage with increasing current density is called the ohmic region; especially the potential losses due to the charge transport in the electrolyte and electrodes cause the cell voltage to decrease in this region. At high current densities, the polarization curve decreases exponentially with rising current density. Named after the limiting transport mechanism this region is the so-called mass transport region. The highest obtainable current density of a fuel cell is called limiting current density.

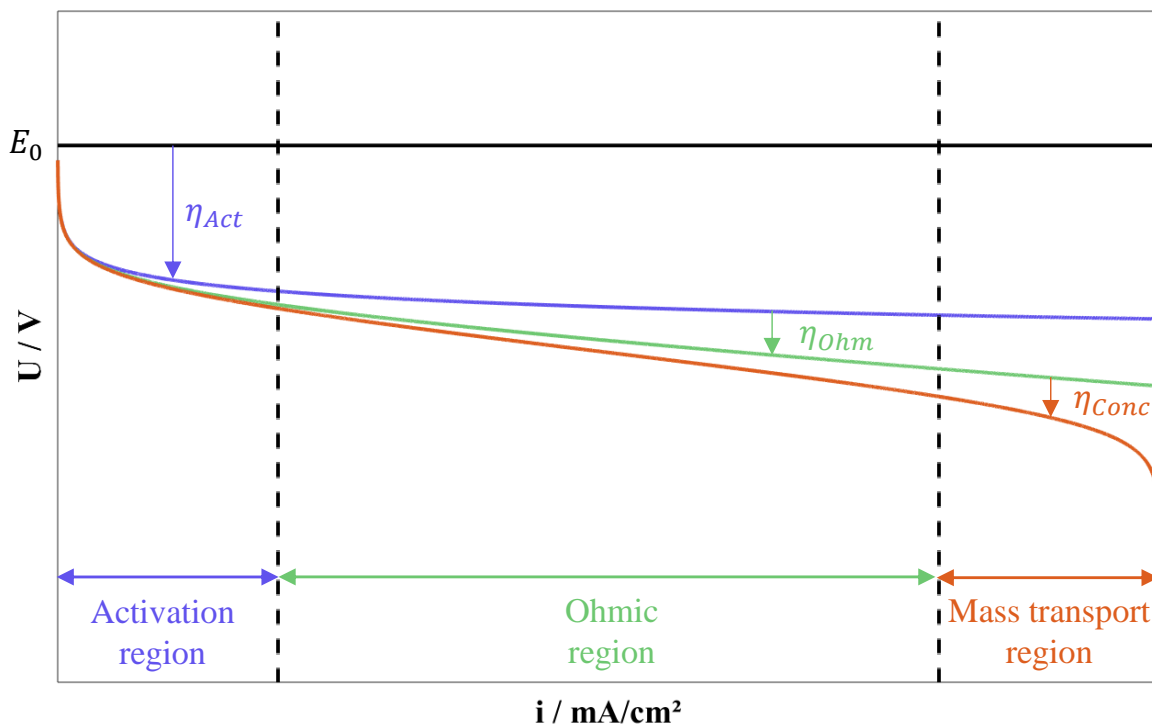


Figure 2.3: General polarization curve of a fuel cell (cf. [3]).

2.7 Thermodynamics

Thermodynamics enables the description of the “transformation of energy from one form to another” [3] and the change in energy of a system. In fuel cells chemical energy is converted into electrical energy and heat. The electrical energy occurs in the form of the cell voltage and becomes an electrical power when current is produced at the one electrode and consumed at the other. However, for the case that the electrochemical reactions at the electrodes are reversible and no losses occur in the cell, the ideal cell voltage can be predicted from thermodynamics. It is the highest possible cell voltage and represents therefore an upper boundary which enables rating a fuel cell in general.

First, most important thermodynamic quantities and their mathematical descriptions are provided in chapter 2.7.1. After that, these quantities are used in chapter 2.7.2 for the derivation of the ideal cell voltage. Finally, in chapter 2.7.3 the Nernst equation is discussed, which allows the calculation of the ideal cell voltage by referring to a certain reference state.

2.7.1 Thermodynamic quantities

The most important quantities for describing the energetic state from the thermodynamic perspective are the intrinsic energy (U), the enthalpy (H), and the Gibbs free energy (G). The intrinsic energy of a system refers to the energy which is required for creating the system [3]. The change in intrinsic energy is given by the fundamental equation according to [30]

$$dU = \underbrace{\left(\frac{\partial U}{\partial S}\right)_{V, N_i}}_T dS + \underbrace{\left(\frac{\partial U}{\partial V}\right)_{S, N_i}}_{-p} dV + \sum \underbrace{\left(\frac{\partial U}{\partial N_i}\right)_{V, S, N_j \neq N_i}}_{\mu_i} dN_i, \quad (2.6)$$

in which S is the entropy, V is the volume, and N_i is the number of species i . Furthermore, in equation (2.6), the temperature T , the pressure p , and the chemical potential μ are defined. In addition to the work for creating the system, the enthalpy accounts also for the work that is required for creating the room for it, expressed by pV [3]:

$$H = U + pV. \quad (2.7)$$

The change in enthalpy is given by differentiating equation (2.7):

$$dH = dU + pdV + Vdp. \quad (2.8)$$

When equation (2.7) is inserted in equation (2.8) it becomes obvious that enthalpy is only a function of pressure, entropy, and species number:

$$dH = Vdp + TdS + \sum \mu_i dN_i. \quad (2.9)$$

Compared to the enthalpy, the Gibbs free energy is decreased by the energy which is provided by the environment, represented by TS [3]:

$$G = U + pV - TS = H - TS. \quad (2.10)$$

Differentiating the Gibbs free energy yields the change in Gibbs free energy in the form

$$dG = dH - TdS - SdT. \quad (2.11)$$

It is only a function of pressure, temperature and species number, which becomes obvious when inserting equation (2.9) in equation (2.11):

$$dG = Vdp - SdT + \sum \mu_i dN_i. \quad (2.12)$$

The partial derivatives of the Gibbs free energy with respect to pressure, temperature, and amount of species i equal the volume, the entropy, and the chemical potential, respectively:

$$\left(\frac{\partial G}{\partial p}\right)_{T, N_i} = V, \quad (2.13)$$

$$\left(\frac{\partial G}{\partial T}\right)_{p, N_i} = -S, \quad (2.14)$$

$$\left(\frac{\partial G}{\partial N_i}\right)_{p, T, N_j \neq N_i} = \mu_i. \quad (2.15)$$

2.7.2 Ideal cell voltage

The calculation of the ideal cell voltage becomes possible through two essential rules, called the first and the second law of thermodynamics. The first law of thermodynamics balances the energetic change of state of a system. For a closed system, where energy can only be transferred to the surroundings as heat (Q) and work (W), the change in internal energy (U) can be written as

$$dU = dQ - dW. \quad (2.16)$$

According to the second law of thermodynamics the universe strives for disorder. The entropy (S), which describes the number of microscopic configurations the system can have, must therefore increase:

$$dS \geq 0. \quad (2.17)$$

For a reversible heat transfer under isobaric conditions (dQ_{rev}), dS may be given as

$$dS = \frac{dQ_{rev}}{T}. \quad (2.18)$$

The first and the second law of thermodynamics can be combined, so that a reversible process under isothermal and isobaric conditions can be described by the following balance:

$$dG - pdV = -dW. \quad (2.19)$$

The work done by the system comprises the mechanical work dW_m and the electrical work dW_e . As the mechanical work can be described by the volume change of the system as [3]

$$dW_m = pdV, \quad (2.20)$$

it follows, that the change in Gibbs free energy of a reversible, isothermal, and isobaric process is just the electrical work done by the system:

$$dG = -dW_e. \quad (2.21)$$

For a reaction, this relation equates the Gibbs free energy of the reaction (Δg_R) and the specific work provided by the reaction (w_e):

$$\Delta g_R = -w_e. \quad (2.22)$$

According to equation (2.15), the Gibbs free energy of the reaction can be replaced by the chemical potential of the reaction ($\Delta\mu_R$) as

$$\Delta g_R = \Delta\mu_R, \quad (2.23)$$

which is given by

$$\Delta\mu_R = \sum v_i \mu_i. \quad (2.24)$$

The stoichiometric coefficient v is positive for the products ($v_{Red} > 0$) but negative for the reactants ($v_{Ox} < 0$) of the reduction reaction, which can be written in the form



where M_i represents the chemical composition of species i .

A chemical reaction is at equilibrium state when the chemical potentials of the products and reactants balance and the Gibbs free energy of the reaction is zero:

$$\Delta\mu_R = 0; \text{ for a chemical reaction at equilibrium.} \quad (2.26)$$

This is not the case for an electrochemical reaction, where the electrical potential created in the interface between the electrode and the electrolyte balances the chemical potential of the reaction. For a species i , the electrochemical potential μ_i^* is defined as the sum of its chemical potential μ_i and the electrical portion $z_i F \phi_i$ representing its state of charge:

$$\mu_i^* = \mu_i + z_i F \phi_i, \quad (2.27)$$

where z_i is the charge number of the species i . Under equilibrium conditions, the electrochemical potential of the reaction is zero:

$$\Delta\mu_R^* = 0; \text{ for an electrochemical reaction at equilibrium.} \quad (2.28)$$

Consequentially, the chemical potential of the reaction is balanced by the electrical potential difference of the reaction ($-\Delta\phi_R$):

$$\Delta\mu_R = -nF\Delta\phi_R, \quad (2.29)$$

where the electrical potential of the reaction $\Delta\phi_R$ is given by

$$\Delta\phi_R = \frac{1}{n} \sum v_i z_i \phi_i. \quad (2.30)$$

With equation (2.30) in equation (2.23), the Gibbs free energy of the reaction can be written as

$$\Delta g_R = -nF\Delta\phi_R. \quad (2.31)$$

Consequentially, the reversible potential (E_0) of an electrochemical device is given by the Gibbs free energy of the cell reaction and can be calculated with thermodynamic quantities by

$$E_0 = -\frac{\Delta g_R}{nF}. \quad (2.32)$$

2.7.3 Nernst equation

For common electrode reactions, the electrode potential measured against the standard hydrogen electrode (SHE) is given in open literature (standard electrode potential). However, most applications require operating conditions that differ from standard conditions which demands a mathematical expression for predicting the reversible cell voltage at given conditions, for example for the use in mathematical models. This raises the question of the change in reversible cell voltage with temperature and species activity. The influence of the

species activity on the reversible cell voltage can be described with the Nernst equation according to [31]

$$E_0 = E_T - \frac{RT}{nF} \ln \left(\prod \left(\frac{a_i}{a_i^{Ref}} \right)^{\nu_i} \right), \quad (2.33)$$

where a_i and a_i^{Ref} are the species activities belonging to the reversible cell voltages E_0 and E_T , respectively. Although equation (2.33) contains the temperature in the last term, it will not fully capture the temperature dependence of the reversible cell voltage, if E_T is kept constant. Neglecting the change in reaction entropy with temperature, E_T may be given as

$$E_T = E_0^{Ref} + \frac{\Delta S_R|_{p,T}}{nF} (T - T^{Ref}), \quad (2.34)$$

in which E_0^{Ref} is the reversible cell potential at temperature T^{Ref} and species activity a_i^{Ref} .

The entropy of the reaction can be written as

$$\Delta S_R = \sum \nu_i S_i. \quad (2.35)$$

Both equation (2.33) and equation (2.34) can be derived from the equality of the chemical potential and the electrical potential at equilibrium state according to equation (2.29).

Typically, the activity equals 1 for pure components and electrons in metals. It can be replaced by the dimensionless partial pressure $p_i^\circ = \gamma \cdot p_i/p^0$ for gases, and with the dimensionless concentration $c_i^\circ = \gamma \cdot c_i/c^0$ for solutions. The activity coefficient γ equals 1 in case of an ideal gas and in case of an ideal diluted solution, respectively [3]. Hence, for the hydrogen-oxygen fuel cell, referring to standard conditions and replacing the activities of hydrogen and oxygen with the dimensionless pressures, and the activity of water by 1 reveals the well-known expression:

$$E_0 = 1.23 \text{ V} + \frac{RT}{2F} \ln \left(p_{H_2}^\circ p_{O_2}^{\circ 1/2} \right). \quad (2.36)$$

2.8 Kinetics

The electrical power of a fuel cell is basically generated in the interfaces between the electrodes and the electrolyte where electrical potential differences and electrochemical charge transfer reactions occur. One of the most prominent expressions for describing charge transfer processes is the Butler-Volmer expression [32], [33]. Initially formulated almost a century ago, the expression has been applied and derived several times for example in [34], [35], [36], [37], [38], [39], [3], [40], [41], and [42]. Basically, it describes the relationship between the current density (i) and the electrical potential in the interface ($\Delta\phi$) as

$$i = i_0 \left(\prod_{Red} \left(\frac{c_{Red}}{c_{Red}^0} \right)^{\vartheta_{Red}} \exp\left(\frac{\alpha_+ n F \eta}{RT}\right) - \prod_{Ox} \left(\frac{c_{Ox}}{c_{Ox}^0} \right)^{\vartheta_{Ox}} \exp\left(\frac{-\alpha_- n F \eta}{RT}\right) \right), \quad (2.37)$$

where i_0 is the exchange current density, η is the overpotential, F is the Faraday's constant, R is the general gas constant, T is the temperature, and α_+ and α_- are the transfer coefficients of the oxidation and reduction reaction, respectively. The concentrations c_{Ox} , c_{Red} , c_{Ox}^0 , and c_{Red}^0 are the reactant and product concentrations (when the reaction is written as reduction reaction³) at the electrode surface under load and under equilibrium conditions, respectively. The reaction orders of the reactants and products are ϑ_{Ox} and ϑ_{Red} , respectively.

The Butler-Volmer expression accounts for the electrical currents due to the oxidation and reduction reactions by the first and the second term on the right, respectively. Under equilibrium conditions, the oxidation and reduction reactions balance. Then, the current density of both reactions is the exchange current density i_0 . The connection to the electrical potential in the interface is created by the overpotential η , which describes the departure of the electrical potential in the interface under load ($\Delta\phi$) from the electrical potential in the interface under equilibrium conditions ($\Delta\phi_0$) as

$$\eta = \Delta\phi - \Delta\phi_0. \quad (2.38)$$

In the form of the concentration ratios of the oxidized species (reactants of the reduction reaction) $\prod_{Ox} (c_{Ox}/c_{Ox}^0)^{\vartheta_{Ox}}$ and the reduced species (products of the reduction reaction)

³ Conventionally electrochemical reactions are evaluated as reduction reactions, thus the stoichiometric coefficients of the reactant species of the reduction reaction are negative and the stoichiometric coefficients of the product species of the reduction reaction are positive.

$\Pi_{Red}(c_{Red})/c_{Red}^0$, the Butler-Volmer expression accounts for the change in concentrations at the electrode surface with the current density (c_{Red} , c_{Ox}) relatively to the concentrations at the electrode surface under equilibrium conditions (c_{Red}^0 , c_{Ox}^0). In some cases, the Butler-Volmer expression can be written without these concentration ratios:

$$i = i_0 \left(\exp\left(\frac{\alpha_+ n F \eta}{RT}\right) - \exp\left(\frac{-\alpha_- n F \eta}{RT}\right) \right). \quad (2.39)$$

As no concentration ratios arise in this expression it can be called ‘‘concentration independent Butler-Volmer expression’’⁴.

The Butler-Volmer expression refers to equilibrium conditions represented by the exchange current density i_0 and the equilibrium potential $\Delta\phi_0$. In order to provide a transparent explanation of the equilibrium parameters and the meaning of the overpotential, the concentration independent expression and the concentration dependent expression are derived in chapter 2.8.1 and chapter 2.8.2, respectively. As the concentration dependent expression is derived by accounting for the concentration variation but not the change in temperature at the electrode surface, a third thermodynamically consistent expression is derived in chapter 2.8.3, that accounts for both concentration and temperature variations. This derivation enables an absolute clear explanation of the temperature and concentration dependences of $\Delta\phi_0$ and i_0 and a detailed analysis of the overpotential used in the Butler-Volmer expression. It is shown, that the concentration dependent expression accounts for the concentration dependences of $\Delta\phi_0$ and i_0 , thus they must not vary with concentrations in equation (2.37). Also it is shown that equation (2.39) equals equation (2.37), when $\Delta\phi_0$ and i_0 , are not kept constant but are parameterized dependent on concentrations, for example for the use in mathematical models. In order to keep the derivations comprehensive, the electrochemical reaction at the electrode is assumed to arise in one step, whereby the electrons are directly transferred, just like the case of an elementary reaction; this assumption leads to the Butler-Volmer expression. Finally, common simplifications of the Butler-Volmer expression are discussed in chapter 2.8.4 and the method of deriving kinetic parameters from measurements is described in chapter 2.8.5.

⁴ As shown in chapter 2.8.1, this expression does not take into consideration concentration losses when i_0 and $\Delta\phi_0$ are kept constant. However, as derived in chapter 2.8.3 this expression can account for concentration losses when i_0 and $\Delta\phi_0$ are parameterized (in mathematical models) as function from concentrations.

2.8.1 Surface overpotential

An electrochemical reaction where n electrons are transferred can generally be written as



where M_{Ox} and M_{Red} represent the chemical compositions of the reactants and products of the reduction reaction. Their stoichiometries are v_{ox} and v_{Red} , respectively.

At the electrode surface, oxidation as well as reduction reactions take place, causing an anodic current density (i_+) and a cathodic current density (i_-), respectively. The observable current density is therefore the difference between the anodic and cathodic current densities:

$$i = i_+ - i_-. \quad (2.41)$$

Consequentially, the current is positive when the electrode is an anode, but negative when the electrode is a cathode. Under equilibrium conditions, the anodic current and the cathodic current balance and the net current equals zero. At this equilibrium state, the current density of the oxidation (i_+^0) and reduction reactions (i_-^0) is called exchange current density i_0 :

$$i_0 = i_+^0 = i_-^0. \quad (2.42)$$

According to Faraday's law, the reaction rate (r_j) and the current density (i_j) of the partial reaction j are related to one another by

$$i_j a_l = n F r_j, \quad (2.43)$$

where a_l is the specific surface area of the catalyst. For a simple reversible one-step reaction, which can be treated as elementary reaction, the reaction rate is given by

$$r_j = k_j \prod_h c_h^{\vartheta_h}, \quad (2.44)$$

where k_j is the reaction rate constant of the reaction j , the index h refers to the reactant species of reaction j , and ϑ_h is the reaction order of species h . In some cases the reaction orders can be replaced by absolute values of the stoichiometric coefficients ($\vartheta_h \rightarrow |\nu_h|$).

Following the activated state theory, an energetic barrier must be overcome for an electrochemical reaction to take place. Hence, even if energy is freed when reactants react to products from the thermodynamic point of view, a certain amount of energy must be supplied to the reactants to overcome this energetic barrier from a kinetic point of view. The size of this energetic barrier is quantified as the activation energy. The dependence of the reaction rate constant k_j on the activation energy can be written in an Arrhenius form:

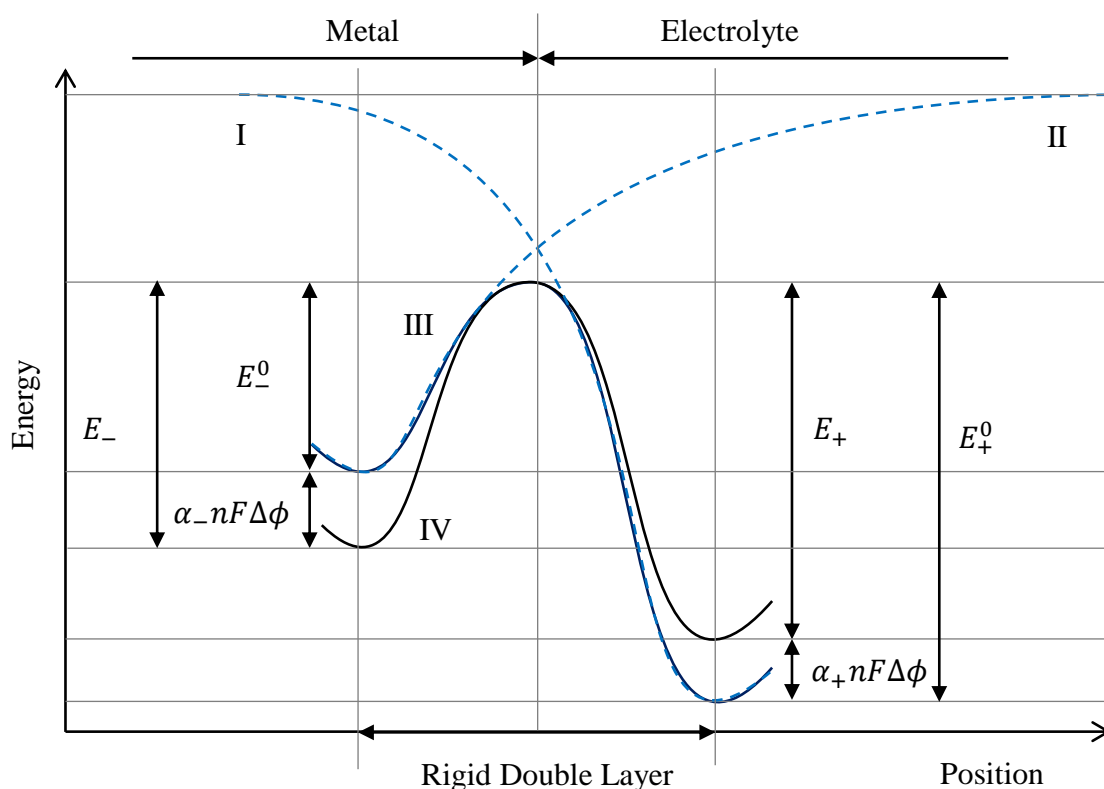
$$k_j = k'_j \exp\left(\frac{-E_j(\Delta\phi)}{RT}\right), \quad (2.45)$$

where $E_j(\Delta\phi)$ is the activation energy of reaction j which depends on the potential drop $\Delta\phi$ across the electrochemical reaction interface. The constant k'_j only depends on the temperature. Consequentially, by combining equations (2.43)-(2.45), the current density of the reaction j can be written as

$$i_j a_l = nF k'_j \prod_h c_h^{\vartheta_h} \exp\left(\frac{-E_j(\Delta\phi)}{RT}\right). \quad (2.46)$$

Especially the work by Helmholtz, Gouy, Chapman, Stern, and Grahame on the double layer between two adjacent electrical conductive phases led to the understanding of the electrical potential difference in the interface [35]. The double layer between a solid electrode and a liquid electrolyte basically consists of two regions of a double layer, namely the rigid double layer and the diffuse double layer. The rigid double layer comprises the inner Helmholtz layer (defined by distance of dehydrated ions from the electrode surface; also called inner layer, compact, Helmholtz, or Stern layer [35]) and the outer Helmholtz layer (defined by the reachable distance of solvated ions from the electrode). The interface between the inner and outer Helmholtz layers is called inner Helmholtz plane (IHP), whereas the interface between the rigid and diffuse layers is called outer Helmholtz plane (OHP). Taking place in the rigid double layer, the electrochemical reaction is primarily driven by the potential drop across this layer, whereas an additional potential difference can arise in the diffuse double

layer, for example caused by transport processes. The potential difference between an electrode and an electrolyte cannot be measured and so the magnitude of the potential drop in the rigid double layer is schematic. The energetic barrier in the rigid double layer is illustrated in Figure 2.4. [35]



- | |
|---|
| I: Electron transfer process from electrolyte to charge-free vacuum |
| II: Electron transfer from charge-free vacuum to electrode |
| III: Electron transfer from electrolyte to electrode (superimposition of I and II) without potential difference in the phase boundary |
| IV: Electron transfer from electrolyte to electrode (superimposition of I and II) with potential difference in the phase boundary |

Figure 2.4: Schematic illustration of the energetic barrier in the double layer (cf. [40]).

As shown in Figure 2.4, the transfer of an electron from electrolyte to electrode during an electrochemical redox reaction can be divided into two hypothetical transfer processes by introducing a charge-free vacuum to which the electron is transferred from the electrolyte (curve I) and from which the electron is transferred to the electrode phase (curve II) [40]. curve III is obtained by superimposing curve I and curve II. As it was derived based on charge transfer to and from a charge free vacuum, curve III does not take into account the potential difference in the phase boundary which will be present between metal and electrolyte ($\Delta\phi = 0$). When this potential difference is also taken into account, curve IV is

obtained ($\Delta\phi \neq 0$). Hence, the activation energies of the oxidation reaction (E_+) and the reduction reaction (E_-) can be written as

$$E_j(\Delta\phi) = E_j^0 - \epsilon_j \alpha_j n F \Delta\phi, \quad (2.47)$$

where the parameter ϵ_j serves as algebraic sign, being positive in case of an oxidation ($\epsilon_+ = +1$), but negative in case of a reduction reaction ($\epsilon_- = -1$). The chemical activation free energies of the oxidation and reduction reactions are E_+^0 and E_-^0 , respectively. The symmetry factors α_+ and α_- (also called transfer coefficients) apportion the electrical energy due to the applied potential between the reduction and oxidation reactions based on Volmer [33]. The sum of the anodic symmetry factor α_+ and the cathodic symmetry factor α_- equals one:

$$\alpha_+ + \alpha_- = 1. \quad (2.48)$$

Notice: This does not correspond for more complicated reactions where one particular step in the reaction mechanism might be the rate determining one, for example as described by Bockris and Nagy [43].

Hence, inserting the activation energy according to equation (2.47) in equation (2.46) yields

$$i_j a_l = n F k'_j \prod_h c_h^{\vartheta_h} \exp\left(\frac{-E_j^0}{RT}\right) \exp\left(\frac{\epsilon_j \alpha_j n F \Delta\phi}{RT}\right). \quad (2.49)$$

Replacing the anodic and cathodic current densities in equation (2.41) according to equation (2.49) leads to the following expression:

$$i a_l = n F k'_+ \prod_{Red} c_{Red}^{\vartheta_{Red}} \exp\left(\frac{-E_+^0}{RT}\right) \exp\left(\frac{\alpha_+ n F \Delta\phi}{RT}\right) - n F k'_- \prod_{Ox} c_{Ox}^{\vartheta_{Ox}} \exp\left(\frac{-E_-^0}{RT}\right) \exp\left(\frac{-\alpha_- n F \Delta\phi}{RT}\right). \quad (2.50)$$

As the exchange current density is measurable (see chapter 2.8.5), it can be used as reference which enables replacing several unknown kinetic parameters. Based on equation (2.49), the exchange current density can be written as

$$i_j^0 a_l = nFk'_j \prod_h c_h^{\nu_h} \exp\left(\frac{-E_j^0}{RT}\right) \exp\left(\frac{\epsilon_j \alpha_j nF \Delta\phi_0}{RT}\right). \quad (2.51)$$

Thereupon, inserting the exchange current density according to equation (2.51) in equation (2.50) leads to

$$i = i_0 \left(\exp\left(\frac{\alpha_+ nF \eta_s}{RT}\right) - \exp\left(\frac{-\alpha_- nF \eta_s}{RT}\right) \right), \quad (2.52)$$

where the overpotential η_s is given by

$$\eta_s = \Delta\phi - \Delta\phi_0. \quad (2.53)$$

Equation (2.52) is the concentration independent Butler-Volmer expression. Following Newman [12], η_s can be called “surface overpotential”. It describes the departure of the electrical potential in the interface under load from the electrical potential in the interface at equilibrium state. In order to describe η_s from a more practical point of view, a reference electrode (reference electrode A) shall be imagined, being of the same material as the working electrode and being placed directly at its surface so that it is under the same conditions as the working electrode (with respect to concentrations and temperature). As no current passes through reference electrode A, equilibrium conditions can be assumed at its surface, no matter what happens at the surface of the working electrode. When no current passes through the working electrode, the potential difference between the working electrode and the electrolyte is the same as the potential difference between reference electrode A and the electrolyte. But when current passes through the working electrode, an electrical potential difference will occur between the two electrodes. Consequentially, η_s describes the overpotential at the working electrode’s surface and equals zero when the current does.

2.8.2 Concentration dependent kinetics

As equation (2.52) only describes the surface overpotential, it does not account for mass transport losses due to the change in concentrations at the electrode surface with the current density. In order to account for the fact that the concentrations at the electrode surface under load (c_h) might differ from those present at the electrode surface when the exchange current density applies (c_h^0), the exchange current density must be written as

$$i_j^0 a_l = nFk_j' \prod_h c_h^{0\vartheta_h} \exp\left(\frac{-E_j^0}{RT}\right) \exp\left(\frac{\epsilon_j \alpha_j nF \Delta\phi_0(c^0)}{RT}\right). \quad (2.54)$$

Then, inserting i_0 in equation (2.50) yields

$$i = i_0 \left(\prod_{Red} \left(\frac{c_{Red}}{c_{Red}^0} \right)^{\vartheta_{Red}} \exp\left(\frac{\alpha_+ nF\eta}{RT}\right) - \prod_{Ox} \left(\frac{c_{Ox}}{c_{Ox}^0} \right)^{\vartheta_{Ox}} \exp\left(\frac{-\alpha_- nF\eta}{RT}\right) \right), \quad (2.55)$$

in which the overpotential η is defined as

$$\eta = \Delta\phi - \Delta\phi_0(c^0), \quad (2.56)$$

where $\Delta\phi_0(c^0)$ is the concentration independent equilibrium potential, which means that it does not vary with the concentrations at the electrode surface in a mathematical model.

Equation (2.55) is known as the concentration dependent Butler-Volmer expression. The meaning of η becomes more clearly, by again considering a reference electrode (reference electrode B), being of the same material as the working electrode. In contrast to reference electrode A, which was directly placed near the working electrode, reference electrode B shall be placed so far from the working electrode, that the concentrations at its surface remain constant, while the concentrations at the working electrode change with the current density. Again, no current shall pass through reference electrode B at any time. When the working electrode is at equilibrium state, the same conditions shall be present at its surface and at the surface of reference electrode B, thus no potential difference occurs between the electrodes and η equals zero. With the current density, the conditions at the working electrode change and η increases, describing the departure of the electrical potential of the working electrode

from the electrical potential of reference electrode B. Hence, in addition to the surface overpotential η_s , losses due to the change in the concentrations at the working electrode's surface are contained in η .

2.8.3 Concentration and temperature dependent kinetics

With the current density, the concentrations and the temperature at the electrode surface may vary. When deriving equation (2.55), the change in concentrations was taken into consideration, whereas the change in temperature was not. Although the temperature occurs in the expression, the impact of the local temperature on the electrode kinetics is not fully captured. Therefore, the difference between the variable exchange current density (i_0) and the constant exchange current density (i_{00}) must be made. The variable exchange current density i_0 depends on the momentary concentrations c_{Red} and c_{Ox} and the temperature T at the electrode surface and may therefore vary with the current density. In other words, it is the exchange current density which could be observed if the momentary concentrations and temperature were present at the electrode surface but no current passed through it. In contrast, the constant exchange current density i_{00} is the exchange current density at a certain reference equilibrium state, where the concentrations c_{Red}^0 and c_{Ox}^0 and the temperature T^0 are present at the electrode surface. It can be understood as the exchange current density which in fact can be observed for the initial concentrations and the initial temperature. Hence, based on equation (2.49), i_0 and i_{00} can be written as follows:

$$i_j^0 a_l = nFk_j' \prod_h c_h^{0\vartheta_h} \exp\left(\frac{-E_j^0}{RT}\right) \exp\left(\frac{\epsilon_j \alpha_j nF \Delta\phi_0(c^0, T)}{RT}\right), \quad (2.57)$$

$$i_j^{00} a_l = nFk_j'^{0} \prod_h c_h^{0\vartheta_h} \exp\left(\frac{-E_j^0}{RT^0}\right) \exp\left(\frac{\epsilon_j \alpha_j^0 nF \Delta\phi_0(c^0, T^0)}{RT^0}\right). \quad (2.58)$$

Then, dividing i_0 by i_{00} yields

$$\frac{i_j^0(c, T)}{i_j^{00}(c^0, T^0)} = \prod_h \left(\frac{c_h}{c_h^0}\right)^{\vartheta_h} \exp\left(\frac{-E_j^0(T^0 - T)}{RTT^0}\right) \cdot \exp\left(\frac{\epsilon_j \alpha_j nF(\Delta\phi_0(c, T)T^0 - \Delta\phi_0(c^0, T^0)T)}{RT^0T}\right), \quad (2.59)$$

where the temperature dependence of the reaction rate constants ($k'_j \approx k'_j{}^0$) and the temperature dependence of the transfer coefficients ($\alpha_j \approx \alpha_j^0$) were neglected.

Mathematical expressions for the variable equilibrium potential $\Delta\phi_0(c, T)$ and the constant equilibrium potential $\Delta\phi_0(c^0, T^0)$ can be derived by equating the anodic and cathodic exchange current densities under constant and variable equilibrium conditions, which yields

$$\Delta\phi_0(c^0, T^0) = \frac{RT^0}{nF} \ln\left(\frac{k'_-}{k'_+}\right) + \frac{RT^0}{nF} \ln\left(\frac{\prod_{Ox} c_{Ox}^0{}^{\vartheta_{Ox}}}{\prod_{Red} c_{Red}^0{}^{\vartheta_{Red}}}\right) - \frac{-E_+^0 + E_-^0}{nF}, \quad (2.60)$$

and

$$\Delta\phi_0(c, T) = \frac{RT}{nF} \ln\left(\frac{k'_-}{k'_+}\right) + \frac{RT}{nF} \ln\left(\frac{\prod_{Ox} c_{Ox}{}^{\vartheta_{Ox}}}{\prod_{Red} c_{Red}{}^{\vartheta_{Red}}}\right) - \frac{-E_+^0 + E_-^0}{nF}, \quad (2.61)$$

respectively. Thereupon, inserting equations (2.60) and (2.61) in equation (2.59), yields the following expression for the concentration and temperature dependence of the exchange current density:

$$i_0(c, T) = i_{00} \prod_{Red} \left(\frac{c_{Red}}{c_{Red}^0}\right)^{\vartheta_{Red}\alpha_-} \prod_{Ox} \left(\frac{c_{Ox}}{c_{Ox}^0}\right)^{\vartheta_{Ox}\alpha_+} \exp\left(\frac{-E_{Act}^0(T^0 - T)}{RTT^0}\right), \quad (2.62)$$

where E_{Act}^0 is the measurable activation energy (see chapter 2.8.5), defined as

$$E_{Act}^0 = \alpha_- E_+^0 + \alpha_+ E_-^0. \quad (2.63)$$

Notice: Equation (2.62) equals the combination of the expressions for the concentration dependence and the temperature dependence of the exchange current density provided by Hamann and Vielstich in [36] (see equations 4.44 and 4.88a in [36], respectively). Also, it is consistent with the expression presented by Gasteiger et al. in [44] for the exchange current density of the ORR in PEMFCs as function from temperature and oxygen partial pressure (see equation 3 in [44]).

In analogy with the Nernst-equation for the equilibrium potential, equation (2.62) enables the prediction of the exchange current density at given temperature and concentrations based on a certain reference state. It also enables the parametrization of the exchange current density occurring in equation (2.52), for example for the use in mathematical models. The current density can therefore be written as

$$i = i_0(c, T) \left(\exp\left(\frac{\alpha_+ n F \eta^*}{RT}\right) - \exp\left(\frac{-\alpha_- n F \eta^*}{RT}\right) \right), \quad (2.64)$$

with the overpotential η^* given as

$$\eta^* = \Delta\phi - \Delta\phi_0(c, T). \quad (2.65)$$

The overpotential η^* comprises the surface overpotential as well as the concentration losses due to mass transport (but not the Nernstian losses η_N as described below). A more practical explanation for η^* can be given by referring to reference electrode B again. Again, no current shall pass through reference electrode B at any time. This time, not only the concentrations, but also the temperature shall remain constant at reference electrode B, being placed far away from the working electrode. Thus, when the temperature at the working electrode rises, its kinetics improve compared to the kinetics at reference electrode B, taken into account by the temperature dependence of the exchange current density. Additionally, the concentrations at the working electrode change, while the concentrations at reference electrode B remain constant, which is (partly) taken into account by the concentration dependence of the exchange current density (the temperature T and the concentrations c_{Red} and c_{Ox} in equation (2.62) vary with the current density). Also with increasing current density, the (theoretical) equilibrium potential in the interface between the working electrode and the electrolyte ($\Delta\phi_0(c, T)$) departs from the equilibrium potential in the interface between the reference electrode and the electrolyte ($\Delta\phi_0(c^0, T^0)$); $\Delta\phi_0(c, T)$ is the equilibrium potential which would be present in the interface between the electrode and the electrolyte, if the momentary concentrations and temperature were present at the electrode surface but no electrical current passed through it. Combining equations (2.60) and (2.61) yields an expression which describes the temperature and concentration dependence of the equilibrium potential in analogy with equations (2.33) and (2.34):

$$\Delta\phi_0(c, T) = \Delta\phi_0(c^0, T^0) + \frac{\partial\Delta\phi_0}{\partial T}(T - T^0) + \eta_N, \quad (2.66)$$

where the temperature coefficient of the equilibrium potential is

$$\frac{\partial\Delta\phi_0}{\partial T} = \frac{R}{nF} \left(\ln \left(\frac{k'_-}{k'_+} \right) + \ln \left(\frac{\prod_{Ox} c_{Ox}^0 \vartheta_{Ox}}{\prod_{Red} c_{Red}^0 \vartheta_{Red}} \right) \right), \quad (2.67)$$

and the Nernstian losses η_N are

$$\eta_N = \frac{RT}{nF} \ln \left(\prod_{Ox} \left(\frac{c_{Ox}}{c_{Ox}^0} \right)^{\vartheta_{Ox}} \prod_{Red} \left(\frac{c_{Red}^0}{c_{Red}} \right)^{\vartheta_{Red}} \right). \quad (2.68)$$

When the concentration losses are extracted from the exchange current density and from the equilibrium potential, the concentration dependent Butler-Volmer expression is obtained:

$$i = i_0(c^0, T) \left(\prod_{Red} \left(\frac{c_{Red}}{c_{Red}^0} \right)^{\vartheta_{Red}} \exp \left(\frac{\alpha_+ n F \eta^{**}}{RT} \right) - \prod_{Ox} \left(\frac{c_{Ox}}{c_{Ox}^0} \right)^{\vartheta_{Ox}} \exp \left(\frac{-\alpha_- n F \eta^{**}}{RT} \right) \right), \quad (2.69)$$

where the overpotential η^{**} , the temperature dependent exchange current density $i_0(c^0, T)$, and the temperature dependent equilibrium potential $\Delta\phi_0(c^0, T)$ can be given as follows

$$\eta^{**} = \Delta\phi - \Delta\phi_0(c^0, T), \quad (2.70)$$

$$i_0(c^0, T) = i_0(c^0, T^0) \exp \left(\frac{-E_{Act}^0 (T^0 - T)}{RTT^0} \right), \quad (2.71)$$

and

$$\Delta\phi_0(c^0, T) = \Delta\phi_0(c^0, T^0) + \frac{\partial\Delta\phi_0}{\partial T}(T - T^0). \quad (2.72)$$

Consequentially, the overpotential in the concentration dependent Butler-Volmer expression accounts for the surface overpotential, the kinetic concentration losses due to the impact of the local change in concentrations on the electrode kinetics, but also for the Nernstian concentration losses due to the concentration dependence of the equilibrium potential. In order to consider the effect of temperature accurately, the temperature dependence of i_0 and of the temperature dependence of $\Delta\phi_0$ have to be respected in mathematical models.

2.8.4 Simplified kinetics

In the Butler-Volmer expression, the kinetics of the electrode reaction are represented by the exchange current density i_0 and the transfer coefficients α_+ and α_- . When the exchange current density has a certain order of magnitude or the transfer coefficients equal one another the kinetics can be described with simplified expressions. This can reduce the complexity of mathematical models. The simplifications of the Butler-Volmer expression for relatively high exchange current densities (small overpotentials) and relatively small exchange current densities (large overpotentials) are presented in chapter 2.8.4.1 and chapter 2.8.4.2, respectively. The rearranged expression for symmetric transfer coefficients is provided in chapter 2.8.4.3.

2.8.4.1 Small overpotentials (HOR)

In the Butler-Volmer expression two exponential functions occur, which only differ in the transfer coefficients and the algebraic sign. The exponential function can be approached by a Taylor series expansion according to

$$e^x = \sum_{n=0}^{\infty} \frac{x^n}{n!}. \quad (2.73)$$

For small values of x the Taylor series expansion performed up to the power of one is already in a good approximation, so that the exponential terms can be replaced according to

$$e^x \approx 1 + x ; \text{ for small } x. \quad (2.74)$$

Therefore, in case of small overpotentials, the Butler-Volmer expression can be simplified to describe the relationship between the current density and the overpotential by

$$i = i_0 \frac{nF\eta}{RT}. \quad (2.75)$$

As the HOR generally shows low overpotentials, this simplification is commonly made when modeling the HOR. For example, at 25 °C, the relative error of this simplification is smaller than 1 % as long as the overpotential is smaller than ca. 6.32 mV, for $\alpha_+ = \alpha_- = 0.5$, and $n = 2$. However, when mass transport becomes significant, concentration losses must be taken into consideration additionally.

2.8.4.2 Large overpotentials (ORR) – Tafel equation

For large values of η , the forward current is already a good approximation for the net current, thus the reverse reaction can be neglected. Then the current density can be written as

$$i = \epsilon_f i_0 \exp\left(\frac{\epsilon_f \alpha_f nF\eta}{RT}\right), \quad (2.76)$$

where the lower index f denotes the forward reaction and the parameter ϵ serves as algebraic sign, being positive in case of an oxidation ($\epsilon_+ = +1$), but negative in case of a reduction reaction ($\epsilon_- = -1$).

For example, at 25 °C, the relative error for this simplification is smaller than 1 % as long as (the absolute value of) the overpotential is larger than ca. 29.64 mV, for $\alpha_+ = \alpha_- = 0.5$, and $n = 4$. As the ORR is very sluggish, the overpotential increases rapidly with the current density and reaches high values even in the region of low current densities. Therefore, this simplification is commonly used when modeling the ORR.

Equation (2.76) can be rearranged to obtain an expression for the overpotential as function from the current density in the form

$$\epsilon_f \eta = \underbrace{\frac{2.3RT}{\alpha_f nF}}_{s_{Tafel}} \log(\epsilon_f i) - \frac{2.3RT}{\alpha_f nF} \log(i_0), \quad (2.77)$$

which is generally known as the Tafel equation. The term s_{Tafel} which is multiplied by the logarithm of the current density is called Tafel slope. This expression is generally used for

determining the exchange current density i_0 at practical constant temperature and concentrations. Also, the transfer coefficient α_f can be derived from the slope (see chapter 2.8.5).

In order to account for mass transport losses too, equation (2.76) can also be written with concentration ratios, for example as

$$i = \epsilon_f \prod_{Red} \left(\frac{c_{Red}}{c_{Red}^0} \right)^{\vartheta_{Red}\alpha_-} \prod_{Ox} \left(\frac{c_{Ox}}{c_{Ox}^0} \right)^{\vartheta_{Ox}\alpha_+} i_0 \exp\left(\frac{\epsilon_f \alpha_f n F \eta}{RT}\right), \quad (2.78)$$

or

$$i = \epsilon_f i_0 \prod_f \left(\frac{c_f}{c_f^0} \right)^{\vartheta_f} \exp\left(\frac{\epsilon_f \alpha_f n F \eta}{RT}\right), \quad (2.79)$$

whereas Nernstian concentration losses are contained in the latter expression and must be taken into account in addition to the former expression (see chapter 2.8.3). Another difference is the assumption of the latter expression that the reactant concentrations are much more influential than the product concentrations (c_f only stands for the reactant concentrations of the forwards reaction thus the product concentrations are neglected).

2.8.4.3 Symmetric kinetics ($\alpha_+ = \alpha_-$)

When the transfer coefficients of the oxidation and reduction reactions equal one another, the exponential functions can be replaced by the hyperbolic sine according to

$$\exp(x) - \exp(-x) = 2 \sinh(x). \quad (2.80)$$

Hence, for $\alpha_+ = \alpha_- = \alpha$, the current density can be written as

$$i = i_0 \left(2 \sinh\left(\frac{\alpha n F \eta}{RT}\right) \right), \quad (2.81)$$

and rearranging yields the following expression for the overpotential:

$$\eta = \frac{RT}{\alpha nF} \operatorname{arsinh}\left(\frac{i}{2i_0}\right). \quad (2.82)$$

In case that the concentrations at the electrode surface vary significantly, concentration losses must be respected additionally.

2.8.5 Determination of the kinetic parameters

The exchange current density can be derived from (practical) isothermal measurements of the overpotential at low current densities, whereas the concentration variation at the catalyst surface and therefore mass transport losses should be negligible. The logarithm of the current density is plotted against the overpotential and a straight line is drawn through the linear region of the curve. The logarithm of the exchange current density is given by the intersection of this straight line with the y-axis, as shown in Figure 2.5 for the two temperatures T_A and T_B in blue and green, respectively.

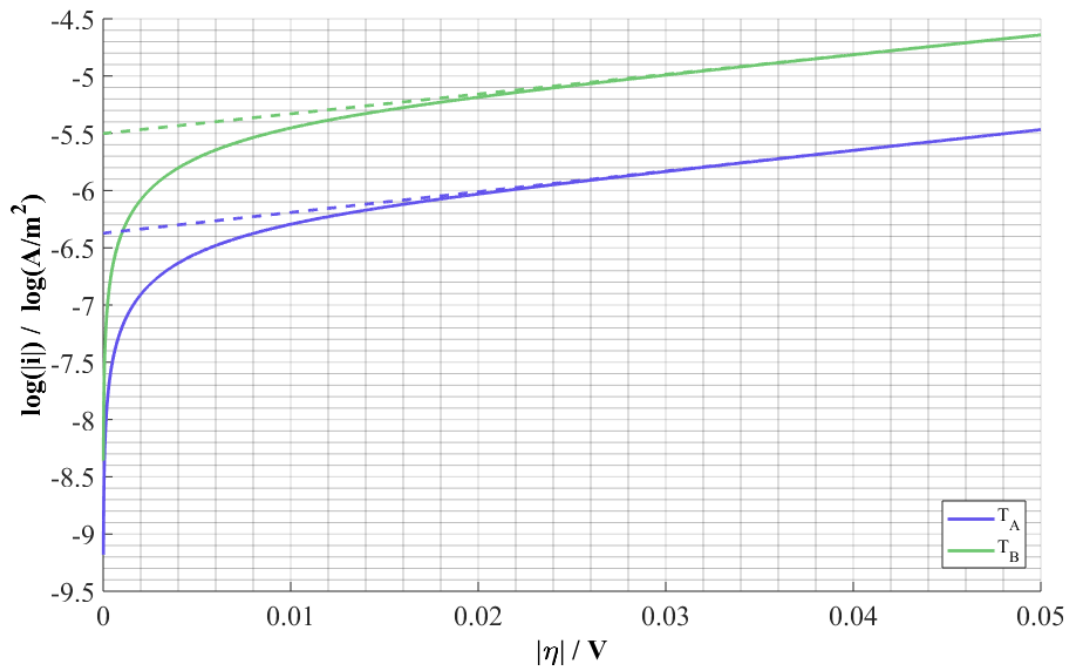


Figure 2.5: Graphical derivation of kinetic parameters.

The transfer coefficient can be obtained from the slope of the curve. As the reverse reaction is negligible in the linear region of $\log(i)$ vs. η , the current density can be estimated with the Tafel expression according to:

$$i = i_0 \left(\exp \left(\frac{\alpha_f n F \eta}{RT} \right) \right). \quad (2.83)$$

Rearranging equation (2.83) yields the Tafel slope s_{Tafel} as

$$s_{Tafel} = \frac{\eta}{\log\left(\frac{i}{i_0}\right)} = \frac{RT}{\alpha_f n F} \cdot 2.3, \quad (2.84)$$

and therefore the transfer coefficient of the forward reaction:

$$\alpha_f = \frac{RT}{nF \cdot s_{Tafel}} \cdot 2.3. \quad (2.85)$$

The transfer coefficient of the reverse reaction α_b can similarly be determined from the Tafel slope of the backward reaction. If it is not available, it can be estimated in some cases from the balance

$$\alpha_f + \alpha_b = 1. \quad (2.86)$$

In order to derive the activation energy, at least one more measurement is required. The concentrations at the catalyst surface must approximately be the same but the temperature must differ from the other measurement. Then, the exchange current densities $i_{0,A}$ and $i_{0,B}$ at the temperatures T_A and T_B , respectively, can be related to one another according to equation (2.71):

$$E_{Act}^0 = \frac{RT_A T_B}{T_B - T_A} \ln \left(\frac{i_{0,B}}{i_{0,A}} \right). \quad (2.87)$$

This mathematical derivation is analog to the graphical determination of the activation energy where the logarithm of the exchange current density is plotted against $1/T$ and E_{Act}^0 is determined from the slope of the curve.

2.9 Transport phenomena in electrolytes

The transport of an ion in an electrolyte solution is caused by different driving forces. For example, concentration gradients in the solution force an ion to move from the higher concentration region towards the lower concentration region. This transport phenomenon is generally known as diffusion. Another form of diffusion is the thermal diffusion where the temperature gradient is the driving force. Being relatively slow, thermal diffusion is negligibly in some cases, especially when the temperature gradients are small. Due to the electrical charge of an ion, it is immediately affected by an electric field and its mass transport is directly coupled with charge transport. The transport process of an ion due to an electrical potential gradient is known as migration. However, even if diffusion and migration were negligible, the electrolyte solution and therefore the ions could be driven externally, for example by a pump, while pressure is the driving force; this transport process is known as convection. One speaks of forced convection when the fluid is externally driven, for example by a pump as described above, whereas it is called natural convection when the movement occurs on its own. These three transport processes, diffusion, migration, and convection, form the essential basis for the transport of an ion in an electrolyte solution.

The transport processes of ions in electrolytes are typically described either based on the diluted theory or based on the concentrated theory. Resulting primary from the work by Nernst [45], [31], [46] and Planck [47], [48], [49] in the 1880's and 1890's, the flux of an ion (N_i) in a highly diluted solution can be described by an expression called Nernst-Planck equation [50]:

$$N_i = -D_i \nabla c_i - z_i u_i F c_i \nabla \phi + c_i v, \quad (2.88)$$

where F is the Faraday's constant, ϕ is the electrical potential of the solution, v is the velocity, and D_i , u_i , z_i , and c_i are the diffusion coefficient, the mobility, the charge number, and the concentration of species i .

The first, the second, and the third term on the right of equation (2.88) refer to diffusion, migration, and convection, respectively. Therefore, in case of the diluted theory the net flux is formed by simply cumulating the individual fluxes caused by the different driving forces. Equation (2.88) can also be rearranged to describe the ion flux in the form

$$N_i = -D_m \nabla c_i + \frac{t_i i}{z_i F} + c_i v, \quad (2.89)$$

where D_m is the diffusion coefficient of the solution, t_i is the transference number of species i (subscript i denotes the species i), and i is the electrical current. The properties of the electrolyte can therefore be derived from separate measurements studying the transport processes individually. Also, in case of highly diluted solutions, the Nernst-Einstein relation applies which relates the diffusion coefficient D_i and the mobility u_i to one another according to [41]

$$D_i = RT u_i, \quad (2.90)$$

in which T is the temperature. However, as the name indicates the diluted theory only applies under highly diluted conditions and already fails for low electrolyte concentrations in some cases [41]. A more accurate description for the transport processes in concentrated solutions is the concentrated electrolyte theory, primarily formulated by Newman [51], [52], [39], [53], [41]. Based on the Maxwell Stefan diffusion law, the concentrated electrolyte theory accounts for the interactions of all species in the solution and describes the ion flux by [41]

$$N_i = -\frac{\nu_i c_T c_e \mathfrak{D}}{RT c_0 \nu} \nabla \mu_e + \frac{i t_i^0}{z_i F} + c_i v_0, \quad (2.91)$$

where ν_i is the dissociation number of species i , ν is the total dissociation number, t_i^0 is the transference number of species i with respect to the solvent velocity v_0 , c_0 is the solvent concentration, c_T is the total concentration of the solution, \mathfrak{D} is the thermodynamic diffusion coefficient of the electrolyte, and c_e is the electrolyte concentration which can be written as

$$c_e = \frac{c_+}{\nu_+} = \frac{c_-}{\nu_-}. \quad (2.92)$$

As the transport of ions is directly coupled with an electrical current, it can be written in both cases, in case of a diluted solution as well as in case of a concentrated solution, as

$$i = F \sum_k z_k N_k. \quad (2.93)$$

When modeling an electrolyte solution, it is commonly assumed that the electrolyte solution is electrical neutral everywhere. This electroneutrality condition can be written as

$$0 = \sum_k z_k c_k. \quad (2.94)$$

The essential difference between both theories is the multicomponent interaction taken into account in the concentrated electrolyte theory but not in the diluted electrolyte theory. Under highly diluted conditions, the ions are practically completely surrounded by the solvent and the transport properties such as the diffusion coefficient and the mobility refer to the interaction of the ion with the solvent; both transport properties can then be related to one another according to the Nernst-Einstein relation. This does not apply for concentrated solutions where the interactions of the species must not be neglected.

The diluted theory is described in chapter 2.9.1, whereas the concentrated theory is discussed in chapter 2.9.2 thoroughly. It is shown that the key difference between both models lays in the definition of the transport properties. In order to keep the derivations comprehensive, thermal diffusion is neglected and a binary electrolyte, such as the KOH electrolyte, is focused. In case of a binary electrolyte, a single salt dissociates into ν_+ positive charged ions with the charge number z_+ and ν_- negative charged ions with the charge number z_- .

2.9.1 Diluted theory

The diluted electrolyte theory assumes that the overall flux of an ion in the electrolyte solution can be calculated by summing up the separate fluxes caused by the different driving forces according to [50]

$$N_i = -D_i \nabla c_i - z_i u_i F c_i \nabla \phi + c_i v, \quad (2.88)$$

which is known as the Nernst-Planck equation. It sums up the fluxes due to diffusion, migration, and convection represented by the first, the second, and the third term on the right, respectively. It only applies when the concentration of the solute species is much lower compared to the concentration of another species, which can be identified as the solvent.

In order to study a single transport mechanism isolatedly, all other transport processes must be eliminated. In order to eliminate the dependence on the electrical potential difference in the solution, it has to be replaced by the dependence on the electrical current. As the transport of charge is directly coupled with the transport of ions, the electrical current through the electrolyte solution is obtained by summing up all ion fluxes according to equation (2.93):

$$i = \underbrace{-F \sum_k z_k D_k \nabla c_k}_{i^D} - \underbrace{F^2 \nabla \phi \sum_k z_k^2 u_k c_k}_{i^M} + \underbrace{Fu \sum_k z_k c_k}_{i^C}. \quad (2.95)$$

In analogy with the molar fluxes in equation (2.88), the first, the second, and the third term on the right side of equation (2.95) represent the electrical currents due to diffusion (i^D), migration (i^M), and convection (i^C), respectively. Assuming electroneutrality in the electrolyte causes the last term on the right of equation (2.95) to vanish and therefore the electrical current to be independent from convection:

$$i = -F \sum_k z_k D_k \nabla c_k - F^2 \nabla \phi \sum_k z_k^2 u_k c_k. \quad (2.96)$$

When the concentration gradient in the solution is negligible, for example due to stirring, the observable current is almost solely caused by migration. Hence, it can be written with Ohm's law in the form

$$i = -\kappa \nabla \phi, \quad (2.97)$$

in which κ is the electrical conductivity of the solution which can be measured:

$$\kappa = F^2 \sum_k z_k^2 u_k c_k. \quad (2.98)$$

The transference number of an ion describes the electrical current taken by the ion, divided by the net current and can therefore be written as

$$t_i = \frac{z_i^2 u_i c_i}{\sum_k z_k^2 u_k c_k} = \frac{F^2 z_i^2 u_i c_i}{\kappa}. \quad (2.99)$$

Hence, the electrical current may be given in the form

$$i = -F \sum_k z_k D_k \nabla c_k - \kappa \nabla \phi, \quad (2.100)$$

and the ion flux may be given as

$$N_i = -D_i \nabla c_i - \frac{t_i}{z_i F} \kappa \nabla \phi + c_i v. \quad (2.101)$$

With equation (2.100) the electrical potential gradient in equation (2.101) can be replaced in order to derive an expression which is dependent on the electrical current but not on the electrical potential gradient:

$$N_i = -D_m \nabla c_i + \frac{t_i i}{z_i F} + c_i v, \quad (2.102)$$

in which D_m is the diffusion coefficient of the solution which may be given as

$$D_m = D_i - \frac{t_i}{z_i} \sum_k z_k D_k. \quad (2.103)$$

The diffusion coefficient D_m can be measured when the concentration gradient is the only driving force causing the movement of ions in the solution, which applies in absence of an electrical current ($i = 0$) and in the stagnation of the solution/solvent ($v = 0$). In case of the diluted theory, the solvent concentration is so high, that the velocities of the solvent and the solution are almost the same. For a binary electrolyte, D_m can be written as

$$D_m = t_- D_+ + t_+ D_-. \quad (2.104)$$

Based on the diluted electrolyte theory, the diffusion coefficient and the mobility are related to one another by the Nernst-Einstein equation

$$D_i = RT u_i, \quad (2.90)$$

thus D_m can also be written as

$$D_m = \frac{D_- D_+ (z_+ - z_-)}{z_+ D_+ - z_- D_-}. \quad (2.105)$$

Also, the electrical conductivity of the solution can be rearranged:

$$\kappa = \frac{z_-^2 \nu_- D_- F^2 c_e}{t_- RT}. \quad (2.106)$$

As the ionic equivalent conductivity λ_i is related to the mobility according to

$$u_i = \frac{\lambda_i}{|z_i| F^2}, \quad (2.107)$$

the electrical conductivity can also be given in the more familiar form

$$\kappa = z_+ \nu_+ \underbrace{(\lambda_+ + \lambda_-)}_{\Lambda} c_e, \quad (2.108)$$

in which Λ is the equivalent conductance. Hence, in case that the diluted theory applies, the properties of the electrolyte can be measured on the basis of equations (2.100) and (2.102) by isolating either diffusion (leading to the diffusion coefficient) or migration (leading to the electrical conductivity, the transference numbers, and the mobilities).

2.9.2 Concentrated theory

The diluted theory only applies in case of very low electrolyte concentrations and neglects multicomponent interactions. In case of moderate to high concentrations, the solutes in the solution strongly affect one another so their interactions with the solvent taken singly are not representative for their transport in the solution. The following mathematical description of the concentrated electrolyte solution is based on Newman [41], whereas a binary electrolyte is focused. Furthermore, electroneutrality according to equation (2.94) is assumed.

The change in electrochemical potential of a component in the solution can be written based on the Stefan-Maxwell diffusion equation for the multicomponent species transport as [41]

$$c_i \nabla \mu_i = \sum_j K_{ij} (v_j - v_i), \quad (2.109)$$

where μ_i is the chemical potential of species i , v_i and v_j are the velocities of species i and j , respectively, and K_{ij} is the drag coefficient of these species, given by [41]

$$K_{ij} = \frac{RT c_i c_j}{c_T \mathfrak{D}_{ij}}. \quad (2.110)$$

In equation (2.110), \mathfrak{D}_{ij} is the binary diffusion coefficient of species i and j , and c_i , c_j , and c_T are the concentration of species i , the concentration of species j , and the total concentration of the solution, respectively; an expression for c_T is provided in equation (2.117). Hence, with equations (2.93), (2.109), and (2.110) the flux of an ion (N_i) in the solution may be given as

$$N_i = -\frac{v_i c_T c_e \mathfrak{D}}{RT c_0 \nu} \nabla \mu_e + \frac{it_i^0}{z_i F} + c_i v_0, \quad (2.111)$$

where μ_e is the chemical potential of the electrolyte, t_i^0 is the transference number with respect to the solvent velocity v_0 , and \mathfrak{D} is the thermodynamic diffusion coefficient of the solution. These parameters can be given as follows:

$$\mu_e = \nu_+ \mu_+ + \nu_- \mu_-, \quad (2.112)$$

$$t_i^0 = \frac{|z_i| \mathfrak{D}_{i0}}{z_+ \mathfrak{D}_{+0} - z_- \mathfrak{D}_{-0}}, \quad (2.113)$$

$$\mathfrak{D} = \frac{\mathfrak{D}_{+0} \mathfrak{D}_{-0} (z_+ - z_-)}{z_+ \mathfrak{D}_{+0} - z_- \mathfrak{D}_{-0}}. \quad (2.114)$$

Notice: The definition of \mathfrak{D} in equation (2.114) is in analogy with the definition of D_m in equation (2.105).

An expression for c_T can be derived from the molar balance. The total amount of species (n_T) in a certain volume (V) is obtained by summing up the molar amounts of the species

contained in this volume. Hence, for an electrolyte solution which consist of solvent (n_0), positive charged ions (n_+), and negative charged ions (n_-) it may be given in the form

$$n_T = n_0 + n_+ + n_- \quad (2.115)$$

Then, dividing equation (2.115) by the volume V yields c_T as follows

$$c_T = \frac{n_T}{V} = \underbrace{\frac{n_0}{V}}_{c_0} + \underbrace{\frac{n_+}{V}}_{c_+} + \underbrace{\frac{n_-}{V}}_{c_-} \quad (2.116)$$

in which the individual amounts of moles divided by the volume can be replaced by the respective concentrations. Inserting equation (2.92) in equation (2.116) yields

$$c_T = c_0 + \nu c_e \quad (2.117)$$

with ν being the dissociation number of the electrolyte, given by

$$\nu = \nu_+ + \nu_- \quad (2.118)$$

In some cases, an expression which describes the ion flux as function from the electrolyte concentration can be more practical than an expression which depends on the chemical potential of the electrolyte. In order to replace the chemical potential in equation (2.111) by the electrolyte concentration, the definition of the chemical potential of the electrolyte solution must be considered, which can be given as [41]

$$\mu_e = \nu RT \ln(m \gamma_{\pm} \lambda_{\pm}^0), \quad (2.119)$$

where m is the molality, γ_{\pm} is the mean molal activity coefficient of the electrolyte, and λ_{\pm}^0 is a proportionality constant “independent from the electrical state” [41]. Thus, the gradient in chemical potential can be replaced by the concentration gradient according to

$$\nabla \mu_e = \frac{\nu RT}{c_e} \left(1 + \frac{d \ln(\gamma_{\pm})}{d \ln(m)} \right) \left(1 - \frac{d \ln(c_0)}{d \ln(c_e)} \right) \nabla c_e \quad (2.120)$$

Inserting equation (2.120) in equation (2.111) yields

$$N_i = -v_i D \left(1 - \frac{d \ln(c_0)}{d \ln(c_e)} \right) \nabla c_e + \frac{it_i^0}{z_i F} + c_i v_0, \quad (2.121)$$

where D is the diffusion coefficient “that is usually measured” [41], defined as

$$D = \mathfrak{D} \frac{c_T}{c_0} \left(1 + \frac{d \ln(\gamma_{\pm})}{d \ln(m)} \right). \quad (2.122)$$

The definition of the diffusion coefficient (on the concentration scale) D_c in the form

$$D_c = \mathfrak{D} \frac{c_T}{c_0} \left(1 + \frac{d \ln(\gamma_{\pm})}{d \ln(m)} \right) \left(1 - \frac{d \ln(c_0)}{d \ln(c_e)} \right) = D \left(1 - \frac{d \ln(c_0)}{d \ln(c_e)} \right), \quad (2.123)$$

yields

$$N_i = -v_i D_c \nabla c_e + \frac{it_i^0}{z_i F} + c_i v_0. \quad (2.124)$$

Equation (2.124) derived for the concentrated electrolyte equals equation (2.101) derived for the diluted electrolyte. Just like D_m , D_c can be derived from measurements in the absence of an electrical current, and when the solvent velocity equals zero. However, in some cases, for example when modeling the transport processes in the electrolyte, referring to the solution velocity might be more practical than referring to the solvent velocity. The total flux of the solution (N_T) can be calculated by the sum of all species fluxes according to

$$N_T = \sum N_i, \quad (2.125)$$

whereas each of the species fluxes can be written as

$$N_i = c_i v_i, \quad (2.126)$$

with c_i and v_i being the concentration and the velocity of species i . Therefore, for an electrolyte solution, which consists of solvent, positive charged ions, and negative charged ions, the total flux can be given as:

$$N_T = c_0 v_0 + c_+ v_+ + c_- v_- \quad (2.127)$$

Also, the total flux can be written as the product of the total concentration and the volume average velocity v^* of the solution according to

$$N_T = c_T v^* \quad (2.128)$$

Then, inserting equation (2.128) in equation (2.127) yields

$$c_T v^* = c_+ v_+ + c_- v_- + c_0 v_0 \quad (2.129)$$

Hence, the product of the ion concentration and the solvent velocity can be written as

$$c_i v_0 = -\frac{c_i}{c_0} \frac{i}{z_k F} + N_i \frac{c_i}{c_0} \left(\frac{z_i}{z_k} - 1 \right) + \frac{c_T}{c_0} c_i v^*, \text{ with index } k \neq i. \quad (2.130)$$

Inserting equation (2.130) in equation (2.124) yields

$$N_i = -v_i D_c \frac{c_0}{c_T} \nabla c_e + \frac{i t_i^*}{z_i F} + c_i v^*, \quad (2.131)$$

where the transference number with respect to the volume average velocity (t_i^*) is

$$t_i^* = \frac{t_i^0 c_0 + c_k}{c_T}, \text{ with } k \neq i. \quad (2.132)$$

In order to derive an expression for the electrical conductivity of the solution, the electrochemical reaction must be considered which can be written as [41]

$$-nF \nabla \phi = s_+ \nabla \mu_+ + s_- \nabla \mu_- + s_0 \nabla \mu_0, \quad (2.133)$$

whereas s_i represents the stoichiometric coefficient of species i . The associated charge balance can be given in the form [41]

$$-n = s_- z_- + s_+ z_+. \quad (2.134)$$

In order to replace $\nabla\mu_0$ in equation (2.133), the Gibbs-Duhem equation can be used [41]:

$$c_0 \nabla\mu_0 + c_e \nabla\mu_e = 0. \quad (2.135)$$

The expression for the electrical current as function from $\nabla\phi$ and $\nabla\mu_e$ can be derived from equation (2.133) in four steps:

1. Replacing $\nabla\mu_0$ by $\nabla\mu_e$ with equation (2.135),
2. replacing $\nabla\mu_+$ by $\nabla\mu_-$ and $\nabla\mu_e$ according to equation (2.112),
3. expressing $\nabla\mu_-$ as function from N_- and N_+ based on equations (2.109) and (2.110), and
4. inserting N_- and N_+ according to equation (2.111).

Rearranging yields finally [41]

$$i = -\kappa \nabla\phi - \frac{\kappa}{F} \left(\frac{s_+}{n\nu_+} + \frac{t_+^0}{\nu_+ z_+} - \frac{s_0 c_e}{n c_0} \right) \nabla\mu_e, \quad (2.136)$$

where the electrical conductivity of the electrolyte is defined as [41]

$$\frac{1}{\kappa} = -\frac{RT}{c_T z_+ z_- F^2} \left(\frac{1}{\mathfrak{D}_{\pm}} + \frac{c_0 t_-^0}{c_+ \mathfrak{D}_{0-}} \right). \quad (2.137)$$

In case that the chemical potential gradient of the electrolyte approaches zero (due to negligible concentration variations in the solution), the relationship between the current density and the potential gradient in the solution follows Ohm's law. This relationship enables the measurement of the electrical conductivity of the solution.

Notice: Thermal diffusion has been neglected in the derivation above. Further information on the transport phenomena in concentrated electrolyte solutions are given by Newman [41] who also provides an expression that accounts for thermal diffusion.

3. Former AFC models with impact on this work

Several mathematical models exist in open literature, focusing different objects. The model presented in this work has primarily been influenced by a consecutive series of mathematical models which focused on the overall performance of an AFC single cell. These works are presented chronologically in this chapter.

One of the first models of a complete AFC was presented by Kimble and White [54] in 1991 and laid the foundation for several mathematical models which were developed afterwards. Predicting the cell performance from low to high current densities under steady state conditions and therefore creating an entire polarization curve was focused. Their one-dimensional (1-D), isothermal model consisted of five layers representing the anodic and cathodic gas diffusion layers (GDL), the anodic and cathodic reaction layers (RL), and the separator layer in between. In the separator layer, an immobile KOH electrolyte was considered, that did not circulate outside the cell. Besides the transport of hydrogen in the anode gas and oxygen in the cathode gas, the transport of water vapor was considered.

When describing the processes occurring in the porous layers, Kimble and White assumed macrohomogeneous, three-phase regions based on the porous electrode theory by Newman and Tiedemann [53]. The HOR in the anodic RL and the ORR in the cathodic RL, were assumed to arise directly as two electron transfer reaction and four electron transfer reaction, respectively. For the transport in the gas phase, the Stefan-Maxwell equation (see equation (3) in [53]) was used. Kimble and White described the transport in the liquid phase with the Nernst-Planck equation (see equation (6) in [53]), related the mobility and the diffusion coefficient by the Nernst-Einstein relation (see equation (8) in [53]), and assumed electroneutrality (see equation (42) in [53]). For the transport of hydrogen and oxygen into the electrolyte, the authors used an expression based on the thin film theory (see equation (13) in [53]). For the kinetics in the anodic RL and in the cathodic RL, the Butler-Volmer expression was used, whereas the effect of water was neglected (see equations (33)-(34) in [53]); the reaction orders of hydrogen and hydroxyl ions in the HOR were both assumed to be 2, whereas the reaction orders of oxygen and hydroxyl ions in the ORR were assumed to be 0.5 and 2, respectively. The equilibrium potential was described with the temperature dependent Nernst equation (see equation (36)-(39) in [53]), where again the concentrations of water were not taken into consideration. For the transport of charge in the electrodes, Ohm's law was assumed.

Kimble and White defined the base case conditions of the model to be 7 N KOH, 80 °C, and 4.1 atm. Based on several parameter studies, the authors concluded that the influence of the gas phase diffusion on the cell performance is negligible, the diffusion of dissolved oxygen is predominately responsible for the mass transport losses at high current densities, and that the electronic resistance causes the most potential losses at low current densities. [54]

In 1992 Kimble and White [55] used their model for predicting the parameter sensitivity and optimal design parameters. They increased certain parameters of interest by 5 % over the base case value and investigated the potential ranges between 1.1-0.93, 0.93-0.85, and 0.85-0.8 V representatively for the activation region, the ohmic region, and the mass transport region, respectively. From their investigation, the authors concluded that the performance of the system depends on various parameters, especially in the ohmic region and mass transport region. The model was significantly affected by the parameters specific to the oxygen electrode. With respect to the optimal RL thicknesses, the authors concluded that it is “a compromise among the number of reaction sites, the solubility of the reactant gases, and the liquid-phase diffusivity of the dissolved reactant gases. A small fraction of the total porosity in the cathode reaction region is needed in the gas phase to sustain a high gas-phase diffusion rate while maintaining a large diffusion rate in the liquid phase” [55]. The greatest improvement in cell performance was found to be obtained “by increasing the gas-liquid interfacial surface area in the cathode followed by increasing the electrocatalytic activity or liquid-solid interfacial surface area and decreasing the separator thickness from the base-case conditions” [55]. Additionally, the authors concluded “the reason for the decrease in the limiting current density beyond an optimal thickness [of the RL] is due to a lowering of the oxygen gas solubility and liquid-phase diffusivity, not to gas-phase diffusional resistances as suggested by Kenjo and Kawatsu [56] and by Björnbom [57]” [55].

Also in 1992 Yang and Björnbom [58] presented a mathematical model for the cathode of an AFC which became the basis for the model of a full AFC they published in the following year [59]. The 1-D, isothermal half-cell model for stationary operating conditions consisted of two macrohomogeneous layers: the gas-supply layer and the catalyst layer (CL). Yang and Björnbom focused on the impact of humidity content in the gas, the current density, and the temperature on the electrode performance [58]. In contrast to Kimble and White, Yang and Björnbom used the concentrated electrolyte theory formulated by Newman [51], [52] and took into account the transport of water in both phases, the gas phase and the liquid

phase. Yang and Björnbom did not neglect Knudsen diffusion in the CL but in the GDL. In the CL, the authors used the agglomerate model, introduced by Giner and Hunter [60] and Tantram and Tseung [61], when they assumed electrolyte-filled agglomerates surrounded by a thin electrolyte film. This assumption defined their formulation of the oxygen reaction rate (see equations (36)-(38) in [58]). The authors did not use the Butler-Volmer expression for describing the current-voltage characteristic, but an expression similar to the Tafel equation (see equation (39) in [58]). As cathode gas they studied humidified air, assumed to consist of oxygen, nitrogen and water vapor.

Based on their simulations Yang and Björnbom concluded that “the flow of water may show a rather complicated pattern within the catalyst layer” [58]. Depending on the operating current density, the temperature, and the humidity at the inlet, the model showed different directions of water: flow from the gas phase to the liquid phase, from the liquid phase to the gas phase, or in both directions, when the water flux changed its direction in the CL. Additionally, they showed the influence of the relative humidity on the electrode potential.

The expanded model of a complete AFC, published by Yang and Björnbom [59] in 1993, consisted of five layers, namely the anodic and cathodic GDLs, the anodic and cathodic CLs, and the separator in between. Again, Yang and Björnbom focused on the water-management but not on the performance of the AFC in general. Based on their simulation results the authors concluded that “exact water balance management may be essential for optimization of the operational efficiency of the fuel cell” [59]. The authors found that “using a wet anode gas together with a dry cathode gas gives a better [electrolyte] concentration distribution than the opposite option” and noticed that “[t]his is somewhat unexpected since water is consumed in the cathode and produced in the anode” [59]. Yang and Björnbom predicted that the “upper boundary on the limiting current in an AFC cathode as a function of the active layer thickness [...] is an effect of the gas diffusion resistance” [59] and refused the conclusion by Kimble and White “that it is an effect of uneven electrolyte concentration distribution which may strongly decrease oxygen solubility and oxygen liquid phase diffusivity in a zone of the active layer” [59]. This conflict, caused by different predictions from two different models, resulted in a discussion [62] without conformity.

However, the modeling work by Kimble and White inspired Jo and Yi [63] who introduced their 1-D, isothermal model of an AFC in 1999. Unlike Kimble and White, they considered water in the Butler-Volmer expression (see equation (33)-(34) in [63]) and in the Nernst equation (see equations (38)-(39) in [63]). Also in contrast to Kimble and White, Jo and Yi replaced the reaction orders in the Butler-Volmer expressions by the absolute value of the stoichiometric coefficients (compare Table 1 in [54] with Table 3 in [63]). The authors derived the specific surface area of the catalyst from the BET surface area and separated the specific surface area from the exchange current density. In contrast, Kimble and White considered both parameters together as product. Additionally, Jo and Yi assumed the exchange current density of the hydrogen reaction to be ten thousand times larger than the one of the oxygen reaction, whereas Kimble and White assumed that the exchange current densities were of the same order of magnitude. With respect to the water-management, the product water was assumed to leave the cell on the anode side. Considering the volume average velocity arising in the Nernst-Planck equation, Jo and Yi derived a different expression than Kimble and White (compare equations (53)-(54) in [63] with equation (59) in [54]). They did not use the Nernst-Einstein relation but calculated the mobility from the electrical conductivity of the solution and the diffusion coefficients of the anions and cations from the diffusion coefficient of the solution.

Jo and Yi defined the same base case conditions as Kimble and White and compared their simulation results with measurements at the Orbiter Fuel Cell [64]. Also, after adjusting a few parameters, especially the operating conditions, they compared their simulation results with measurements at the BZA4 cell by Siemens. In both cases, they found good agreements with the measurements. They also concluded that the gas phase diffusion of oxygen is not rate-limiting and that the oxygen diffusion through the liquid phase causes the limiting current density [63]. The authors called attention “that a model which assumes [an] uniform [electrolyte concentration] cannot represent a high-performance electrode or a single cell” [63]. They referred to the fact that a rising electrolyte concentration decreases the gas solubility. For the studied operating conditions, Jo and Yi predicted the optimal electrolyte concentration to be between 3.0 and 3.5 M for cell voltages between 0.6 and 0.9 V.

In 2000, Jo et al. [65] used their model for studying the influences of the thicknesses of the separator, CLs, and GDLs on the cell performance. Again, the base case temperature, pressure, and electrolyte concentration were 80 °C, 4.1 atm, and 7 M KOH, respectively.

The authors found that “[t]hickening the separator layer decreased the limiting current density and increased the slope of the ohmic polarization region” [65]. The decrease of the limiting current density was explained by the increase in the electrolyte concentration in the cathode catalyst layer with increasing separator thickness which “leads to a decrease in the liquid phase diffusivities and oxygen solubilities” [65]. With respect to the increase of the slope of the polarization curve in the ohmic region, Jo et al. showed that “50.2 % of the increase in [the ohmic resistance] is attributable to the increase in [the potential drop along the separator]” and reasoned that “the remaining 49.8 % [could] be caused by the increase in mass transfer resistance of dissolved oxygen” [65]. With respect to the thickness of the anode catalyst layer, the authors found that the optimum thickness “varied between 0.04-0.15 mm according to the cell voltage” and revealed that “the rate-determining step at [the limiting current density] exists in the anode, not in the cathode” for a very small thickness of the anode catalyst layer [65]. Additionally, the authors found a decrease of the limiting current density with an increase in the thickness of the anode catalyst layer and gave the reason by the “increase in [the electrolyte concentration] in the cathode catalyst layer, which yields a decrease in the solubility and liquid phase diffusivity of dissolved oxygen” [65]. Furthermore Jo et al. showed that “[t]he thickness of the cathode catalyst layer significantly influenced the cell performance” [65]. An enhancement of the cell performance with the thickness of cathode catalyst layer due to the ‘thickness effect’ was presented: “[T]he apparent reaction area and the apparent gas-electrolyte interface area of the catalyst are proportional to [the thickness of the catalyst layer]”, thus “an increase in [the thickness of the catalyst layer] results in a linear increase in [the current density] [...] in all polarization regions” [65]. However, also the limitation of the thickness effect was revealed by the authors and they “considered [this limitation] to be caused by the mass transfer resistance of the electrode” [65]. From the variation of the thicknesses of the anode and cathode GDLs from 0.05 to 0.55 mm “no noticeable variation in the polarization curve was found” [65].

Based on the model developed in the course of Zhou’s doctoral thesis [66] in 2007, Zhou et al. [67] presented their 2-D, non-isothermal model of an AFC for steady state operation in 2011; the model was developed and solved with the software FLUENT[®]. It consisted of seven layers, namely the anodic and cathodic gas channels, the anodic and cathodic GDLs, the anodic and cathodic CLs, and the separator. Just like Kimble and White [54], but unlike Jo and Yi [63], the authors inserted the dimensionless partial pressures of hydrogen and oxygen in the Nernst equations for the HOR and the ORR, respectively, and neglected the

water activity (see equations (6)-(7) in [67]). Zhou et al. used the same Butler-Volmer expression as Jo and Yi (see Table 3 in [67]), as they also accounted for the water concentrations and replaced the reaction orders by the absolute values of the stoichiometric coefficients. Compared with the previous models [54], [55], [63], and [65] progress especially with respect to the description of the transport of momentum and energy was made. For the water evaporation into the gases, the authors introduced an evaporation rate (see Table 2 in [67]) in analogy with the solution rate of hydrogen and oxygen in the electrolyte, used in [54], [55], [63], [65] and finally also in [67]. On the one hand, Zhou et al. focused on the difference between the diluted electrolyte theory and the concentrated electrolyte theory, and on the other hand, they considered the difference between isothermal and adiabatic (non-isothermal) conditions. In case of the diluted electrolyte theory, the Nernst-Planck equation (see equation (11) in [67]) and the Nernst-Einstein relation (see equation 20 in [67]) were used. In case of the concentrated electrolyte theory, thermal diffusion was neglected (see equation (21) in [67]).

The authors chose the same base case conditions as Jo and Yi, compared the polarization curve predicted for the non-ideal system with the polarization curve measured at the Orbiter Fuel Cell [64], and found good agreements with the measurements. Comparing the ideal solution with the non-ideal solution, Zhou et al. concluded that “[t]he ideal solution formulation underestimates the limiting current by about 50 %” and “should not be applied in the modeling and simulation of AFC for conditions similar to that considered” [67]. With respect to the effect of temperature, Zhou et al. reasoned that “[t]he thermal condition can significantly change the result of the calculation. The adiabatic boundary condition can increase the limiting current by 30 %” [67]. As the concentration gradient in the electrolyte solution decreased and the limiting current density raised in case of the non-ideal solution compared with the case of the ideal solution, the authors predicted that “a uniform KOH concentration in the electrolyte [...] will be an effective measure to increase the limiting current density condition” [67].

Also in 2011, Zhou et al. [68] used their model for the prediction of shunt currents, whereas the concentrated electrolyte theory and adiabatic (non-isothermal) conditions were used. Again, 7 M KOH, 80 °C, and 4.1 atm were chosen as base case conditions for the electrolyte concentration, temperature, and pressure, respectively. In order to investigate the effect of the temperature on shunt currents, three isothermal boundary conditions were considered,

namely 80, 50, and 25 °C. Based on their simulations the authors concluded that shunt currents occur “in the regions where there exists a large electric potential gradient and where the primary current is lacking, i.e., in the regions adjacent to the separator inlet and exit” [68]. With respect to the influence of temperature, the authors found that “[s]hunt currents are present regardless of applied thermal boundary conditions being adiabatic or isothermal” [68]. Concerning the humidification of the gases they called attention to the fact that “[t]he level of humidification of the reactant gas streams is important to KOH concentration at low current density conditions, through the loss of [water] due to evaporation to gas channels” [68]. Also, the authors derived information about the potential losses and reasoned that “[a]t high current densities, the IR loss due to the electric potential drop is comparable to the overpotential loss at the anode; both are about an order of magnitude lower than the overpotential loss at the cathode” [68].

In 2014, Kunz, the author of this doctoral thesis, presented a 2-D, steady-state, and isothermal model of an AFC in [69] and in his master’s thesis [70]. The model had been developed previously by Hütten at the Chair of Energy Technology of the University of Duisburg-Essen, using the software COMSOL Multiphysics[®]. In his master’s thesis, Kunz reviewed, modified, and used the model for various simulative studies. The model consisted of seven layers, namely the anodic and cathodic gas channels, the anodic and cathodic support layers, the anodic and cathodic GDLs, and the electrolyte channel. The catalyst layers were modeled as boundaries between the electrodes and the electrolyte channel. The equilibrium potentials of the anode and cathode reactions were calculated with the partial pressures of hydrogen and oxygen, respectively, whereas the activities of water and ions in the electrolyte were neglected (see equation (2-80) and equation (2-81) in [70]). The electrochemical reactions were described with the Butler-Volmer expression. Concentration losses were neglected in the expression for the anode reaction (see equation (2-74) in [70]), but taken into account in the expression for the cathode reaction (see equation (2-75) in [70]), by inserting the liquid phase concentrations of the species participating in the cathode reaction. The reaction orders were replaced by the absolute values of the stoichiometric coefficients (see Table 6 in [70]). In addition to the model by Zhou et al. given in [66], [67], [68], the model presented by Kunz accounted for the temperature dependences of the exchange current densities. However, in contrast to the model by Zhou et al., the model described by Kunz was isothermal and only used the Nernst-Planck equation. Also, different to the model by Zhou et al., the model described by Kunz assumed that the reactions occur

in boundaries but not in layers and did not describe the species transport across the phase boundary by rate expressions but based on equilibria (see equation (2-6) and equation (2-30) in [70] for the partial pressure of water in the gas phase and the oxygen concentration at the catalyst surface, respectively).

Kunz chose 60 °C, 1 atm, and 5 M KOH as base case conditions for temperature, pressure, and electrolyte concentration, respectively, and conducted various parameter studies. For an increase in temperature, an enhancement of the cell performance in the activation region, the ohmic region, as well as in the concentration region was found. With respect to the optimum electrolyte concentration, the model predicted that the 5 M KOH solution performs the best. Also, a high sensitivity of the polarization curve with respect to kinetic parameters, parameters specific to the catalyst, and parameters related to the reactant transport through the liquid phase was predicted. [70]

Further mathematical models of AFCs were presented by Verhaert et al. [71] for predicting the electrolyte temperature and the power output (software Aspen), Dürr et al. [72] for considering the dynamic behavior of an entire stack, Schaefer et al. [73] for the calculation of shunt current in a stack and the investigation of protective current (software Simulink), Verhaert et al. [74] for considering the water management (software Matlab), Zhang et al. [75] for investigating the power output of a typical AFC, and Verhaert et al. [76] for studying the impact of temperature on stack performance.

Especially the model presented by Kunz in [70] and the model by Zhou et al., described thoroughly in [66] and [67], constitute the base for the 2-D, non-isothermal model which is presented in this work. The model consists of nine layers in total, namely the anodic and cathodic gas channels, the electrolyte channel, and a support layer, a GDL and a CL for each electrode, the anode and the cathode. Channel extensions enable the simulation of the inflow and the outflow of the gases and the electrolyte solution. Compared with the previous models, particularly progress is made with respect to the temperature dependence of the kinetics (chapter 4.2). The simplification of the mass transport in the CLs (chapter 4.6) and the transformation of the concentrated electrolyte theory into the Nernst-Planck equation (chapter 4.7) create a numerous stable model, which enables the variation of various parameters. The detailed description of the model is provided in the next chapter.

4. Mathematical modeling

A 2-D model of an entire AFC has been developed with the software COMSOL Multiphysics® for investigating the physical processes in the cell and finding improvement potentials. Following the general operating conditions by the company AFC Energy, the model focuses laminar flows, moderate pressures, and temperatures below 100 °C. In the model, the transport equations for mass, momentum, species, energy, and charge are solved under steady state conditions. Also, the kinetics at the anode and the cathode are described mathematically, and the cell performance is predicted in the entire operating range from the activation region, to the ohmic region, to the mass transport region.

As illustrated in Figure 4.1, the model consists of the anodic gas channel, the cathodic gas channel, the anode, the cathode, and the electrolyte channel in between, where the liquid KOH electrolyte solution flows through the cell. Being based on the ‘beta-cell’ design by AFC Energy, the electrodes consist of three layers which are arranged from the gas side to the electrolyte side in the following order: support layer (SL), gas diffusion layer (GDL), catalyst layer (CL). Hence, the model comprises nine layers in total.

In the channels, the fluids can flow uninterruptedly, which is not the case in the porous electrode layers. Therefore, two main regions must be distinguished: the free regions and the porous media. Following [53], macrohomogeneous continua are assumed for the electrode layers by superposition of the different phases which might occur in the same layer, for example solid phase, gas phase, and liquid phase. At the upper boundaries of the anodic SL and the cathodic SL, the anodic current collector and the cathodic current collector are assumed, respectively, thus this is where the cell voltage is applied to the model⁵.

The anode gas, which is pure hydrogen, and the cathode gas, which is air, enter the cell from the top and leave it at the bottom, while the electrolyte flows through the cell in counter-current with the gases; it enters the cell from the bottom and leaves it at the top. Extensions on the inlet side and on the outlet side of the channels enable accounting for the inflow into and the outflow out of the cell. In the anodic gas channel, hydrogen is distributed to the anode and in the cathodic gas channel oxygen is distributed to the cathode. The gaseous reactants pass through the gas pores of the electrodes in the direction to the KOH electrolyte.

⁵ The model is operated by applying two different potentials to the anode and the cathode, whereas the electrical current is the result.

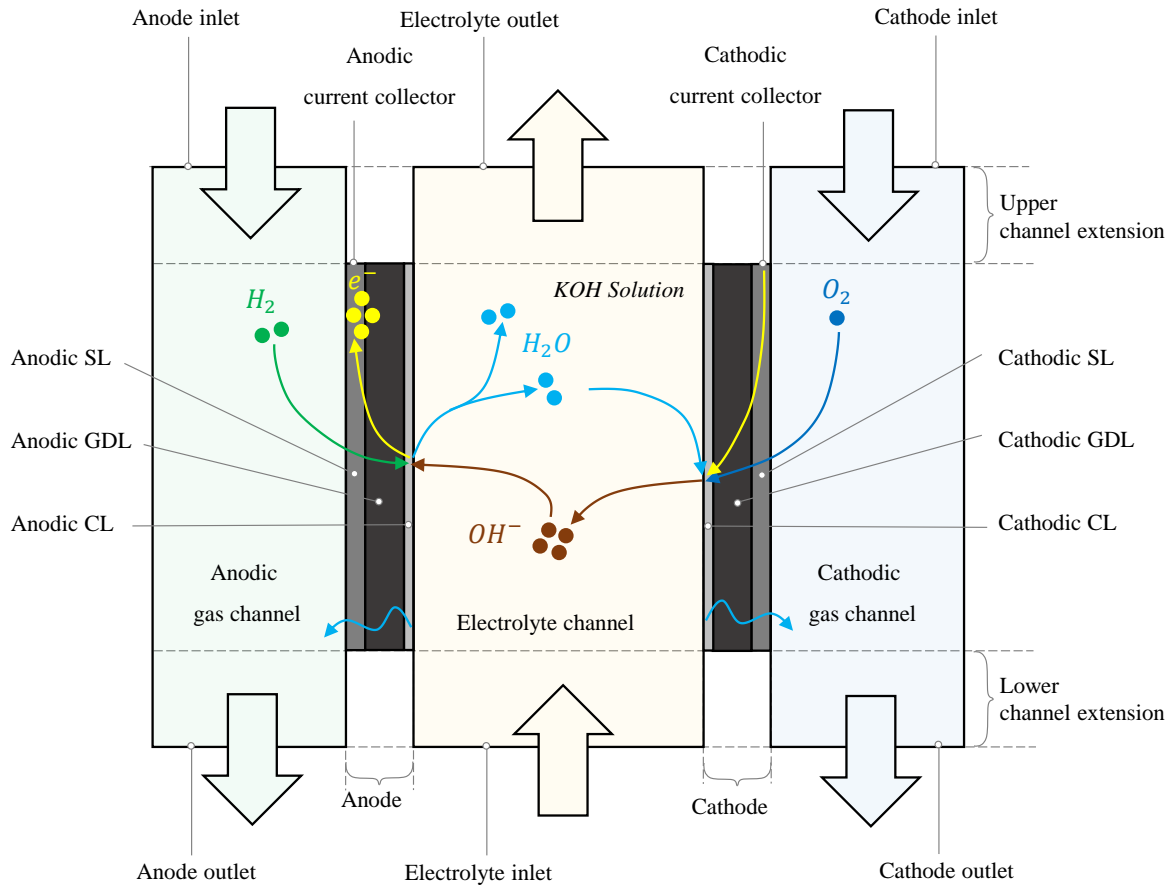


Figure 4.1: Model schema.

Facing the electrolyte, the CL can become flooded by the KOH electrolyte solution. The catalyst surface is therefore typically assumed to be covered by the liquid phase and not easily accessible from the gas phase. As the name indicates, the flooded agglomerate model [60], [61] assumes agglomerates in which the catalyst particles are surrounded by the electrolyte. In analogy with the thin film model [77], [78], the agglomerates are generally assumed to be covered by a thin liquid film as portrayed in Figure 4.2, where the transport processes of oxygen from the gas phase to the catalyst surface are exemplary illustrated. Consequentially, hydrogen and oxygen must dissolve in and diffuse through the electrolyte to the catalyst surface in order to react electrochemically. The HOR at the anode and the ORR at the cathode may be given as



and



respectively, whereas equation (4.1) must occur twice while equation (4.2) takes place once, in order to balance charge. The electrons freed in the anode reaction pass through the solid material of the anode and leave the cell at the anodic current collector. After passing through the external circuit (which is not modeled here), the electrons return to the cell at the cathodic current collector, pass through the solid material of the cathode and are consumed in the cathode reaction. The electrical circuit is closed inside the cell when the hydroxyl ions produced in the cathode reaction, bring the negative charge to the anode where they are consumed in the anode reaction.

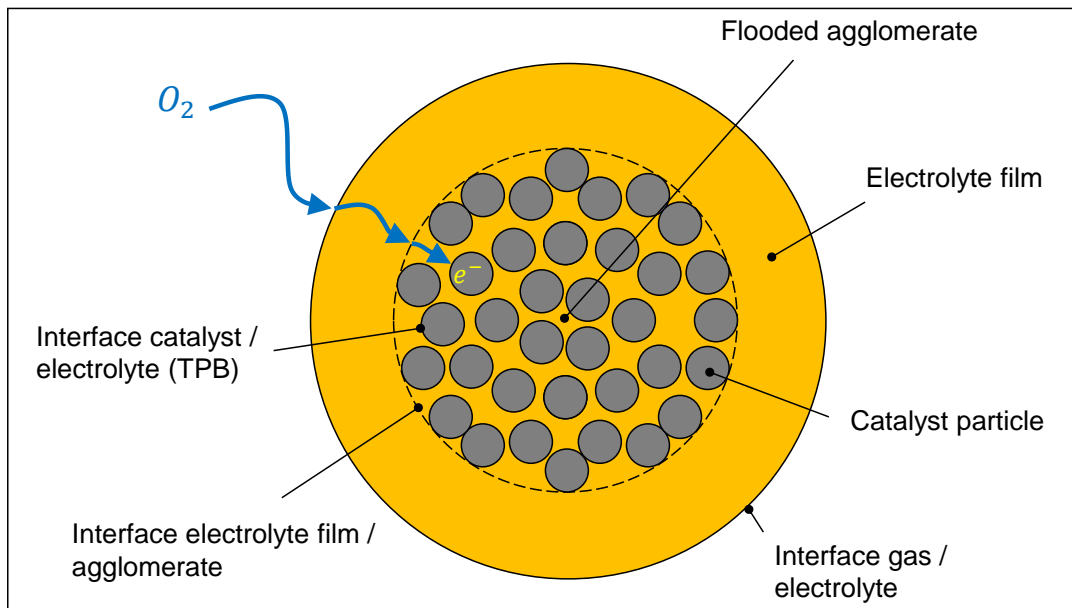


Figure 4.2: Flooded agglomerate with electrolyte film.

The model is described thoroughly in this chapter. First, the calculation of the cell voltage and the electrical potentials in the cell are presented in chapter 4.1. The description of the kinetics at the anode and at the cathode follows in chapter 4.2. After that, the momentum equations for the fluids in the free regions and in the porous media are provided in chapter 4.3. In chapter 4.4, chapter 4.5, and chapter 4.6, the species transport in the gas phase, from the gas phase into the liquid phase, and to the catalyst surface, respectively, are described. After that, the transport in the liquid phase is explained in chapter 4.7. The mass sources and sinks are presented in chapter 4.8. In chapter 4.9 and in chapter 4.10 the transport of charge and the transport of heat, respectively, are considered. After that, the properties of the fluids and the electrodes are presented in chapter 4.11 in the form of mathematical approximations and constant values, respectively. Finally, the boundary and initial conditions used for solving the model are described in chapter 4.12.

In addition to the terms defined by the labels in Figure 4.1, an overview about the boundaries and regions in the model is provided in Table 4.1. As the electrolyte is assumed to be present in the electrolyte channel, the electrolyte channel extensions, and (the liquid filled pores of) the anodic and cathodic CL, this region is the electrolyte region (see also main assumption ii below). Charge transport is only considered in the form of ions in the electrolyte region and in form of electrons in (the solid phase of) the anode and the cathode, thus this is the charge region. The anode gas is present in the anodic gas channel and in (the gas pores of) the anode, whereas the cathode gas is present in the cathodic gas channel and in (the gas pores of) the cathode, which are therefore the anode gas region and the cathode gas region, respectively.

In order to predict a variety of accurate results with a mathematical model, it is desired to describe physical processes as precisely as possible. However, with the increase in complexity and degree of freedom, typically the computation time increases, and the numerical stability decreases. Therefore, in order to prevent modeling and simulations to become too laborious and economically inefficient, simplifications and assumptions are generally made with focus on the object of investigation. Focusing the prediction of the overall cell performance for the entire operating range in this work, the assumptions and simplifications presented below are made primarily in order to rise the numerical stability and reduce the computation time of the model.

Table 4.1: Definitions of boundaries and regions in the model

Boundary/Region	Description
Anode:	Anodic SL, GDL, and CL
Anode gas region:	Anodic gas channel and (gas pores of the) anode
Anode inlet:	Upper boundary of the anodic gas channel
Anode outlet:	Lower boundary of the anodic gas channel
Anodic current collector:	Upper boundary of the anodic SL
Cathode:	Cathodic SL, GDL, and CL
Cathode gas region:	Cathodic gas channel and (gas pores of the) cathode
Cathode inlet:	Upper boundary of the cathodic gas channel
Cathode outlet:	Lower boundary of the cathodic gas channel
Cathodic current collector:	Upper boundary of the cathodic SL
Charge region:	Solid phase of the anode and cathode and electrolyte region
Electrolyte inlet:	Lower boundary of the electrolyte channel
Electrolyte outlet:	Upper boundary of the electrolyte channel
Electrolyte region:	Electrolyte channel and (liquid filled pores of the) CLs
Free regions:	Anodic gas channel, cathodic gas channel, and electrolyte channel
Porous media:	SL, GDL, and CL of the anode and the cathode

Main assumptions

- i. **Gas composition:** Air which enters the cell on the cathode side consist of 21 % O₂ and 79 % N₂. Consequentially, poisoning of the electrolyte due to CO₂ is not considered. The neglect of potential carbonates in the electrolyte can be stated by the circulation of the electrolyte, which brings undesired impurities rapidly out of the cell. The investigation of the impact of CO₂ on the processes in the cell is not in the focus.
- ii. **Electrolyte flooding:** The GDLs prevent any electrolyte from flooding the gas pores and passing through in direction to the gas channels. Hence, the electrolyte solution is only present in the electrolyte channel and in the anodic and cathodic CLs. Therefore, all reactions and phase changes take place either in the anodic CL or in the cathodic CL. This assumption is reasonable due to the hydrophobicity of the GDL. The transport of liquids through the porous electrodes is not an object of this work.
- iii. **Reaction mechanism:** The anode reaction and the cathode reaction take place in one step as given by equation (4.1) and equation (4.2), respectively. Hence, two electrons are directly transferred in the anode reaction and four electrons are directly transferred in the cathode reaction. Consequentially, the actual reaction mechanisms and side reactions are not taken into consideration particularly. This assumption is commonly made when modeling the overall performance of a fuel cell and creates consistent charge and mass balances. Investigating the actual reaction mechanisms is out of the scope of this work.
- iv. **H₂ and O₂ transport in the electrolyte:** H₂ and O₂ that passes through the electrolyte film in the anodic CL and in the cathodic CL, respectively, is consumed directly at the catalyst surface. As a result, their transport in the agglomerate and in the electrolyte channel is neglected. The reason for this assumption is given by the expectation that the transport through the electrolyte film dominates compared to the transport within the agglomerate. The impact of crossover is not focused in this model.
- v. **Water management:** The model does not aim to enable extensive water management studies so that the transport of water in the electrolyte was kept as simple as possible. Hence, it is assumed that convection dominates the transport of water so strongly, that other transport processes, such as diffusion, can be neglected. Due to the low temperatures, the product water of the anode reaction will be liquid. It is assumed that the half of the water produced in the overall reaction of the cell evaporates into the anode gas whereas the other half evaporates into the cathode gas. Consequentially, it leaves the cell with the gases in equal parts. The transport of water from the anode to the cathode is simply coupled with the current densities of the electrochemical reaction.

4.1 Cell voltage and electrical potentials

The cell voltage is the difference between the electrical potential of the anode and the cathode. Measured between the anodic current collector (ϕ_A^{CC}) and the cathodic current collector (ϕ_C^{CC}) the cell voltage E_{cell} can be written as

$$E_{cell} = \phi_C^{CC} - \phi_A^{CC}. \quad (4.3)$$

In the model, the potential of the anode is chosen as reference of the potential scale:

$$\phi_A^{CC} = 0. \quad (4.4)$$

Consequentially, the cell voltage can directly be applied to the cathodic current collector which defines the operating point:

$$\phi_C^{CC} = E_{cell}. \quad (4.5)$$

The potential losses in the solid material of the anode (η_A^s) and the cathode (η_C^s), and the potential losses in the liquid electrolyte (η^l) can be written as

$$\eta_A^s = \phi_A^{CC} - \phi_A^s, \quad (4.6)$$

$$\eta_C^s = \phi_C^{CC} - \phi_C^s, \quad (4.7)$$

and

$$\eta^l = (\phi_C^l - \phi_A^l), \quad (4.8)$$

respectively, where ϕ_A^s is the electrical potential of the anode in the interface between the anode and the electrolyte, ϕ_A^l is the electrical potential of the electrolyte in the interface between the anode and the electrolyte, ϕ_C^s is the electrical potential of the cathode in the interface between the cathode and the electrolyte, and ϕ_C^l is the electrical potential of the electrolyte in the interface between the cathode and the electrolyte. Consequentially, the cell voltage can be written as

$$E_{cell} = \Delta\phi_C - \Delta\phi_A + \eta^l + \eta_C^s - \eta_A^s, \quad (4.9)$$

where $\Delta\phi_A$ is the electrical potential difference in the interface between the anode and the electrolyte, and $\Delta\phi_C$ is the electrical potential difference in the interface between the cathode and the electrolyte, defined as

$$\Delta\phi_A = \phi_A^s - \phi_A^l, \quad (4.10)$$

and

$$\Delta\phi_C = \phi_C^s - \phi_C^l, \quad (4.11)$$

respectively. When $\Delta\phi_A^0$ is the potential difference between the anode and the electrolyte under equilibrium conditions, and $\Delta\phi_C^0$ is the potential difference between the cathode and the electrolyte under equilibrium conditions, the anodic overpotential (η_A) and the cathodic overpotential (η_C) can be introduced as

$$\eta_A = \Delta\phi_A - \Delta\phi_A^0, \quad (4.12)$$

and

$$\eta_C = \Delta\phi_C - \Delta\phi_C^0, \quad (4.13)$$

respectively. These definitions enable writing the cell voltage in the form

$$E_{cell} = \underbrace{\Delta\phi_C^0 - \Delta\phi_A^0}_{E_{cell}^0} + \eta^l + \eta_C^s - \eta_A^s + \eta_C - \eta_A, \quad (4.14)$$

where E_{cell}^0 is the reversible cell voltage.

The dimension of the potential difference between the solid and the liquid phase is of theoretical nature and cannot be measured singularly. However, the standard hydrogen electrode (SHE) can be used as reference. Under equilibrium conditions, the electrical potential difference in the interface can be written according to equation (4.10) and (4.11) as

$$\Delta\phi_i^0 = \phi_i^{s,0} - \phi_i^{l,0}, \quad (4.15)$$

where the lower index i stands for the considered electrode. Then, adding and subtracting the electrical potential of the SHE leads to

$$\Delta\phi_i^0 = \underbrace{\phi_i^0 - \phi_{SHE}}_{E_i^0} + \phi_{SHE} - \phi_i^{l,0}, \quad (4.16)$$

where E_i^0 is the electrical potential of the electrode vs. the SHE under equilibrium conditions. Hence, when the potential difference between the SHE and the electrolyte is neglected, the potential difference between the electrode and the SHE can be assumed to occur in the interface between the electrode and the electrolyte from a mathematical point of view. Neglecting the difference $\phi_{SHE} - \phi_i^{l,0}$ does not cause an error in the overall balance, which becomes obvious when replacing $\Delta\phi_A^0$ and $\Delta\phi_C^0$ in equation (4.14) according to equation (4.16):

$$E_{cell} = \underbrace{E_C^0 - E_A^0}_{E_{cell}^0} + \underbrace{\phi_{SHE} - \phi_{SHE}}_0 + \underbrace{\phi_C^{l,0} - \phi_A^{l,0}}_{\eta^{l,0}} + \eta^l + \eta_C^s - \eta_A^s + \eta_C - \eta_A. \quad (4.17)$$

As the potential gradient in the electrolyte under equilibrium conditions $\eta^{l,0}$ can be assumed to be zero, the result is the same as replacing $\Delta\phi_i^0$ directly by E_i^0 . Therefore, in the model the electrode potential vs. the SHE (E_i) is assumed in the interface between the electrode i and the electrolyte, representatively for $\Delta\phi_i$. As shown above, this only affects the local potential differences in the interfaces between the electrodes and the electrolyte but not the overall potential balance; the electrical potentials which are calculated in the interfaces between the electrodes and the electrolyte are therefore relative to the SHE. As a consequence, the electrical potential of the electrolyte is $-E_A^0$ when the cell is under equilibrium conditions (see also equation (4.4)).

The equilibrium potentials of the HOR and the ORR are calculated with the Nernst equation (see chapter 2.7.3) whereas the activities are replaced by the concentrations of the species:

$$E_A^0 = E_{A,T}^0 + \frac{RT}{2F} \ln \left(\left(\frac{c_{H_2O}^0}{c_{H_2O}^{Ref}} \right)^2 \left(\frac{c_{H_2}^0}{c_{H_2}^{Ref}} \right)^{-1} \left(\frac{c_{OH^-}^0}{c_{OH^-}^{Ref}} \right)^{-2} \right), \quad (4.18)$$

$$E_C^0 = E_{C,T}^0 + \frac{RT}{4F} \ln \left(\left(\frac{c_{H_2O}^0}{c_{H_2O}^{Ref}} \right)^2 \left(\frac{c_{O_2}^0}{c_{O_2}^{Ref}} \right)^1 \left(\frac{c_{OH^-}^0}{c_{OH^-}^{Ref}} \right)^{-4} \right), \quad (4.19)$$

where c_i^0 and c_i^{Ref} are the concentrations present at the catalyst surface under equilibrium conditions and reference equilibrium conditions, respectively. The reference concentrations are derived in chapter 4.12.7. For the calculation of the temperature dependent anode equilibrium potential $E_{A,T}^0$ and the temperature dependent cathode equilibrium potential $E_{C,T}^0$, the standard electrode potentials (vs. the SHE) by Bratsch [79] at pH 13.996 and 25 °C are used. Hence, $E_{A,T}^0$ can be given as

$$E_{A,T}^0 = -0.8280 \text{ V} - 0.8360 \frac{\text{mV}}{\text{K}} \cdot (T - 298.15 \text{ K}), \quad (4.20)$$

and $E_{C,T}^0$ can be written as

$$E_{C,T}^0 = 0.4011 \text{ V} - 1.6816 \frac{\text{mV}}{\text{K}} \cdot (T - 298.15 \text{ K}). \quad (4.21)$$

This methodology is in conformity with the previous models [54], [55], [63], [65], [67].

4.2 Kinetics

The reaction mechanisms of the HOR and the ORR depend on several factors. Taking into consideration the several steps in the reaction mechanisms accurately can become complicated and laborious. As the detailed analysis of the reaction mechanisms is out of the scope of this work, whereas the overall performance of the cell is of interest, it is assumed that the electrochemical reaction at the anode given by equation (4.1) and the electrochemical reaction at the cathode given by equation (4.2) take place in one step (see main assumption iii). Consequentially, two electrons are directly transferred from the electrolyte to the anode when one hydrogen molecule is consumed, and four electrons are directly transferred from the cathode to the electrolyte when one oxygen molecule is consumed. Therefore, the anode reaction takes place twice while the cathode reaction occurs once. The Butler-Volmer expression (see chapter 2.8) is used for describing the kinetics of the HOR in the anodic CL and the kinetics of the ORR in the cathodic CL:

$$i^A = i_0^A \left(\left(\frac{c_{H_2}}{c_{H_2}^0} \right)^{\vartheta_{H_2}^A} \left(\frac{c_{OH^-}}{c_{OH^-}^0} \right)^{\vartheta_{OH^-}^A} \exp \left(\frac{\alpha_+^A n^A F \eta^A}{RT} \right) - \left(\frac{c_{H_2O}}{c_{H_2O}^0} \right)^{\vartheta_{H_2O}^A} \exp \left(\frac{-\alpha_-^A n^A F \eta^A}{RT} \right) \right), \quad (4.22)$$

$$i^C = i_0^C \left(\left(\frac{c_{OH^-}}{c_{OH^-}^0} \right)^{\vartheta_{OH^-}^C} \exp \left(\frac{\alpha_+^C n^C F \eta^C}{RT} \right) - \left(\frac{c_{O_2}}{c_{O_2}^0} \right)^{\vartheta_{O_2}^C} \left(\frac{c_{H_2O}}{c_{H_2O}^0} \right)^{\vartheta_{H_2O}^C} \exp \left(\frac{-\alpha_-^C n^C F \eta^C}{RT} \right) \right). \quad (4.23)$$

In equations (4.22) and (4.23), the upper indices A and C mark parameters specific to the anode and cathode reaction, respectively, i_0 is the exchange current density, c_i is the concentration of species i at the catalyst surface (under load), c_i^0 is the concentrations of species i at the catalyst surface under equilibrium conditions where the exchange current density applies, ϑ_i is the reaction order of species i , and α_+ and α_- are the anodic transfer coefficient and the cathodic transfer coefficient of the considered reaction, respectively. Furthermore, n is the number of exchanged electrons, and η is the overpotential. The expressions used in the model are slightly different to equations (4.22) and (4.23) and obtained by rearrangement. After the description of the transport processes into and through the electrolyte film in chapter 4.5 and chapter 4.6, respectively, the rearranged expression is given in chapter 4.6.

The exchange current densities are described as functions from concentrations and temperature. The concentration dependence of the anode and cathode exchange current densities is described by

$$i_0^A = i_{0,T}^{A,Ref} \left(\frac{c_{H_2}^0}{c_{H_2}^{Ref}} \right)^{\alpha_-^A \vartheta_{H_2}^A} \left(\frac{c_{OH^-}^0}{c_{OH^-}^{Ref}} \right)^{\alpha_-^A \vartheta_{OH^-}^A} \left(\frac{c_{H_2O}^0}{c_{H_2O}^{Ref}} \right)^{\alpha_+^A \vartheta_{H_2O}^A}, \quad (4.24)$$

and

$$i_0^C = i_{0,T}^{C,Ref} \left(\frac{c_{O_2}^0}{c_{O_2}^{Ref}} \right)^{\alpha_+^C \vartheta_{O_2}^C} \left(\frac{c_{OH^-}^0}{c_{OH^-}^{Ref}} \right)^{\alpha_-^C \vartheta_{OH^-}^C} \left(\frac{c_{H_2O}^0}{c_{H_2O}^{Ref}} \right)^{\alpha_+^C \vartheta_{H_2O}^C}, \quad (4.25)$$

respectively, where c_i^{Ref} is the reference concentration of species i at the catalyst surface belonging to the reference exchange current density i_0^{Ref} . The temperature dependence of the anode and cathode exchange current densities is respected by the expressions

$$i_{0,T}^A = i_0^{A,Ref} \exp\left(\frac{-E_{Act}^A (T^{A,Ref} - T)}{RT^{A,Ref}}\right), \quad (4.26)$$

and

$$i_{0,T}^C = i_0^{C,Ref} \exp\left(\frac{-E_{Act}^C (T^{C,Ref} - T)}{RT^{C,Ref}}\right), \quad (4.27)$$

respectively, in which E_{Act}^A and E_{Act}^C are the activation energies of the anode reaction and the cathode reaction, respectively. Consequentially, T^{Ref} is the temperature at which the reference exchange current density i_0^{Ref} is derived from measurements (see chapter 2.8.5).

The kinetics of the anode reaction and the kinetics of the cathode reaction are described based on measurements at platinum and are presented in Table 4.2. The reference concentrations $c_{H_2O}^{Ref}$, $c_{H_2}^{Ref}$, and $c_{O_2}^{Ref}$ are derived in chapter 4.12.7. In order to account for the temperature dependences of the transfer coefficients, linear relationships are assumed. Focusing the forward reactions, the anodic transfer coefficient of the anode reaction (α_+^A) can be given as [80]

$$\alpha_+^A n^A = 0.5028 + 0.0026 \cdot T, \quad (4.28)$$

and the cathodic transfer coefficient of the cathode reaction (α_-^C) can be given as [81]

$$\alpha_-^C n^C = 1.02 + 0.002 \cdot T, \quad (4.29)$$

where T is the temperature in °C. The transfer coefficient of the reverse reaction, which is the cathodic transfer coefficient in case of the anode reaction (α_-^A) and the anodic transfer coefficient in case of the cathode reaction (α_+^C), is calculated by assuming the sum of the anodic and cathodic transfer coefficients equals one:

$$\alpha_+ + \alpha_- = 1. \quad (2.48)$$

Table 4.2: Kinetic parameters

Parameter	Value	Ref
$i_0^{A,Ref}$	0.57 mA/cm ²	[80]
$T^{A,Ref}$	294 K	[80]
E_{Act}^A	29.5 kJ/mol	[80]
$c_{OH^-}^{A,Ref}$	0.1 M	[80]
$i_0^{C,Ref}$	$4.2 \cdot 10^{-11}$ A/cm ²	[81]
$T^{C,Ref}$	298.15 K	[81]
E_{Act}^C	47.31 kJ/mol	[81]
$c_{OH^-}^{C,Ref}$	6.88 M	[81]

4.3 Momentum equation

The momentum transport has been modeled with “The Free and Porous Media Flow Interface” by COMSOL [82]. The continuity equation for the anode gas, the cathode gas, and the electrolyte solution can be given as

$$\nabla \cdot (\rho v) = R^m, \quad (4.30)$$

where ρ is the density, v is the velocity, and R^m is the reaction rate. Considering a single-phase flow, R^m stands for the net amount of mass that is brought in and out the phase due to (electro-) chemical reactions and phase changes. A detailed description of the reaction rates is given in chapter 4.8. As all reactions and phase changes are assumed to take place either in the anodic CL or in the cathodic CL, R^m equals zero for all domains despite the CLs.

The model assumes that each of the three fluids, the anode gas, the cathode gas, and the electrolyte solution, enters the cell as laminar flow with moderate pressure and velocity. In the free regions, the pressure and velocity fields are calculated with the Navier-Stokes

equation, whereas in the porous media the Brinkman equation is used. Hence, the momentum equations for the free regions and the porous media can be given as [82]

$$\rho v \cdot \nabla v = -\nabla p + \nabla \cdot \left(\mu(\nabla v + (\nabla v)^T) - \frac{2}{3}\mu(\nabla \cdot v)I \right) + \rho g, \quad (4.31)$$

and

$$\begin{aligned} \frac{\rho}{\varepsilon}(v \cdot \nabla) \frac{v}{\varepsilon} = -\nabla p + \nabla \cdot \left(\frac{1}{\varepsilon} \left(\mu(\nabla v + (\nabla v)^T) - \frac{2}{3}\mu(\nabla \cdot v)I \right) \right) \\ - \left(\frac{\mu}{\kappa} + \frac{R^m}{\varepsilon^2} \right) v + \rho g, \end{aligned} \quad (4.32)$$

respectively, in which p is the pressure, μ is the viscosity, g is the gravity constant, I is the unit matrix, ε is the porosity, and κ is the permeability. The influence of gravity is neglected in the momentum equation causing the last term on the right of equations (4.31) and (4.32) to vanish.

4.4 Species transport in the gas phase

The transport of hydrogen and water vapor in the anode gas and the transport of oxygen, nitrogen, and water vapor in the cathode gas are modeled with “The Transport of Concentrated Species Interface” by COMSOL [83]. For a species i , the continuity equation can be written in the form

$$\nabla \cdot N_i^m = R_i^m, \quad (4.33)$$

where N_i^m is the flux of species i , and R_i^m is the production rate of species i . As described in and chapter 4.8, the reaction rate captures (electro-) chemical reactions as well as phase changes. It is assumed to equal zero in all domains despite the CLs (see chapter 4.3).

The total flux of a species can be written as

$$N_i^m = M_i c_i v_i = \rho w_i v_i, \quad (4.34)$$

where ρ is the density, M_i is the molar mass, c_i is the concentration, v_i is the velocity, and w_i is the mass fraction of species i . When v is the volume average velocity of the mixture, the flux N_i can be written as the combination of the convective flux $\rho w_i v$ and the relative flux j_i according to

$$N_i^m = \underbrace{\rho w_i (v_i - v)}_{j_i} + \rho w_i v. \quad (4.35)$$

The relative flux j_i is modeled based on the Maxwell-Stefan diffusion law and can be given in the form [83]

$$j_i = -\rho w_i \sum_k \mathbb{D}_{ik} d_k - D_i^T \nabla \ln T, \quad (4.36)$$

in which \mathbb{D}_{ik} is the multicomponent Fick diffusivity of species i and k , D_i^T is the thermal diffusion coefficient of species i , T is the temperature, and d_k represents the driving force. The derivation of the multicomponent Fick diffusivities from the binary Stefan-Maxwell diffusivities is given below. The last term on the right of equation (4.36) accounts for thermal diffusion, which is generally negligible compared to concentration diffusion, especially in case of low temperature gradient, thus it is neglected in the model. The driving force d_k may be given as [83]

$$d_k = \nabla x_k + \frac{1}{p} ((x_k - w_k) \nabla p) + \frac{1}{p} \left(-w_k \rho g_k + w_k \sum_l \rho w_l g_l \right), \quad (4.37)$$

where x_k is the mole fraction of species k , p is the pressure, ρ is the density, and g_k represents an external driving force acting on species k , such as an electrical potential gradient acts on a charged species. In analogy with the lower index k , the lower index l stands for the species in the solution. Hence, the last two terms drop out by the assumption that gravity is the only external driving force acting on all species in the gas phase equally.

Also, it is assumed, that the ideal gas law applies

$$pv = RT, \quad (4.38)$$

thus, the density is calculated as

$$\rho = \frac{p}{RT} \sum x_k M_k. \quad (4.39)$$

The multicomponent Fick diffusivities (\mathbb{D}) are calculated from the binary Maxwell-Stefan diffusivities (\mathcal{D}) according to [84], [83]

$$\mathcal{D}_{ik} = -\frac{x_i x_k \sum_{l \neq i} \mathbb{D}_{il} (\text{adj } B_i)_{lk}}{w_i w_k \sum_{l \neq i} (\text{adj } B_i)_{lk}}, \quad (4.40)$$

in which $(\text{adj } B_i)_{lk}$ is the lk –component of the adjoint to the matrix B_i for which the lk –components are given by

$$(B_i)_{kl} = -\mathbb{D}_{kl} + \mathbb{D}_{il}. \quad (4.41)$$

In the porous media, the diffusion coefficient \mathcal{D}_{ik} must be replaced by the effective diffusivity \mathcal{D}_{ik}^{eff} which is corrected by volume available for the mass transport. The most commonly used equation for calculating the effective diffusion coefficient is given by [3]

$$\mathcal{D}_{ik}^{eff} = \mathcal{D}_{ik} \frac{\varepsilon}{\tau}. \quad (4.42)$$

The tortuosity τ is assumed to be related to the porosity ε by the Bruggeman equation [3]:

$$\tau = \frac{1}{\varepsilon^{0.5}}. \quad (4.43)$$

4.5 Gas/liquid interface

At the interface between the gas phase and the liquid phase species can be exchanged which changes the concentrations in both phases. When the concentrations in both phases reach constant values, equilibrium state is present and the net flow from the one phase to the other equals zero. At the interface between the anode gas and the electrolyte and at the interface between the cathode gas and the electrolyte, equilibrium conditions are assumed for

hydrogen and oxygen, respectively. Hence, the partial pressure (p_i) and the liquid phase concentration (c_i) are related to one another by Henry's law:

$$c_i = H_i^e \cdot p_i, \quad (4.44)$$

where H_i^e is the Henry constant for the solubility in the electrolyte.

Rather than H_i^e , the salting out coefficient (k_i^s) and the Henry constant for the solubility in water (H_i^w) are available, whereas k_i^s describes the deviation of the solubility in the electrolyte from the solubility in water. An expression for the species concentration in the electrolyte as function from H_i^e and k_i^s is therefore derived in the following. It is show that H_i^e can be calculated for the KOH electrolyte according to

$$H_i^e = \frac{(c_0 + 2c_e)}{H_i^w 10^{k_i^s \cdot c_e} - p_i}, \quad (4.45)$$

where c_0 is the solvent concentration, and c_e is the electrolyte concentration. The concentration c_i can be written as the product of the molar fraction (x_i^e) and the total concentration (c_T):

$$c_i = x_i^e c_T. \quad (4.46)$$

An expression for the total concentration of the electrolyte solution is given by equation (2.117) for the case that only solvent and ions are present in a volume element. However, the solubility of the additional species i is considered here, thus its presence in the electrolyte solution must not be neglected at this point. In analogy with equation (2.115), the total amount of species (n_T) in a certain volume (V) is obtained by summing up the molar amounts of the species contained in this volume. Assuming species i is locally the only species in the electrolyte solution (n_i), n_T may be written as

$$n_T = n_0 + n_+ + n_- + n_i, \quad (4.47)$$

where n_0 , n_+ , and n_- are the molar amounts of solvent, positive charged ions, and negative charged ions, respectively, in the considered volume. Dividing equation (4.47) by V yields

$$c_T = \frac{n_T}{V} = \underbrace{\frac{n_0}{V}}_{c_0} + \underbrace{\frac{n_+}{V}}_{c_+} + \underbrace{\frac{n_-}{V}}_{c_-} + \underbrace{\frac{n_i}{V}}_{c_i}. \quad (4.48)$$

Then, replacing c_+ and c_- by c_e according to equation (2.92) leads to

$$c_T = c_0 + \nu c_e + c_i. \quad (4.49)$$

In case of the KOH electrolyte the dissociation number is 2, thus the total concentration can be given in the form

$$c_T = c_0 + 2c_e + c_i. \quad (4.50)$$

Combining equations (4.46) and (4.50) yields [54]:

$$c_i = (c_0 + 2c_e) \frac{x_i^e}{1 - x_i^e}. \quad (4.51)$$

The mole fraction of species i in the electrolyte (x_i^e) and the mole fraction of species i in water (x_i^w) can be related to one another by the salting out coefficient according to [63]

$$x_i^e = x_i^w \cdot 10^{-k_i^s \cdot c_e}, \quad (4.52)$$

whereas the mole fraction in water can again be calculated with Henry's law according to

$$H_i^w \cdot x_i^w = p_i. \quad (4.53)$$

Inserting equation (4.52) and (4.53) in equation (4.51) leads to the final expression

$$c_i = (c_0 + 2c_e) \left(\frac{H_i^w}{p_i} \cdot 10^{k_i^s \cdot c_e} - 1 \right)^{-1}. \quad (4.54)$$

The so obtained expression is used for describing the transfer of hydrogen and oxygen from the gas to the liquid phase at the gas/liquid interface. Therefore, the transport resistance

across the phase boundary is neglected by the assumption of an equilibrium state. Inserting equation (4.54) in equation (4.44) yields H_i^e as given in equation (4.45).

4.6 Transport of hydrogen and oxygen to the catalysts

Kimble and White [54] introduced the following expression for describing the solution rate of hydrogen and oxygen in the electrolyte solution (R_i^{sol}):

$$R_i^{sol} = a_g D_i \frac{c_i^{l/a} - c_i^{g/l}}{d_l}, \quad (4.55)$$

where a_g represents the specific surface area of the electrolyte film at the gas/liquid interface, d_l is the thickness of the electrolyte film, D_i is the diffusion coefficient of species i in the electrolyte, and $c_i^{g/l}$ and $c_i^{l/a}$ are the liquid phase concentrations of species i at the gas/liquid interface and at the film/agglomerate interface, respectively (see Figure 4.2).

With the assumption that all reactants are consumed directly at the catalyst surface after diffusing through the electrolyte film (see main assumption iv), the solution rate given by equation (4.55) equals the electrochemical reaction at the catalyst surface (R_i^{elec}) which can be written with Faraday's law as

$$R_i^{elec} = -\frac{\nu_i i a_l}{nF}, \quad (4.56)$$

in which ν_i is the stoichiometric coefficient of species i (index i denotes the species i), i is the electrical current density with respect to the catalyst surface, a_l is the specific surface area of the catalyst, and n is the number of exchanged electrons. Hence, equating equations (4.55) and (4.56) yields

$$\frac{c_i^{l/a}}{c_i^{g/l}} = 1 - \frac{\nu_i a_l}{nF} \frac{d_l}{\underbrace{a_g D_i c_i^{g/l}}_{\xi}} \cdot i. \quad (4.57)$$

Notice: This expression is very similar to the one which is generally used for calculating the limiting current density but accounts additionally for the difference between a_l and a_g :

4. Mathematical modeling

When the concentration $c_i^{l/a}$ approaches zero, the limiting current density can be calculated from the concentration $c_i^{g/l}$. The expression for the limiting current density that is typically given in open literature is obtained by ignoring the difference between a_l and a_g .

The concentration $c_i^{g/l}$ follows from Henry's law (see chapter 4.5). With the assumption that hydrogen and oxygen are consumed directly after passing through the liquid electrolyte film, $c_i^{l/a}$ becomes the concentration at the catalyst ($c_i^{l/a} \rightarrow c_i$). When the hydrogen concentration ratio in equation (4.22) and the oxygen concentration ratio in equation (4.23) are replaced according to equation (4.57), the anodic Butler-Volmer expression and the cathodic Butler-Volmer expression can be written as

$$i^A = \left(\frac{c_{H_2}}{c_{H_2}^{g/l}} \right)^{\vartheta_{H_2}^A} \underbrace{i_0^A \left(\frac{c_{H_2}^{g/l}}{c_{H_2}^0} \right)^{\vartheta_{H_2}^A} \left(\frac{c_{OH^-}}{c_{OH^-}^0} \right)^{\vartheta_{OH^-}^A} \exp \left(\frac{\alpha_+^A n^A F \eta^A}{RT} \right)}_{j_+^A} - \underbrace{i_0^A \left(\frac{c_{H_2O}}{c_{H_2O}^0} \right)^{\vartheta_{H_2O}^A} \exp \left(\frac{-\alpha_-^A n^A F \eta^A}{RT} \right)}_{j_-^A}, \quad (4.58)$$

and

$$i^C = \underbrace{i_0^C \left(\frac{c_{OH^-}}{c_{OH^-}^0} \right)^{\vartheta_{OH^-}^C} \exp \left(\frac{\alpha_+^C n^C F \eta^C}{RT} \right)}_{j_+^C} - \underbrace{\left(\frac{c_{O_2}}{c_{O_2}^{g/l}} \right)^{\vartheta_{O_2}^C} i_0^C \left(\frac{c_{O_2}^{g/l}}{c_{O_2}^0} \right)^{\vartheta_{O_2}^C} \left(\frac{c_{H_2O}}{c_{H_2O}^0} \right)^{\vartheta_{H_2O}^C} \exp \left(\frac{-\alpha_-^C n^C F \eta^C}{RT} \right)}_{j_-^C}. \quad (4.59)$$

It is assumed that the reaction orders of hydrogen and oxygen can be replaced by the absolute values of the stoichiometric coefficients, thus they become 1 (see equations (4.1) and (4.2)). Hence, the kinetics at the anode is described as

$$i^A = \frac{i_+^A - i_-^A}{1 + \xi^A i_+^A}, \quad (4.60)$$

with i_+^A and i_-^A given in equation (4.58), and ξ^A following from equation (4.57) as

$$\xi^A = \frac{a_l^A}{2F} \frac{d_l^A}{a_g^A D_{H_2} c_{H_2}^{g/l}} \quad (4.61)$$

Analogously, the kinetics at the cathode are modeled, thus i^C can be given in the form

$$i^C = \frac{i_+^C - i_-^C}{1 - \xi^C i_-^C} \quad (4.62)$$

with i_+^C and i_-^C given in equation (4.59), and ξ^C following from equation (4.57) in the form

$$\xi^C = -\frac{a_l^C}{4F} \frac{d_l^C}{a_g^C D_{O_2} c_{O_2}^{g/l}} \quad (4.63)$$

In the model, equations (4.60) and (4.62) are used for describing the kinetics of the anode reaction and the kinetics of the cathode reaction, respectively. The concentrations $c_{H_2}^{g/l}$ and $c_{O_2}^{g/l}$ can directly be derived from the gas phase concentrations (see chapter 4.5). Therefore, equations (4.60) and (4.62) enable taking into account the concentration losses caused by the liquid phase transport of hydrogen and oxygen, respectively, based on the gas phase concentrations. As a result, relatively high numerical stability is obtained as the degree of freedom is decreased enormously compared with uncoupling the liquid phase transport processes and the electrochemical reactions.

Notice: In order to account for the hydrogen and oxygen transport in the electrolyte solution more accurately, it could be described based on the diluted theory (equation (2.88)), and the solution rates given by equation (4.55) could be decoupled from the electrochemical reactions. This was for example done by Zhou et al. in [66], [67] but also by Kunz et al. in [85]. In order to raise the numerical stability and decrease the computation time, the degree of freedom needed to be decreased. For this purpose, the hydrogen and oxygen transport have been coupled with the electrochemical reactions as described above. This is the main modification of the model since it was presented in [85] and has enabled using the model flexibly for the simulations presented in this work.

4.7 Species transport in the electrolyte solution

COMSOL [83] provides “The Tertiary Current Distribution Interface” for modeling the ion transport in a diluted electrolyte solution based on the Nernst-Planck equation (equation (2.88)). The model presented in this work uses this interface, whereas the concentrated electrolyte theory is respected by adapting the transport properties of the ions. For this purpose, the expression for the transport of an ion in the concentrated electrolyte is transformed into the Nernst-Planck form. The so obtained expression directly reveals the mathematical expressions for the transport properties to use in the Nernst-Planck equation in order to account for a concentrated electrolyte. For the purpose of modeling, an expression with respect to the volume average velocity can be more practical than an expression with respect to the solvent velocity, thus the equation (2.131) but not equation (2.124) is used.

As described in chapter 2.9.2, the ion flux with respect to the volume average velocity can be given for a concentrated electrolyte as

$$N_i = -v_i D_c \frac{c_0}{c_T} \nabla c_e + \frac{it_i^*}{z_i F} + c_i v^*, \quad (2.131)$$

whereas the electrical current density can be written in the form

$$i = -\kappa \nabla \phi - \frac{\kappa}{F} \left(\frac{s_+}{n\nu_+} + \frac{t_+^0}{\nu_+ z_+} - \frac{s_0 c_e}{nc_0} \right) \nabla \mu_e. \quad (2.136)$$

When and the chemical potential of the electrolyte is replaced by equation (2.120), the electrical current density may be given as

$$i = -\kappa \nabla \phi - \frac{\kappa \nu RT}{F c_e} \left(\frac{s_+}{n\nu_+} + \frac{t_+^0}{\nu_+ z_+} - \frac{s_0 c_e}{nc_0} \right) \left(1 + \frac{d \ln(\gamma_{\pm})}{d \ln(m)} \right) \cdot \left(1 - \frac{d \ln(c_0)}{d \ln(c_e)} \right) \nabla c_e. \quad (4.64)$$

Hence, when equation (4.64) is inserted in equation (2.131), the so obtained expression can be rearranged to describe the ion flux in the form

$$N_i = -v_i D_i^* \nabla c_e - \frac{t_i^*}{z_i F} \kappa \nabla \phi + c_i v^*, \quad (4.65)$$

where the diffusion coefficient D_i^* is defined as

$$D_i^* = D_c \frac{c_0}{c_T} + \frac{t_i^* v R T \kappa}{v_i z_i F^2 c_e} \left(\frac{s_+}{n v_+} + \frac{t_+^0}{v_+ z_+} - \frac{s_0 c_e}{n c_0} \right) \left(1 + \frac{d \ln(\gamma_{\pm})}{d \ln(m)} \right) \left(1 - \frac{d \ln(c_0)}{d \ln(c_e)} \right). \quad (4.66)$$

The diffusion coefficient D_i^* has only a mathematical meaning. It enables the transformation of the flux expression of an ion in the concentrated electrolyte to the Nernst-Planck form. The diffusion coefficient D_i^* is based on the diffusion coefficient D “that is usually measured” [41] for a concentrated electrolyte (see equation (2.122)) due to its dependence on the diffusion coefficient D_c on the concentration scale (see equation (2.123)).

Equation (4.65) is similar to the Nernst-Planck equation for diluted solutions (compare equation (2.88)) but differs in the definition of the transport properties. While in case of a diluted electrolyte the diffusion coefficient of a species and the electrical conductivity of the solution are given by equation (2.90) and equation (2.106), respectively, in case of a concentrated electrolyte, these parameters are given by equation (4.66) and equation (2.137), respectively. Hence, the diffusion coefficient of hydroxyl ions and potassium ions are calculated in the model by

$$D_{OH^-}^* = D_c \frac{c_0}{c_T} - \frac{2 t_{OH^-}^* R T \kappa}{F^2 c_e} \left(t_+^0 - \frac{c_e}{2 c_0} \right) \left(1 + \frac{d \ln(\gamma_{\pm})}{d \ln(m)} \right) \left(1 - \frac{d \ln(c_0)}{d \ln(c_e)} \right), \quad (4.67)$$

and

$$D_{K^+}^* = D_c \frac{c_0}{c_T} + \frac{2 t_{K^+}^* R T \kappa}{F^2 c_e} \left(t_+^0 - \frac{c_e}{2 c_0} \right) \left(1 + \frac{d \ln(\gamma_{\pm})}{d \ln(m)} \right) \left(1 - \frac{d \ln(c_0)}{d \ln(c_e)} \right), \quad (4.68)$$

respectively. The diffusion coefficient on the concentration scale D_c is calculated based on the diffusion coefficient that can be measured (D) according to equation (2.123). However, no measurements are used for D , but it is calculated based on the diffusion coefficients of

hydroxyl and potassium ions in water and the activity coefficient of the electrolyte, according to equations (2.122) and (2.114).

The transference numbers of hydroxyl ions ($t_{OH^-}^*$) and potassium ions ($t_{K^+}^*$) with respect to the solvent velocity are calculated with equation (2.132):

$$t_{OH^-}^* = \frac{t_{OH^-}^0 c_0 + c_e}{c_T}, \quad (4.69)$$

$$t_{K^+}^* = \frac{t_{K^+}^0 c_0 + c_e}{c_T}. \quad (4.70)$$

In equations (4.69) and (4.70), $t_{OH^-}^0$ and $t_{K^+}^0$ are the transference numbers of hydroxyl ions and potassium ions with respect to the solvent velocity, respectively.

The transport of water molecules in the solution, for example due to concentration gradients, is not taken into consideration. The production of water in the anode reaction, the consumption of water in the cathode reaction, and the evaporation of water into the anode gas and into the cathode gas are considered in the momentum equation and affect the transport of the ions through the volume average velocity.

Notice: Equation (2.124) describes the flux of an ion in the concentrated electrolyte with respect to the solvent velocity but not with respect to the volume average velocity. When this equation is used for the transformation to the Nernst-Planck form, the following equations are obtained for the ion flux and the diffusion coefficient:

$$N_i = -D_i \nabla c_i - \frac{t_i^0}{z_i F} \kappa \nabla \phi + c_i v_0, \quad (4.71)$$

$$D_i = D_c + \frac{t_i^0 \nu R T \kappa}{\nu_i z_i F^2 c_e} \left(\frac{s_+}{\nu v_+} + \frac{t_+^0}{\nu_+ z_+} - \frac{s_0 c_e}{n c_0} \right) \left(1 + \frac{d \ln(\gamma_{\pm})}{d \ln(m)} \right) \left(1 - \frac{d \ln(c_0)}{d \ln(c_e)} \right). \quad (4.72)$$

4.8 Mass sources and sinks

According to Faraday's law the reaction rate of a species (R_i) is related to the electrical current density (i) by [83]

$$R_i = -\frac{\nu_i i a_l}{nF}, \quad (4.73)$$

where ν_i is the stoichiometric coefficient of species i , n is the number of exchanged electrons, and a_l is the specific surface area of the electrode where the reaction takes place.

The mass specific reaction rate of a species (R_i^m) is given by multiplying the molar reaction rate R_i by the molar mass of the species (M_i):

$$R_i^m = R_i M_i. \quad (4.74)$$

The total reaction rate (R^m) follows by summing up the reaction rates of all species in a domain:

$$R^m = \sum_i R_i^m. \quad (4.75)$$

As described in chapter 4.6, hydrogen and oxygen are assumed to be consumed directly after diffusing through the electrolyte film (see main assumption iv). The hydrogen transport in the gas phase is therefore coupled with the electrochemical reaction in the anodic CL (R_{H_2}) by the faradaic reaction rate:

$$R_{H_2} = -\frac{i^A a_l^A}{2F}. \quad (4.76)$$

In analogy with the hydrogen transport, the oxygen transport in the gas phase is coupled with the electrochemical reaction in the cathodic CL (R_{O_2}) according to Faraday's law:

$$R_{O_2} = \frac{i^C a_l^C}{4F}. \quad (4.77)$$

The reaction rate of hydroxyl ions in the anodic CL ($R_{OH^-}^A$) and in the cathodic CL ($R_{OH^-}^C$) can be given as

$$R_{OH^-}^A = -\frac{i^A a_l^A}{F}, \quad (4.78)$$

$$R_{OH^-}^C = -\frac{i^C a_l^C}{F}. \quad (4.79)$$

At low temperatures, it can be expected that the product water of the anode reaction will be liquid and therefore enter the electrolyte solution. When dry cathode gas enters the cell on the cathode side, the reactant water must be provided by the electrolyte. If these were the only phenomena, the consumption of two hydrogen molecules and one oxygen molecule would dilute the electrolyte solution by two water molecules. However, the low humidity in the gases forces water to evaporate additionally. In the model, the evaporation of water is taken into account by assuming that the product water of the overall reaction leaves the cell with the anode gas and the cathode gas in equal parts (see main assumption v). For this purpose, the evaporation rates are coupled with the electrochemical reaction rates. This enables taking into account the decrease in the hydrogen concentration in the anode gas and the decrease in oxygen concentration in the cathode gas, as well as the temperature reduction due to the evaporation of water. Additionally, a consistent water balance is created. These simplifications are made as the investigation of the water transport processes and their impact on the cell performance are out of the scope of this work.

According to Faraday's law, the electrochemical reaction rate of water produced in the anodic CL ($R_{H_2O}^A$) and the reaction rate of water consumed in the cathodic CL ($R_{H_2O}^C$) can be given by

$$R_{H_2O}^A = \frac{i^A a_l^A}{F}, \quad (4.80)$$

$$R_{H_2O}^C = \frac{i^C a_l^C}{2F}. \quad (4.81)$$

As (only) the product water of the overall reaction is assumed to leave the cell with the anode gas and with the cathode gas in equal parts, the evaporation rates in the anodic CL ($R_{H_2O}^{A,g}$) and in the cathodic CL ($R_{H_2O}^{C,g}$) are calculated as

$$R_{H_2O}^{A,g} = \frac{1}{4} R_{H_2O}^A, \quad (4.82)$$

$$R_{H_2O}^{C,g} = -\frac{i^C a_l^C}{4F} = -\frac{1}{2} R_{H_2O}^C. \quad (4.83)$$

Consequentially, considering the water balance, the water production rate applied to the electrolyte in the anodic CL ($R_{H_2O}^{A,l}$) and in the cathodic CL ($R_{H_2O}^{C,l}$) are

$$R_{H_2O}^{A,l} = R_{H_2O}^A - R_{H_2O}^{A,g} = \frac{3}{4} R_{H_2O}^A, \quad (4.84)$$

$$R_{H_2O}^{C,l} = R_{H_2O}^C - R_{H_2O}^{C,g} = \frac{3}{4} R_{H_2O}^C. \quad (4.85)$$

Notice: In analogy with equation (4.55), which describes the solution rate of hydrogen and oxygen in the anodic CL and in the cathodic CL, respectively, Zhou et al propose the following expression for the evaporation rate of water into the gases ($R_{H_2O}^{eva.}$) [66], [67]:

$$R_{H_2O}^{eva.} = a_g D_{H_2O} \frac{\frac{p_s}{RT} - \frac{p_{H_2O}}{RT}}{d_g}, \quad (4.86)$$

where a_g is the specific surface area of the electrolyte at the gas/liquid interface, D_{H_2O} is the diffusion coefficient of water in the gas phase, R is the general gas constant, T is the temperature, d_g is the diffusive length, and p_s and p_{H_2O} are the saturation vapor pressure and the vapor pressure of water, respectively. Using this expression in the model presented in this work caused unreasonable high heat sinks and temperature gradients and decreased the stability and usability of the model enormously. Therefore, it was deleted again, and the simplified assumption was made, that water produced according to the cell reaction evaporates into the anode gas and into the cathode gas in equal parts, as described above.

4.9 Charge transport

The transport of charge in the solid and in the liquid phase have been modeled with “The Tertiary Current Distribution Interface” by COMSOL [83]. With the assumption that the hydrophobicity of the GDLs prevents any liquids from flooding the gas pores (see main assumption ii), the KOH electrolyte solution is only present in the electrolyte channel and in the anodic and cathodic CLs. For the liquid phase, the conservation of charge can be written

$$\nabla \cdot i_l = Q_l, \quad (4.87)$$

in which i_l is the electrical current density through the electrolyte, and Q_l is the current source. In the electrolyte channel, no electrochemical reactions take place thus the source term Q_l equals zero. However, in the anodic and cathodic CLs it can be given in the form

$$Q_l = F \sum_k z_k R_k, \quad (4.88)$$

where z_k is the charge number, and R_k is the reaction rate of species k . With the reaction rate of potassium ions being zero, the source term is only dependent from the reaction rate of hydroxyl ions R_{OH^-} :

$$Q_l = -FR_{OH^-}. \quad (4.89)$$

Hence, with the reaction rates provided in chapter 4.8, the source terms for the anodic CL (Q_l^A) and for the cathodic CL (Q_l^C) can be given as

$$Q_l^A = i^A a_l^A, \quad (4.90)$$

$$Q_l^C = i^C a_l^C. \quad (4.91)$$

The electrical current density through the electrolyte solution is given by summing up all ion fluxes (N_k) according to

$$i_l = F \sum_k z_k N_k. \quad (4.92)$$

In analogy with equation (4.87), for the electrodes the conservation of charge can be written as

$$\nabla \cdot i_s = Q_s, \quad (4.93)$$

in which i_s is the electrical current density, and Q_s is the current source. In the GDLs and the SLs, no charge transfer reactions are assumed, thus Q_s equals zero in these domains. In the CLs, the source term for charge in the solid phase and the source term for charge in the liquid phase balance according to

$$\nabla \cdot j_s + \nabla \cdot j_l = 0. \quad (4.94)$$

Consequentially, for the anodic CL (Q_s^A) and the cathodic CL (Q_s^C) the source terms can be given in the form

$$Q_s^A = -Q_l^A = -i_A a_l^A, \quad (4.95)$$

$$Q_s^C = -Q_l^C = -i_C a_l^C. \quad (4.96)$$

The relationship between the electrical current density i_s and the potential difference in the electrodes ($\nabla\phi$) is described with the Ohm's law according to

$$i_s = -\sigma^{eff} \nabla\phi, \quad (4.97)$$

in which σ^{eff} is the effective electrical conductivity of the electrode layer. In analogy with the gas phase diffusion coefficient, the Bruggeman equation is assumed when calculating the effective electrical conductivity:

$$\sigma^{eff} = \sigma \theta_s^{3/2}, \quad (4.98)$$

where θ_s is the volume fraction of the solid phase, and σ is the electrical conductivity of the raw material.

4.10 Heat transport

In order to describe the energy transport “The Heat Transfer in Porous Media Interface” by COMSOL [86] has been used. In the model, the heat transfer by radiation, the heat production due to pressure changes, and the viscous dissipation in the fluid are neglected. Hence, the heat transport equation under stationary conditions can be given as [86]

$$\rho C_p v \cdot \nabla T + \nabla \cdot \dot{q}_c = \dot{Q}, \quad (4.99)$$

where ρ is the density, C_p is the heat capacity, v is the velocity, T is the temperature, \dot{q}_c is the heat flux due to conduction, and \dot{Q} is the heat source. The heat flux by thermal conduction can be written as

$$\dot{q}_c = -k \nabla T, \quad (4.100)$$

in which k is the thermal conductivity. In contrast to the free regions where only one phase is present, up to three phases must be considered in the porous media. Hence, ρC_p and k are calculated based on the volume average technique and can be given as

$$\rho C_p = \sum_{\varphi} \theta_{\varphi} \rho_{\varphi} C_{p \varphi}, \quad (4.101)$$

and

$$k = \sum_{\varphi} \theta_{\varphi} k_{\varphi}, \quad (4.102)$$

respectively, where θ_{φ} stands for the volume fraction of the phase φ in the considered region.

Basically, four phenomena cause the temperature to vary in the model, namely

1. the reversible heat of the reactions (\dot{Q}_{rev}),
2. the irreversible heat of the reactions (\dot{Q}_{irrev}),
3. the Joule heat due to charge transport in the solid and liquid phases ($\dot{Q}_{JH,\varphi}$), and
4. the evaporation of water (\dot{Q}_v).

Even if no potential losses occurred in the cell, the electrode reactions would produce reversible heat, which can be written as

$$\dot{Q}_{rev} = T \frac{\partial E}{\partial T} i a_l = T \frac{\Delta s}{nF} i a_l, \quad (4.103)$$

where $\partial E/\partial T$ is the change in equilibrium potential with temperature (temperature coefficient of the reaction), T is the temperature, i is the electrical current density, and a_l is the specific surface area; $\partial E/\partial T$ can be replaced by the entropy of the reaction Δs divided by the number of exchanged electrons n and the Faraday's constant. According to the temperature coefficients of the HOR and the ORR provided by Bratsch [79], the reversible heat sources of the anode reaction (\dot{Q}_{rev}^A) and the cathode reaction (\dot{Q}_{rev}^C) are calculated as

$$\dot{Q}_{rev}^A = -8.36 \cdot 10^{-4} \frac{V}{K} \cdot T i_A a_l^A, \quad (4.104)$$

$$\dot{Q}_{rev}^C = -1.6816E - 3 \frac{V}{K} \cdot T i_C a_l^C. \quad (4.105)$$

For an oxidation reaction the current density is defined positive, whereas for a reduction reaction the current density is defined negative. Consequentially, \dot{Q}_{rev}^A is negative for the endothermal anode reaction and \dot{Q}_{rev}^C is positive for the exothermal cathode reaction, causing the temperature to decrease on the anode side and to rise on the cathode side, respectively.

The irreversible heat \dot{Q}_{irrev} of an electrode reaction can be given by

$$\dot{Q}_{irrev} = \eta i a_l, \quad (4.106)$$

where η is the overpotential of the reaction. Hence, the irreversible heat in the anodic CL (\dot{Q}_{irrev}^A) and the irreversible heat in the cathodic CL (\dot{Q}_{irrev}^C) are calculated as

$$\dot{Q}_{irrev}^A = \eta^A i^A a_l^A, \quad (4.107)$$

$$\dot{Q}_{irrev}^C = \eta^C i^C a_l^C. \quad (4.108)$$

Just like the current density, the overpotential is positive in case of an oxidation reaction but negative in case of a reduction reaction. As a result, both overpotentials cause the temperature to rise with the current density.

The Joule heat due to the charge transport is calculated by

$$\dot{Q}_{JH,\varphi} = -i_{\varphi} \cdot \nabla \phi_{\varphi}, \quad (4.109)$$

where ϕ_{φ} is the electrical potential of the phase φ . In the CLs both the solid phase and the liquid phase are present. Hence, the total Joule heat can be given as

$$\dot{Q}_{JH}^{tot} = -i_s \cdot \nabla \phi_s - i_l \cdot \nabla \phi_l. \quad (4.110)$$

The flux of positive charge is conventionally taken to be a positive electrical current. As electrical current flows from the higher to the lower potential, $\nabla \phi$ is negative when i is positive. Consequentially, this causes a positive Joule heat which raises the temperature.

In the anodic CL and in the cathodic CL, water evaporates from the liquid electrolyte solution into the anode gas and into the cathode gas, respectively. The heat of evaporation can be written as

$$\dot{Q}_v = -\Delta h_v \cdot R_{H_2O}^g, \quad (4.111)$$

where Δh_v is the enthalpy of evaporation (positive), and $R_{H_2O}^g$ is the rate of evaporation of water. When water leaves the liquid phase, $R_{H_2O}^g$ is positive and causes \dot{Q}_v to be a heat sink. Hence, the evaporation rates can be described by equations (4.82) and (4.83), and the heats of evaporation in the anodic CL (\dot{Q}_v^A) and in the cathodic CL (\dot{Q}_v^C) are calculated by

$$\dot{Q}_v^A = -\Delta h_v^A \cdot R_{H_2O}^{A,g}, \quad (4.112)$$

$$\dot{Q}_v^C = -\Delta h_v^C \cdot R_{H_2O}^{C,g}. \quad (4.113)$$

4.11 Properties

In order to describe the physical processes taken into consideration by the model adequately, mathematical approximations are required for the anode gas, the cathode gas, the KOH electrolyte, and the electrodes. These properties are presented in this chapter based on measurements, accepted theories, and assumptions.

The properties for the transport processes in the anode gas and in the cathode gas are presented in Chapter 4.11.1. The transport of hydrogen and oxygen into and through the KOH electrolyte depends on electrolyte specific properties, which are presented separately in chapter 4.11.2. Chapter 4.11.3 deals with the properties of the KOH electrolyte solution, whereas chapter 4.11.4 is about the properties of the electrodes. The values used for the molar masses in the model are given in Table 4.3 [87].

Table 4.3: Molar masses [87]

	H₂	N₂	O₂	H₂O	KOH
Molar mass in g/mol	2.0158	28.0134	31.9988	18.0152	56.1056

4.11.1 Gas phase

In the gas phase the transport of momentum, species, and energy is considered. For the momentum transport the density and the viscosity are required. The former is derived from the ideal gas law, whereas the latter is given in chapter 4.11.1.1. For the species transport in the anode gas and in the cathode gas, the calculation of the diffusion coefficients is provided in chapter 4.11.1.2. For the transport of energy, approximations for the thermal conductivity and the heat capacity are given in chapter 4.11.1.3 and chapter 4.11.1.4, respectively.

4.11.1.1 Viscosity

The viscosities of the gas mixture (η_m) are calculated according to the method of Wilke [88]:

$$\eta_m = \sum_{i=1}^n \frac{x_i \eta_i}{\sum_{j=1}^n x_j f_{ij}}, \quad (4.114)$$

with x_i and η_i being the mole fraction and the viscosity of species i , and f_{ij} being the binary coefficient of species i and j . The binary coefficient f_{ij} is given by [88]

$$f_{ij} = \frac{\left[1 + (\eta_i/\eta_j)^{1/2} (M_i/M_j)^{1/4}\right]^2}{\left[8(1 + M_i/M_j)\right]^{1/2}}, \quad (4.115)$$

where M_i and M_j are the molar masses of species i and j , respectively. Furthermore, η_i and η_j are the viscosities of species i and j , respectively, which are approximated by [89]

$$\eta_i = A_i + B_i \cdot T + C_i \cdot T^2 + D_i \cdot T^3 + E_i \cdot T^4, \quad (4.116)$$

in which η_i is in Pa·s, T is the temperature in K, and $A_i - E_i$ are the component specific parameters given in Table 4.4 for hydrogen, oxygen, nitrogen, and water vapor.

Table 4.4: Parameters for the gas viscosities [89]

	A·10⁵	B·10⁷	C ·10¹⁰	D·10¹²	E·10¹⁵
H₂	0.18024	0.27174	-0.13395	0.00585	-0.00104
O₂	-0.10257	0.92625	-0.80657	0.05113	-0.01295
N₂	-0.01020	0.74785	-0.59037	0.03230	-0.00673
H₂O	0.64966	-0.15102	1.15935	-0.10080	0.03100

4.11.1.2 Diffusion coefficient

The binary diffusion coefficient for the diffusion of a species in a binary mixture (\mathcal{D}_{ik}) can be estimated with the method by Fuller [90], [88] according to

$$\mathcal{D}_{ik} = 0.00143 \frac{T^{1.75} \left((M_i)^{-1} + (M_j)^{-1} \right)^{1/2}}{p\sqrt{2} \left((\sum \Delta_{v_i})^{1/3} + (\sum \Delta_{v_j})^{1/3} \right)^2}, \quad (4.117)$$

where \mathcal{D}_{ik} is in cm²/s, T is the temperature in K, p is the pressure in bar, and M_i and M_j are the molar masses of species i and j in g/mol. Furthermore, $\sum \Delta_v$ is the atomic diffusion volume, given in Table 4.5 for hydrogen, nitrogen, oxygen, and water vapor.

Table 4.5: Atomic diffusion volumes of the gases [88]

	H₂	N₂	O₂	H₂O
$\sum \Delta_v$	6.12	18.5	16.3	13.1

4.11.1.3 Thermal conductivity

The average thermal conductivity of the gas mixture (λ_m) is calculated according to

$$\lambda_m = \sum_i x_i \lambda_i, \quad (4.118)$$

where x_i and λ_i are the mole fraction and the thermal conductivity of species i , respectively.

The thermal conductivities of the pure species are calculated as [90]

$$\lambda_i = A_i + B_i \cdot T + C_i \cdot T^2 + D_i \cdot T^3 + E_i \cdot T^4, \quad (4.119)$$

where λ_i is in W/(K·m), and T is the temperature in K. The component specific coefficients $A_i - E_i$ of hydrogen, oxygen, nitrogen, and water vapor are given in Table 4.6.

Table 4.6: Parameters for the thermal conductivities of the gases [90]

	$A \cdot 10^3$	$B \cdot 10^3$	$C \cdot 10^6$	$D \cdot 10^9$	$E \cdot 10^{12}$
H₂	0.65	0.767	-0.687050	0.506510	-0.138540
O₂	-1.29	0.107	-0.052630	0.025680	-0.005040
N₂	-0.13	0.101	-0.060650	0.033610	-0.007100
H₂O	0.46	0.046	0.051150	0	0

4.11.1.4 Heat capacity

The average heat capacities of the gas mixtures (c_p^m) can be given as

$$c_p^m = \sum_i w_i c_p^i, \quad (4.120)$$

with w_i and c_p^i being the mass fraction and the specific heat capacity of species i , respectively. The specific heat capacities of the pure species are calculated in the form [90]

$$c_p^i = A_i + B_i \cdot T + C_i \cdot T^2 + D_i \cdot T^3 + E_i \cdot T^{-2}, \quad (4.121)$$

where c_p^i is in J/(kg·K), and T is the temperature in K. The component specific coefficients $A_i - E_i$ of hydrogen, oxygen, nitrogen, and water vapor are given in Table 4.7.

Table 4.7: Parameters for the heat capacities of the gases [90]

	<i>A</i>	<i>B</i>	<i>C</i>	<i>D</i> ·10 ³	<i>E</i> ·10 ³
H₂	13973.40	1.256	-0.000892	0.000660	-0.000229
O₂	885.40	0.071	0.000277	-0.000143	-0.000004
N₂	1049.90	-0.158	0.000439	-0.000166	-0.000016
H₂O	1833.10	-0.035	0.000696	-0.000215	-0.000026

4.11.2 Gas transport into and through the electrolyte

In the model the solution of hydrogen and oxygen in the KOH electrolyte and their diffusion in the solution are considered. It is assumed that Henry's law applies at the gas/liquid interface. In chapter 4.5, the Henry constant for the solubility in the electrolyte is expressed as function from the Henry constant for the solubility in water and the salting out coefficient. These two parameters are provided in chapter 4.11.2.1 and chapter 4.11.2.2, respectively. After that, in chapter 4.11.2.3 mathematical approximations for the diffusion coefficients of hydrogen and oxygen in the KOH electrolyte are given.

4.11.2.1 Henry constants for the gas solution in water

Derived from studies of the solubility of various inert gases in water, Himmelblau [91] provides the following approximation for the Henry constant (H_i^W), valid between 0 °C and the critical temperature of water:

$$H_i^W = H_i^* \cdot H_i^{max}, \quad (4.122)$$

where the parameter H_i^* considers the temperature dependence in the form [91]

$$-\log(H^*) = 1.142 - 2.846 \cdot T_i^* + 2.486T_i^{*2} - 0.9761T_i^{*3} + 0.2001T_i^{*4}. \quad (4.123)$$

In equation (4.123), T_i^* is the dimensionless temperature which can be written as [91]

$$T_i^* = \frac{T_i^{max}}{T} \frac{T_c - T}{T_c - T_i^{max}}. \quad (4.124)$$

The parameters T and T_c are the temperature and the critical temperature, respectively, both in K. The parameter H^{max} is the maximum value of the Henry constant when it is plotted

against the reciprocal temperature. The temperature for which H^{max} is obtained is T^{max} . For hydrogen and oxygen the pairs of values are given in Table 4.8. The Henry constant for the solubility in the KOH electrolyte is calculated with equation (4.45), using the Henry constant for the solubility in water and the salting out coefficients given in chapter 4.11.2.2. The Henry constants of hydrogen and oxygen for the solubility in the KOH electrolyte are plotted in Figure 5.11 and Figure 5.12, respectively.

Table 4.8: Parameters for the Henry constants of hydrogen and oxygen [91]

	$1/T^{max} \cdot 10^3 \text{ K}$	$H^{max} \cdot 10^{-4} \text{ atm}$
H₂	3.09	7.54
O₂	2.73	7.08

4.11.2.2 Salting out coefficients

The solubility of hydrogen and oxygen in KOH electrolytes were studied by Shoor and Gubbins [92] and Shoor et al. [93]. In [93], the authors provide the salting out coefficients for hydrogen ($k_{H_2}^S$) and oxygen ($k_{O_2}^S$) in the KOH electrolyte for 25, 40, 60, 80, and 100 °C. They revealed that $k_{H_2}^S$ is the same for all considered temperatures:

$$k_{H_2}^S = 0.129 \frac{l}{mol} \tag{4.125}$$

In contrast, $k_{O_2}^S$ varies. Based on the data by Schoor et al, Zhou [66] provides the following mathematical approximation:

$$k_{O_2}^S = -4.1315 \cdot 10^{-8} T^3 + 1.4405 \cdot 10^{-5} T^2 - 1.5914 \cdot 10^{-3} T + 2.1139 \cdot 10^{-1}, \tag{4.126}$$

where $k_{O_2}^S$ is in l/mol, and T is the temperature in °C.

4.11.2.3 Diffusion coefficients

Based on the experimental evaluated diffusion coefficients by Tham et al. [94], in the concentration range between 0 and 14 M and in the temperature range between 25 and 100 °C, Zhou [66] provides the following approximation:

$$D_i = (A_i + B_i w_e^{0.5} + C_i w_e + D_i w_e^{1.5} + E_i w_e^2) \cdot T^{F_i}, \quad (4.127)$$

where w_e is the mass fraction of KOH in the electrolyte solution, D_i is the diffusion coefficient of species i in the electrolyte in cm^2/s , and T is the temperature in °C. The component specific constants $A_i - F_i$ of hydrogen and oxygen are provided in Table 4.9. The diffusion coefficients of hydrogen and oxygen in the KOH electrolyte are plotted against both the electrolyte concentration and the temperature in Figure 5.8 and Figure 5.9, respectively. Additionally, they are solely plotted against the electrolyte concentration in Figure 5.15 and Figure 5.16 and against the temperature in Figure 5.20 and Figure 5.21.

Table 4.9: Parameters for the diffusion coefficients of H₂ and O₂ in KOH [66]

	$A \cdot 10^7$	$B \cdot 10^6$	$C \cdot 10^6$	$D \cdot 10^6$	$E \cdot 10^6$	F
H₂	13.0048	-8.43475	27.8220	-41.5930	22.4150	1.28968
O₂	5.54211	-2.33930	6.39231	-9.63130	5.45764	1.20838

4.11.3 KOH electrolyte

The model considers the transport of momentum, species, charge, and energy in the KOH electrolyte solution. The density and the viscosity, basically required for the momentum transport, are calculated as given in chapter 4.11.3.1 and chapter 4.11.3.2, respectively. The transport of ions and the transport of charge are directly coupled. In chapter 4.11.3.3 the mathematical expression for the activity coefficient of the KOH electrolyte is provided. The diffusion coefficients of the ions are approximated as described in chapter 4.11.3.4. The electrical conductivity of the KOH electrolyte, the transference numbers, and the limiting equivalent conductivities of the ions are calculated according to chapter 4.11.3.5, chapter 4.11.3.6, and chapter 4.11.3.7, respectively. The thermal properties, needed for the transport of energy, are the thermal conductivity and the heat capacity which are presented in chapter 4.11.3.8 and chapter 4.11.3.9, respectively. The enthalpy of evaporation of water is given in chapter 4.11.3.10, used for the calculation of the heats of evaporation.

4.11.3.1 Density

The density of the KOH electrolyte solution is modeled based on Söhnel and Novotny [95], who provide a general mathematical approximation for the density of aqueous solutions in the form

$$\rho_e = \rho_w + c_e(A + B \cdot T + C \cdot T^2) + c_e^{\frac{3}{2}}(D + E \cdot T + F \cdot T^2), \quad (4.128)$$

which is valid up to 100 °C and up to full saturation. In equation (4.128), ρ_e and ρ_w are the densities of the electrolyte solution and water, respectively, both in kg/m³. Furthermore, c_e is the electrolyte concentration in mol/l, T is the temperature in °C, and $A - F$ are substance specific parameters. From the measured data by Akerlof and Bender [96], Tham et al. [97], and Linke [98], Söhnel and Novotny derived the specific constants for the KOH electrolyte given in Table 4.10. For the density of water between 5 and 100 °C, the authors provide the following function

$$\rho_w = 999.65 + 2.0438 \cdot 10^{-1}T - 6.1744 \cdot 10^{-2}T^{\frac{3}{2}}, \quad (4.129)$$

where T is again the temperature in °C.

Table 4.10: Parameters for density of the KOH electrolyte [95]

<i>A</i>	<i>B</i>·10¹	<i>C</i>·10³	<i>D</i>	<i>E</i>·10²	<i>F</i>·10⁴
54.59	-1.156	1.009	-4.383	2.343	-1.865

4.11.3.2 Viscosity

Maksimova and Sergeev [99] provide measured data for densities, electrical conductivities, and viscosities of KOH electrolyte solutions between ca. 18 and 45 % KOH and at temperatures in the range between 10 and 60 °C. Based on these measurements, Zhou [66] provides the following expression for the viscosity which is used in the model:

$$\mu_e = (1.71468 \cdot 10^{-2} - 0.102529w_e + 0.272493w_e^2)T^{-0.5414}, \quad (4.130)$$

where w_e is the electrolyte mass fraction, μ_e is the electrolyte viscosity in kg/(m·s), and T is the temperature in °C.

It has to be mentioned that a parameterization of the electrolyte viscosity as function from the temperature and the electrolyte concentration enables a precious description of the pressure and velocity fields in a flowing electrolyte solution. The viscosity of the KOH electrolyte is plotted against the temperature in Figure 4.3 for electrolyte concentrations between 10 and 50 % KOH with an increment of 10 % KOH. Dashed lines indicate extrapolations beyond the validity range of 10-60 °C and 18-45 % KOH. The viscosity decreases logarithmically with temperature, which has an enormous impact on the viscosity in the temperature region below the lower boundary. In contrast, above the upper boundary, the viscosity decreases only slightly with rising temperature. Additionally, the viscosity is plotted against the KOH mass fraction in Figure 4.4 for temperatures between 10 and 100 °C with an increment of 10 °C. Again, dashed lines indicate extrapolations beyond the validity range. With respect to the electrolyte concentration, the function shows a minimum at the lower boundary of 18 % KOH. Above the upper boundary of 45 % KOH, the run of the curve keeps rising with temperature. Beyond the validity range, the impact of the temperature and the electrolyte concentration on the KOH electrolyte viscosity could unfortunately not be verified. However, it is assumed that equation (4.130) can be used for extrapolating the viscosity down to concentrations of highly diluted solutions and up to high temperature around 100 °C.

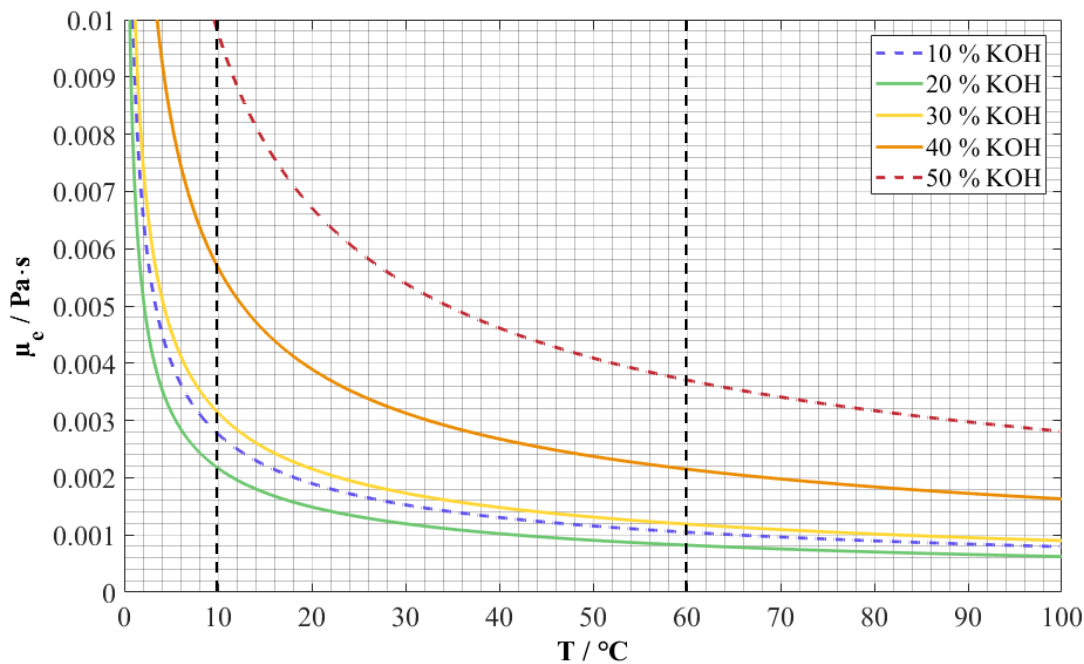


Figure 4.3: Viscosity of the KOH electrolyte vs. T .

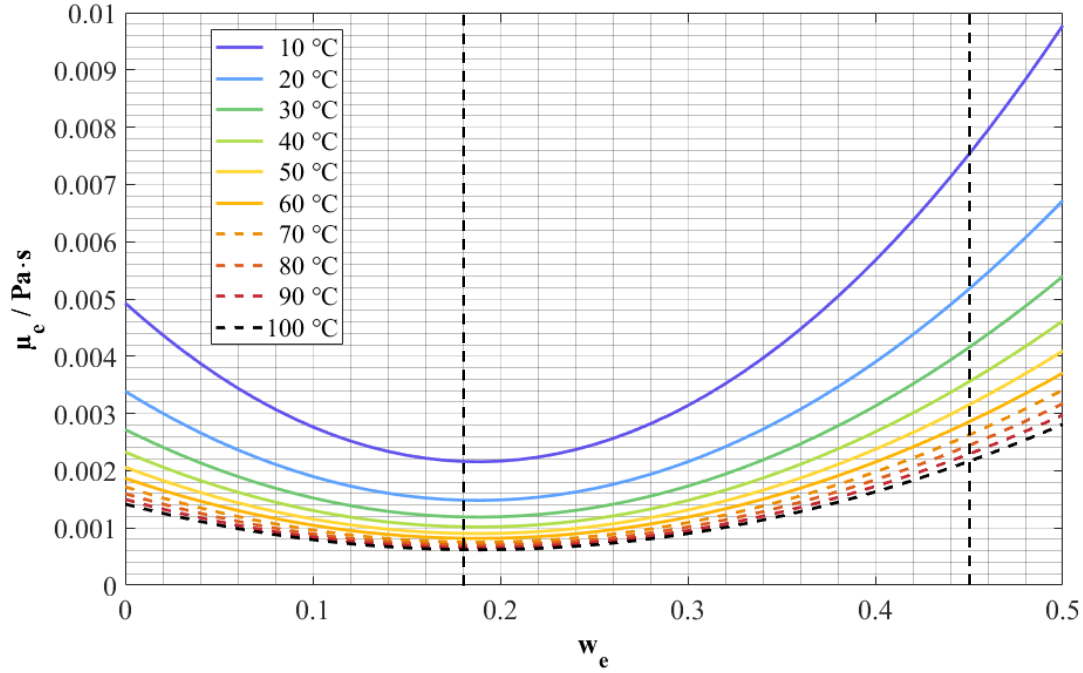


Figure 4.4: Viscosity of the KOH electrolyte vs. w_e .

4.11.3.3 Activity coefficient

Akerlof and Bender [100] provide the following approximation for the activity coefficient of KOH electrolyte solutions derived from experimental measurements between 0 and 70 °C and between 0 and 18 mol/kg:

$$\log(\gamma_{\pm,m}) = \frac{-A \cdot \sqrt{m}}{1 + \sqrt{2}m} + B \cdot m + C \cdot m^2 + D \cdot m^3 + E \cdot m^4, \quad (4.131)$$

with m being the molality in mol/kg. Concerning parameter A , Akerlof and Bender give values at temperatures between 0 and 70 °C with an increment of 10 °C, which were used for deriving the following approximation:

$$A = 4.871 \cdot 10^{-1} + 6 \cdot 10^{-4}T + 5 \cdot 10^{-6}T^2 + 3 \cdot 10^{-8}T^3, \quad (4.132)$$

where the temperature T is in °C. The other coefficients $B - E$ are given by the authors as

$$B = 6.629 \cdot 10^{-2} + 6.135 \cdot 10^{-4}T - 1.1018 \cdot 10^{-5}T^2 + 4.096 \cdot 10^{-8}T^3, \quad (4.133)$$

$$C = 1.0909 \cdot 10^{-2} - 1.7108 \cdot 10^{-4}T + 1.6895 \cdot 10^{-6}T^2 - 7.969 \cdot 10^{-9}T^3, \quad (4.134)$$

$$D = -7.351 \cdot 10^{-4} + 9.973 \cdot 10^{-6}T - 9.347 \cdot 10^{-8}T^2 + 6.215 \cdot 10^{-10}T^3, \quad (4.135)$$

and

$$E = 1.5502 \cdot 10^{-5} - 1.980 \cdot 10^{-7}T + 1.8424 \cdot 10^{-9}T^2 - 1.764 \cdot 10^{-11}T^3, \quad (4.136)$$

where T is again the temperature in °C. The activity coefficient is plotted against the electrolyte concentration in Figure 4.5. The density of the KOH electrolyte solution (equations (4.128) and (4.129)) was used for transferring the molality to the electrolyte concentration, thus the lower boundary of the validity range is 5 °C. The molality can be written as

$$m = \frac{n_e}{m_0} = \frac{c_e}{c_0} \frac{1}{M_0} = \frac{c_e}{(\rho_e - c_e M_e)}, \quad (4.137)$$

whereas the last equation is obtained by inserting c_0 according to equation (4.140).

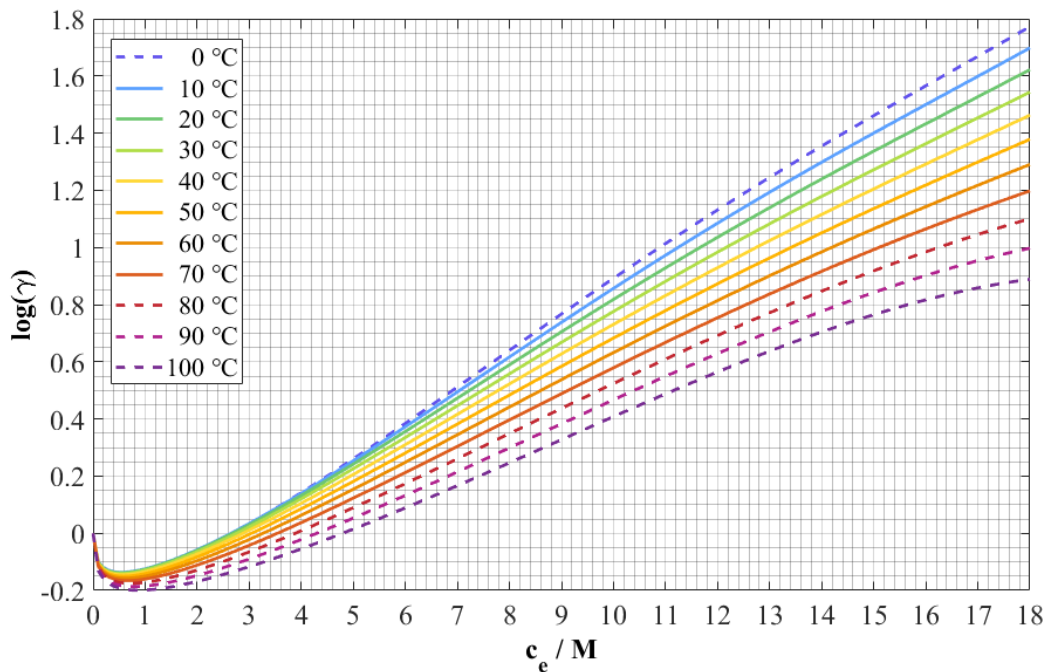


Figure 4.5: Logarithm of the activity coefficient of the KOH electrolyte plotted vs. c_e .

4.11.3.4 Diffusion coefficient

The diffusion coefficient D_c is calculated by

$$D_c = \mathfrak{D} \frac{c_T}{c_0} \left(1 + \frac{d\ln(\gamma_{\pm})}{d\ln(m)} \right) \left(1 - \frac{d\ln(c_0)}{d\ln(c_e)} \right), \quad (2.123)$$

in which \mathfrak{D} is given in equation (2.124) and can be written as

$$\mathfrak{D} = \frac{2\mathfrak{D}_{K^+0}\mathfrak{D}_{OH^-0}}{\mathfrak{D}_{K^+0} + \mathfrak{D}_{OH^-0}}, \quad (4.138)$$

where \mathfrak{D}_{K^+0} and \mathfrak{D}_{OH^-0} are the diffusion coefficients of potassium ions and hydroxyl ions in water. The diffusion coefficients \mathfrak{D}_{+0} and \mathfrak{D}_{-0} are assumed to be independent on the electrolyte concentration and calculated from the limiting equivalent conductivities based on the Nernst-Einstein relation:

$$\mathfrak{D}_{i0} = \frac{RT\lambda_i^0}{|z_i|F^2}. \quad (4.139)$$

The factor $(1 + d\ln(c_0)/d\ln(c_e))$ can be derived from the expression for the electrolyte density (ρ_e), given in chapter 4.11.3.1. The concentration of water c_0 can be expressed as

$$c_0 = \frac{\rho_e - c_e M_e}{M_0}, \quad (4.140)$$

thus using equation (4.128) yields

$$\left(1 - \frac{d\ln(c_0)}{d\ln(c_e)} \right) = 1 - \frac{c_e}{c_0} \frac{1}{M_0} \left(A + B \cdot T + C \cdot T^2 + \frac{3}{2} c_e^{\frac{1}{2}} (D + E \cdot T + F \cdot T^2) - M_e \right). \quad (4.141)$$

In equation (4.141), the temperature T is in °C, the electrolyte concentration c_e is in mol/l, and the molar masses of water M_0 and KOH M_e are in g/mol. The parameters $A - F$ are given in Table 4.10.

The factor $(1 + d\ln(\gamma_{\pm,m})/d\ln(m))$ is derived from the activity coefficient given in chapter 4.11.3.3. Hence, it can be calculated as

$$\left(1 + \frac{d\ln(\gamma_{\pm,m})}{d\ln(m)}\right) = 1 + 2.3m \cdot \left(\frac{-0.5A}{\sqrt{m} \cdot (1 + \sqrt{2m})^2} + B + 2C \cdot m + 3D \cdot m^2 + 4E \cdot m^3\right), \quad (4.142)$$

where the molality m is in mol/kg, and the coefficients $A - E$ are given by equations (4.132)-(4.136).

Based on the validity of the electrolyte density (equations (4.128) and (4.129)) and the validity of the activity coefficient of the KOH electrolyte (equations (4.131)-(4.136)) the calculation of D_c is only valid between 0 and 70 °C. The calculated diffusion coefficient D_c is plotted against the electrolyte concentration and against the temperature in Figure 4.6 and Figure 4.7, respectively. Extrapolations beyond the validity range are indicated by dashed lines. The dimension of $1 \cdot 10^{-5}$ - $1 \cdot 10^{-4}$ cm²/s is reasonable for the diffusion coefficient of an electrolyte [101], [102]. Also, an increase in the diffusion coefficient with temperature is justifiable as the mobility of the molecules rise; it is also reported in [101], [102]. It is known, that the diffusion coefficient of the KOH electrolyte increases with the electrolyte concentration and shows an optimum at high concentrations [101], [102]. Nevertheless, the optimum and the dramatical decrease of the calculated diffusion coefficient in the region of high electrolyte concentrations, predicted for temperatures above the upper temperature boundary, seems to be unreasonable (see Figure 4.6). Also, for electrolyte concentrations above 14 M KOH an optimum with respect to the temperature can be observed in Figure 4.7 within the valid temperature range. As the dramatically decrease of D_c could not be verified, it is recommended to use the calculated diffusion coefficient only with cautions in concentration regions where it decreases. However, for concentrations up to 11 M the calculation method seems to provide plausible results even for temperatures up to 100 °C.

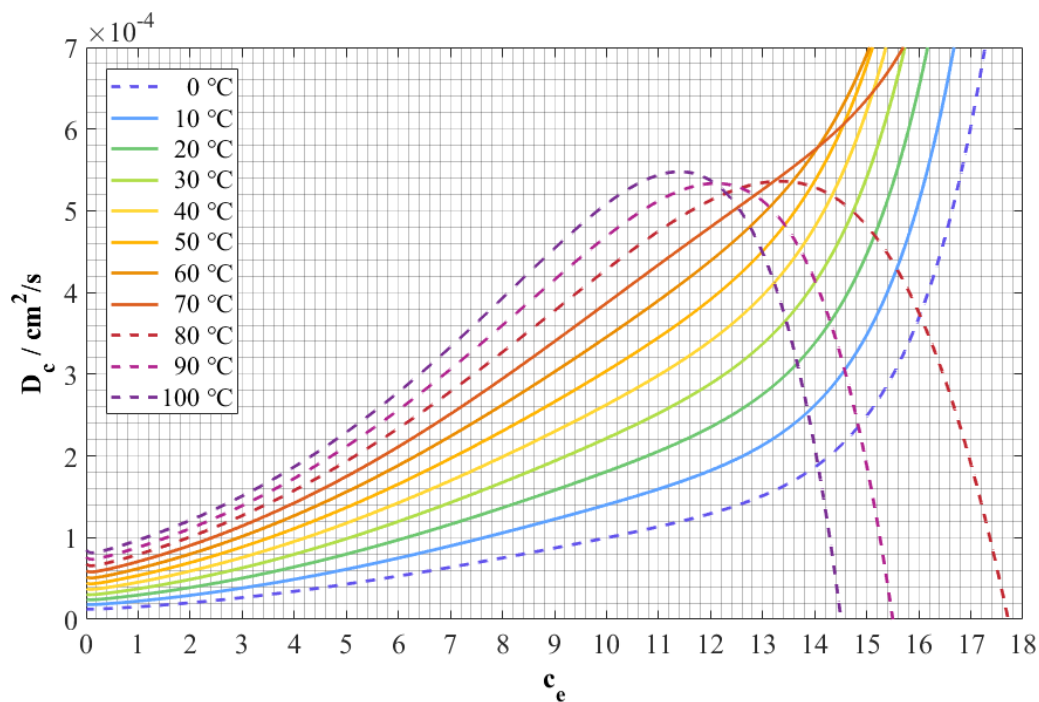


Figure 4.6: Calculated diffusion coefficient D_c plotted vs. c_e .

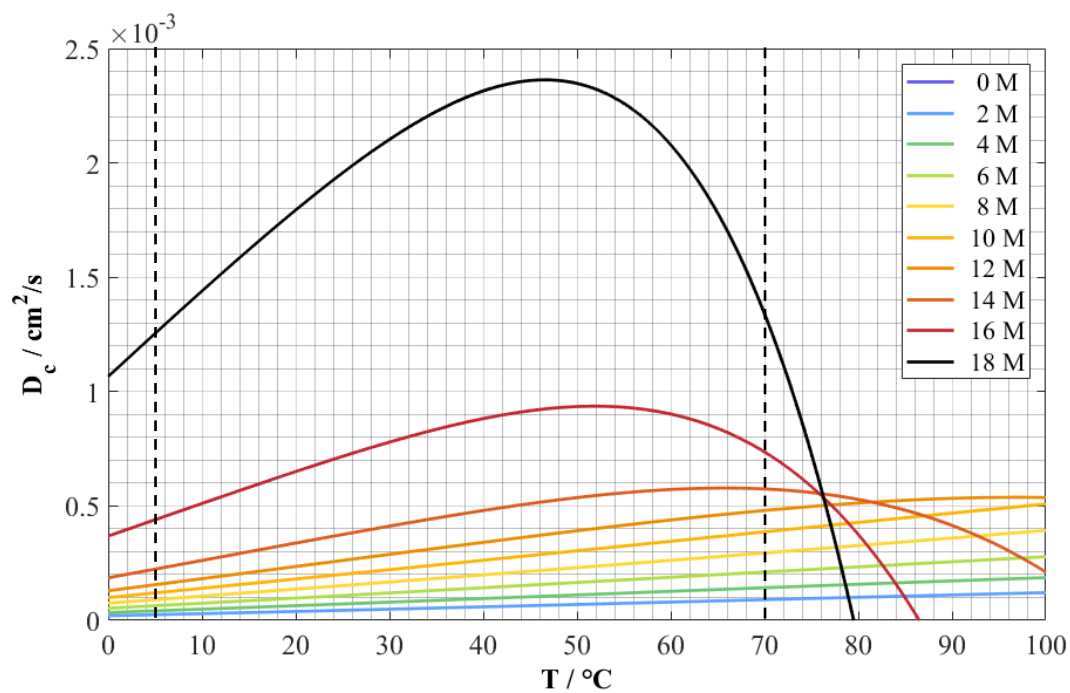


Figure 4.7: Calculated diffusion coefficient D_c plotted vs. T .

4.11.3.5 Electrical conductivity

The electrical conductivity of the KOH electrolyte solution (κ_e) is described based on Horvath [103], who presents the following approximation valid above 0 °C:

$$\kappa_e = 0.0262w_e + 6.7 \cdot 10^{-4}w_e \cdot T - 4.8 \cdot 10^{-4}w_e^2 - 8.8 \cdot 10^{-6}w_e^2 \cdot T, \quad (4.143)$$

where κ_e is in S/cm, the temperature T is in °C, and the electrolyte mass fraction w_e is in %. The electrical conductivity is plotted in Figure 5.14.

Notice: Data on the electrical conductivity of KOH electrolyte solutions are also provided in [104], [105], and [106].

4.11.3.6 Transference numbers

Due to a lack of available data, the transference number with respect to the solvent velocity is assumed to be independent from the electrolyte concentration. Therefore, it is derived from the limiting equivalent conductivity according to

$$t_i^0 = \frac{\lambda_i^0}{\lambda_{OH^-}^0 + \lambda_{K^+}^0}. \quad (4.144)$$

The transference number with respect to the volume average velocity (t_i^*) is calculated based on t_i^0 by using equation (2.132).

4.11.3.7 Limiting equivalent conductivities

From the limiting equivalent conductivities provided by Robinson and Stokes [107] for potassium ($\lambda_{K^+}^0$) and hydroxyl ions ($\lambda_{OH^-}^0$) following mathematical expressions have been derived valid between 0 and 100 °C:

$$\lambda_{OH^-}^0 = 112.36 + 3.4079T, \quad (4.145)$$

$$\lambda_{K^+}^0 = 35.982 + 1.5552T, \quad (4.146)$$

where $\lambda_{OH^-}^0$ and $\lambda_{K^+}^0$ are in S·cm²/mol, and the temperature T is in °C.

4.11.3.8 Thermal conductivity

From measurements in the concentration range between 1.5 and 16.1 mol/l, Losenicky [108] provides the concentration dependence of the thermal conductivity of the KOH electrolyte (λ_e) in the form

$$\lambda_e = \lambda_w - 8.36197 \cdot 10^{-4} c_e - 2.30274 \cdot 10^{-4} c_e^2, \quad (4.147)$$

where the thermal conductivities of the electrolyte λ_e and water λ_w are in W/(m·K), and the electrolyte concentration c_e is in mol/l. The thermal conductivity of liquid water is calculated depending on temperature according to [89]

$$\lambda_w = -2.4149 + 2.45165 \cdot 10^{-2} T - 0.73121 \cdot 10^{-4} T^2 + 0.99492 \cdot 10^{-7} T^3 - 0.53730 \cdot 10^{-10} T^4, \quad (4.148)$$

where T is in K. It is assumed that λ_e and λ_w depend on temperature equally so that no additional temperature correction is taken into consideration.

4.11.3.9 Heat capacity

Based on measurements between 25 and 150 °C, Ginzburg et al. [109] present the heat capacity of the KOH electrolyte (c_p) at constant electrolyte concentration as follows

$$c_p = A + B \cdot T, \quad (4.149)$$

where c_p is in J/(g·K) and the temperature T is in °C. The coefficients A and B are given in Table 4.11 for KOH electrolyte solutions with concentrations of 10, 20, 30, 40, and 50 % KOH. Below 10 and above 50 % KOH, the heat capacity is kept constant by the model, whereas between these limits the heat capacity is interpolated according to the law of the lever:

$$c_p(w) = \frac{w^{high} - w}{w^{high} - w^{low}} c_p(w^{low}) + \frac{w - w^{low}}{w^{high} - w^{low}} c_p(w^{high}), \quad (4.150)$$

where w^{low} is the next lower mass fraction and w^{high} is the next higher mass fraction for which $c_p(w^{low})$ and $c_p(w^{high})$, respectively, are given in Table 4.11.

Table 4.11: Parameters for the heat capacity of the KOH electrolyte [109]

$w_e / \%$	A	$B \cdot 10^3$
10	3.5588	2.6796
20	3.1820	2.6796
30	2.9308	2.0934
40	2.6921	1.6747
50	2.4493	1.6747

4.11.3.10 Enthalpy of evaporation of water

The enthalpy of evaporation of water is approximated according to [89]

$$\frac{\Delta h_v}{R \cdot T_c} = 6.85307T^{*\frac{1}{3}} + 7.43804T^{*\frac{2}{3}} - 2.937595T^* - 3.282093T^{*2} + 8.397378T^{*6}, \quad (4.151)$$

where R is the general gas constant, T_c is the critical temperature of water, and the dimensionless temperature T^* is given by

$$T^* = 1 - \frac{T}{T_c}. \quad (4.152)$$

In equation (4.152), T is the temperature in K.

4.11.4 Electrodes

Different materials are typically used for the SL, GDL, and CL. To achieve a high electrical conductivity, nickel is typically used as material for the SL. For preventing the liquids from flooding the gas pores of the GDL, it is generally made of PTFE. As the electrical conductivity of PTFE is insufficient, a highly conductive material such as carbon is generally added. Although the AFC is known to be operable with nonprecious catalyst materials, platinum is mostly used in the CLs for enhancing the kinetics in the low temperature range.

The model is based on the beta-cell design by AFC Energy. However, due to the lack of available data, various assumptions needed to be made with respect to the electrode materials. Hence, nickel and platinum are assumed to be the raw materials (without empty pores) of the SLs and the CLs, respectively. The properties of the GDLs are estimated based

on the commercially available TGP-H-090 by Toray [110], whereby the properties of the raw material were derived as

$$x_{raw} = \frac{x_{bulk}}{(1 - \varepsilon)}, \quad (4.153)$$

where x_{raw} is the property of the raw material, x_{bulk} is the given property of the bulk material, and ε is the gas porosity. In order to account for contact resistances and the possibility that the GDL by AFC Energy might be less conductive, the electrical conductivity was reduced to 1 % of the so calculated value⁶. For the heat capacity of the GDL, the heat capacity of graphite is assumed. The values used in the model are given in Table 4.12. The structure parameters, primary assumed based on literature data, are given in Table 4.13.

Table 4.12: Electrode properties

	SL (Ni)	GDL	CL (Pt)
$\rho / \text{g/cm}^3$	8.9 _a	2 _f	21.5 _c
$\sigma / 10^6 \text{ S/m}$	14.0449 _a	0.00012114 _{f,g}	9.346 _c
$k / \text{W/(cm}\cdot\text{K)}$	0.9070 _b	0.077 _f	0.716 _d
$c_p / \text{J/(g}\cdot\text{K)}$	0.4450 _a	0.708 _e	0.133 _c

a) Nickel at 25 °C [111]; b) Nickel at 27 °C [111], c) Platinum at 25 °C [111], d) Platinum at 27 °C [111], e) Graphite at 25 °C [111], f) Toray TGP-H-090 [110], g) Assumption

Table 4.13: Structure parameters of the electrodes

Parameter	Value	Notes	Ref.
θ_{SL}^g	0.3	Volume fraction of the gas phase in the SL	Assumption
θ_{SL}^l	0	Volume fraction of the liquid phase in the SL	Assumption
θ_{SL}^s	0.7	Volume fraction of the solid phase in the SL	Assumption
θ_{GDL}^g	0.7	Volume fraction of the gas phase in the GDL	[54]
θ_{GDL}^l	0	Volume fraction of the liquid phase in the GDL	[54]
θ_{GDL}^s	0.3	Volume fraction of the solid phase in the GDL	[54]

⁶ The reduction to 1 % of the calculated value is only based on an assumption. The actual conductivity of the GDLs and the total electrodes should be measured in the future and implemented in the model in order to derive more adequate results.

θ_{CL}^g	0.05	Volume fraction of the gas phase in the CL	[54]
θ_{CL}^l	0.65	Volume fraction of the liquid phase in the CL	[54]
θ_{CL}^s	0.3	Volume fraction of the solid phase in the CL ($\theta_{CL}^g + \theta_{CL}^l + \theta_{CL}^s = 1$)	From balance
κ_{SL}	$1 \cdot 10^{-10} \text{ m}^2$	Gas permeability of the SL	Assumption
κ_{GDL}	$1 \cdot 10^{-12} \text{ m}^2$	Gas permeability of the GDL	Assumption
κ_{CL}^g	$1 \cdot 10^{-11} \text{ m}^2$	Gas permeability of the CL	Assumption
κ_{CL}^l	$1 \cdot 10^{-14} \text{ m}^2$	Liquid permeability of the CL	Assumption

4.12 Boundary conditions

In this chapter the boundary and initial conditions are given which are used for solving the model. In chapter 4.12.1, the required conditions for the momentum transport in the gas and liquid phases are presented. After that, the boundary and initial conditions for the mass transport in the gas phase and in the liquid phase are described in chapter 4.12.2 and chapter 4.12.3, respectively. The charge and the energy transport are solved based on the conditions given in chapter 4.12.4 and chapter 4.12.5, respectively. The inlet velocity of the gases can be designed for an aimed conversion rate, which is explained in chapter 4.12.6. Finally, the reference concentrations (see chapter 4.1 and chapter 4.2) are calculated in chapter 4.12.7.

4.12.1 Momentum transport

The main boundary conditions for the flows in the anodic gas channel, the cathodic gas channel, and the electrolyte channel are the three velocities at the inlets and the pressures at the channel outlets. The fluids are assumed to enter the cell as laminar flows. For this purpose, an entrance length of the height of the cell is assumed. At the outer points of the inlets (where the walls are located), the velocities are forced to zero. At the outlets, normal flows are assumed and backflows are suppressed. At all other outer boundaries of the anode gas region, the cathode gas region, and the electrolyte region, the Dirichlet condition is applied as [82]

$$v = 0. \quad (4.154)$$

In the anodic gas region, the cathodic gas region, and the electrolyte region, 0 m/s is used as initial velocity and the outlet pressure is used as initial pressure.

4.12.2 Species transport in the gas phase

The boundary conditions at the anode inlet and at the cathode inlet are the mole fractions. At the anodic gas channel outlet and at the cathodic gas channel outlet, diffusion is neglected. At all other outer boundaries of the anode gas region and of the cathode gas region, the fluxes normal to the boundary ($n \cdot N_i$) are forced to zero

$$-n \cdot N_i = 0. \quad (4.155)$$

The mole fractions at the anode inlet and at the cathode inlet are taken as initial values in the anode gas region and the cathode gas region, respectively.

4.12.3 Species transport in the liquid phase

For the ion transport in the KOH electrolyte solution, the electrolyte concentration at the inlet is the boundary condition (initial electrolyte concentration). In analogy with the mass transport in the gas phase, diffusion is neglected at the electrolyte channel outlet. At all other outer boundaries of the electrolyte region the normal fluxes ($n \cdot N_i$) are forced to zero:

$$-n \cdot N_i = 0. \quad (4.156)$$

The electrolyte concentration at the electrolyte inlet is also used as initial value within the electrolyte region.

4.12.4 Charge transport

The boundary conditions for driving the electrical current are the electric potentials of the anodic current collector and the cathodic current collector. As described in chapter 4.1 the ground potential is applied to the anodic current collector (0 V), whereas the cell voltage is applied to the cathodic current collector. At all other outer boundaries of the charge region, electrical isolation is assumed:

$$-n \cdot i = 0, \quad (4.157)$$

where $n \cdot i$ is the electrical current normal to the considered boundary. In the anode and the cathode, the electrical potential of the anodic current collector and the electrical potential of the cathodic current collector, respectively, are used as initial values. Based on chapter 4.1,

it can be expected that the electrical potential of the electrolyte solution equals ca. the negative value of the reversible potential of the anode reaction vs. the SHE. Therefore, using a potential as initial value that is similar to the negative reversible potential of the anode reaction has caused relatively high numerical stability.

4.12.5 Heat transport

The specifying boundary conditions for the heat transfer are the inlet temperatures of the anode gas, the cathode gas, and the electrolyte solution at the anode inlet, the cathode inlet, and the electrolyte inlet, respectively. At the outer boundaries of the cell, thermal isolation is assumed according to

$$-n \cdot q = 0, \quad (4.158)$$

where $n \cdot q$ is the heat flux normal to the boundary. The anodic inlet temperature and the cathodic inlet temperature are taken as initial values in the anodic inlet extension and in the cathodic inlet extension, respectively. In all other regions, the electrolyte inlet temperature is used as initial value.

4.12.6 Designed gas velocity

In order to obtain a certain conversion efficiency at a certain current density, the inlet velocity can be designed, as presented in the following. The stoichiometry λ_i , which is the reciprocal value of the conversion efficiency, can be written as

$$\lambda_i = \frac{N_i}{R_i}, \quad (4.159)$$

where N_i is the flux of the reactant species i at the inlet, and R_i is the reaction rate with respect to the active cell surface area. Assuming convection dominates at the inlet, while diffusion is negligible, the species fluxes can be written as

$$N_i = c_i v_i \approx c_i v, \quad (4.160)$$

where c_i and v_i are the concentration and the velocity of species i , respectively, and v is the average velocity of the mixture. The reaction rate can be written with Faraday's law as

$$R_i = \frac{\nu_i i_{cell}}{nF}, \quad (4.161)$$

where ν_i is the stoichiometric coefficient of species i , n is the number of transferred electrons, and i_{cell} is the electrical current density with respect to the active cell surface area. Hence, assuming a homogeneous current density all over the active cell surface area A_{cell} , and a homogeneous inflow at the gas channel inlet (with the cross sectional area A_{in}), the velocity can be given as function from a desired stoichiometry at a certain current density:

$$v = \frac{\lambda_i \nu_i i_{cell} A_{cell}}{nF c_i A_{in}}. \quad (4.162)$$

By using the ideal gas law, this expression can be rearranged to calculate the inlet velocity as function from the initial mole fraction x_i and the temperature T :

$$v = \frac{\lambda_i \nu_i i RT A_{cell}}{nF x_i p A_{in}}. \quad (4.163)$$

This expression is used for designing the inlet velocities of the anode gas and the cathode gas. Thereby, the inlet temperature of the electrolyte is inserted for T and the outlet pressure is inserted for p .

4.12.7 Reference concentrations

Following the theory that hydrogen and oxygen must dissolve in and diffuse through the electrolyte in order to reach the catalyst surface, the equilibrium potentials (equations (4.18) and (4.19)), the exchange current densities (equations (4.24) and (4.25)), and the Butler-Volmer expressions (equations (4.22) and (4.23)) are calculated with the liquid phase concentrations. Consequentially, also the reference concentrations in these expressions are liquid phase concentrations. Typically, the temperature, the pressure, the gas phase concentration, and the electrolyte concentration are provided in open literature in addition to data for exchange current densities and equilibrium potentials. With the electrolyte concentration and the temperature, the water concentration can be calculated according to

$$c_0 = \frac{\rho_e - M_e c_e}{M_0}. \quad (4.140)$$

The concentrations of hydrogen and oxygen can then be derived with equation (4.54):

$$c_{H_2} = (c_0 + 2c_e) \left(\frac{H_{H_2}^W}{p_{H_2}} \cdot 10^{k_{H_2}^s \cdot c_e} - 1 \right)^{-1}, \quad (4.164)$$

$$c_{O_2} = (c_0 + 2c_e) \left(\frac{H_{O_2}^W}{p_{O_2}} \cdot 10^{k_{O_2}^s \cdot c_e} - 1 \right)^{-1}. \quad (4.165)$$

The reference concentrations used in the model are summed up in Table 4.14. They are calculated for the equilibrium potentials based on Bratsch [79] at 25 °C, 1 atm, pH 13.996, and $x_{H_2} = x_{O_2} = 1$. The kinetics of the anode reaction (at platinum) is described based on Sheng et al. [80] at 294 K, 1 atm, 0.1 M, and $x_{H_2} = 1$. The kinetics of the ORR (at platinum) is described based on Blurton [81] at 25 °C, 1 atm, 6.88 M, and $x_{O_2} = 1$.

The same method is used for the calculation of the initial concentrations in order to compute the equilibrium potentials and the exchange current densities automatically dependent on the initial conditions. At 60 °C, 1 atm, and 5 M, the initial water concentration is 50,975 mol/m³, the initial hydrogen concentration in the electrolyte is 0.18681 mol/m³ for $x_{H_2} = 1$, and the initial oxygen concentration in the electrolyte is 0.032139 mol/m³ for $x_{O_2} = 0.21$.

Table 4.14: Reference concentrations

	<i>Anode</i>		<i>Cathode</i>	
	E_0	i_0	E_0	i_0
$c_{OH^-}^{Ref} / \text{mol/m}^3$	1,000	100 [80]	1,000	6,880 [81]
$c_{H_2O}^{Ref} / \text{mol/m}^3$	54,918	55,373	54,918	49,982
$c_{H_2}^{Ref} / \text{mol/m}^3$	0.59705	0.77612	-	-
$c_{O_2}^{Ref} / \text{mol/m}^3$	-	-	0.85206	0.083457

5. Simulation and discussion

The AFC model described thoroughly in chapter 4 has been developed for investigating the processes in the cell and finding improvement potentials with respect to the overall performance of the cell. Being based on the beta-cell design by the company AFC Energy, the cell geometries shown in Table 5.1 (see also Figure 4.1 for the model schema) and the base case conditions listed in Table 5.2 were chosen on the basis of provided information. Parameters specific to the anodic and cathodic CLs and parameters with respect to the electrochemical reactions are provided in Table 5.3 and Table 5.4, respectively. A plurality of simulation and various adjustments of the model, the mesh, and the solver have led the way to the simulation results which are presented in this chapter.

In this chapter, the cell performance is typically portrayed as polarization curve, where the cell voltage is plotted against the current density with respect to the active cell surface area (see chapter 2.6). The model is operated by applying the ground potential and the cell voltage to the anodic current collector and the cathodic current collector, respectively, (see chapter 4.1) whereas the current density is measured. For this purpose, the electrical current of the cell is derived by an integral measurement of the current density normal to the cathodic current collector. The so obtained current is then related to the active cell surface area ($13 \times 47 \text{ cm}^2$) and leads to the illustrated current density.

In order to ensure plausibility of the model, the simulation results are compared with measurements provided by AFC Energy in chapter 5.1. Additionally, in chapter 5.2, the cell performance and the gradients in the cell are discussed for this base case condition. In the course of this analysis, the predicted KOH concentration, temperature, and hydrogen mole fraction and oxygen mole fraction fields are discussed in chapter 5.2.1, chapter 5.2.2, and chapter 5.2.3, respectively. Also, the polarization curve is analyzed in chapter 5.2.4 with focus on the processes which are responsible for the different overpotentials. A short interim conclusion is made in chapter 5.3.

The model has been used for parameter studies, which are presented in chapter 5.4. Focusing the main operating conditions, the impact of the electrolyte concentration, the pressure, and the temperature are considered in chapter 5.4.1, chapter 5.4.2, and chapter 5.4.3, respectively. Taking into account the temperature dependences of the transfer coefficients and of the exchange current densities, particular attention has been paid to the impact of

temperature on kinetics. These temperature dependences are studied in chapter 5.4.4. After that, in chapter 5.4.5, the impact of the anodic and cathodic kinetic parameters on the polarization curve are investigated. Then, the sensitivity of the polarization curve with respect to the electrolyte film parameters is examined in chapter 5.4.6. These studies reveal important correlations which can lead to an improvement of the cell performance.

Table 5.1: Cell geometries

Parameter	Value	Notes	Ref.
h_{cell}	14 cm	Height of the cell	[112]
d_{cell}	47 cm	Depth of the cell (in the third dimension)	[112]
$w_{Channel}^A$	1.5 mm	Thickness of the anodic gas channel (half of the gas channel width in the stack)	[112]
$w_{Channel}^C$	1.5 mm	Thickness of the cathodic gas channel (half of the gas channel width in the stack)	[112]
$w_{Channel}^E$	3 mm	Thickness of the electrolyte channel	[112]
$h_{Channel}^{Top}$	5 cm	Height of the upper channel extension	Assumption
$h_{Channel}^{Bottom}$	5 cm	Height of the lower channel extension	Assumption
w_{SL}^A	250 μm	Thickness of the anodic SL	[112]
w_{SL}^C	250 μm	Thickness of the cathodic SL	[112]
w_{GDL}^A	510 μm	Thickness of the anodic GDL	[112]
w_{GDL}^C	440 μm	Thickness of the cathodic GDL	[112]
w_{CL}^A	100 μm	Thickness of the anodic CL (assumed to be the same as w_{CL}^C)	Assumption
w_{CL}^C	100 μm	Thickness of the cathodic CL	[63]

Table 5.2: Base case operating conditions

Parameter	Value	Notes	Ref.
T	60 °C	Temperature (at the inlets)	[112]
p	1 atm	Pressure (at the outlets)	[112]
c_e	5 M	Electrolyte concentration (at the electrolyte inlet)	[112]
$x_{H_2}^{in}$	100 %	Hydrogen fraction (at the anode inlet)	[112]
$x_{O_2}^{in}$	21 %	Oxygen fraction (at the cathode inlet)	[112]
$x_{N_2}^{in}$	79 %	Nitrogen fraction (at the cathode inlet)	[112]
v_e^{in}	$1.584 \cdot 10^{-3}$ m/s	Electrolyte velocity (at the electrolyte inlet)	[112]
v_A^{in}	3.148 m/s	Anode gas velocity (at the anode inlet; assumed to equal v_C^{in})	Estimation
v_C^{in}	3.148 m/s	Cathode gas velocity (at the cathode inlet; designed for reaching current densities up to 10 A/cm ² with air at 1 atm (see chapter 4.12.6))	Estimation

Table 5.3: Parameters specific to the anodic CL and the cathodic CL

Parameter	Value	Notes	Ref.
a_t^A	$4 \cdot 10^5$ cm ² /cm ³	Specific surface area of the anodic catalyst (estimated based on [63], [67])	Estimation
a_t^C	$4 \cdot 10^5$ cm ² /cm ³	Specific surface area of the cathodic catalyst (estimated based on [63], [67])	Estimation
a_g^A	$7 \cdot 10^5$ cm ² /cm ³	Specific surface area of the electrolyte film in the anodic CL	[63]
a_g^C	$7 \cdot 10^5$ cm ² /cm ³	Specific surface area of the electrolyte film in the cathodic CL	[63]
d_t^A	$5 \cdot 10^{-5}$ cm	Thickness of the electrolyte film in the anodic CL	[63]
d_t^C	$5 \cdot 10^{-5}$ cm	Thickness of the electrolyte film in the cathodic CL	[63]

Table 5.4: Parameters specific to the electrochemical reactions

Parameter	Value	Notes	Ref.
$\vartheta_{H_2}^A$	1	Reaction order of hydrogen in the anode reaction	a
$\vartheta_{H_2O}^A$	2	Reaction order of water in the anode reaction	a
$\vartheta_{OH^-}^A$	2	Reaction order of hydroxyl ions in the anode reaction	a
n^A	2	Number of exchanged electrons in the anode reaction	Equation (4.1)
$\vartheta_{O_2}^C$	1	Reaction order of oxygen in the cathode reaction	a
$\vartheta_{H_2O}^C$	2	Reaction order of water in the cathode reaction	a
$\vartheta_{OH^-}^C$	4	Reaction order of hydroxyl ions in the cathode reaction	a
n^C	4	Number of exchanged electrons in the cathode reaction	Equation (4.2)

a) The reaction order of the species participating in the anode reaction (equation (4.1)) and in the cathode reaction (equation (4.2)) are assumed to equal the absolute value of the stoichiometric coefficients of these species

5.1 Comparison with measurements

The accuracy of the overall performance of a fuel cell model can be verified by comparing the polarization curve predicted by the model with a measured curve. Thereby, the model should agree with the real cell on operating conditions, material properties, and geometrical data. Being based on the beta-cell design by AFC Energy, the model must be validated with measurements at this specific cell. However, AFC Energy does not run the beta-cell individually but only in a stack of at least three cells where the cells are alternately arranged. Two adjacent anodes share a common anodic gas channel and two adjacent cathodes share a common cathodic gas channel. Therefore, when the gas channels of the single cell model are assumed to be 1.5 mm, they are half as thick as the gas channels in the stack. Based on the experience by AFC Energy the impact of the neighboring cells on the performance of the middle cell is negligible in small stacks [112]. Therefore, the polarization curve measured at the middle cell of the three cell stack has been used for the validation of this model.

The polarization curves measured at the real cell by AFC Energy and predicted by the model are illustrated in Figure 5.1 in red and black, respectively. An excellent agreement of the simulating results with the measurements becomes directly visible. As the real cell has only been operated up to moderated current densities where the limitation due to mass transport cannot be observed, the simulation results can only be compared with respect to the activation region and the ohmic region. However, the simulation model predicts a limitation at ca. 265 mA/cm². This is due to oxygen mass transport through the liquid electrolyte film, as described in chapter 5.2.4 thoroughly.

Both curves start at approximately 1 V and decrease logarithmically with rising current density in the region of low current densities (activation region). The transition from the activation region to the ohmic region is slightly more abrupt in case of the real polarization curve than in case of the numerically predicted one. In the model, the kinetics of the anode reaction and the kinetics of the cathode reaction are described with the Butler-Volmer expression which is only a simple approach and does not capture the total reaction mechanism. The actual reaction mechanism arising in a real cell is much more complex so that a deviation of the simulated polarization curve from the measured one in the activation region is only reasonable.

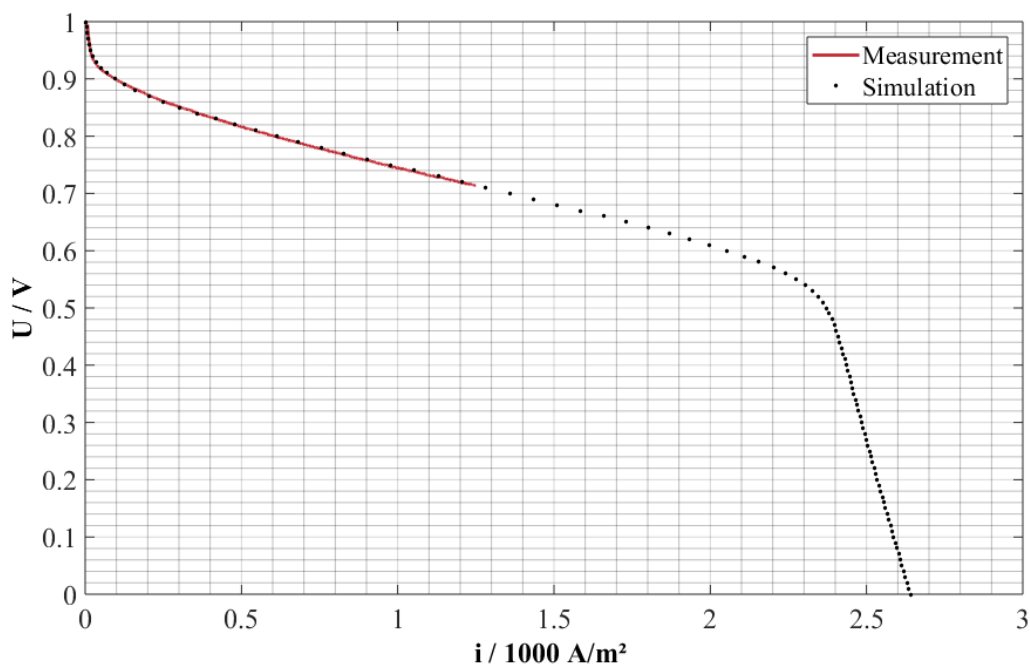


Figure 5.1: Comparison of the simulation results with measurement.

In the ohmic region the slopes of the simulated polarization curve and of the measured polarization curve are the same, thus no deviation can be observed. Due to the lack of available data, the properties of the electrodes needed to be assumed, especially the properties of the GDLs. However, the so assumed electrode properties seem to enable an adequate description of the electrodes with respect to the overall cell performance. Nevertheless, for an appropriate validation more information particularly with respect to the electrode properties are required.

5.2 Analysis of the cell performance

With rising current density, the gradients in the cell increase and cause the cell voltage to decrease. In order to verify the processes in the model, the gradients in the cell and the polarization curve are analyzed in this chapter. For this purpose, the KOH concentration field, the temperature field, and the hydrogen and oxygen mole fraction fields predicted for the base case scenario (see chapter 5.1) are investigated in chapter 5.2.1, chapter 5.2.2, and chapter 5.2.3, respectively. Also, the polarization curve is discussed in chapter 5.2.4 with focus on the shares of the individual overpotentials in the overall overpotential that causes the departure of the cell voltage from the reversible cell voltage.

5.2.1 Electrolyte concentration

The distribution of the electrolyte concentration in the electrolyte channel and in the anodic and cathodic CLs is shown in Figure 5.2 at 1.0, 0.8, 0.6, and 0.4 V from the left to the right. According to the rainbow color-legend below the four pictures, the lower limit blue and the upper limit red stand for 4 and 6 M KOH, respectively. As no electrolyte is present in the gas channels, the SLs, and the GDLs, these regions are shown in white color.

At 1.0 V, the electrolyte concentration is ca. the initial concentration (5 M) everywhere in the electrolyte. At this operating point, the production rate of hydroxyl ions at the cathode and the consumption rate of hydroxyl ions at the anode are very small. Therefore, the concentration gradient in between both electrodes is negligible. The cell voltage decreases due to an increase in current density as portrayed by the polarization curve. Consequentially, the hydroxyl ion consumption at the anode and the hydroxyl ion production at the cathode rise with the current density, when the cell voltage decreases from the left to the right. This results in an increasing electrolyte concentration on the cathode side (becoming more red), but a decreasing electrolyte concentration on the anode side (becoming more blue).

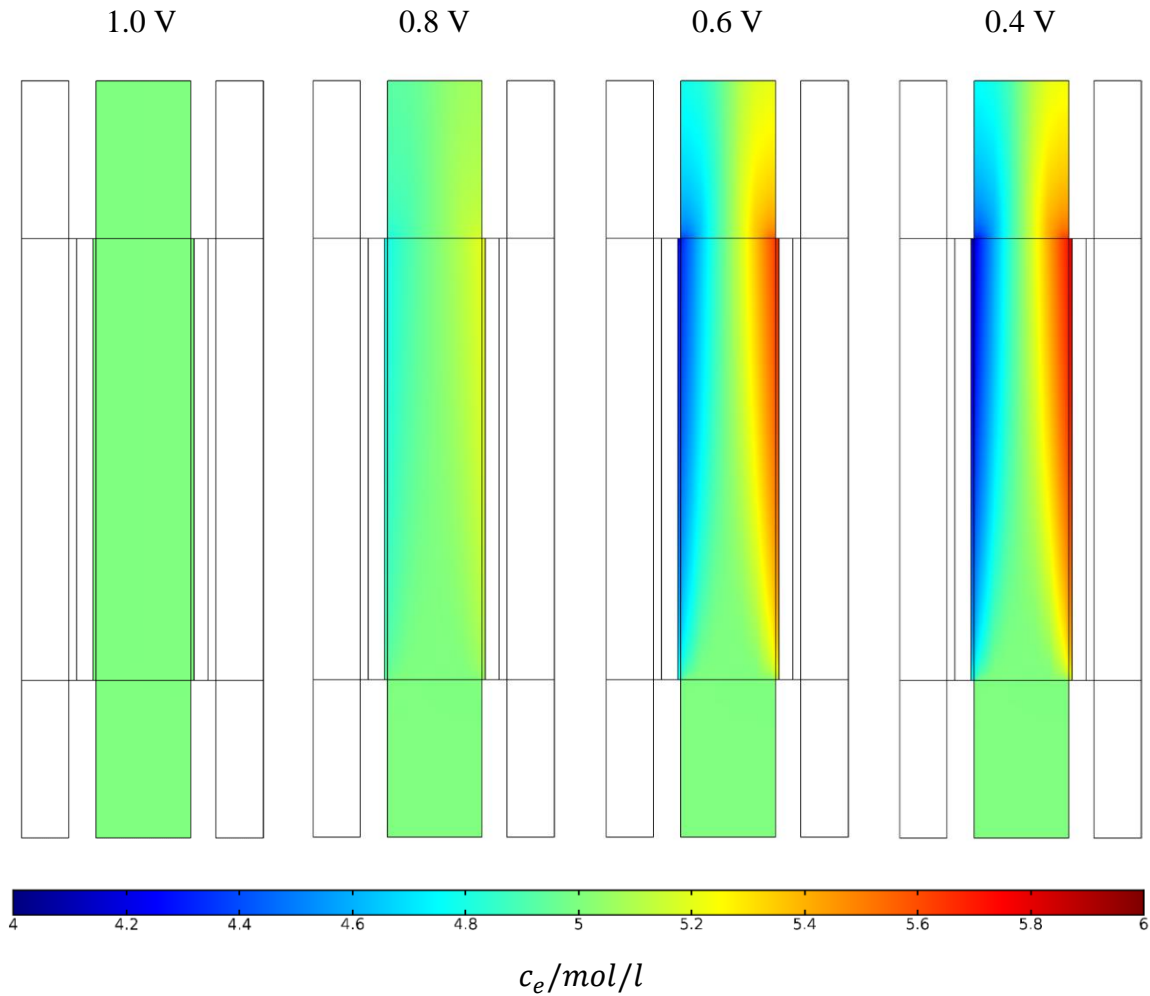


Figure 5.2: Electrolyte concentration in the cell (vertically scaled by the factor 0.1).

The electrolyte solution enters the cell from the bottom with the initial concentration and leaves the cell at the top thus the concentration gradient is the smallest at the bottom and the highest at the top of the cell. It is obvious, the faster the electrolyte solution flows, the more homogeneous the electrolyte concentration will be. For the considered electrolyte velocity a considerable gradient is created, especially at the electrolyte outlet. For example, at 0.4 V the concentration gradient is almost 2 M. If the electrolyte flow rate was lower or if the electrolyte solution was even stagnant, higher concentration gradients could be expected. Therefore, it is recommended to rise the electrolyte velocity in order to obtain a more homogeneous concentration.

5.2.2 Temperature distribution

For the cell voltages of 1.0, 0.8, 0.6, and 0.4 V, the temperature distribution in the cell is shown in Figure 5.3 from the left to the right. The lower limit blue represents 50 °C, while the upper limit red stands for 80 °C as given by the rainbow color-legend at the bottom.

At 1.0 V the electrical current is negligible, thus the initial temperature (60 °C) arises almost everywhere in the cell. With the decrease in the cell voltage, the electrical current and therefore the conversion rates of hydrogen and oxygen rise. When the conversion rates increase, the endothermic anode reaction and the exothermic cathode reaction cause the temperature to decrease on the anode side but to rise on the cathode side. With the electrical current, the irreversible heats of the reactions and the Joule heats caused by charge transport rise. As a consequence, the temperature in the cell increases. As the heat sources dominate strongly, no temperature reduction due to the endothermy of the anode reaction and the evaporation of water can be detected.

The model predicts, that the hottest region evolves on the cathode side, creating an actual hot spot in the upper region of the cell. This is a consequence of the enormous heat production on the cathode side, especially caused by the overpotential of the cathode reaction (see chapter 5.2.4), coupled with the flow directions of the gases and the electrolyte. At the gas inlets and at the electrolyte inlet, the fluids enter with the initial temperature, so that the temperature of these regions is ca. 60 °C, even for a cell voltage of 0.4 V. Flowing from the bottom to the top, the electrolyte solution is heated up due to the plurality of heat sources in the cell. In the upper region of the cell, where the electrolyte exits and the gases enter, the electrolyte is again cooled down slightly. At the same time the anode gas and the cathode gas are heated up very rapidly. When the gases continue their course along the channels, they are again cooled down by the electrolyte so that the hottest region can evolve in the upper region of the cell. As much more heat is produced on the cathode side than on the anode side, the cathode gas leaves the cell at a higher temperature than the anode gas. However, most of the heat is taken out by the electrolyte, which is due to its great thermal properties, especially the high heat capacity. Consequentially, the flowing electrolyte is an effective measure for the heat management in the cell. In order to decrease the temperature in the cell and proceed against the hot region on the cathode side, raising the electrolyte flow rate is recommended. In the real cell, increasing the electrolyte flow rate can cause the fluid being pushed through the electrodes into the gas channels which needs to be considered.

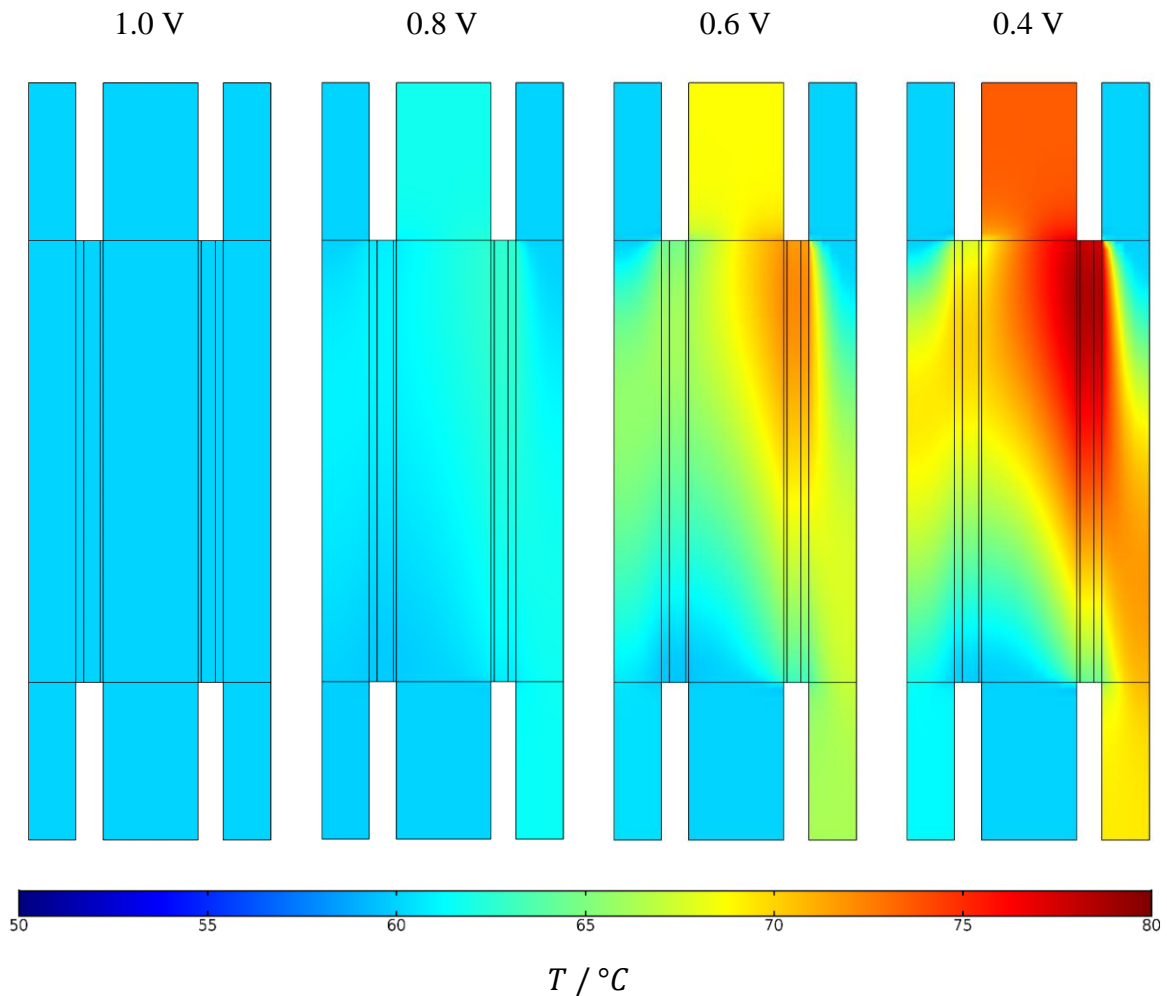


Figure 5.3: Temperature distribution in the cell (vertically scaled by the factor 0.1).

In contrast to the simulation model, the real cell can show water evaporation into the gases even if the cell is not under load. This can cause the temperature in the cell to be slightly lower than the temperature predicted by the model and can cause the cell to cool down when it is not under load. For a detailed thermal analysis, the water evaporation should be modeled more accurately. However, it is known that the electrolyte takes out most of the heat produced in the cell due to its great thermal properties. Additionally, it is reasonable, that the gases are heated up in the upper region of the cell and are cooled down in the lower region of the cell, because the electrolyte enters the cell from the bottom at initial temperature. Also, it is known, that the sluggish kinetics of the ORR causes high potential losses on the cathode side being coupled with an enormously heat production. Hence, the temperature gradients and especially the creation of a hot region in the upper half of the cell on the cathode side can be expected to be qualitatively correct.

5.2.3 Anodic and cathodic gas compositions

Figure 5.4 shows the relative hydrogen mole fraction ($x_{H_2}/x_{H_2}^{in}$) on the left side of the cell and the relative oxygen mole fraction ($x_{O_2}/x_{O_2}^{in}$) on the right side of the cell at 1.0, 0.8, 0.6, and 0.4 V from the left to the right; the relative mole fraction is the local mole fraction related to the initial mole fraction. The rainbow color-legend below the four pictures indicates that the lower limit blue and the upper limit red stand for 75 and 100 %, respectively. As no gas phase is present in the electrolyte channel, it appears in white color.

In the model, the consumption rate of hydrogen in the anodic CL, the consumption rate of oxygen in the cathodic CL, as well as the evaporation rates of water in the anodic and cathodic CLs equal zero when the electrochemical reaction rates do. This is due to the assumptions that the electrochemical reaction rates of hydrogen and oxygen equal the solution rates in the electrolyte (main assumption iv) and that only electrochemically produced water evaporates into the gases (main assumption v). Consequentially, at 1.0 V, the consumption of hydrogen and oxygen, as well as the evaporation of water into the gases are so low, that no noticeable changes in the gas phase concentrations arise along the anodic and cathodic gas channels.

As hydrogen is consumed from the anode gas and oxygen is consumed from the cathode gas, while water enters both the anode gas and the cathode gas, the hydrogen mole fraction in the anode gas and the oxygen mole fraction in the cathode gas, respectively, are reduced with increasing current density. However, the gases enter the cell with relatively high velocities so that only a small decrease in hydrogen and oxygen mole fractions can be expected. As pure hydrogen enters the cell on the anode side, no change in the hydrogen mole fraction can be detected along the channel, not even at 0.4 V. In contrast, air enters the cell on the cathode side, consisting of only 21 % oxygen. Therefore, the impact of the oxygen consumption on the cathode gas composition is much stronger than the influence of the hydrogen consumption on the anode gas composition. With rising current density, the mole fraction gradient along the channel and the mole fraction gradient through the electrode becomes more and more visible.

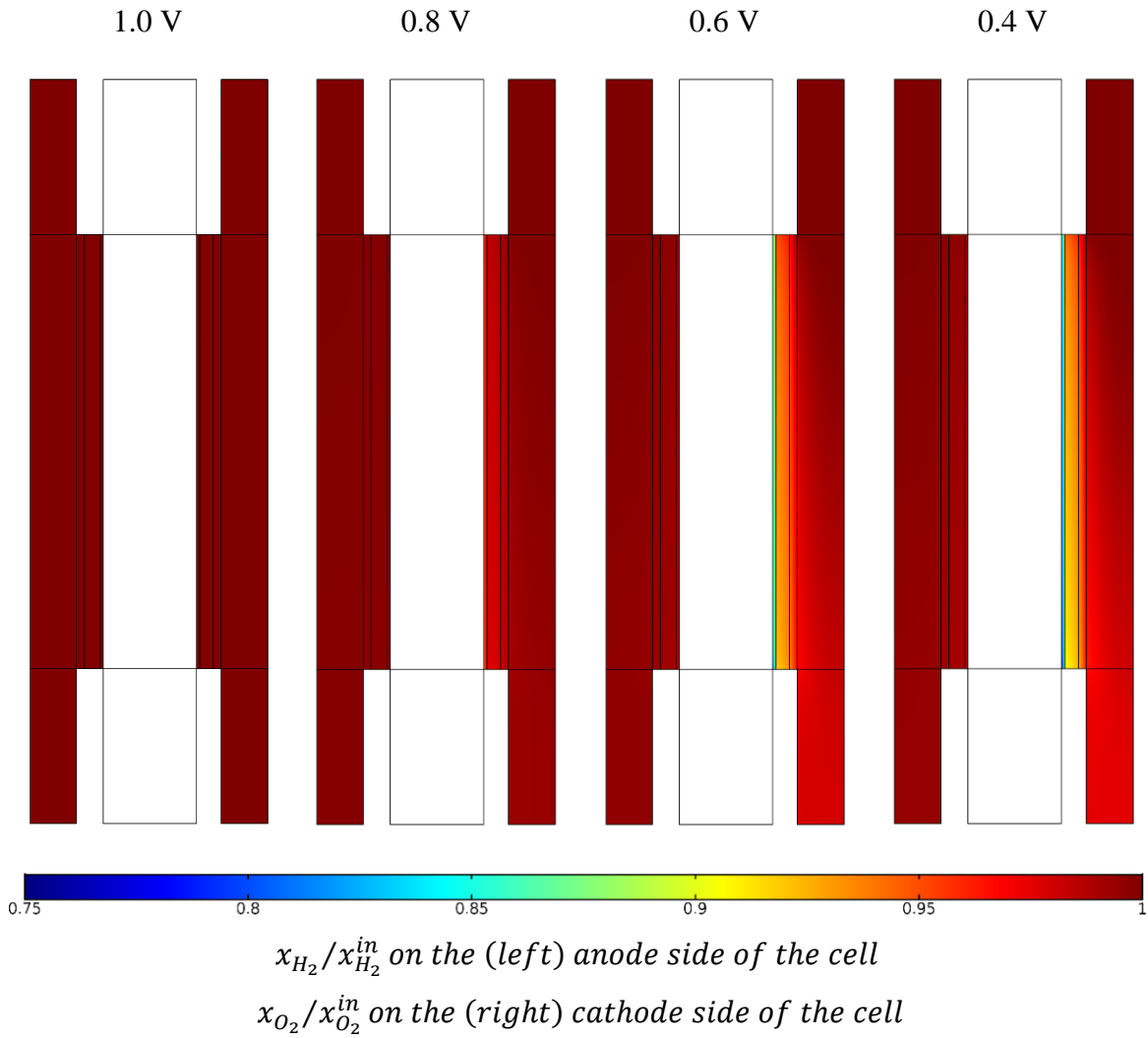


Figure 5.4: Hydrogen and oxygen mole fractions (vertically scaled by the factor 0.1).

The base case velocities have been chosen relatively high in order to ensure that neither the anodic nor the cathodic feed becomes limiting during the parameter studies in chapter 5.4. For lower gas velocities, higher mole fraction gradients can be expected, especially along the channels. In case of the real cell water evaporates into the gases rather dependent on the partial pressure of water in the gas phase than dependent on the electrical current density as it is the case in the model. Therefore, in case of the real cell the evaporation of water into the gases can be higher causing also larger gradients in the gas phase. This deviation of the model from the real cell can particularly be expected in the region of low current densities. Hence, it is possible, that adjustments become necessary when comparing the simulation results at lower gas velocities or with more accurate water evaporation rates. However, the prediction of decreasing reactant mole fraction gradients along the channels and in the direction perpendicular to the active cell surface area is qualitatively correct.

5.2.4 Analysis of the potential losses

Calculated with the Nernst equation, the reversible cell voltage is ca. 1.16 V for the considered conditions (calculated with liquid phase concentrations, 60 °C, 5 M, hydrogen partial pressure above the solution 1 atm, oxygen partial pressure above the solution 0.21 atm). The departure of the cell voltage from the reversible cell voltage (E_0) is illustrated in Figure 5.5 as the cumulation of the potentials losses in the anode (η_A^S), the overpotential of the anode reaction (η_A), the potential losses in the electrolyte (η_E^l), the overpotential of the cathode reaction (η_C), and the potential losses in the cathode (η_C^S)⁷.

The overpotentials η_A and η_C belong to the kinetic expressions for the anode reaction (equation (4.22)) and the cathode reaction (equation (4.23)), respectively. Therefore, they comprise the activation overpotential (η_{Act}) as well as the concentration overpotential (η_{Conc}). This relationship becomes obvious when neglecting the backward reaction so that the overpotential η_j of reaction j can be written as

$$|\eta_j| = \underbrace{\frac{RT}{\alpha_f^j F} \ln \left(\frac{|i|}{i_0^j} \right)}_{|\eta_j^{Act}|} - \underbrace{\frac{RT}{\alpha_f^j F} \ln \left(\prod_h \left(\frac{c_h}{c_h^0} \right)^{\vartheta_h} \right)}_{|\eta_j^{Conc}|}, \quad (5.1)$$

where the index j stands for the electrode reaction (anode or cathode), the index f stands for the forward reaction (oxidation when the electrode is an anode; reduction when the electrode is a cathode), and the index h stands for the reactants of the forward reaction.

It can be seen, that η_C is almost solely responsible for the activation losses observable in the polarization curve of the cell. The reason is given by the sluggish kinetics of the ORR, which can be seen at the exchange current density of the cathode reaction (cathode exchange current density) being several orders of magnitude smaller than the exchange current density of the anode reaction (anode exchange current density). Consequentially, the activation losses of the much faster anode reaction are negligibly small.

⁷ The individual potential losses shown in Figure 5.5 are obtained by integral measurements. η_A and η_C are measured in the anodic CL and in the cathodic CL, respectively. The other potential losses are calculated as potential differences between two boundaries. Hence, η_A^S is the potential difference between the anodic current collector and the boundary between the anodic CL and the electrolyte channel. Analogously, η_C^S is the potential difference between the cathodic current collector and the boundary between the cathodic CL and the electrolyte channel. The liquid phase potentials measured at the boundaries between the CLs and the electrolyte channel are used for the calculation of η_E^l .

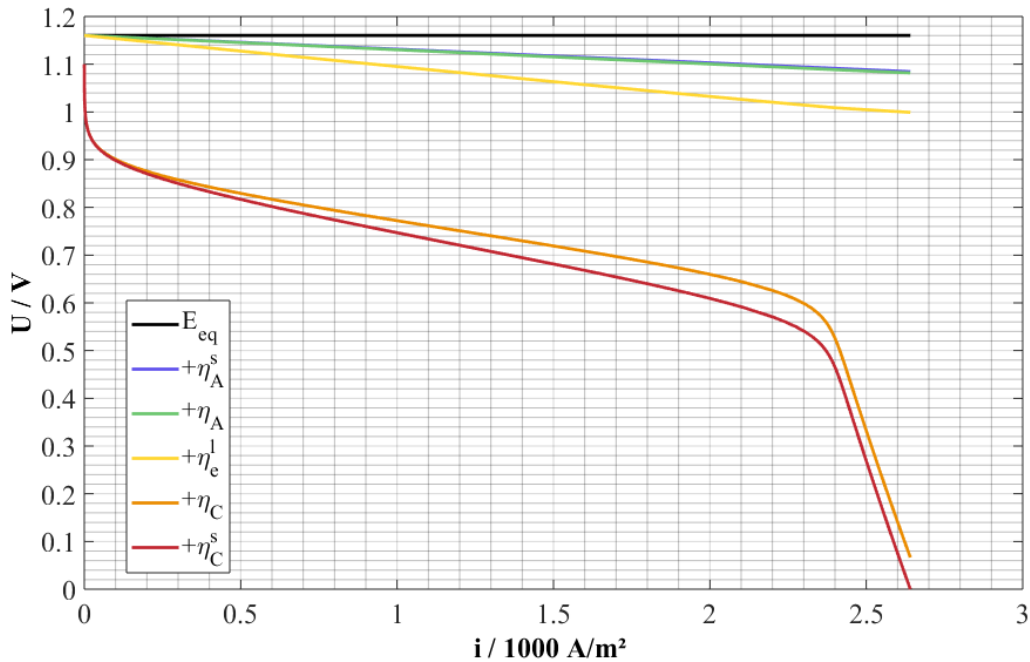


Figure 5.5: Effects of the potential losses on the polarization curve (cumulative).

As can be expected based on Ohm's law, the potential losses in the electrodes rise linearly with the current density. The potential losses in the anode are slightly higher than the potential losses in the cathode, which is due to the anode being a little bit thicker than the cathode. Also, the potential losses in the electrolyte show a linear dependence on the current density. Typically, the electrolyte can be made responsible for the ohmic losses of a fuel cell. In case of the considered cell, η_E^l is also larger than η_A^s and η_C^s , but the difference is very small. The reason is especially given by the electrical conductivity of the GDLs which are assumed to be very low, among other things, in order to account for contact resistances. An overestimation of the potential losses in the electrodes is conceivable, for example the high ohmic losses could also occur outside the cell in the external circuit. In order to verify the shares of the electrodes and the electrolyte in the cell resistance, more information about the real cell is needed which can require adjustments of the model. However, as described in chapter 5.1 the model predicts the overall performance of the cell qualitatively correct.

Besides the activation region, the mass transport region is solely determined by η_C . Liquid phase diffusion is much slower than gas phase diffusion, which can be seen at the diffusion coefficient being generally several orders of magnitude smaller. Therefore, it seems reasonable that the mass transport losses are caused in the liquid phase. As water and hydroxyl ions are sufficiently available (for the considered operating conditions), either the

transport of hydrogen or the transport of oxygen can become the limiting factor. Because the mass transport losses occur in η_C but not in η_A , the transport of oxygen through the electrolyte film can be identified causing the mass transport losses. For the overall reaction to arise, the amount of oxygen that must be brought to the cathodic catalyst is only half of the amount of hydrogen that must be brought to the anodic catalyst. Therefore, one could expect that the transport of hydrogen is decisive. The reason why it is the transport of oxygen but not the transport of hydrogen that becomes the limiting factor can be found in the gas phase concentration, the solubility, and the liquid phase diffusion.

The Henry constants of hydrogen ($H_{H_2}^e$) and oxygen ($H_{O_2}^e$) for the solubility in the KOH electrolyte are illustrated in Figure 5.6 and in Figure 5.7, respectively. They are plotted against the electrolyte concentration from 3 to 7 M KOH and against the temperature from 40 to 80 °C. In order to highlight the dependence of the Henry constants on electrolyte concentration and temperature, isolines are drawn in black color every 1 M and every 10 °C. An increase in electrolyte concentration causes both Henry constants to decrease exponentially. The dependence on temperature is not that obvious. Following a line of constant electrolyte concentration, $H_{H_2}^e$ shows a low point while $H_{O_2}^e$ seems to decrease exponentially with temperature. This is due to the influence of the Henry constant for the solubility in water (H_i^w), which is used for the calculation of H_i^e . The Henry constant $H_{H_2}^w$ shows a minimum for hydrogen at ca. 50 °C and the Henry constant $H_{O_2}^w$ shows a minimum for oxygen at ca. 90 °C [91]. Consequentially, at higher temperatures $H_{O_2}^e$ increases again.

Both Henry constants, $H_{O_2}^e$ and $H_{H_2}^e$, equal one another with respect to the order of magnitude. Hence, if the oxygen partial pressure above the electrolyte solution in the cathodic CL was the same as the hydrogen partial pressure above the electrolyte in the anodic CL, almost the same concentrations would arise in the electrolyte solution. However, the mole fraction of oxygen in the cathode gas is much smaller than the mole fraction of hydrogen in the anode gas, caused by air entering the cell on the cathode side, while pure hydrogen enters the cell on the anode side. As a result, the oxygen concentration in the electrolyte becomes much smaller than the hydrogen concentration. When the oxygen concentration at the gas/liquid interface is decreased, also the oxygen concentration at the catalyst surface is affected, thus it can directly raise mass transport losses. When the electrolyte concentration rises on the cathode side with the current density, the solubility of oxygen in the KOH electrolyte solution decreases which reduces the oxygen concentration

in the electrolyte additionally. At the same time, the consumption of hydroxyl ions at the anode has a positive effect on the hydrogen solubility when the electrolyte concentration decreases with rising current density. As a consequence, the oxygen transport is much more influential than the hydrogen transport, even though only half as much oxygen must be brought to the cathodic catalyst than hydrogen must be brought to the anodic catalyst.

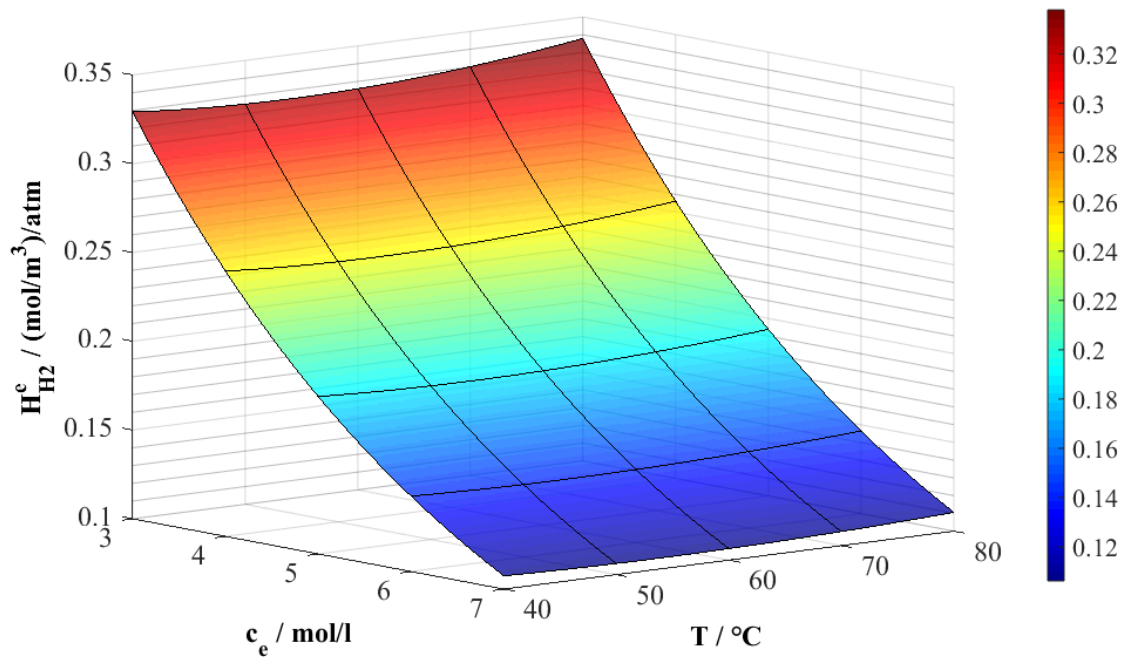


Figure 5.6: Henry constant for the solubility of hydrogen in KOH.

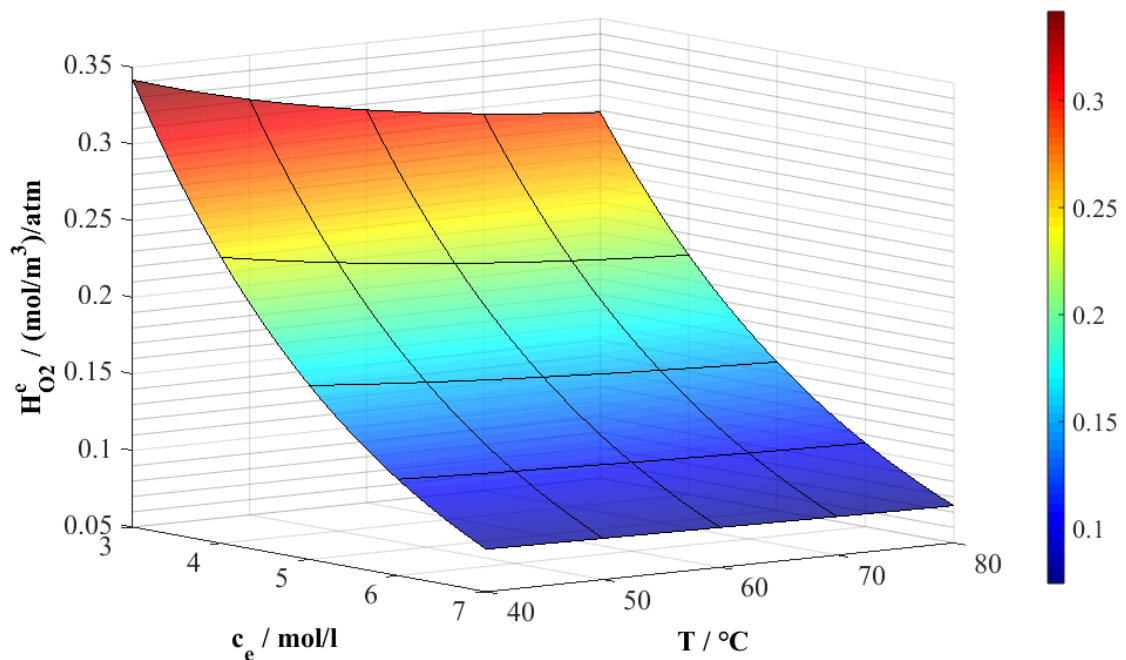


Figure 5.7: Henry constant for the solubility of oxygen in KOH.

In addition to the solubility, the transport of oxygen through the electrolyte film is worse than the transport of hydrogen. That is evident from the difference between the diffusion coefficients of hydrogen ($D_{H_2}^e$) and oxygen ($D_{O_2}^e$), which are shown in Figure 5.8 and in Figure 5.9, respectively. In analogy with the Henry constants, the diffusion coefficients are plotted against the electrolyte concentration from 3 to 7 M KOH and against the temperature from 40 to 80 °C, whereby isolines are drawn in black color every 1 M and every 10 °C. Due to oxygen transport being slower than hydrogen transport, $D_{O_2}^e$ is less than half of $D_{H_2}^e$. As a result, the oxygen concentration gradient must be larger than the hydrogen concentration gradient which causes the concentration of oxygen at the cathodic catalyst to be much smaller than the hydrogen concentration at the anodic catalyst. The decrease of the diffusion coefficient in the KOH electrolyte solution with rising electrolyte concentration even causes the oxygen transport to become worse when the electrolyte concentration increases on the cathode side with the current density; the hydrogen transport becomes better at the same time as the electrolyte concentration decreases on the anode side with increasing current density.

The transport of oxygen through the electrolyte solution can therefore clearly be identified, being responsible for the mass transport losses arising in the polarization curve of the cell. The low oxygen concentration in the cathode gas and the increase in the electrolyte concentration on the cathode side with current density intensify this effect.

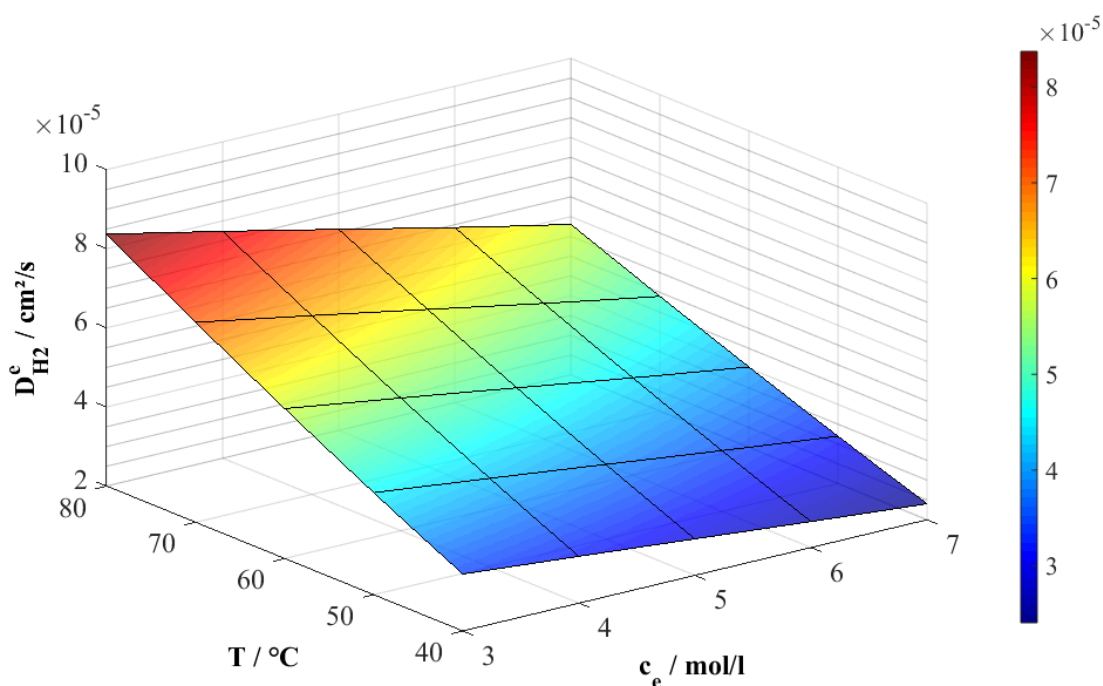


Figure 5.8: Diffusion coefficient of hydrogen in the KOH electrolyte.

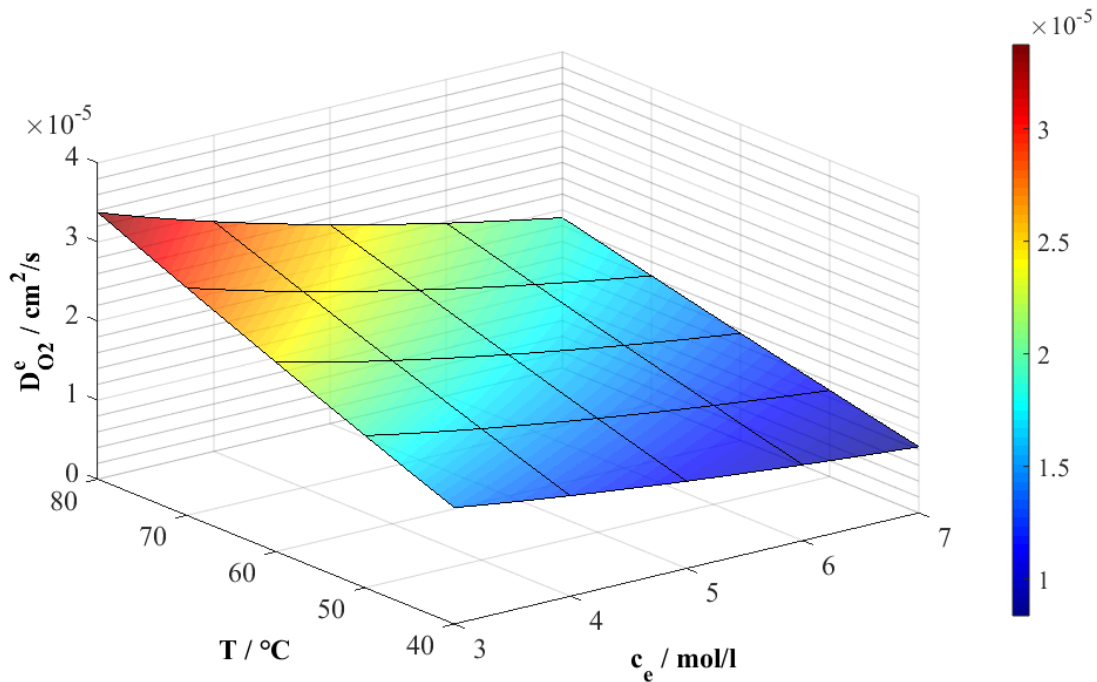


Figure 5.9: Diffusion coefficient of oxygen in the KOH electrolyte.

Hence, the cathode performance is decisive for the overall performance of the AFC. The sluggish kinetics of the ORR determine the activation losses and the slow oxygen transport through the electrolyte film and to the catalyst defines the limiting current density. At the same time the performance of the anode is negligible. The optimization of the cathode is therefore the key for improving the overall cell performance.

5.3 Interim conclusion

The comparison of the simulation results with measurements has shown great agreements. The model does not take into consideration the actual reaction mechanisms. Nevertheless, the difference between the polarization curve predicted by the model and the polarization curve measured at the real cell by AFC Energy has been determined to be negligible in the activation region. With respect to the ohmic region, no disagreement has been detected. As the real cell had not been operated up to high current densities where mass transport becomes limiting, the mass transport region could not be compared with measurements. However, the model has predicted the limiting current density to be ca. 265 mA/cm² due to oxygen transport, whereas it has been shown that this limitation is reasonable basically because the oxygen transport through the electrolyte is much slower than the hydrogen transport. It is recommended to derive the limiting current density from measurements in the future and adjust the parameters specific to the oxygen transport through the electrolyte film if necessary.

The simulation results have shown that the electrolyte concentration decreases on the anode side, while it increases on the cathode side with rising current density. The consumption of hydroxyl ions in the anode reaction and the production of hydroxyl ions in the cathode reaction have been made responsible. An increase in the electrolyte velocity is recommended for obtaining a more homogeneous electrolyte concentration. The resulting reduction of the electrolyte concentration in the cathodic CL can enhance the oxygen solubility and therefore decrease the mass transport losses. This can enable higher current densities which can make the AFC more attractive for conventional applications.

With respect to temperature, an increase in the upper half of the cell has been observed; an actual hot region on the cathode side has been created. It has been noticed that this is the result of the enormous heat production on the cathode side, coupled with the flow directions of the fluids. Also, an increase in the electrolyte flow rate is suggested for reducing the temperature in the hot region and creating a more homogeneous temperature in the cell.

As a result of the relative high gas velocities, only small hydrogen mole fraction gradients in the anode gas and small oxygen mole fraction gradients in the cathode gas have been found. Because the mole fraction of oxygen in the cathode gas (21 %) is less than the mole fraction of hydrogen in the anode gas (100 %), the impact of the oxygen consumption on the cathode gas composition has been higher than the impact of the hydrogen consumption on the anode gas composition.

The cathode has been verified to be responsible for the activation and the mass transport losses occurring in the polarization curve of the cell. Optimizing the cathode performance is therefore the key for enhancing the overall performance of the AFC.

Due to the lack of available data various assumptions needed to be made in the model. For an adequate validation, the properties and structure parameters of the electrodes should be determined in the future. This will enable the verification of the high potential losses predicted to occur in the electrodes. Also, it is recommended to measure the polarization curves under a variety of operating conditions. With these curves, the influence of the operating parameters can be verified.

5.4 Parameter study

The simulation model has been used for some parameter studies with the intention of finding optimal operating conditions and potentials for improvement which are presented in this chapter. The base case scenario is defined at the beginning of chapter 5 and is studied in chapter 5.1 and in chapter 5.2. It must be emphasized, that some of the mathematical approximations given in chapter 4.11 can be used outside of their validity range, assuming an adequate extrapolation.

5.4.1 Electrolyte concentration

In order to study the effect of the KOH electrolyte concentration on the cell performance, it has been varied from 1 to 9 M with an increment of 2 M. The polarization curves created by the model are shown in Figure 5.10.

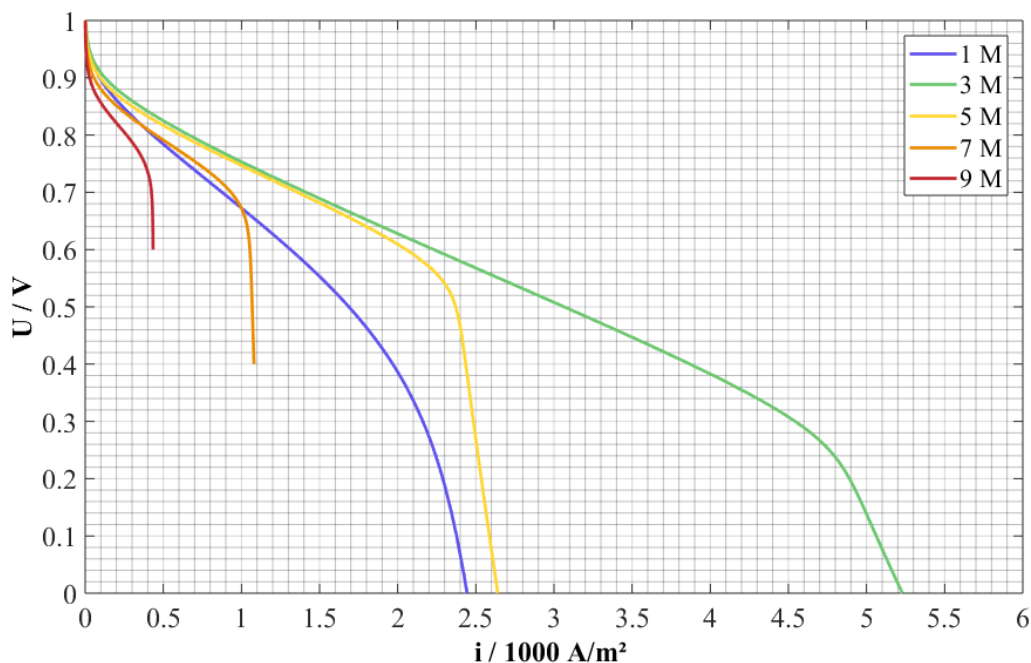


Figure 5.10: Variation of the electrolyte concentration.

The model predicts a strong dependence of the cell performance from the electrolyte concentration. However, in the activation region only small differences between the curves can be noticed. Focusing the ohmic region and the mass transport region, it is immediately apparent that the 3 M solution performs the best while the 9 M solution performs the worst. In the ohmic region, the 1 M solution and the 5 M solution show almost the same slopes as the 9 M solution and the 3 M solution, respectively, while the slope of the 7 M solution is in

the midfield. With respect to the mass transport losses, the highest limiting current density is predicted for the 3 M solution. For higher concentrations and for lower concentrations, the limiting current density decreases enormously with increasing and decreasing electrolyte concentration, respectively. Although the slope of the 1 M solution is much worse than the slope of the 5 M solution almost the same limiting current density can be obtained.

With rising electrolyte concentration, the solubility of hydrogen and oxygen is reduced. This becomes visible by the Henry constants of hydrogen ($H_{H_2}^e$) and oxygen ($H_{O_2}^e$) which are plotted against the KOH electrolyte concentration in Figure 5.11 and Figure 5.12, respectively. When the Henry constants decrease exponentially with rising electrolyte concentration, the concentrations of hydrogen and oxygen in the electrolyte solution do the same. As a result the equilibrium potential, which is calculated with the liquid phase concentrations of hydrogen and oxygen, decreases with rising electrolyte concentration as shown in Figure 5.13 for the case that the hydrogen pressure above the electrolyte in the anodic CL is 1 atm and the oxygen pressure above the electrolyte in the cathodic CL is 0.21 atm. As a consequence, the polarization curve is shifted downwards with rising electrolyte concentration, which can primarily be observed in the activation region. It must be emphasized that the electrolyte concentration by itself has no effect on the reversible cell potential as it vanishes in the Nernst equation of the cell. Therefore, if hydrogen and oxygen directly reacted from the gas phase, the equilibrium potentials were calculated with the gas phase concentrations but not with the liquid phase concentrations and the reversible cell voltage would not decrease at all.

The electrical conductivity of the KOH electrolyte shows an optimum at a certain electrolyte concentration (c_e^k) as illustrated in Figure 5.14, where the electrical conductivity is plotted against the temperature from 0 to 100 °C and against the electrolyte concentration from 0 to 14 M; every 10 °C and every 1 M isolines are shown in black color. At 60 °C this optimum is at ca. 7.5 M and moves slightly towards higher concentrations with rising temperature. Hence, if the electrolyte conductivity was the only parameter being dependent on the electrolyte concentration, the 7 M concentration should perform the best of all considered electrolyte concentrations. Based on the electrical conductivity the potential losses in the 1, 3, 5, 7, and 9 M solutions can be estimated to be 90.49, 38.90, 29.95, 27.55, and 27.97 mV per 100 mA/cm² at 60 °C. These quantities directly explain the strong negative slope of the 1 M solution and the small difference in the slopes of the other solutions.

The mass transport region is affected the most by the electrolyte concentration. As long as the electrolyte concentration is high enough and does not become the limiting factor, it is the transport of oxygen through the electrolyte film that causes the mass transport losses (see chapter 5.2.4). In addition to the solubility in the KOH electrolyte, the mass transport through the electrolyte solution gets worse with the increase in electrolyte concentration, as illustrated by the diffusion coefficients of hydrogen ($D_{H_2}^e$) and oxygen ($D_{O_2}^e$) which are plotted against the electrolyte concentration in Figure 5.15 and in Figure 5.16, respectively. Also, close ups of the diffusion coefficients in the range from 3 to 9 M are shown in both figures. With an increase in the electrolyte concentration, the transport of hydrogen and oxygen in the KOH electrolyte solution is decelerated thus the diffusion coefficients decrease. Focusing oxygen, as it is responsible for the mass transport losses, for example at 9 M the diffusion coefficient is less than the half of the diffusion coefficient at 3 M. Consequentially, the concentration gradient must be more than the double for the same oxygen flux. This is reflected in high concentration losses. As a result, the limiting current density decreases with rising electrolyte concentration which also affects the ohmic region slightly. The increase of hydroxyl ions at the cathode with the current density even strengthens this effect. The reason for the 1 M solution performing worse, although the diffusion coefficients rise exponentially with decreasing electrolyte concentration below 3 M, is given in the transport of ions. In case of the 1 M solution, the consumption of hydroxyl ions at the anode causes the electrolyte concentration to drop locally near zero and the ion transport to become the limiting factor.

The simulation results presented in this work agree with simulation results from literature. Jo and Yi [63] compared the polarization curves of 1, 4, 7, and 10 M KOH solutions at 80 °C and predicted the best performance for the 3.5 M solution. In analogy with the simulation results presented in this work, in their study the 4 M solution showed the highest limiting current density, followed by the 1 M solution. The limiting current density of the 7 M solution was worse than the one of the 1 M solution and better than the one of the 10 M solution. Also, Zhou [66] compared the polarization curves of 1, 4, 7, 11 M KOH solutions at 80 °C. In his studies also the 4 M solution performed the best while the solution with the highest concentration (11 M) performed the worst. In contrast to the simulation results by Jo and Yi, the performance of the 7 M solution was better than the performance of the 1 M solution. Additionally, the simulation results presented in this work agree qualitatively with the experimental results presented by Brushett et al. [113] for 1, 3, 5, 7, and 9 M KOH

solutions at room temperature. The authors also concluded 3 M to be the optimum electrolyte concentration. It can be concluded that the model presented in this work agrees with simulation results predicted in previous studies with respect to the impact to the electrolyte concentration on the cell performance.

An impressive impact of the electrolyte concentration on the fuel cell performance has been found. Although the electrical conductivity of the KOH electrolyte shows an optimum at a certain concentration c_e^k , the overall performance of the cell can be the best at an electrolyte concentration which differs from that. The decreasing solubility and the decelerated transport of hydrogen and especially oxygen can cause the overall performance to become worse with rising electrolyte concentration. Therefore, an electrolyte concentration which is smaller than c_e^k can perform better. Consequentially, as long as the transport of ions does not become the limiting factor, reducing the electrolyte concentration can raise the limiting current density and therefore improve the cell performance. In particular for the cell and the base case operating conditions which have been studied in this work, 3 M has been found to be the optimum electrolyte concentration. Up to ca. 1500 A/m² the difference between the 3 M and the base case concentration (5 M) might be negligible, but in order to reach much higher power densities, reducing the electrolyte concentration might become necessary.

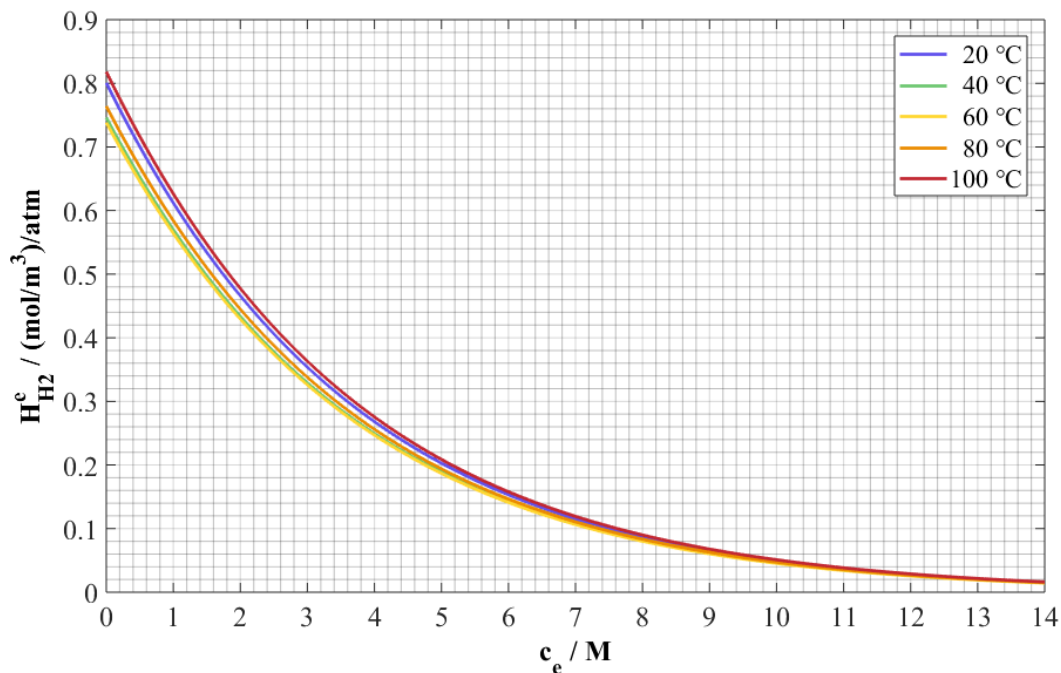


Figure 5.11: Henry constant for the solubility of hydrogen in KOH vs. c_e .

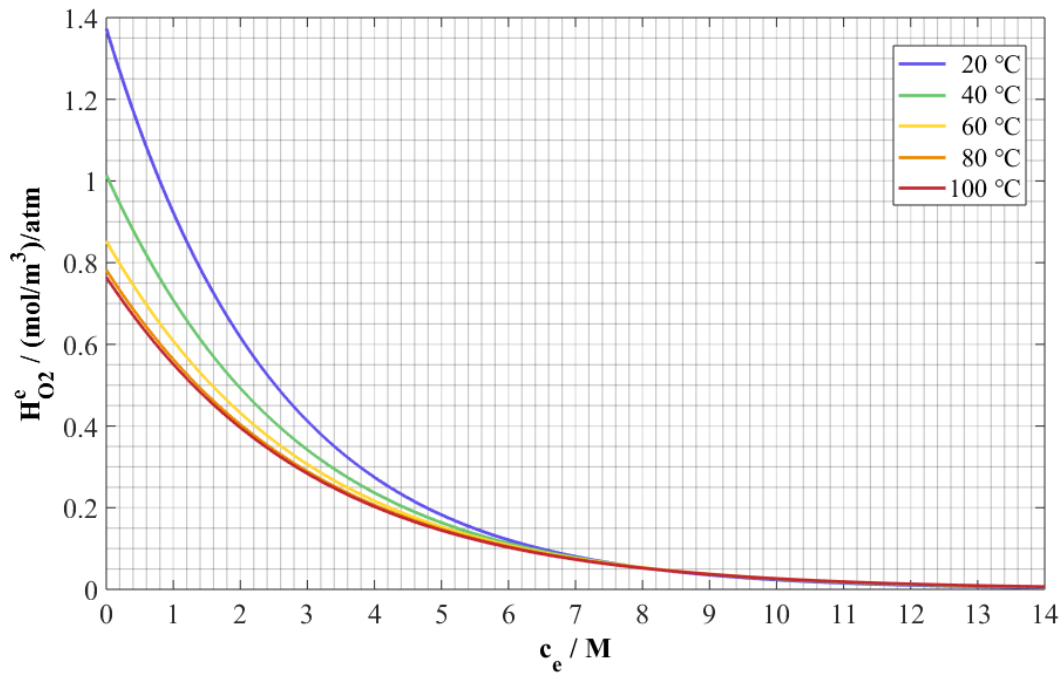


Figure 5.12: Henry constant for the solubility of oxygen in KOH vs. c_e .

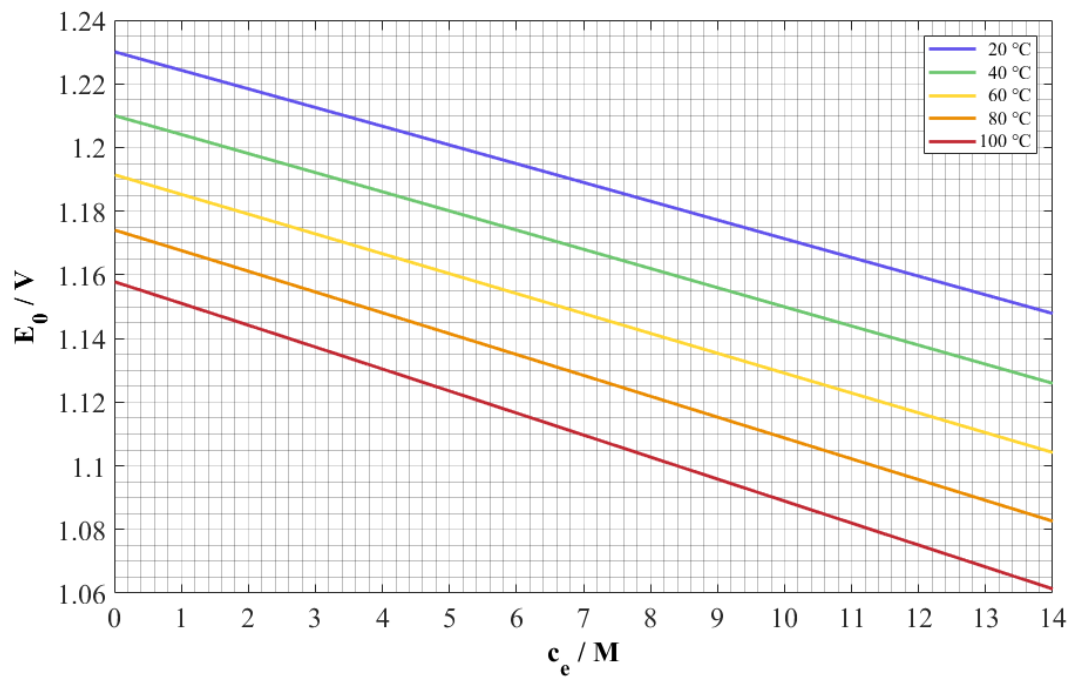


Figure 5.13: Equilibrium potential calculated with the Nernst equation.

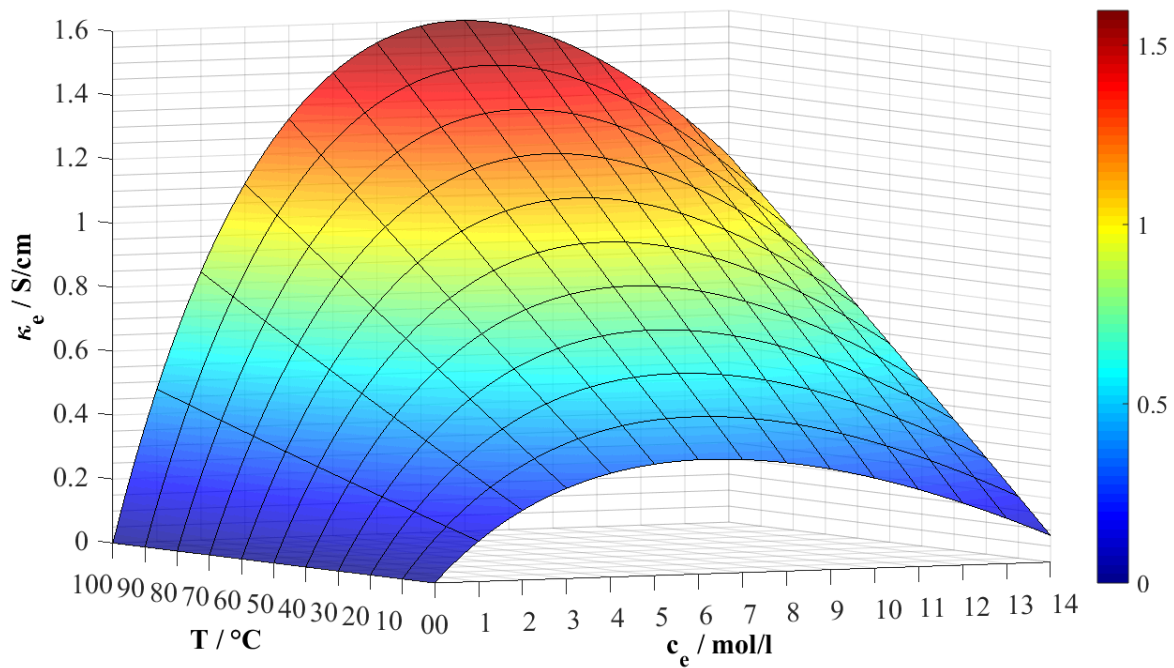


Figure 5.14: Electrical conductivity of the KOH electrolyte.

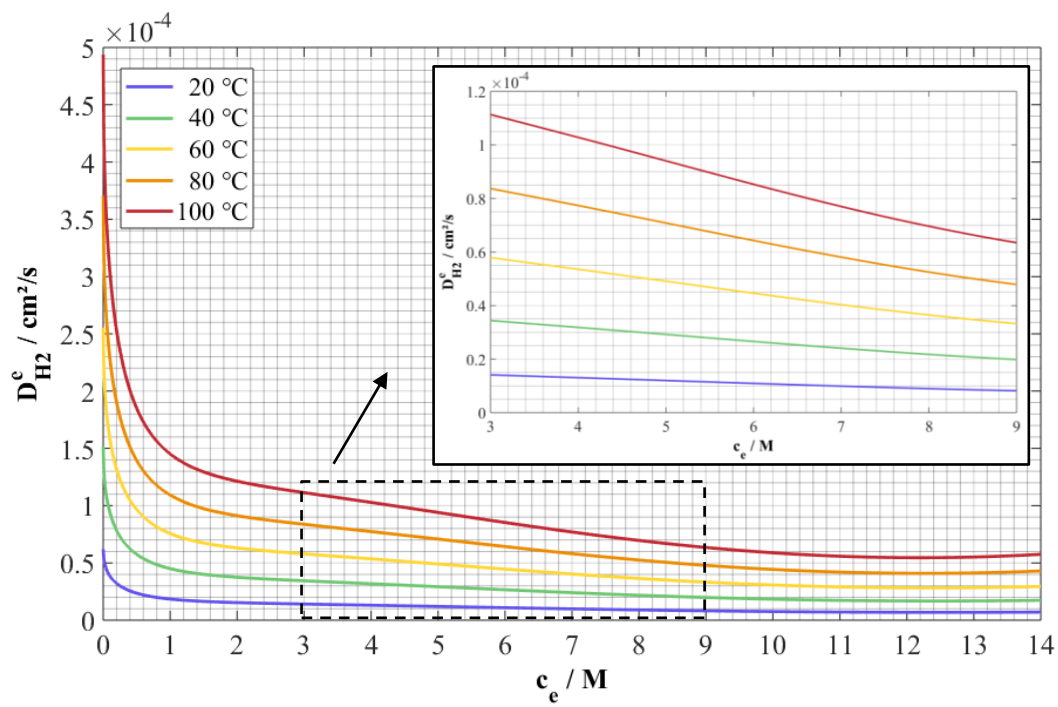


Figure 5.15: Diffusion coefficient of hydrogen in KOH vs. c_e .

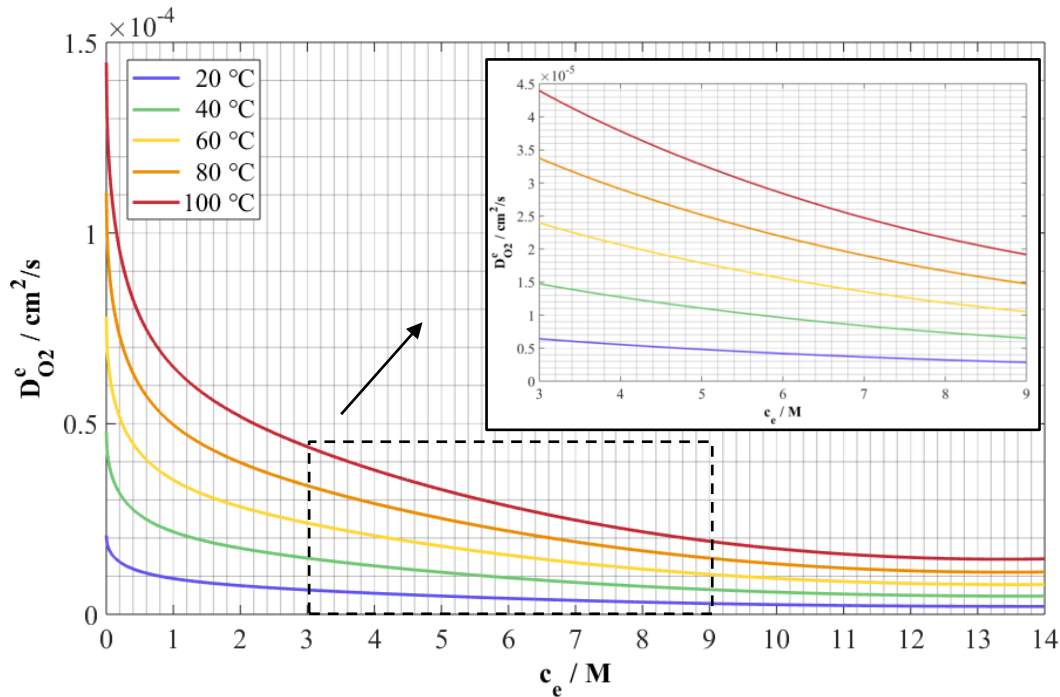


Figure 5.16: Diffusion coefficient of oxygen in KOH vs. c_e .

5.4.2 Operating pressure

For studying the impact of the operating pressure on the polarization curve, the pressure at the outlets of the gas channels and at the outlet of the electrolyte channel has been increased from 1 to 5 atm with an increment of 1 atm; the simulation results are shown in Figure 5.17.

Raising the pressure shifts the polarization curve upwards and causes an increase in the limiting current density. The former can be explained with the increase in the equilibrium potential according to the Nernst equation. The latter, the increase in the limiting current density, is due to the enhanced gas solubility. In the field of the process technology it is known, that the liquid phase concentration of a species can generally be raised by increasing the pressure and reducing the temperature. According to Henry's law, doubling the gas pressure, doubles the liquid phase concentration. This rises the liquid phase concentration at the catalyst surface in the next step and increases the limiting current density.

Kimble and White [54] as well as Zhou [66] used their models to predict the cell performance at 1, 4.1, and 10 atm, whereas both considered a 7 M KOH electrolyte at 80 °C. Also at 7 M and 80 °C, Jo and Yi studied the cell performance at 1, 4.1, 7, and 10 atm. In analogy with the results presented in this work, all three models predicted that a rise in pressure causes the polarization curve to be shifted upwards and the limiting current density to be enhanced.

As a result, the model has predicted the higher the pressure, the better the cell performance. However, it needs to be noticed that the gas/liquid interface is very sensitive with respect to pressure. In the real cell, rising the pressure uncarefully and unsteadily can cause the gas on the one side being pushed through the electrolyte to the other side. Additionally, the electrolyte itself could be pressed through the electrodes. All three scenarios must be taken into consideration when raising the pressure in the cell and must absolutely be prevented.

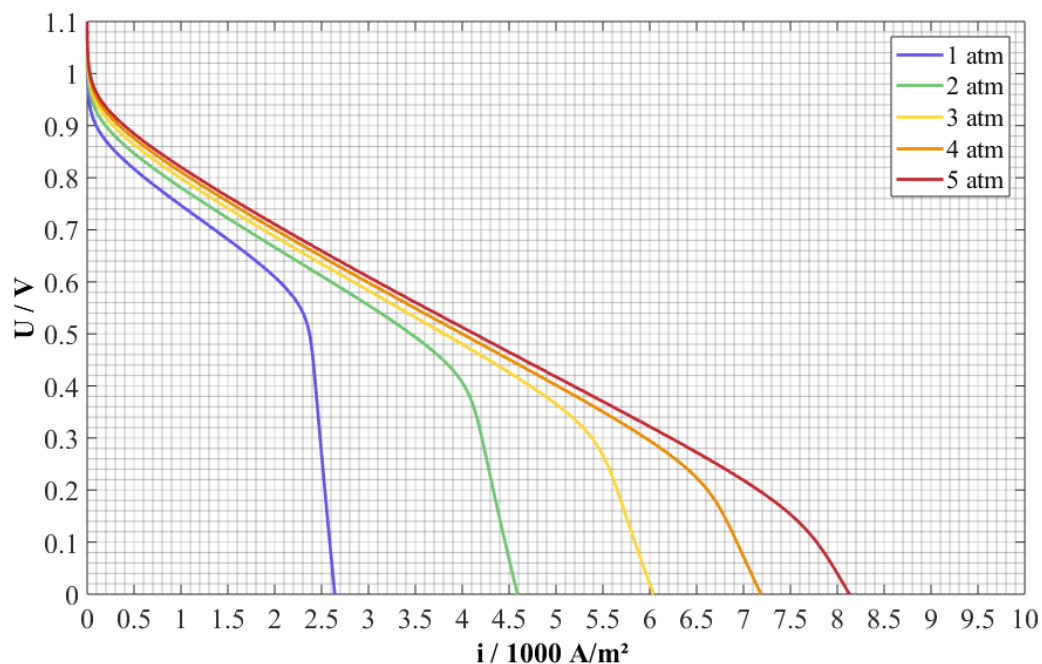


Figure 5.17: Effect of the operating pressure on the polarization curve.

5.4.3 Operating temperature

In order to investigate the influence of the operating temperature on the cell performance, the inlet temperatures of the gases and the electrolyte solution have been collectively raised from 20 to 80 °C with an increment of 20 °C. Based on the results, illustrated in Figure 5.18, an improvement of the cell performance with the rise in temperature is forecasted. While the activation region is negligibly affected, the ohmic region and the mass transport region are enormously enhanced with the rise in temperature.

From a thermodynamic point of view, the cell voltage tends to decrease with rising temperature, as the reversible cell voltage decreases (see equations (4.20) and (4.21)). This decrease cannot be observed as kinetics enhances with rising temperature. This appears as exponential rises of the exchange current densities shown in Figure 5.19. At 80 °C the

exchange current density of the cathode reaction, determining the activation losses of the cell, is ca. 27 times larger than at 20 °C. This enormous increase reduces the activation losses greatly. In addition to the exchange current density, the transfer coefficients of the forward reactions are assumed to increase linearly with temperature causing an additional improvement of the cell performance (see also chapter 5.4.4 for a more detailed consideration of the temperature dependence of the kinetic parameters). The consequence of the two counteracting phenomena, the decreasing reversible cell voltage on the one hand and the improving kinetics on the other hand, is that no effect of the temperature on the cell voltage can be detected in the activation region. If kinetics enhanced much more with rising temperature, also an improvement in the activation region would be observable. This could be the case for other catalyst materials with larger temperature coefficients.

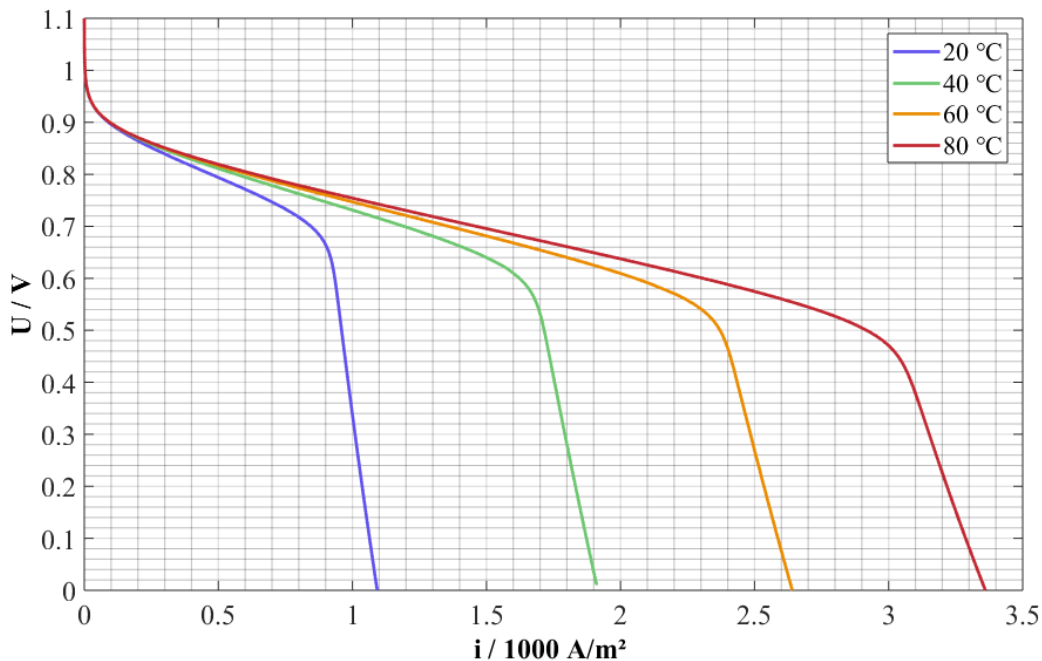


Figure 5.18: Effect of the temperature on the polarization curve.

In the ohmic region, the cell performance rises as the electrical conductivity of the KOH electrolyte solution increases with temperature (see Figure 5.14). When the temperature is raised from 20 to 80 °C, the electrical conductivity of the 5 M KOH electrolyte solution more than doubles, which halves the ohmic losses in the electrolyte.

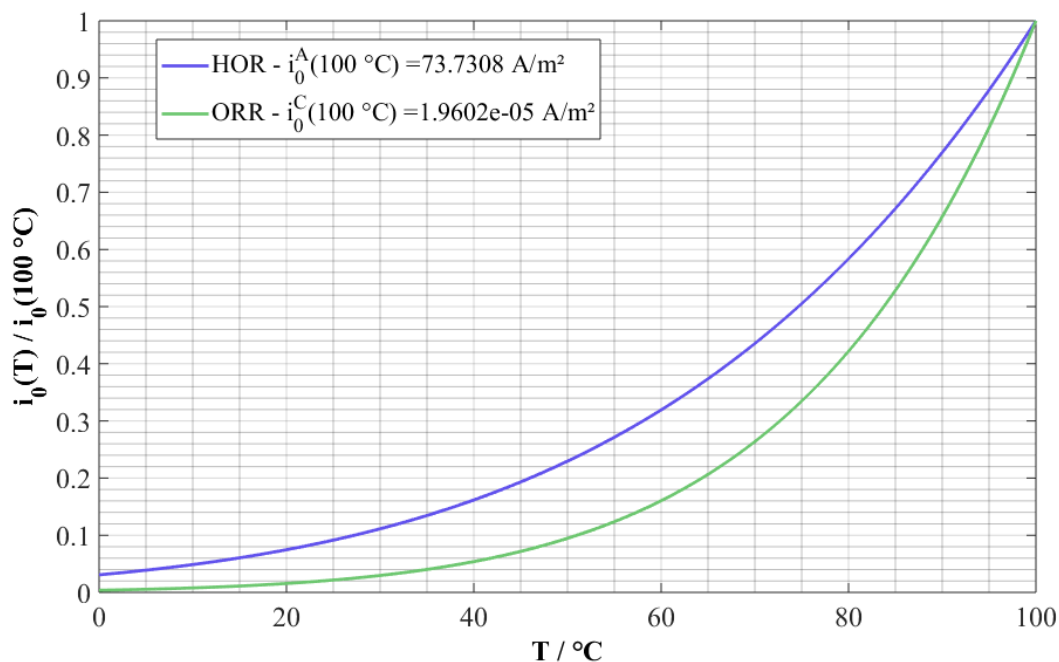


Figure 5.19: Exchange current densities vs. T .

As the mass transport losses are predominately caused by oxygen transport through the liquid phase, the limiting current density increases when this process is accelerated with increasing temperature; see Figure 5.20 and Figure 5.21 for the diffusion coefficients of hydrogen and oxygen in the KOH electrolyte, respectively, plotted against the temperature (their validity starts at 25 °C). With an increase in temperature, the diffusion coefficients of hydrogen and oxygen increase for all considered electrolyte concentrations; this rise is even stronger for lower electrolyte concentrations. For example, at 80 °C the oxygen diffusion coefficient in the 5 M KOH electrolyte solution is more than five times larger than at 20 °C. As a consequence, at 20 °C the oxygen concentration gradient must be more than five times larger than at 80 °C. This results in much higher concentration losses and a much lower limiting current density, respectively. The decline of the oxygen solubility with growing temperature is negligible compared with the dramatical rise of the diffusion coefficient.

Consequentially, the better becoming oxygen transport in the KOH electrolyte solution and to the catalyst surface can rise the limiting current density with temperature. This also affects the ohmic region slightly. Such an increase in the limiting current density was also predicted by previous models. Kimble and White [54] considered a 7 M KOH electrolyte and compared the cell performance at 70, 82, and 100 °C. In the activation region and in the ohmic region, their model predicted a decrease of the cell voltage with increasing

temperature. With respect to the mass transport region, their model also showed an increase in the limiting current density with temperature. Also for a 7 M KOH solution, Zhou [66] compared the cell performance at 60, 80, and 100 °C. His model showed the same effect of temperature on the polarization curve as the model by Jo and Yi. Therefore, the results predicted by the model which is presented in this work agree with the results of previous models with respect to the influence of temperature on the limiting current density. However, this model does not predict a decrease of the cell voltage in the activation region and in the ohmic region for an increase in temperature. This is primary due to taking into considerations the enhancement of the kinetics with rising temperature. Therefore, this is an advancement to the previous models and enables a more accurate investigation of the influence of temperature on the cell performance. The impact of the temperature dependences of the kinetic parameters is studied separately in chapter 5.4.4.

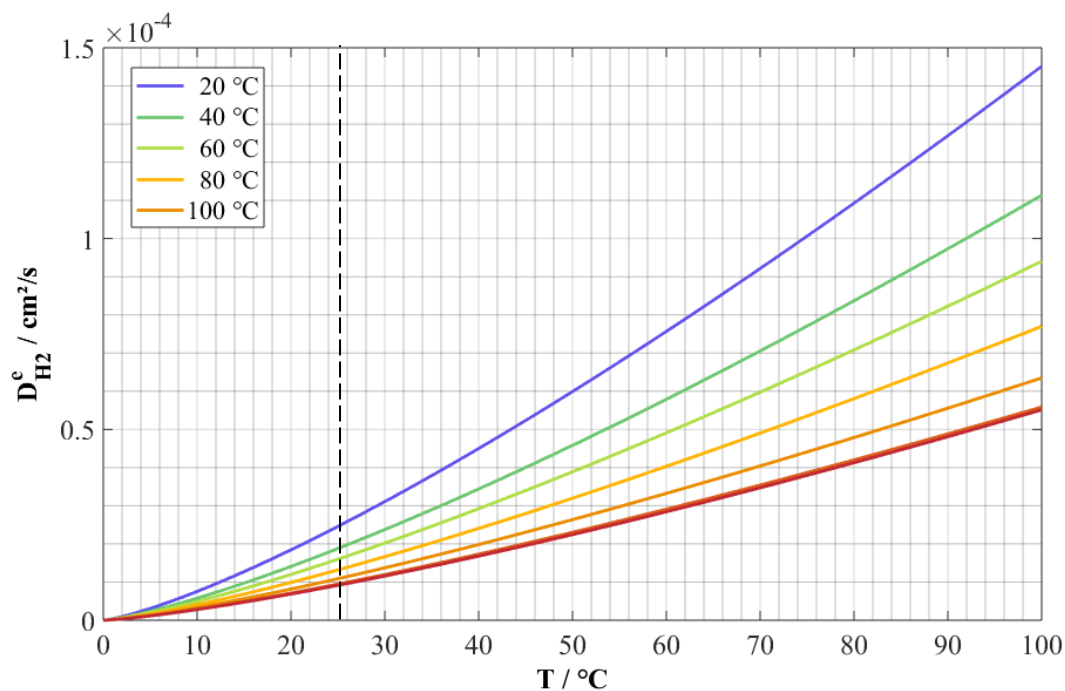


Figure 5.20: Diffusion coefficient of hydrogen in KOH vs. T .

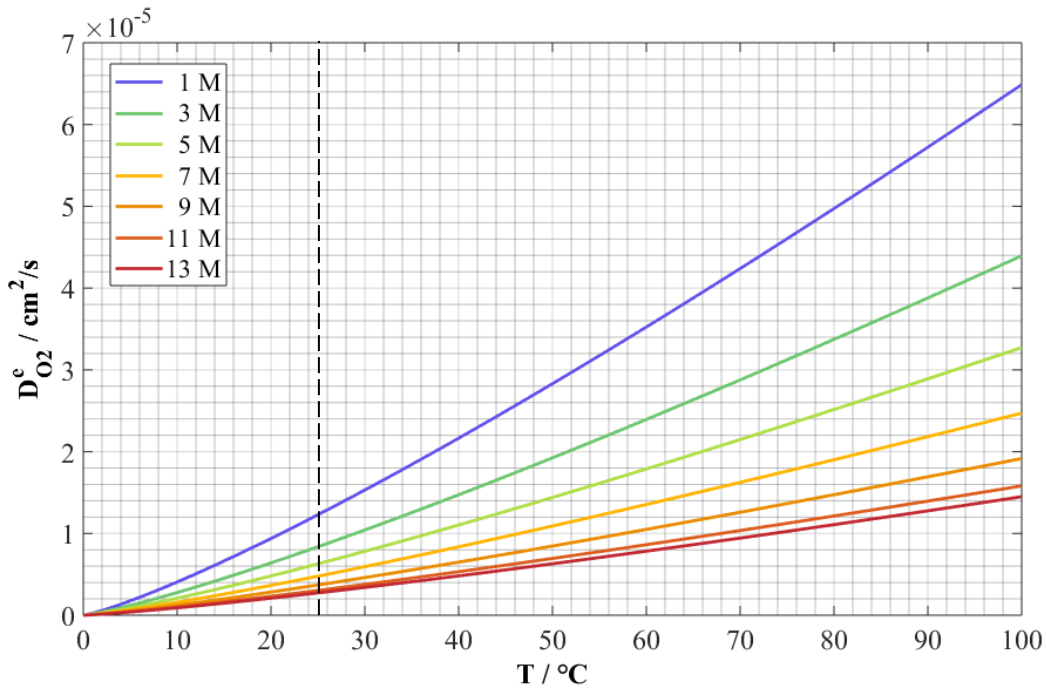


Figure 5.21: Diffusion coefficient of oxygen in KOH vs. T .

5.4.4 Temperature dependence of kinetic parameters

In advance to the previous mathematical models of AFCs reported in [54], [55], [63], [67], and [70], the model presented in this work accounts for the temperature dependences of the transfer coefficients as well as the temperature dependences of the exchange current densities. In order to determine the extent of this temperature correction, the temperature has again been raised from 20 to 80 °C, with an increment of 20 °C, whereas first the temperature dependences of the transfer coefficients (study 1) and secondly also the temperature dependences of the exchange current densities (study 2) have been neglected. For this purpose, the base case temperature 60 °C has been inserted in the equations of the transfer coefficients and the exchange current densities, respectively. The simulation results of study 1 and study 2 are illustrated in Figure 5.22 and Figure 5.23, respectively. For comparative purposes, the simulation results from Figure 5.18, where the kinetic parameters depend on temperature, are given in the graphs in pale colors.

According to equations (4.28) and (4.29) the forward transfer coefficient of the anodic reaction and the forward transfer coefficient of the cathodic reaction are assumed to rise linearly with temperature. Consequentially, compared to the temperature dependent transfer coefficient of the forward reaction (α_f^T), the isothermal transfer coefficient of the forward reaction (α_f^{const}) is larger at temperatures below 60 °C but smaller at temperatures above

60 °C. Hence, compared with the results derived with temperature dependent transfer coefficients, keeping the transfer coefficients constant causes the 20 and 40 °C curves to be shifted upwards and the 60 and 80 °C curves to be shifted downwards. At 60 °C, the increase in temperature in the cell causes α_f^T to rise and therefore to become larger than α_f^{const} . As described above, the decrease of the reversible cell voltage creates the tendency of the cell voltage to decrease with rising temperature. When the forward transfer coefficient of the cathode reaction is assumed to be constant, the improvement of the exchange current density solely cannot compensate this decrease of the reversible cell voltage, thus the cell voltage decreases. However, as the ohmic region and especially the mass transport region improve with increasing temperature, this phenomena only affects the activation region. As a consequence, the polarization curves intersect one another.

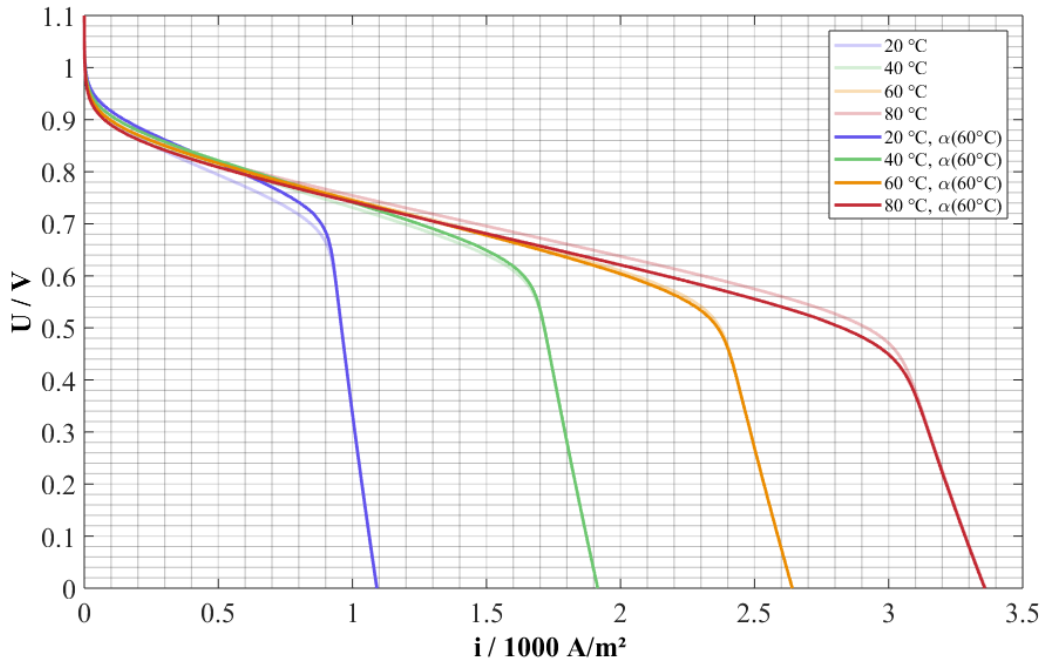


Figure 5.22: Effect of temperature on the polarization curve for $\alpha_f \neq f(T)$.

According to equations (2.26) and (2.27) the exchange current densities of the anode reaction and of the cathode reaction increase exponentially with temperature. When the temperature dependences of the exchange current densities are also ignored, by calculating them with the base case temperature 60 °C constantly (i_0^{const}), the dubious effect of the temperature on the activation region, which could already be observed in Figure 5.22, becomes much stronger. Then kinetics does not counteract the decrease of the reversible cell voltage so that the cell voltage decreases with rising temperature in the activation region. Calculated with the base

case temperature, i_0^{const} is larger than the exchange current density calculated with variable temperature (i_0^T) in case that the temperature is below 60 °C. This causes the polarization curves of the simulations at 20 and 40 °C to be shifted upwards. For 80 °C, i_0^{const} is smaller than i_0^T which causes the polarization curve at 80 °C to be shifted downwards. When the cell temperature rises with the current density, due to an increased heat production, i_0^T also does. Hence, the 60 °C curve created with i_0^{const} is also moved downwards compared with the 60 °C curve derived with i_0^T . As only kinetics has changed when the temperature dependences of the exchange current densities have been ignored, the ohmic region (slopes) and the mass transport region (limiting current density) remain unaffected.

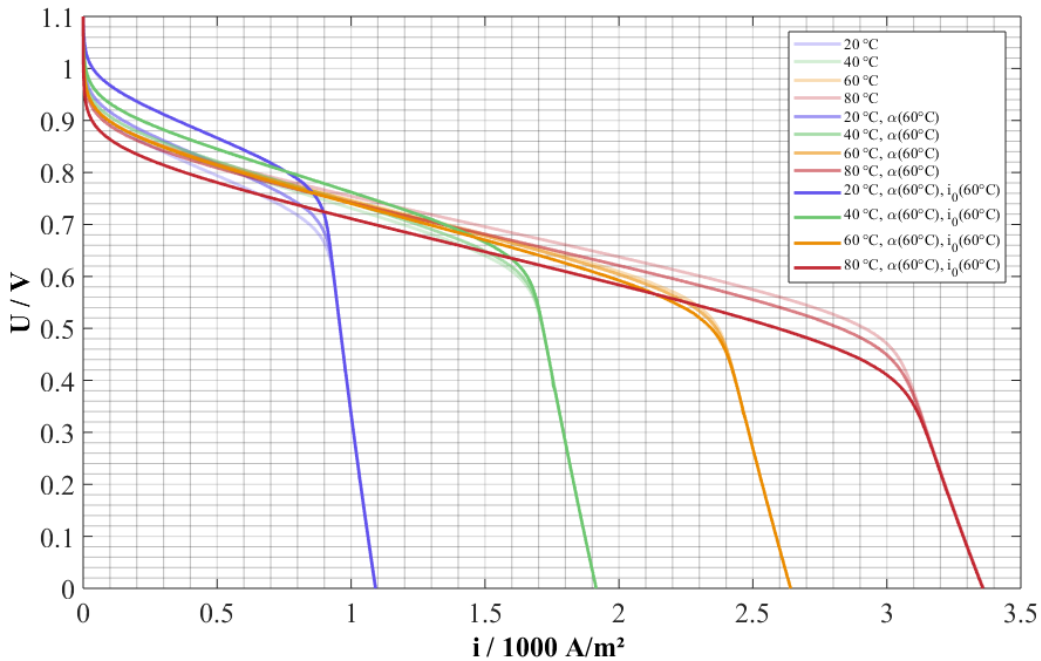


Figure 5.23: Effect of temperature on the polarization curve for $\alpha_f \neq f(T)$, $i_0 \neq f(T)$.

As illustrated in Figure 5.22 and Figure 5.23 the neglect of the temperature dependences of the transfer coefficients and of the exchange current densities has caused the cell voltage to be shifted downwards with increasing temperature. Therefore, it has caused the model to predict the same dependence of the cell voltage from temperature as predicted by the previous models [54], [66]. It is known, that kinetics improves with temperature causing the activation region to become better but not to become worse.

The model was used for predicting the impact of temperature on the polarization curve in [85]. At that time the solution rates for the solubility of hydrogen and oxygen in the KOH

electrolyte (equation (4.55)) and the kinetics at the anodic catalyst surface (equation (4.22)) and at the cathodic catalyst surface (equation (4.23)), respectively, were not directly coupled and the transport of hydrogen and oxygen within the electrolyte solution was described based on the Nernst-Planck equation (equation (2.88)). In order to raise the numerical stability of the model, so that it can flexibly be used for different parameter studies, the transport into the electrolyte was directly coupled with the electrochemical reaction at the catalyst surface in this work (main assumption iv). At the same time, further transport processes of hydrogen and oxygen in the liquid phase, for example in agglomerates or in the electrolyte channel, were neglected. Also, in [85], the temperature dependences of the transfer coefficients were not taken into consideration. Despite the difference in the mathematical description of the transport into and within the electrolyte, the simulation results predicted in [85] and the simulation results shown in Figure 5.22 agree qualitatively. This shows, that the simplification made in this work for the mass transport processes of hydrogen and oxygen in the electrolyte does not affect the polarization curve significantly.

It has been found that the temperature dependences of the exchange current densities are much more influential than the temperature dependences of the transfer coefficients. Due to the cathode being predominantly responsible for the activation losses (see chapter 5.2.4), the phenomenon of an improved activation region with rising temperature can be assigned to the kinetics of the cathode. Consequentially, in order to account for the impact of temperature on the activation region of the polarization curve, the temperature dependences of the kinetic parameters should be considered in mathematical models. It is especially recommended to respect the temperature dependence of the cathode exchange current density.

5.4.5 Kinetic parameter

The performance of a fuel cell is mostly dependent on the materials used as catalysts. The catalyst properties and the nature of the catalyst can be quantified by the exchange current density i_0 and the specific surface area a_l , respectively. Another kinetic parameter is the transfer coefficient α , giving information about the change of the activation barrier with the electrical potential difference in the interface.

The model uses kinetic parameters measured at platinum, that is a very effective noble metal catalyst. Scaling down the kinetic parameters enables predicting the cell performance for less precious catalysts such as Raney nickel on the anode side and silver on the cathode side.

This can reduce the material costs of the fuel cell and can help achieving economic success. Additionally, scaling up the kinetic parameters allows to predict the cell performance for catalyst materials that are more effective. This can help to decide, whether a more effective but probably also more expensive catalyst should be used or not. Also, the predictions give information, if researching in the field of more effective catalysts is promising.

As the parameters i_0 and a_l enter the model together as product ($i_0 a_l$) they are studied collectively in chapter 5.4.5.1. After that, the sensitivity of the cell performance with respect to transfer coefficients of the forward reactions (α_f) is investigated in chapter 5.4.5.2.

5.4.5.1 Exchange current density and specific surface area

The variation of the anodic kinetic parameters ($i_0^A a_l^A$) and the variation of the cathodic kinetic parameters ($i_0^C a_l^C$) are shown in Figure 5.24 and Figure 5.25, respectively. Both kinetic parameters, $i_0^A a_l^A$ and $i_0^C a_l^C$, have been raised from the thousandth to the thousandfold of the reference values as given in the legends.

As the HOR is much faster than the ORR, the anode exchange current density i_0^A is several orders of magnitude larger than the cathode exchange current density i_0^C ; as outlined in Figure 5.19, for the base case i_0^C is ca. $1 \cdot 10^{-6}$ smaller than i_0^A . Consequentially, the activation losses observable in the polarization curve of the cell are mostly caused by the sluggish kinetics of the ORR (see also chapter 5.2.4). Even for the case that the anode exchange current density is the thousandfold of the anodic reference exchange current density, it is still thousand times smaller than the cathode exchange current density. Therefore, the activation losses remain nearly solely caused by the cathode reaction and changing the anodic kinetic parameters shows no noticeable effect on the polarization curve. As a result, less effective materials with lower specific surface areas could be used on the anode side without impairing the cell performance. However, in case of a real cell using less effective catalysts with respect to $i_0 a_l$ might probably be coupled with different transfer coefficients (see below) or maybe undesired side reactions. Those effects are out of the scope of this work but must also be considered when changing the catalyst material in a real cell.

In contrast to the variation of $i_0^A a_l^A$ shown in Figure 5.24, the variation of $i_0^C a_l^C$ shown in Figure 5.25 has an enormous impact on the cell performance. Rising and decreasing $i_0^C a_l^C$ causes the polarization curve to be shifted upwards and downwards, respectively. In the same

time, the slope and the limiting current density remain unaffected. This dependence of the polarization curve on $i_0^C a_l^C$ directly shows the high sensitivity of the fuel cell performance with respect to the kinetics of the cathode reaction; rising $i_0^C a_l^C$ by the factor 10 reduces the activation losses by ca. 0.06 V. Hence, high catalytic materials with high specific surface areas are recommended on the cathode side, while replacing the noble metal catalyst by a less effective one is unrecommended. As platinum shows, in comparative terms, very good catalytic qualities, it is the standards catalyst for the ORR. However, the simulation model predicts that the cell power could be significantly raised, thus researching in the field of more effective catalysts for the ORR in the alkaline electrolyte is promising.

With respect to the dependence of the cell performance on $i_0 a_l$, the model agrees with the results which were presented by Kimble and White [54]. They compared the polarization curves predicted by their model for the cases that $i_0^C a_l^C$ is 0.1, 0.6, and 10 A/cm³. Their model also predicted that increasing $i_0^C a_l^C$ shifts the polarization curve upwards with no effect on the slope of the curve in the ohmic region and no impact on the limiting current density. In their study the cell performance was also increased by ca 0.06 V when $i_0^C a_l^C$ was raised tenfold. They did not study the influence of $i_0^A a_l^A$, which would probably had caused the same results because they assumed $i_0^A a_l^A$ to equal $i_0^C a_l^C$.

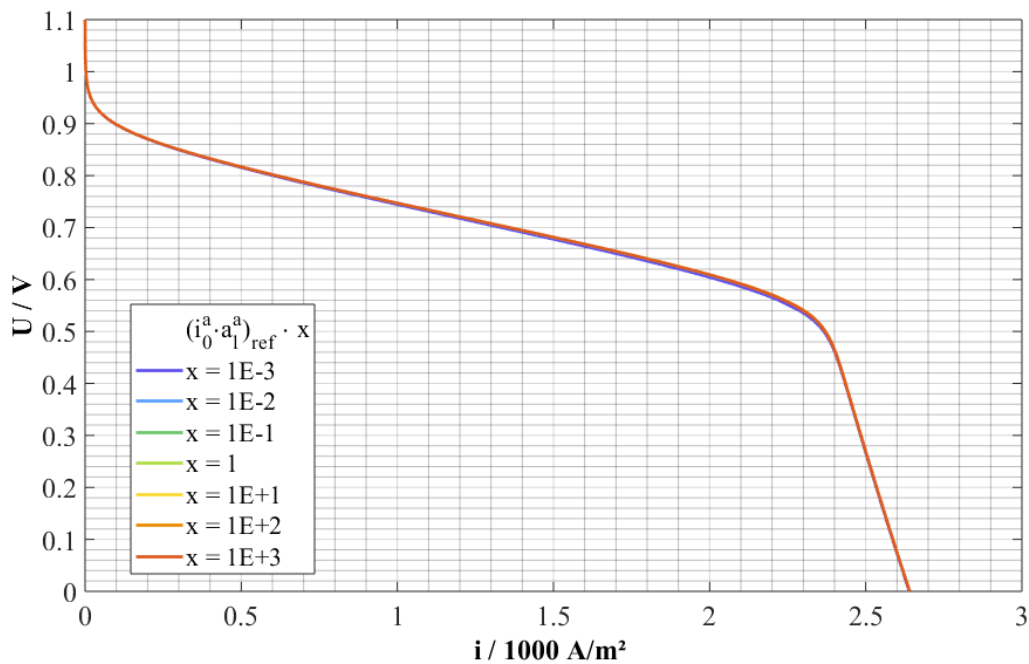


Figure 5.24: Effect of $i_0^A a_l^A$ on the polarization curve.

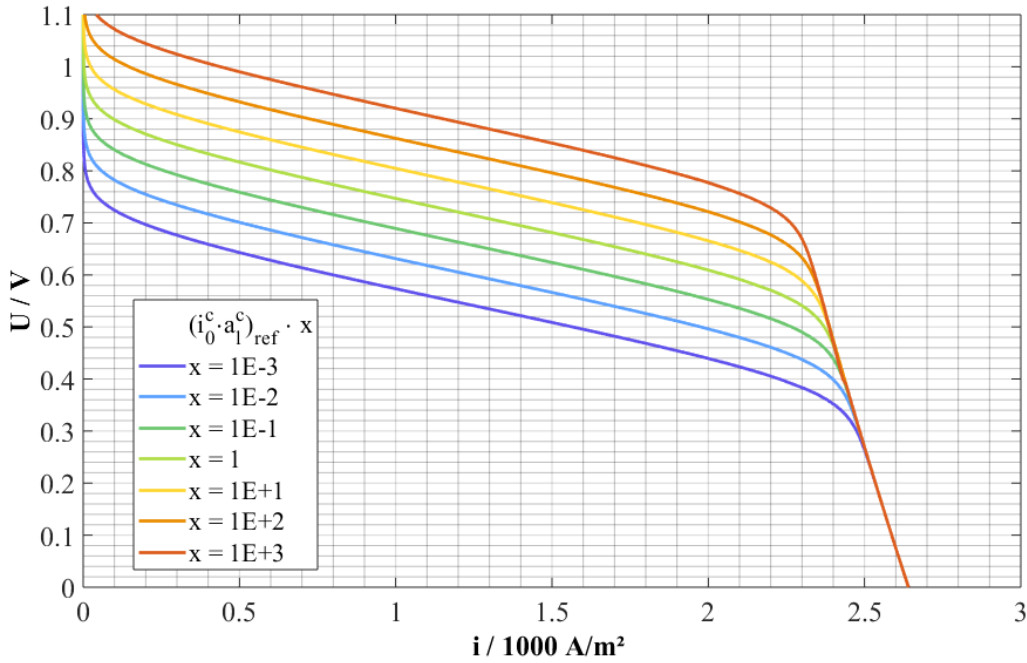


Figure 5.25: Effect of $i_0^c a_1^c$ on the polarization curve.

5.4.5.2 Transfer coefficient

In order to investigate the sensitivity of the polarization curve with respect to the transfer coefficients, the forward transfer coefficient of the anode reaction (α_+^A) and the forward transfer coefficient of the cathode reaction (α_-^C) have been varied, while the transfer coefficients of the backward reactions α_-^A and α_+^C , respectively, have been derived from

$$\alpha_+ + \alpha_- = 1. \quad (2.48)$$

In the course of this study, α_+^A and α_-^C have been decreased and raised by 0.05 and 0.01 from the references $\alpha_{+,Ref}^A$ and $\alpha_{+,Ref}^C$, respectively. The simulation results of the variation of α_+^A and α_-^C are provided in Figure 5.26 and Figure 5.27, respectively.

Rising and reducing the transfer coefficient causes the activation barrier to decrease and increase compared to the reference, respectively. However, no response of the polarization curve with respect to the change in α_+^A can be noticed. This is again due to the cathodic reaction being nearly solely responsible for the activation losses. As a result, the variation of α_+^A shows no influence on the polarization curve, which is in analogy with the negligible impact of the variation of $i_0^A a_1^A$ on the cell performance predicted in chapter 5.4.5.1.

While changing $i_0^c a_l^c$ has only affected the activation region (see chapter 5.4.5.1), shifting the polarization curve upwards and downwards, changing α_c^c also affects the slope of the curve in the ohmic region. At the same time, the limiting current density remains unaffected. The reason for this impact of α_c^c on the polarization curve can be found, when neglecting the backward reaction, so that the activation losses can be written as (see chapter 2.8.4.2)

$$|\eta_{Act}| = \frac{RT}{\alpha_f F} \ln\left(\frac{|i|}{i_0}\right). \quad (5.2)$$

Obviously, the larger the transfer coefficient of the forward reaction α_f , the smaller the activation overpotential, but also the less the increase of the overpotential with current density. Hence, the combination from both effects cause the polarization curve to be shifted upwards and the slope to be enhanced with rising α_c^c . For the base case conditions, the polarization curve decreases by ca. $-13.38 \text{ mV}/(\text{A}/\text{m}^2)$. Reducing α_c^c by -0.05 and -0.1 causes the slope to decrease on ca. $-14.02 \text{ mV}/(\text{A}/\text{m}^2)$ and ca. $-14.96 \text{ mV}/(\text{A}/\text{m}^2)$, respectively. Analogously, rising α_c^c by $+0.05$ and $+0.1$ enhances the slope on ca. $-13.83 \text{ mV}/(\text{A}/\text{m}^2)$ and ca. $-12.41 \text{ mV}/(\text{A}/\text{m}^2)$, respectively. Consequentially, improving the forward transfer coefficient of the ORR is a powerful measure for enhancing the performance of the fuel cell. Although it is a kinetic parameter, it also affects the cell performance in the ohmic region.

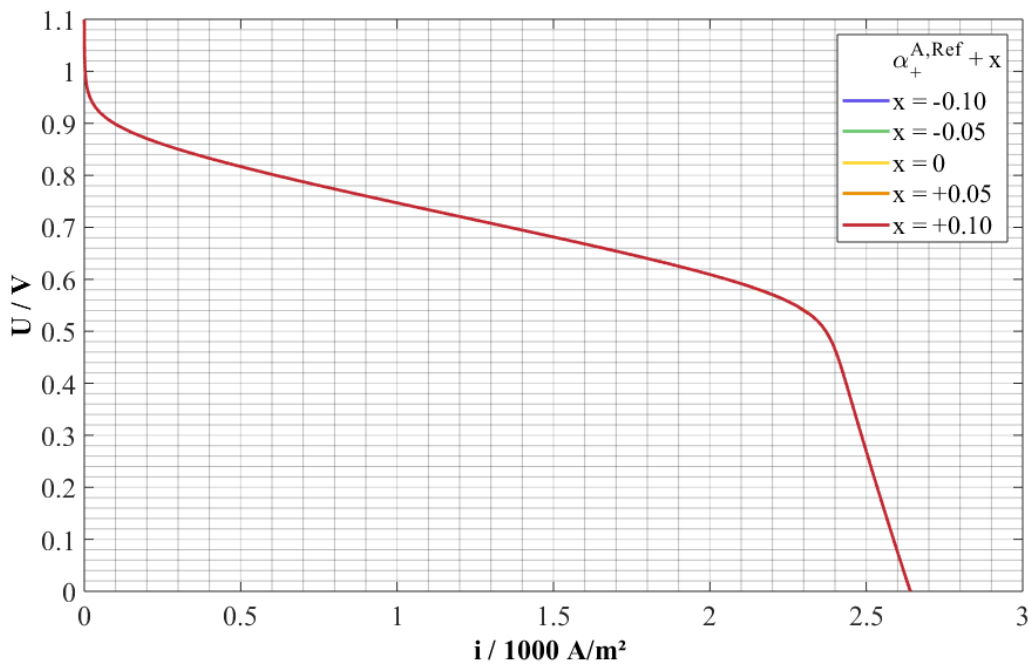


Figure 5.26: Effect of α_+^A on the polarization curve.

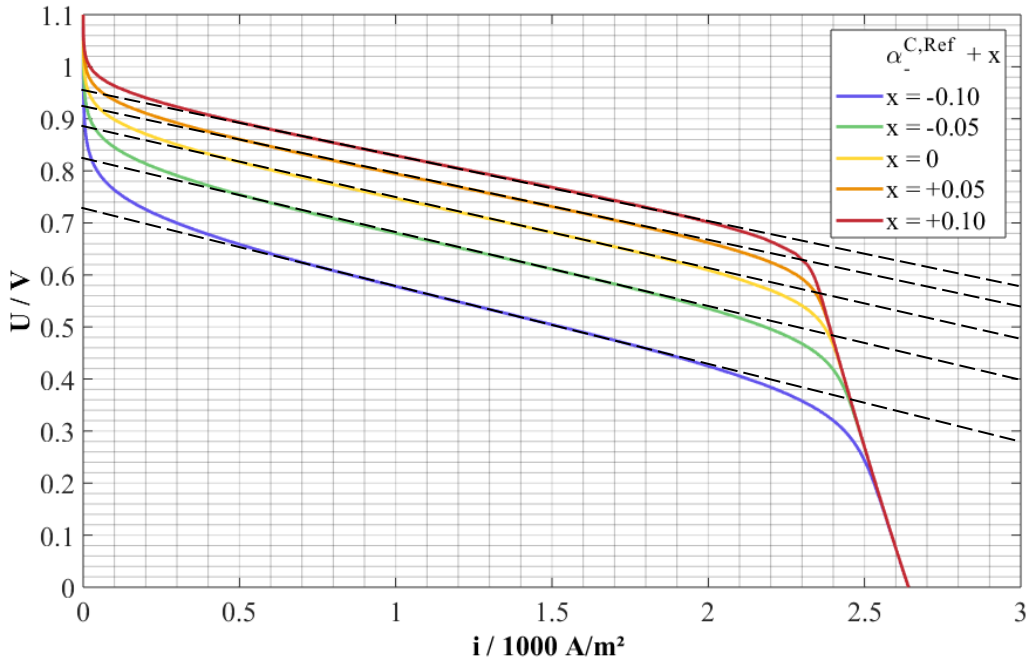


Figure 5.27: Effect of α_c^C on the polarization curve.

5.4.6 Electrolyte film

The electrolyte film is characterized by two essential parameters, its thickness d_l and its specific surface area a_g . Both parameters can be studied together at the same time, because they arise together as the quotient a_g/d_l in the model. In order to determine the sensitivity of the model with respect to the anodic electrolyte film parameters (a_g^A/d_l^A) and with respect to the cathodic electrolyte film parameters (a_g^C/d_l^C), they have been varied from the tenth to the tenfold of the reference. The simulation results of the variation of a_g^A/d_l^A and a_g^C/d_l^C are given in Figure 5.28 and Figure 5.29, respectively.

For the base case scenario, the liquid phase diffusion of oxygen is solely responsible for the mass transport losses in the polarization curve (see chapter 5.2.4). Therefore, increasing a_g^A/d_l^A shows no remarkable enhancement of the polarization curve. If hydrogen transport contributed to the mass transport losses, the rise in a_g^A/d_l^A would enhance the slope of the polarization curve slightly and eventually even increase the limiting current density.

While raising a_g^A/d_l^A reduces the transport barrier of hydrogen, reducing a_g^A/d_l^A increases the transport barrier of hydrogen. When a_g^A/d_l^A is a tenth of the reference, a small impact on the cell performance can be detected. Then, not only oxygen transport but also hydrogen transport causes noticeable mass transport losses. As only the ohmic region but not the

limiting current density is affected, the limitation due to hydrogen transport would occur at a limited current density which is larger than the one caused by oxygen transport. If a_g^A/d_l^A was further decreased, hydrogen transport would become predominant and the limiting current density would become smaller. However, such a thick electrolyte film and small specific surface area are rather unlikely.

The variation of the a_g^C/d_l^C shows an enormous impact on the polarization curve. Raising a_g/d_l means reducing the electrolyte film thickness, increasing the specific surface area of the electrolyte at the gas/liquid interface, or both. Consequentially, the limiting current density increases and decreases with a_g^C/d_l^C . This is reasonable as reducing the electrolyte film thickness reduces the diffusive pathway, whereas raising the specific surface area provides more space for the gas solution into the electrolyte. Both phenomena cause the concentration of oxygen at the catalyst surface to rise and therefore the concentration losses to decrease. In the same way the oxygen concentration at the catalyst surface decreases when the diffusive pathway becomes longer or the specific surface area becomes smaller.

The impact of a_g/d_l on the polarization curve can be verified by comparing the simulation results predicted by this model with the simulation results predicted by Kimble and White [54]. They considered the cases that a_g^C/d_l^C is $1 \cdot 10^8$, $5 \cdot 10^8$, and $10 \cdot 10^8 \text{ cm}^{-2}$ and the cases that a_g^A/d_l^A is $1 \cdot 10^8$, and $5 \cdot 10^8 \text{ cm}^{-2}$. They also showed that the limiting current density increases and decreases with a_g/d_l . Also, the polarization curve was more sensitive with respect to a_g^C/d_l^C than with respect to a_g^A/d_l^A . However, decreasing a_g^A/d_l^A caused the limiting current density to decrease. The reason can be given by the much higher oxygen mole fraction in the cathode gas so that hydrogen and oxygen transport become comparable. When the oxygen mole fraction in the cathode gas is raised, the impact of oxygen mass transport on the polarization curve is diminished. This enables reaching current densities where also hydrogen mass transport can contribute to the mass transport losses.

Consequentially, in order to raise the limiting current density, improving the catalyst with respect to wetting is recommended. Based on the simulation results, a full coverage of the catalyst surface by a very thin electrolyte film is desired for obtaining the highest possible limiting current density. It must be emphasized that the responsiveness of the cell model with respect to the electrolyte film parameters is mainly caused by the assumption that hydrogen and oxygen must dissolve in and diffuse through the electrolyte film in order to

react electrochemically. Therefore, if the gases reacted directly from the gas phase, the predicted sensitivity would not be reasonable.

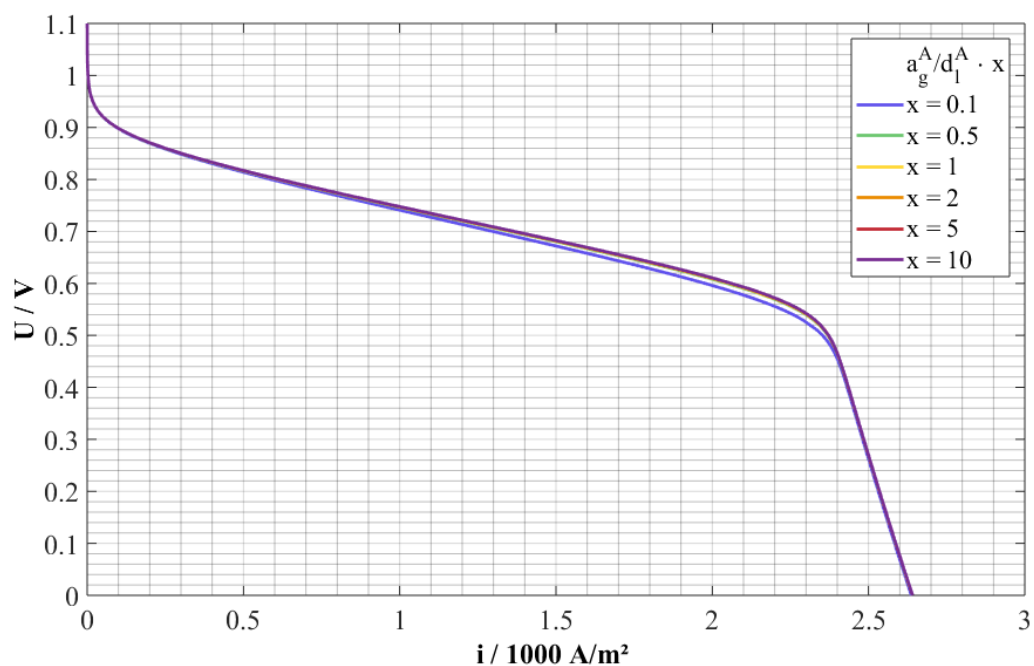


Figure 5.28: Effect of a_g^A/d_l^A on the polarization curve.

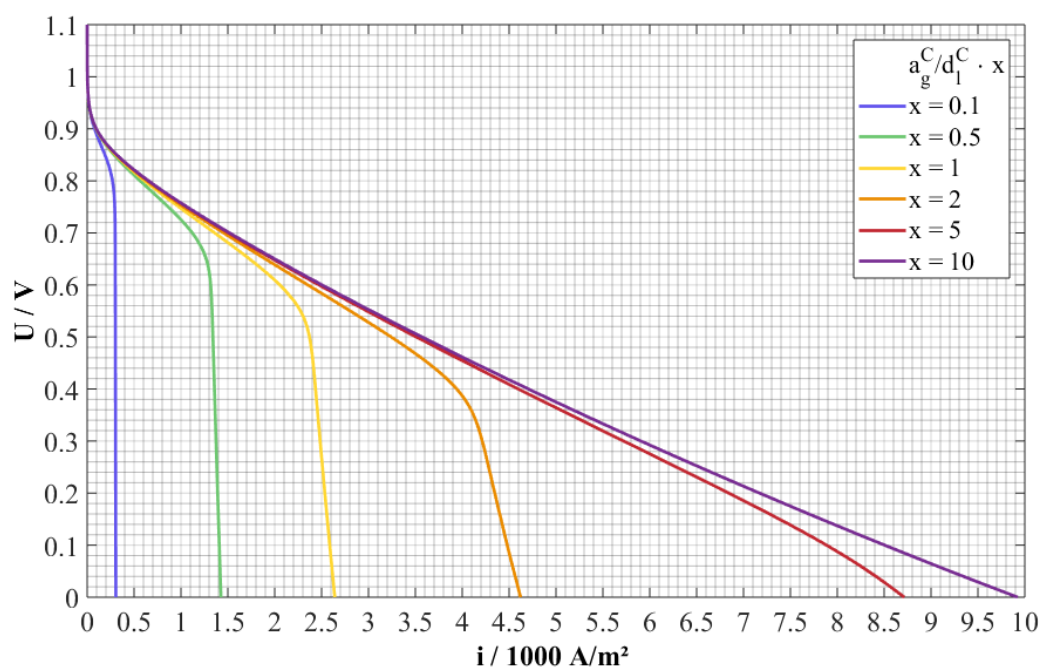


Figure 5.29: Effect of a_g^C/d_l^C on the polarization curve.

6. Conclusion

A mathematical, 2-D model of a complete alkaline fuel cell (AFC) has been developed with the software COMSOL Multiphysics[®]. The model predicts the physical processes in the cell by solving mass, momentum, species, charge and energy transport equations fully coupled and under steady state conditions. The model consists of the anodic gas channel, the cathodic gas channel, the anode, the cathode, and the electrolyte channel in between, where the KOH electrolyte solution circulates. Three-layer electrodes are considered, in which the layers are arranged from the gas side to the liquid side in the following order: support layer (SL), gas diffusion layer (GDL), catalyst layer (CL). In the electrode layers, macrohomogeneous continua are assumed, where the different phases are superimposed. The GDLs are assumed to prevent any liquids from flooding the gas pores and the anode reaction and the cathode reaction are considered in the anodic CL and in the cathodic CL, respectively. The catalyst surface is assumed to be covered by a thin electrolyte film, thus hydrogen and oxygen must dissolve in and diffuse through the electrolyte in order to react electrochemically. The model accounts for the concentration dependences and the temperature dependences of the exchange current densities. Additionally, linear temperature dependences are assumed for the transfer coefficients.

Being developed based on the beta-cell design by the company AFC Energy, the model has been compared to the real cell with regard to the polarization curve. For this purpose, the base case operating conditions have been defined on the basis of information provided by AFC Energy. The comparison of the polarization curves has shown excellent agreements, when the cell performance has been predicted quantitatively correct in the activation region and in the ohmic region. The curve progression in the mass transport region has been found to be qualitatively correct whereas it could not be compared with measurements due to a lack of available data. Therefore, it can be concluded that the simulation model captures the relevant processes in the cell which cause the potential losses in an adequate manner.

For the base case scenario, the cathode performance has been found to be predominantly responsible for the overall cell performance. On the one hand, the sluggish kinetics of the cathode reaction has been identified being primary casual for the activation losses. On the other hand, the mass transport limitation has been caused by the slow oxygen transport through the electrolyte film. Therefore, optimizing the cathode performance is the key for enhancing the overall performance of the AFC.

Rising the pressure and the temperature have been proven to be very effective strategies in enhancing the cell performance. Through increasing pressure, the reversible cell voltage and the gas solubility in the electrolyte improve. An increase in temperature enhances the kinetics as well as the mass transport in the liquid phase. As a result, higher current densities can be achieved.

It has been shown that the temperature dependences of the kinetic parameters, especially of the cathode exchange current density, should not be neglected in mathematical models. When the transfer coefficients are kept constant, the cell voltage decreases with increasing temperature (especially in the activation region). This effect is much stronger when additionally the temperature dependences of the exchange current densities are neglected. Therefore, it is recommended to take into consideration the temperature dependences of the kinetic parameters in non-isothermal models as well as in isothermal models which are used at various temperatures.

The investigation of the sensitivity of the cell performance with respect to the exchange current densities, has shown no response to the change in the anode exchange current density, but an enormous dependence on the cathode exchange current density. The reason has been given by the sluggish kinetics of the ORR represented by the cathode exchange current density which is several orders of magnitude smaller than the anode exchange current density. The change in the cathode exchange current density has caused the polarization curve to be shifted. It has been noticed that rising the cathode exchange current density by the factor 10 can shift the polarization curve upwards by ca. 0.06 V. As a consequence, less effective catalysts can be used on the anode side, as long as no undesired side reactions follow. Additionally, the cathodic catalyst should be as effective as possible, thus researching in the field of catalyst materials for the ORR in alkaline media would be desirable for alkaline fuel cell improvement.

With respect to concentration losses, the mass transport in the gas phase has been found to be negligible while the mass transport in the liquid phase has been identified to be responsible. The reason has been given by the diffusion coefficient in the liquid phase being several orders of magnitude lower than the diffusion coefficient in the gas phase. Again, the cathode performance has been determined as causal. On the one hand, the low oxygen gas concentration above the electrolyte, caused by air being fed to the cathode, results in low

oxygen concentrations in the electrolyte. On the other hand, the diffusion coefficient of oxygen in the KOH electrolyte solution is smaller than the diffusion coefficient of hydrogen. Both effects together cause the oxygen concentration at the cathodic catalyst surface to be much smaller than the hydrogen concentration at the anodic catalyst surface. The increase in the electrolyte concentration on the cathode side with the current density exacerbates these effects, as the solubility and the diffusion coefficient decrease with rising electrolyte concentration. Therefore, the fuel cell performance has been much more sensitive with respect to the cathodic electrolyte film parameters than with respect to the anodic electrolyte film parameters. By varying the electrolyte film parameters, it has been found that the cell performance is almost independent on the anodic electrolyte film parameters, but highly dependent on the cathodic electrolyte film parameters: The better the cathodic electrolyte film parameters, the higher the limiting current density. This is the case as long as no other effect becomes limiting, such as the electrolyte concentration. Consequentially, optimizing the cathodic catalyst with respect to wetting is suggested for increasing the limiting current density.

Hence, the mathematical model of an AFC developed in this dissertation enables studying the impact of various parameters on the performance of an AFC. As a result, the model can help improving the economic success of AFCs and can contribute to the success of the energy transition.

7. Recommendations and outlook

In this work, predicting the polarization curve of an AFC for the entire operating range and under variable conditions has been focused. In order to decrease computation time and raise the numerical stability, assumptions and simplifications have been made. They mainly include liquid transport through the electrodes, water transport in general, hydrogen and oxygen transport in the electrolyte, electrode materials, and the reaction mechanisms. For studying these processes more accurately, creating further models or even developing the presented model further is recommended. Due to a lack of available data, assumptions needed to be made concerning the electrode materials, their properties, and their structure parameters. In order to create more precise information with the model, the data of the actual electrodes should be derived from measurements and be used in the model. Also deriving measurements under different operating conditions and in the mass transport region is suggested in order to validate the model more precisely.

References

- [1] Bundesministerium für Wirtschaft und Energie (BMWi), Gesamtausgabe der Energiedaten - Datensammlung des BMWi (22.01.2019), Germany, 2019.
- [2] Bundesministerium für Wirtschaft und Energie (BMWi), Renewable Energy Sources Act (EEG 2017), Germany, 2018.
- [3] R. O'Hayre, S.-W. Cha, W. Colella and F. B. Prinz, Fuel Cell Fundamentals, 2. ed., New Jersey: John Wiley & Sons, 2009.
- [4] K. Kordesch, V. Hacker, J. Gsellmann, M. Cifrain, G. Faleschini, P. Enzinger, R. Fankhauser, M. Ortner, M. Muhr and R. R. Aronson, Alkaline Fuel Cells Applications, *Journal of Power Sources*, vol. 86, pp. 162-165, 2000.
- [5] B. J. Crowe, Fuel Cells - A Survey, Washington: National Aeronautics and Space Administration, 1973.
- [6] A. J. Appleby and F. R. Foulkes, Fuel Cell Handbook, Florida: Krieger Publishing Company, 1993.
- [7] L. Mond and C. Langer, A new Form of Gas Battery, *Proceedings of the Royal Society of London*, vol. 46, pp. 296-304, 1889.
- [8] W. R. Grove, VIII. On the Gas Voltaic Battery.-Experiments Made with a View of Ascertaining the Rationale of Its Action and Its Application to Eudiometry, *Philosophical Transactions of the Royal Society of London*, vol. 133, pp. 91-112, 1843.
- [9] K. Kordesch, V. Hacker, K. Reichmann, M. Cifrain, T. Hejze and R. R. Aronsson, The Safe and Economic Revival of Alkaline Hydrogen/Air Fuel Cells with Circulating Electrolytes, Recommended for Vehicles using Battery Hybrid Systems and Hydrogen from Ammonia Crackers, *ECS Transactions*, vol. 11, no. 32, pp. 167-185, 2008.
- [10] K.-D. Kreuer, Fuel Cells - Selected Entries from the Encyclopedia of Sustainability Science and Technology, New York: Springer, 2012.
- [11] EG&G Technical Services Inc., Fuel Cell Handbook, 7. ed., Morgantown, West Virginia: U.S. Department of Energy, Office of Fossil Energy, National Energy Technology Laboratory, 2004.
- [12] J. Larminie und A. Dicks, Fuel Cell Systems Explained, 2. Hrsg., West Sussex: John Wiley & Sons, 2003.

- [13] E. De Geeter, M. Mangan, S. Spaepen, W. Stinissen and G. Vennekens, Alkaline Fuel Cells for Road Traction, *Journal of Power Sources*, vol. 80, p. 207–212, 1999.
- [14] E. Gülzow, M. Schulze and U. Gerke, Bipolar Concept for Alkaline Fuel Cells, *Journal of Power Sources*, vol. 156, pp. 1-7, 2006.
- [15] K. Kordesch and V. Hacker, Stack Materials and Design, in *Handbook of Fuel Cells – Fundamentals, Technology and Applications*, Chichester, John Wiley & Sons, 2003, p. 765–773.
- [16] F. Bidault, D. J. L. Brett, P. H. Middleton and N. P. Brandon, Review of Gas Diffusion Cathodes for Alkaline Fuel Cells, vol. 187, pp. 39-48, 2009.
- [17] G. F. McLean, T. Niet, S. Prince-Richard and N. Djilali, An Assessment of Alkaline Fuel Cell Technology, *International Journal of Hydrogen Energy*, vol. 27, pp. 507-526, 2002.
- [18] E. Gülzow and M. Schulze, Long-Term Operation of AFC Electrodes with CO₂ Containing Gases, *Journal of Power Sources*, vol. 127, p. 243–251, 2004.
- [19] M. Schulze and E. Gülzow, Degradation of Nickel Anodes in Alkaline Fuel Cells, *Journal of Power Sources*, vol. 127, pp. 252-263, 2004.
- [20] N. Wagner, M. Schulze and E. Gülzow, Long Term Investigations of Silver Cathodes for Alkaline Fuel Cells, *Journal of Power Sources*, vol. 127, pp. 264-272, 2004.
- [21] B. Cox and K. Treyer, Environmental and Economic Assessment of a Cracked Ammonia Fuelled Alkaline Fuel Cell for Off-Grid Power Applications, vol. 275, pp. 322-335, 2015.
- [22] F. Bidault, D. J. L. Brett, P. H. Middleton, N. Abson and N. P. Brandon, A New Application for Nickel Foam in Alkaline Fuel Cells, *International Journal of Hydrogen Energy*, vol. 34, pp. 6799-6808, 2009.
- [23] F. Bidault, D. J. L. Brett, P. H. Middleton, N. Abson and N. P. Brandon, An Improved Cathode for Alkaline Fuel Cells, *International Journal of Hydrogen Energy*, vol. 35, pp. 1783-1788, 2010.
- [24] D. H.-J. Kohnke (gaskatel GmbH), Alkalische Brennstoffzellen zur Hausenergieversorgung?, in *Sechstes Kasseler Symposium Energie-Systemtechnik: Erneuerbare Energien und Rationelle Energieverwendung*, Hanau, Institut für

Solare Energieversorgungstechnik - Verein an der Universität Gesamthochschule Kassel e.V., 2001, pp. 87-94.

- [25] Gaskatel GmbH, gaskatel, [Online]. Available: http://www.gaskatel.de/de/fedienstleistung/eloflux_index.html. [Accessed 24 02 2019].
- [26] M. Cifrain and K. Kordesch, Hydrogen/Oxygen (Air) Fuel Cells with Alkaline Electrolytes, in *Handbook of Fuel Cells – Fundamentals, Technology and Applications*, Vols. 1, part 4, Chichester, John Wiley & Sons, 2003, pp. 267-280.
- [27] Independent Power Technologies. [Online]. Available: <http://www.independentpower.biz/>. [Accessed 22 02 2019].
- [28] GenCell. [Online]. Available: www.gencellenergy.com. [Accessed 24 02 2019].
- [29] AFC Energy. [Online]. Available: www.afcenergy.com. [Accessed 24 02 2019].
- [30] Institut für Technische Verbrennung (RWTH) - Univ.-Prof. Dr.-Ing. Dr. h.c. Dr.-Ing. E.h. N. Peters, Technische Verbrennung I, [Online]. Available: http://decane.itv.rwth-aachen.de/fileadmin/LehreSeminar/TechnischeVerbrennung/Technische_Verbrennung.pdf. [Accessed 28 04 2018].
- [31] W. Nernst, Die elektromotorische Wirksamkeit der Ionen, *Zeitschrift für Physikalische Chemie*, vol. 4, pp. 129-181, 1889.
- [32] J. A. V. Butler, Studies in heterogeneous Equilibria. Part II - The kinetic Interpretation of the Nernst Theory of Electromotive Force, *Transactions of the Faraday Society*, vol. 19, pp. 729-733, 1924.
- [33] T. Erdey-Grúz and M. Volmer, Zur Theorie der Wasserstoffüberspannung, *Zeitschrift für Physikalische Chemie*, vol. 150, no. 1, pp. 203-213, 1930.
- [34] P. W. Atkins and J. De Paula, *Physikalische Chemie*, 5. ed., Weinheim: Wiley-VCH, 2013.
- [35] A. J. Bard and L. R. Faulkner, *Electrochemical Methods: Fundamentals and Applications*, 2. ed., New York - Chichester - Weinheim - Brisbane - Singapore - Toronto: John Wiley & Sons, 2001.
- [36] C. H. Hamann and W. Vielstich, *Elektrochemie*, 4. ed., Weinheim: Wiley-VCH, 2005.

- [37] J. Goodisman, *Electrochemistry: Theoretical Foundations - Quantum and Statistical Mechanics, Thermodynamics, the Solid State*, New York: John Wiley & Sons, 1987.
- [38] G. Kortüm, *Lehrbuch der Elektrochemie*, 5. ed., Weinheim: Verlag Chemie, 1972.
- [39] J. Newman, *Electrochemical Systems*, Englewood Cliffs, New Jersey: Prentice-Hall, Inc., 1973.
- [40] K. J. Vetter, *Elektrochemische Kinetik*, Berlin, Göttingen, Heidelberg: Springer-Verlag, 1961.
- [41] J. Newman and K. E. Thomas-Alyea, *Electrochemical Systems*, 3. ed., New Jersey: Wiley & Sons, 2004.
- [42] S. Srinivasan, *Fuel Cells: From Fundamentals to Applications*, New York: Springer, 2006.
- [43] J. O. Bockris and Z. Nagy, Symmetry Factor and Transfer Coefficient - A source of confusion in electrode kinetics, *Journal of Chemical Education*, vol. 50, no. 12, pp. 839-843, 1973.
- [44] H. A. Gasteiger, Y. Liu, D. Baker and W. Gu, Kinetics and Kinetically Limited Performance in PEMFCs and DMFCs with State-of-the-Art Catalysts, in *Mini-Micro Fuel Cells: Fundamentals and Applications*, The Netherlands, Springer Science & Business Media, 2008, pp. 209-224.
- [45] W. Nernst, Zur Kinetik der in Lösung befindlichen Körper, *Zeitschrift für Physikalische Chemie*, vol. 2, pp. 613-637, 1888.
- [46] W. Ostwald and W. Nernst, Über freie Ionen, *Zeitschrift für Physikalische Chemie*, vol. 3, pp. 120-130, 1888.
- [47] M. Planck, Ueber die Erregung von Electricität und Wärme in Electrolyten, *Annalen der Physik und Chemie*, vol. 275, no. 2, p. 161-186, 1890a.
- [48] M. Planck, Ueber die Potentialdifferenz zwischen zwei verdünnten Lösungen binärer Electrolyte, *Annalen der Physik und Chemie*, vol. 276, no. 8, pp. 561-576, 1890b.
- [49] M. Planck, Zur Theorie der Elektrizitätserregung in Elektrolyten, *Zeitschrift für Physik*, vol. 94, no. 7-8, pp. 469-472, 1935.
- [50] R. Taylor and R. Krishna, *Multicomponent Mass Transfer*, New York: John Wiley & Sons, 1993.

-
- [51] J. Newman, D. Bennion and C. W. Tobias, Mass Transfer in Concentrated Binary Electrolytes, *Berichte der Bunsengesellschaft für physikalische Chemie*, vol. 69, no. 7, pp. 608-612, 1965.
- [52] J. Newman, Transport Processes in Electrolytic Solutions, *Advances in Electrochemistry and Electrochemical Engineering*, vol. 5, pp. 87-136, 1967.
- [53] J. Newman and W. Tiedemann, Porous-Electrode Theory with Battery Applications, *American Institute of Chemical Engineers (AIChE) Journal*, vol. 21, no. 1, pp. 25-41, 1975.
- [54] M. C. Kimble and R. E. White, A Mathematical Model of a Hydrogen/Oxygen Alkaline Fuel Cell, *Journal of the Electrochemical Society*, vol. 138, no. 11, pp. 3370-3382, 1991.
- [55] M. C. Kimble and R. E. White, Parameter Sensitivity and Optimization Predictions of a Hydrogen/Oxygen Alkaline Fuel Cell Model, *Journal of the Electrochemical Society*, vol. 139, no. 2, pp. 478-484, 1992.
- [56] T. Kenjo and K. Kawatsu, Current-Limiting Factors and the Location of the Reaction Area in PTFE-Bonded Double-Layered Oxygen Electrodes, *Electrochimica Acta*, vol. 30, no. 2, pp. 229-233, 1985.
- [57] P. Björnbom, Modelling of a Double-Layered PTFE-Bonded Oxygen Electrode, *Electrochimica Acta*, vol. 32, no. 1, pp. 115-119, 1987.
- [58] P. Björnbom and S.-C. Yang, Modeling and Simulation of the Operation of an AFC Cathode by Using Concentrated Electrolyte Solution Transport Theory, *Electrochimica Acta*, vol. 37, no. 10, pp. 1831-1843, 1992.
- [59] P. Björnbom and S.-C. Yang, Modeling and Simulation of the Operation of a Whole Alkaline Fuel Cell by Using Concentrated Electrolyte Solution Transport Theory, *Electrochimica Acta*, vol. 38, no. 17, pp. 2599-2609, 1993.
- [60] J. Giner and C. Hunter, The Mechanism of Operation of the Teflon-Bonded Gas Diffusion Electrode: A Mathematical Model, *Journal of the Electrochemical Society*, vol. 116, no. 8, pp. 1124-1130, 1969.
- [61] A. D. S. Tantram and A. C. C. Tseung, Structure and Performance of Hydrophobic Gas Electrodes, *Nature*, vol. 221, pp. 167-168, 1969.
- [62] P. Björnbom, vs., M. C. Kimble and R. White, Comment on "Parameter Sensitivity and Optimization Predictions of a Hydrogen/Oxygen Alkaline Fuel

- Cell Model", *Journal of the Electrochemical Society*, vol. 139, no. 9, p. 2686, 1992.
- [63] J.-H. Jo and S.-C. Yi, A Computational Simulation of an Alkaline Fuel Cell, *Journal of Power Sources*, vol. 84, no. 1, pp. 87-106, 1999.
- [64] R. E. Martin and M. A. Manzo, Alkaline Fuel Cell Performance Investigation, *23rd Intersociety Energy Conversion Engineering Conference*, pp. NASA TM-100937, 1988.
- [65] J. H. Jo, S. K. Moon and S. C. Yi, Simulation of Influences of Layer Thicknesses in an Alkaline Fuel Cell, *Journal of Applied Electrochemistry*, vol. 30, pp. 1023-1031, 2000.
- [66] G. Zhou, L.-D. Chen and J. P. Seaba, Modeling and Simulation of Electrolyte Transport in Alkaline Fuel Cells, Iowa City, Ph. D thesis, University of Iowa, 2007.
- [67] G. Zhou, L.-D. Chen and J. P. Seaba, Effects of Property Variation and Ideal Solution Assumption on the Calculation of the Limiting Current Density Condition of Alkaline Fuel Cells, *Journal of Power Sources*, vol. 196, p. 4923–4933, 2011.
- [68] G. Zhou, L.-D. Chen and J. P. Seaba, CFD Prediction of Shunt Currents Present in Alkaline Fuel Cells, *Journal of Power Sources*, vol. 196, p. 8180– 8187, 2011.
- [69] G. Lewis, M. Boland, J. McIntyre, N. Akhtar, C. Hütten, F. Kunz, J. Roes and A. Heinzl, Development of an Alkaline Fuel Cell Simulation Model - Electrochemistry and Mass Transfer -, Fuel Cells 2014 Science & Technology – A Grove Fuel Cell Event, Amsterdam, 2014.
- [70] F. A. E. Kunz, A. Heinzl and J. Roes, Verification and Validation of a Simulation Model of an Alkaline Fuel Cell (AFC), Master's thesis, Universität Duisburg-Essen, Duisburg, 2014.
- [71] I. Verhaert, M. D. Paepe and G. Mulder, Thermodynamic Model for an Alkaline Fuel Cell, *Journal of Power Sources*, vol. 193, pp. 233-240, 2009.
- [72] M. Dürr, S. Gair, A. Cruden and J. M. Donald, Dynamic Electrochemical Model of an Alkaline Fuel Cell Stack, *Journal of Power Sources*, vol. 171, pp. 1023-1032, 2007.

-
- [73] J. A. Schaeffer, L.-D. Chen and J. P. Seaba, Shunt Current Calculation of Fuel Cell Stack Using Simulink®, *Journal of Power Sources*, vol. 182, pp. 599-602, 2008.
- [74] I. Verhaert, S. Verhelst, G. Janssen, G. Mulder and M. D. Paepe, Water Management in an Alkaline Fuel Cell, *International Journal of Hydrogen Energy*, vol. 36, pp. 11011-11024, 2011.
- [75] H. Zhang, G. Lin and J. Chen, The Performance Analysis and Multi-Objective Optimization of a Typical Alkaline Fuel Cell, *Energy*, vol. 36, pp. 4327-4332, 2011.
- [76] I. Verhaert, S. Verhels, H. Huisseune, I. Poels and G. Janssen, Thermal and Electrical Performance of an Alkaline Fuel Cell, *Applied Thermal Engineering*, no. 40, pp. 227-235, 2012.
- [77] F. G. Will, Electrochemical Oxidation of Hydrogen on Partially Immersed Platinum Electrodes - I. Experiments and Interpretation, *Journal of the Electrochemical Society*, vol. 110, no. 2, pp. 145-151, 1963.
- [78] F. G. Will, Electrochemical Oxidation of Hydrogen on Partially Immersed Platinum Electrodes - II. Theoretical Treatment, *Journal of the Electrochemical Society*, vol. 110, no. 2, pp. 152-160, 1963.
- [79] S. G. Bratsch, Standard Electrode Potentials and Temperature Coefficients in Water at 298.15 K, *Journal of Physical and Chemical Reference Data*, vol. 18, no. 1, pp. 1-21, 1989.
- [80] W. Sheng, H. A. Gasteiger and Y. Shao-Horn, Hydrogen Oxidation and Evolution Reaction Kinetics on Platinum: Acid vs Alkaline Electrolytes, *Journal of the Electrochemical Society*, vol. 157, no. 11, pp. B1529-B1536, 2010.
- [81] K. F. Blurton, The Low-Temperature Polarization of Platinum-Catalyzed Air Cathodes in Alkaline Electrolyte, *Journal of the Electrochemical Society*, vol. 119, no. 12, pp. 1605-1609, 1972.
- [82] COMSOL, CFD Module - User's Guide 5.2a, vol. 5.2a, 2016.
- [83] COMSOL, Batteries & Fuel Cells Module - User's Guide 5.2a, vol. 5.2a, 2016.
- [84] R. B. Bird, W. E. Stewart and E. N. Lightfoot, *Transport Phenomena*, 2. ed., New York: John Wiley & Sons, 2007.

- [85] F. Kunz, A. Heinzl and J. Roes, Two-Dimensional, Non-Isothermal Simulation Model of an Alkaline Fuel Cell (AFC): Effect of Temperature on the Polarization Curve, *6th EUROPEAN PEFC & Electrolyser Forum 2017*, Lucerne, 2017.
- [86] COMSOL, Heat Transfer Module - User's Guide 5.2a, 2016.
- [87] Solomons and T. W. Graham, Organic Chemistry, 5. ed., United States of America: John Wiley & Sons, 1992.
- [88] B. E. Poling, J. M. Prausnitz and J. P. O'Connell, The Properties of Gases and Liquids, 5. ed., New York: Mc Graw-Hill, 2001.
- [89] Verein Deutscher Ingenieure (VDI), VDI-Wärmeatlas, 11. ed., Berlin, Heidelberg: Springer, 2013.
- [90] Verein Deutscher Ingenieure (VDI), VDI-Wärmeatlas, 10. ed., Berlin, Heidelberg: Springer, 2006.
- [91] D. M. Himmelblau, Solubilities of Inert Gases in Water. 0 °C. to Near the Critical Point of Water, *Journal of Chemical and Engineering Data*, vol. 5, no. 1, pp. 10-15, 1960.
- [92] S. K. Shoor and K. E. Gubbins, Solubility of Nonpolar Gases in Concentrated Electrolyte Solutions, *The Journal of Physical Chemistry*, vol. 73, no. 3, pp. 498-505, 1969.
- [93] S. K. Schoor, R. D. Walker, Jr. and K. E. Gubbins, Salting Out of Nonpolar Gases in Aqueous Potassium Hydroxide Solutions, *The Journal of Physical Chemistry*, vol. 73, no. 2, pp. 312-317, 1969.
- [94] M. K. Tham, R. D. Walker and K. E. Gubbins, Diffusion of Oxygen and Hydrogen in Aqueous Potassium Hydroxide Solutions, *The Journal of Physical Chemistry*, vol. 74, no. 8, pp. 1747-1751, 1970.
- [95] O. Söhnel and P. Novotny, Density of Aqueous Solutions of Inorganic Substances (Physical Science Data), vol. 22, Amsterdam: Elsevier, 1985.
- [96] G. Akerlof and P. Bender, The Density of Aqueous Solutions of Potassium Hydroxide, *Journal of the American Chemical Society*, vol. 63, no. 4, pp. 1085-1088, 1941.
- [97] M. K. Tham, K. E. Gubbins and R. D. Walker JR., Densities of Potassium Hydroxide Solutions, *Journal of Chemical and Engineering Data*, vol. 12, no. 4, pp. 525-526, 1967.

-
- [98] A. Seidell and W. F. Linke, Solubilities of Inorganic and Metal Organic Compounds, 4. ed., Washington D.C.: American Chemical Society, 1958.
- [99] I. N. Maksimova and S. V. Sergeev, Equations for Calculating Density, Viscosity, and Electrical Conductivity of Potassium Hydroxide Solutions at Temperature from -60 to +60 °C, *Journal of Applied Chemistry of the USSR*, vol. 47, no. 7, pp. 1712-1714, 1974.
- [100] G. C. Akerlof and P. Bender, Thermodynamics of Aqueous Solutions of Potassium Hydroxide, *Journal of the American Chemical Society*, vol. 70, no. 7, pp. 2366-2369, 1948.
- [101] N. R. Bhatia, K. E. Gubbins and R. D. Walker, Mutual Diffusion in Concentrated Aqueous Potassium Hydroxide Solutions, *Transactions of the Faraday Society*, vol. 64, pp. 2091-2099, 1968.
- [102] D. M. See and R. E. White, Diaphragm Cell Measurement of Mutual Diffusion Coefficients for Potassium Hydroxide in Water from 1 °C to 25 °C, *Journal of Chemical and Engineering Data*, vol. 43, no. 6, pp. 986-988, 1998.
- [103] A. L. Horvath, Handbook of Aqueous Electrolyte Solutions: Physical Properties, Estimation and Correlation Methods, New York: Ellis Horwood, 1985.
- [104] R. Appel, K. Cruse, P. Drossbach, H. Falkenhagen, G. G. Grau, G. Kelbg, E. Schmutzer and H. Strehlow, Landolt-Börnstein: Zahlenwerte und Funktionen aus Physik, Chemie, Astronomie, Geophysik und Technik, 6. ed., vol. 2, Berlin, Göttingen, Heidelberg: Springer, 1960.
- [105] D. M. See and R. E. White, Temperature and Concentration Dependence of the Specific Conductivity of Concentrated Solutions of Potassium Hydroxide, *Journal of Chemical and Engineering Data*, vol. 42, no. 6, pp. 1266-1268, 1997.
- [106] R. J. Gilliam, J. W. Graydon, D. W. Kirk and S. J. Thorpe, A Review of Specific Conductivities of Potassium Hydroxide Solutions for Various Concentrations and Temperatures, *International Journal of Hydrogen Energy*, vol. 32, pp. 359-364, 2007.
- [107] R. A. Robinson and R. H. Stokes, Electrolyte Solutions, 2. ed., London: Butterworth & Co., 1959.
- [108] Z. Losenicky, The Thermal Conductivity of Aqueous Solutions of Alkali Hydroxides, *The Journal of Physical Chemistry*, vol. 73, no. 2, pp. 451-452, 1969.

- [109] D. M. Ginzburg, V. E. Kochkaldal and N. I. Guba, Enthalpies and Heat Capacities in the Potassium Hydroxide-Water System, *Russian Journal of Physical Chemistry*, vol. 47, no. 8, pp. 1214-1215, 1973.
- [110] Toray, Fuel Cells Etc, [Online]. Available:
<http://www.fuelcellsetc.com/store/DS/Toray-Paper-TGP-H-Datasheet.pdf>.
[Accessed 21 04 2018].
- [111] D. R. Lide, CRC Handbook of Chemistry and Physics, 90. ed., New York: Taylor & Francis Group, 2009.
- [112] AFC Energy PLC.
- [113] F. R. Brushett, M. S. Naughton, J. W. D. Ng, L. Yin and P. J. A. Kenis, Analysis of Pt/C Electrode Performance in a Flowing-Electrolyte Alkaline Fuel Cell, *International Journal of Hydrogen Energy*, vol. 37, pp. 2559-2570, 2012.

List of Figures

Figure 2.1: Fuel cell operating principle at the example of an AFC.	5
Figure 2.2: Gas voltaic battery by Sir William Robert Grove (taken from [8]).	6
Figure 2.3: General polarization curve of a fuel cell (cf. [3]).	14
Figure 2.4: Schematic illustration of the energetic barrier in the double layer (cf. [40]). ...	25
Figure 2.5: Graphical derivation of kinetic parameters.	36
Figure 4.1: Model schema.	58
Figure 4.2: Flooded agglomerate with electrolyte film.	59
Figure 4.3: Viscosity of the KOH electrolyte vs. T	96
Figure 4.4: Viscosity of the KOH electrolyte vs. w_e	97
Figure 4.5: Logarithm of the activity coefficient of the KOH electrolyte plotted vs. c_e	98
Figure 4.6: Calculated diffusion coefficient D_c plotted vs. c_e	101
Figure 4.7: Calculated diffusion coefficient D_c plotted vs. T	101
Figure 5.1: Comparison of the simulation results with measurement.	115
Figure 5.2: Electrolyte concentration in the cell (vertically scaled by the factor 0.1).	117
Figure 5.3: Temperature distribution in the cell (vertically scaled by the factor 0.1).	119
Figure 5.4: Hydrogen and oxygen mole fractions (vertically scaled by the factor 0.1). ...	121
Figure 5.5: Effects of the potential losses on the polarization curve (cumulative).	123
Figure 5.6: Henry constant for the solubility of hydrogen in KOH.	125
Figure 5.7: Henry constant for the solubility of oxygen in KOH.	125
Figure 5.8: Diffusion coefficient of hydrogen in the KOH electrolyte.	126
Figure 5.9: Diffusion coefficient of oxygen in the KOH electrolyte.	127
Figure 5.10: Variation of the electrolyte concentration.	129
Figure 5.11: Henry constant for the solubility of hydrogen in KOH vs. c_e	132
Figure 5.12: Henry constant for the solubility of oxygen in KOH vs. c_e	133
Figure 5.13: Equilibrium potential calculated with the Nernst equation.	133
Figure 5.14: Electrical conductivity of the KOH electrolyte.	134
Figure 5.15: Diffusion coefficient of hydrogen in KOH vs. c_e	134
Figure 5.16: Diffusion coefficient of oxygen in KOH vs. c_e	135
Figure 5.17: Effect of the operating pressure on the polarization curve.	136
Figure 5.18: Effect of the temperature on the polarization curve.	137
Figure 5.19: Exchange current densities vs. T	138
Figure 5.20: Diffusion coefficient of hydrogen in KOH vs. T	139
Figure 5.21: Diffusion coefficient of oxygen in KOH vs. T	140

Figure 5.22: Effect of temperature on the polarization curve for $\alpha_f \neq f(T)$ 141

Figure 5.23: Effect of temperature on the polarization curve for $\alpha_f \neq f(T), i_0 \neq f(T)$. 142

Figure 5.24: Effect of $i_0^A a_l^A$ on the polarization curve. 145

Figure 5.25: Effect of $i_0^C a_l^C$ on the polarization curve..... 146

Figure 5.26: Effect of α_{\ddagger}^A on the polarization curve..... 147

Figure 5.27: Effect of α_{\ddagger}^C on the polarization curve..... 148

Figure 5.28: Effect of a_g^A/d_l^A on the polarization curve. 150

Figure 5.29: Effect of a_g^C/d_l^C on the polarization curve..... 150

List of Tables

Table 2.1: Common fuel cells and their characteristics 9

Table 4.1: Definitions of boundaries and regions in the model 61

Table 4.2: Kinetic parameters 69

Table 4.3: Molar masses [87]..... 89

Table 4.4: Parameters for the gas viscosities [89]..... 90

Table 4.5: Atomic diffusion volumes of the gases [88] 90

Table 4.6: Parameters for the thermal conductivities of the gases [90] 91

Table 4.7: Parameters for the heat capacities of the gases [90] 92

Table 4.8: Parameters for the Henry constants of hydrogen and oxygen [91]..... 93

Table 4.9: Parameters for the diffusion coefficients of H₂ and O₂ in KOH [66] 94

Table 4.10: Parameters for density of the KOH electrolyte [95] 95

Table 4.11: Parameters for the heat capacity of the KOH electrolyte [109]..... 104

Table 4.12: Electrode properties 105

Table 4.13: Structure parameters of the electrodes 105

Table 4.14: Reference concentrations 110

Table 5.1: Cell geometries 112

Table 5.2: Base case operating conditions 113

Table 5.3: Parameters specific to the anodic CL and the cathodic CL 113

Table 5.4: Parameters specific to the electrochemical reactions..... 114

List of Abbreviations

1-D	One-dimensional
2-D	Two-dimensional
AFC	Alkaline fuel cell
AR	Anode reaction
BMWI	German Federal Ministry of Economics and Technology
CL	Catalyst layer
CR	Cathode reaction
DMFC	Direct Methanol Fuel Cell
EEG	German Renewable Energy Sources Act
FCH JU	Fuel Cells and Hydrogen Joint Undertaking
GDL	Gas diffusion layer
HOR	Hydrogen oxidation reaction
IHP	Inner Helmholtz plane
KOH	Potassium hydroxide
MCFC	Molten Carbonate Fuel Cell
NASA	National Aeronautics and Space Administration
OCV	Open cell voltage
OHP	Outer Helmholtz plane
ORR	Oxygen reduction reaction
PAFC	Phosphoric Acid Fuel Cell
PEMFC	Proton exchange membrane fuel cell
PTFE	Polytetrafluorethylene
RL	Reaction layer
SHE	Standard hydrogen electrode
SL	Support layer
SOFC	Solid Oxide Fuel Cell
TPB	Triple phase boundary

List of Symbols

Roman

a_g	Specific surface area of the electrolyte, m^2/m^3
a_i	Activity of species i , 1
a_l	Specific surface area of the electrode where the reaction occurs, m^2/m^3
c_0	Solvent concentration, mol/m^3
c_i	Concentration of species i , mol/m^3
c_i^0	Concentration of species i under equilibrium conditions (belonging to i_0), mol/m^3
$c_{O_2}^{g/l}$	Concentration of species i in the electrolyte at the gas/liquid interface, mol/m^3
$c_i^{l/a}$	Concentration of species i in the electrolyte at the electrolyte film/agglomerate interface, mol/m^3
c_i°	Dimensionless concentration of species i , 1
c_T	Total concentration, mol/m^3
C_p	Specific heat capacity, $\text{J}/(\text{kg}\cdot\text{K})$
d_g	Diffusion length in the gas phase, m
d_l	Electrolyte film thickness, m
d_{cell}	Cell depth (third dimension), m
D	Diffusion coefficient of the concentrated electrolyte that can be measured, m^2/s
D_c	Diffusion coefficient on the concentration scale, m^2/s
D_i	Diffusion coefficient of species i , m^2/s
D_i^*	Designed diffusion coefficient of species i with respect to the volume average velocity (based on the concentrated electrolyte theory but for the use in the Nernst-Planck equation), m^2/s
D_i^T	Thermal diffusion coefficient of species i , m^2/s
D_m	Diffusion coefficient of the diluted electrolyte that can be measured, m^2/s
\mathfrak{D}	Thermodynamic diffusion coefficient of the electrolyte, m^2/s
\mathfrak{D}_{ij}	Binary diffusion coefficient of species i and j , m^2/s
\mathfrak{D}_{ik}	Binary Maxwell-Stefan diffusion coefficient of species i and k , m^2/s
\mathfrak{D}_{ik}^{eff}	Effective binary Maxwell-Stefan diffusion coefficient of species i and k , m^2/s

\mathbb{D}_{ik}	Binary Fick diffusion coefficient of species i and k , m^2/s
E	Potential, V
E_0	Reversible cell voltage, V
$E_j, E_j(\Delta\phi)$	Activation energy of reaction j dependent from $\Delta\phi$, J/mol
E_j^0	Chemical activation free energy of reaction j , J/mol,
E_T	Temperature dependent reversible cell voltage, V
E_0^{Ref}	Reference reversible cell voltage, e.g. under standard conditions, V
E_{Act}^0	Activation energy that can be measured, J/mol
F	Faraday's constant, 96,485 A·s/mol
g	Gravity constant, 9.81 m/s^2
G	Gibbs free energy, J
Δg_R	Gibbs free energy of the reaction, J/mol
h_{cell}	Cell height, m
$h_{Channel}^{Top}$	Height of the upper channel extension, m
$h_{Channel}^{Bottom}$	Height of the lower channel extension, m
Δh_v^A	Enthalpy of evaporation of water, J/mol
H	Enthalpy, J
H_i^e	Henry constant of species i for the solubility in the electrolyte on the concentration scale, $\text{mol}/(\text{Pa}\cdot\text{m}^3)$
H_i^w	Henry constant of species i for the solubility in the water (on the molar fraction scale), Pa
i	Electrical current density, A/m^2
i_0	Exchange current density, A/m^2
$i_{0,A}$	Exchange current density at state A (T_A), A/m^2
$i_{0,B}$	Exchange current density at state B (T_B), A/m^2
i_{00}	Exchange current density at fixed concentrations c^0 and fixed temperature T^0 , A/m^2
i_+^0	Exchange current density written with the kinetic parameters of the oxidation reaction (anodic reaction), A/m^2
i_-^0	Exchange current density written with the kinetic parameters of the reduction reaction (cathodic reaction); A/m^2
i_j	Current density of the partial reaction j , A/m^2

i_l	Current density through the electrolyte (liquid phase), A/m ²
j_i	Relative flux of species i , kg/(m ² ·s)
k	Thermal conductivity, W/(m·K)
k_i^s	Salting out coefficient of species i , m ³ /mol
k_j	Reaction constant of reaction j ; its units depend on the reaction order of the reaction, mol/(m ³ ·s) / $[\prod_h c_h^{\nu_h}]$
k'_j	Reaction constant of reaction j which is only dependent on temperature; its units depend on the reaction order of the reaction, mol/(m ³ ·s) / $[\prod_h c_h^{\nu_h}]$
K_{ij}	Binary drag coefficient of species i and j , J·s/m ⁵
m	Molality, mol/kg
M_i	Molar mass of species i , kg/mol
M_{Ox}	Represents the chemical composition of the reactant species of the reduction reaction, -
M_{Red}	Represents the chemical composition of the product species of the reduction reaction, -
n	Number of exchanged electrons, 1
N_i	Species number, mol
N_i	Molar flux of species i , mol/(m ² ·s)
N_i^m	Mass specific flux of species i , kg/(m ² ·s)
p	Pressure, Pa
p_i	Partial pressure of species i , Pa
p_i°	Dimensionless partial pressure of species i , Pa
p_s	Saturation pressure, Pa
\dot{q}_c	Heat flux due to thermal conduction, W/m ²
Q	Heat, J
Q_l	Electrical current source with respect to the liquid phase, A/m ³
Q_{rev}	Reversible heat, J
Q_s	Electrical current source with respect to the solid phase, A/m ³
\dot{Q}	Heat source, W/m ³
\dot{Q}_{irrev}	Irreversible heat of the reaction, W/m ³
\dot{Q}_{JH}	Joule heat, W/m ³
\dot{Q}_{JH}^{tot}	Total Joule heat, W/m ³

\dot{Q}_{rev}	Reversible heat of the reaction, W/m ³
\dot{Q}_v	Evaporation heat, W/m ³
r_i	Reaction rate of reaction j , mol/(m ³ ·s)
R	General gas constant, 8.314 J/(mol·K)
R	Reaction rate, mol/(m ³ ·s)
R^m	Mass specific reaction rate, kg/(m ³ ·s)
R_i^{sol}	Solution rate of species i into the electrolyte, mol/(m ³ ·s)
R_i^{elec}	Electrochemical reaction rate of species i , mol/(m ³ ·s)
s_i	Molar entropy of species i , J/(mol·K)
s_i	Stoichiometric coefficient of species i , 1
s_{Tafel}	Tafel slope, V/dec
S	Entropy, J/K
t_i	Transference number of species i , 1
t_i^0	Transference number of species i with respect to the solvent velocity, 1
t_i^*	Transference number of species i with respect to the volume average velocity, 1
T	Temperature, K
T_A	Temperature at state A, K
T_B	Temperature at state B, K
T_c	Critical temperature of water, 647 K
T^0	Temperature belonging to i_0 , K
u_i	Mobility of species i , mol·s/kg
u_i	Velocity of species i , m/s
U	Cell voltage, V
U	Internal energy, J
v	Velocity, m/s
v_0	Solvent velocity, m/s
v_i	Molar volume of species i , m ³ /mol
v^*	Volume average velocity, m/s
V	Volume, m ³
$w_{Channel}^A$	Thickness of the anodic gas channel, m
$w_{Channel}^C$	Thickness of the cathodic gas channel, m

$w_{Channel}^E$	Thickness of the electrolyte channel, m
w_{SL}^A	Thickness of the anodic SL, m
w_{SL}^C	Thickness of the cathodic SL, m
w_{GDL}^A	Thickness of the anodic GDL, m
w_{GDL}^C	Thickness of the cathodic GDL, m
w_{CL}^A	Thickness of the anodic CL, m
w_{CL}^C	Thickness of the cathodic CL, m
W	Work, J
W_m	Mechanical work, J
W_e	Electrical work, J
w_e	Specific work provided by the reaction, J/mol
w_i	Mass fraction of species i , 1
x_i^e	Mole fraction of species i in the electrolyte, 1
x_i^w	Mole fraction of species i in water, 1
z_i	Charge number of species i , 1

Greeks

α_+	Anodic symmetry factor; anodic transfer coefficient, 1
α_-	Cathodic symmetry factor; cathodic transfer coefficient, 1
γ	Activity coefficient, 1
γ_{\pm}	Mean molal activity coefficient of the electrolyte, 1
ε	Porosity, 1
ϵ_j	Algebraic sign of reaction j : $\epsilon_+ = +1$; $\epsilon_- = -1$
η	Overpotential, V
η^*	Overpotential comprising η_s and concentration losses partly (without η_N), V
η^{**}	Overpotential comprising η_s and concentration losses (including η_N), V
η_{Act}	Activation overpotential, V
η_{Conc}	Concentration overpotential, V
η_j^{Act}	Activation overpotential of reaction j , V
η_j^{conc}	Concentration overpotential of reaction j , V
η_N	Nernstian concentration losses, V

η_{Ohm}	Ohmic overpotential, V
η_s	Surface overpotential, V
θ_φ	Volume fraction of phase φ , 1
θ_{SL}^φ	Volume fraction of phase φ in the SL, 1
θ_{GDL}^φ	Volume fraction of phase φ in the GDL, 1
θ_{CL}^φ	Volume fraction of phase φ in the CL, 1
ϑ_h	Reaction order of species h , 1
κ	Electrical conductivity, S/m
κ	Permeability, m ²
κ_{SL}	Permeability of the SL, m ²
κ_{GDL}	Permeability of the GDL, m ²
κ_{CL}	Permeability of the CL, m ²
λ_e	Thermal conductivity of the electrolyte, W/(m·K)
λ_i	Ionic equivalent conductivity of species i , S·m ² /mol
λ_i	Stoichiometry of species i (reciprocal value of the conversion efficiency), 1
λ_w	Thermal conductivity of water, W/(m·K)
λ_i^0	Limiting equivalent conductivity of species i , S·m ² /mol
λ_\pm^0	Proportionality constant for the molal activity of the electrolyte, kg/mol
Λ	Equivalent conductance, S·m ² /mol
μ	Viscosity, Pa·s
μ_e	Chemical potential of the electrolyte, J/mol
μ_i	Chemical potential of species i , J/mol
μ_i^*	Electrochemical potential of species i , J/mol
$\Delta\mu_R$	Chemical potential of the reaction, J/mol
$\Delta\mu_R^*$	Electrochemical potential of the reaction, J/mol
ν_i	Stoichiometric coefficient of species i , 1
ν_i	Dissociation number of species i , 1
ν	Dissociation number of the electrolyte, 1
ξ^A	Anodic hydrogen concentration coefficient, 1
ξ^C	Cathodic oxygen concentration coefficient, 1
ρ	Density, kg/m ³

σ	Electrical conductivity, S/m
τ	Tortuosity, 1
ϕ	Electrical potential, V
$\Delta\phi$	Electrical potential in the interface, V
$\Delta\phi_0$	Electrical potential in the interface under equilibrium conditions; equilibrium potential, V
ϕ_i	Electrical potential of species i , V
$\Delta\phi_R$	Electrical potential of the reaction, V

Superscripts

0	Standard state
0	Equilibrium state
0	Solvent
A	Anode
C	Cathode
CC	Current collector
in	Initial, inlet
l	Liquid
Ref	Reference state
s	Solid
T	Transposed

Subscripts

0	Equilibrium state
0	Solvent
+	Oxidation reaction; anodic current
+	Positive charged ions; cations
–	Reduction reaction; cathodic current
–	Negative charged species; anions
A	Anode
b	Backward (reverse) reaction
$cell$	Cell
C	Cathode

<i>f</i>	Forward reaction
<i>e</i>	Electrolyte
<i>h</i>	Species <i>h</i>
<i>i</i>	Species <i>i</i>
<i>j</i>	Reaction <i>j</i>
<i>j</i>	Species <i>j</i>
<i>k</i>	Species <i>k</i>
<i>l</i>	Species <i>l</i>
<i>l</i>	Liquid phase
<i>Ox</i>	Oxidized species; reactant of the reduction reaction
<i>Red</i>	Reduced species; product of the reduction reaction
<i>SHE</i>	Standard hydrogen electrode
<i>T</i>	Temperature dependent parameter
<i>w</i>	Water
φ	Phase φ ; stands for gas, liquid, or solid

Scientific contributions

Oral presentations

G. Lewis, M. Boland, J. McIntyre, N. Akhtar, C. Hütten, F. Kunz, J. Roes and A. Heinzl, Development of an Alkaline Fuel Cell Simulation Model - Electrochemistry and Mass Transfer -, Fuel Cells 2014 Science & Technology – A Grove Fuel Cell Event, Amsterdam, 2014.

F. Kunz, A. Heinzl and J. Roes, Two-Dimensional, Non-Isothermal Simulation Model of an Alkaline Fuel Cell (AFC): Effect of Temperature on the Polarization Curve, *6th EUROPEAN PEFC & Electrolyser Forum 2017*, Lucerne, 2017.

Posters

F. Kunz, A. Heinzl and J. Roes, Two-Dimensional, Non-Isothermal Simulation Model of an Alkaline Fuel Cell (AFC): Effect of Temperature on the Polarization Curve, *6th EUROPEAN PEFC & Electrolyser Forum 2017*, Lucerne, 2017.

DuEPublico

Duisburg-Essen Publications online

UNIVERSITÄT
DUISBURG
ESSEN

Offen im Denken

ub | universitäts
bibliothek

Diese Dissertation wird über DuEPublico, dem Dokumenten- und Publikationsserver der Universität Duisburg-Essen, zur Verfügung gestellt und liegt auch als Print-Version vor.

DOI: 10.17185/duepublico/70291

URN: urn:nbn:de:hbz:464-20190718-134433-0

Alle Rechte vorbehalten.